Prediction of non-linear responses and bifurcations of impacting systems : Contribution to the understanding of steam generator vibrations

Roberto Alcorta Galvan

N° d'ordre NNT :2021LYSEI032

THÈSE de DOCTORAT DE L'UNIVERSITÉ DE LYON
préparée au sein de
l'INSA LYON

École Doctorale ED 162 MEGA
Mécanique, Énergétique, Génie Civil, Acoustique

Spécialité de doctorat :
MÉCANIQUE - GÉNIE MÉCANIQUE - GÉNIE CIVIL

Soutenue publiquement le 27/05/2021, par :
Roberto ALCORTA

Prediction of non-linear responses and bifurcations of impacting systems: Contribution to the understanding of steam-generator vibrations

Devant le jury composé de

A. TANGUY	Professeur, ONERA, LaMCoS, INSA-LYON	Examinatrice
C. TOUZÉ	Professeur, IMSIA, ENSTA	Rapporteur
A. LAZARUS	Maître de Conférences HDR, Institut Jean le Rond d'Alembert	Rapporteur
G. JACQUET	Professeur, LaMCoS, INSA-LYON	Directeur de thèse
S. BAGUET	Maître de Conférences, LaMCoS, INSA-LYON	Co-Encadrant
B. PRABEL	Ingénieur chercheur HDR, CEA-Saclay	Co-Encadrant
S. TERRIEN	Chargée de recherche CNRS, LAUM	Examinatrice
B. COCHELIN	Professeur, LMA, Centrale Marseille	Examinateur
L. SALLES	Docteur, Imperial College London	Invité

LaMCoS - UMR CNRS 5259 - INSA de Lyon
20, avenue Albert Einstein, 69621 Villeurbanne Cedex (France)

Département FEDORA – INSA Lyon - Ecoles Doctorales

SIGLE	ECOLE DOCTORALE	NOM ET COORDONNEES DU RESPONSABLE
CHIMIE	**CHIMIE DE LYON** **https://www.edchimie-lyon.fr** Sec. : Renée EL MELHEM Bât. Blaise PASCAL, 3e étage secretariat@edchimie-lyon.fr	**M. Stéphane DANIELE** C2P2-CPE LYON-UMR 5265 Bâtiment F308, BP 2077 43 Boulevard du 11 novembre 1918 69616 Villeurbanne **directeur@edchimie-lyon.fr**
E.E.A.	**ÉLECTRONIQUE, ÉLECTROTECHNIQUE, AUTOMATIQUE** **https://edeea.universite-lyon.fr** Sec. : Stéphanie CAUVIN Bâtiment Direction INSA Lyon Tél : 04.72.43.71.70 secretariat.edeea@insa-lyon.fr	**M. Philippe DELACHARTRE** INSA LYON Laboratoire CREATIS Bâtiment Blaise Pascal, 7 avenue Jean Capelle 69621 Villeurbanne CEDEX Tél : 04.72.43.88.63 **philippe.delachartre@insa-lyon.fr**
E2M2	**ÉVOLUTION, ÉCOSYSTÈME, MICROBIOLOGIE, MODÉLISATION** **http://e2m2.universite-lyon.fr** Sec. : Sylvie ROBERJOT Bât. Atrium, UCB Lyon 1 Tél : 04.72.44.83.62 secretariat.e2m2@univ-lyon1.fr	**M. Philippe NORMAND** Université Claude Bernard Lyon 1 UMR 5557 Lab. d'Ecologie Microbienne Bâtiment Mendel 43, boulevard du 11 Novembre 1918 69 622 Villeurbanne CEDEX **philippe.normand@univ-lyon1.fr**
EDISS	**INTERDISCIPLINAIRE SCIENCES-SANTÉ** **http://ediss.universite-lyon.fr** Sec. : Sylvie ROBERJOT Bât. Atrium, UCB Lyon 1 Tél : 04.72.44.83.62 secretariat.ediss@univ-lyon1.fr	**Mme Sylvie RICARD-BLUM** Institut de Chimie et Biochimie Moléculaires et Supramoléculaires (ICBMS) - UMR 5246 CNRS - Université Lyon 1 Bâtiment Raulin - 2ème étage Nord 43 Boulevard du 11 novembre 1918 69622 Villeurbanne Cedex Tél : +33(0)4 72 44 82 32 **sylvie.ricard-blum@univ-lyon1.fr**
INFOMATHS	**INFORMATIQUE ET MATHÉMATIQUES** **http://edinfomaths.universite-lyon.fr** Sec. : Renée EL MELHEM Bât. Blaise PASCAL, 3e étage Tél : 04.72.43.80.46 infomaths@univ-lyon1.fr	**M. Hamamache KHEDDOUCI** Université Claude Bernard Lyon 1 Bât. Nautibus 43, Boulevard du 11 novembre 1918 69 622 Villeurbanne Cedex France Tél : 04.72.44.83.69 **hamamache.kheddouci@univ-lyon1.fr**
Matériaux	**MATÉRIAUX DE LYON** **http://ed34.universite-lyon.fr** Sec. : Yann DE ORDENANA Tél : 04.72.18.62.44 yann.de-ordenana@ec-lyon.fr	**M. Stéphane BENAYOUN** Ecole Centrale de Lyon Laboratoire LTDS 36 avenue Guy de Collongue 69134 Ecully CEDEX Tél : 04.72.18.64.37 **stephane.benayoun@ec-lyon.fr**
MEGA	**MÉCANIQUE, ÉNERGÉTIQUE, GÉNIE CIVIL, ACOUSTIQUE** **http://edmega.universite-lyon.fr** Sec. : Stéphanie CAUVIN Tél : 04.72.43.71.70 Bâtiment Direction INSA Lyon mega@insa-lyon.fr	**M. Jocelyn BONJOUR** INSA Lyon Laboratoire CETHIL Bâtiment Sadi-Carnot 9, rue de la Physique 69621 Villeurbanne CEDEX **jocelyn.bonjour@insa-lyon.fr**
ScSo	**ScSo*** **https://edsciencessociales.universite-lyon.fr** Sec. : Mélina FAVETON INSA : J.Y. TOUSSAINT Tél : 04.78.69.77.79 melina.faveton@univ-lyon2.fr	**M. Christian MONTES** Université Lumière Lyon 2 86 Rue Pasteur 69365 Lyon CEDEX 07 **christian.montes@univ-lyon2.fr**

*ScSo : Histoire, Géographie, Aménagement, Urbanisme, Archéologie, Science politique, Sociologie, Anthropologie

Contents

List of Figures

List of Tables

General Overview

Heat-exchange applications -such as boilers, evaporators and condensers- make use of tube bundles as their key component. The main idea is to accumulate a large number of fluid-carrying tubes inside a vessel which encloses the main fluid flow, from which heat is to be either transferred or extracted. Temperature differences between the fluid on both sides of the tubes leads to heat transfer over a large effective contact area, thus rendering the process highly efficient. The span of applications for tube bundles is thus enormous, ranging from the pharmaceutical to the aerospace industries and covering virtually everything in between. They have a particular importance in nuclear power generation, as Steam Generators (SG) constitute the link between the primary coolant loop -which carries the hot, radioactive fluid from the reactor- and the secondary loop -with clean fluid destined to the production of steam-. Ensuring integrity of the tubes in this case is thus a major concern for economical as well as safety reasons. Hence, the past decades have seen significant efforts been made to better understand the behaviour of tube bundles. This has proved to be a challenging task, as the multi-physics setup involving flow-induced vibrations within a two-phase, turbulent flow, is extremely complex. While outstanding developments have been accomplished, namely in the form of technological solutions to mitigate excessive vibrations, a full understanding of the problem is yet to be reached today, both in terms of the fluid-elastic coupling mechanisms responsible for vibrations and the efficient prediction of long-term tube dynamics, especially in abnormal situations (e.g., misalignment, widened gaps due to wear, excessively fast flows).

One part of the issue is thus a modelling problem, in which one seeks to accurately described the fluid-elastic coupling phenomena. On the other hand, once a reasonable model has been found, one must be able to exploit it thoroughly for predictive analyses. Due to the geometrical complexity of engineering structures and the non-linear nature of their governing equations, this necessarily calls for the use of numerical methods, which must be both accurate and efficient for practical predictive analyses. In this regard it must be noted that the traditional approach, which consists in using time-integration algorithms to obtain the predicted history of motions for the tubes, is not well-suited for industrial use, mainly due to: the small time steps necessary to capture tube-support impacts, the numerous degrees of freedom, and the large number of parameters to be varied in order to fully cover the range of possible outcomes. The latter of these aspects is all the more important when nonlinear equations are involved, as it is well known that some parameter combinations lead to coexisting vibration regimes, some of which may

be undesirable (for instance, permanent friction must be avoided if possible in order to limit premature failure due to wear). Specialized techniques are thus required to map the parameter space of a given system and associate each of the regimes to a particular dynamical behaviour, thus allowing a full control of the problem and even an optimal design.

The present thesis aims to contribute to the solution of the second of the aforementioned problems, namely: the development of reliable and fast algorithms for the parametric analysis of nonlinear flow-induced vibration problems. More precisely, the objectives sought are:

- to generalize the existing methods for frequency-domain bifurcation analysis to arbitrary codimension,
- to extend the stability analysis methods to dynamical systems with memory and to quasi-periodic solutions,
- to create a robust numerical platform for these methods, rending them available for practical engineering use, and
- to study simplified systems representative of the SG vibration phenomenology, including experimental validation of results when possible.

This manuscript is divided into two parts, with the first one dedicated to the development of numerical methods. Chapter 1 presents a state of the art covers the previous attempts to tackle the SG vibration problem, as well as the corresponding framework from the theory of nonlinear dynamical systems and the associated numerical and mathematical techniques. This justifies the structure of the thesis and the need for the developments herein presented.
Chapter 2 establishes the selected framework for numerical analysis, which consists of a frequency-domain solver employing the Harmonic Balance Method (HBM) coupled to a continuation algorithm equipped with stability analysis and bifurcation detection. Furthermore, the numerical contributions are described in detail.
The second part contains the application of these methods to selected systems related to SG vibrations.
Chapter 3 deals with forced systems with impacts, in which fluid flows are absent. Experimental measurements are used to validate numerical results.
Finally, chapter 4 presents a purely numerical analysis of two simplified systems with a memory effect due to fluid-elastic coupling. The latter one, in particular, is a realistic representation of a U-tube typically found with SG bundles.

Chapter 1

State of the Art

This chapter offers an overview of the current state of the art regarding steam-generator vibrations.
Firstly, the concept of fluidelastic instability is presented and its importance is stressed within the industrial context of pressurised water reactors. A detailed summary of the associated scientific literature follows, which leads to identifying the key aspects of the underlying dynamics problem. Next, the theoretical considerations of said aspects are reviewed; this includes stability, bifurcations, linear and nonlinear modal analyses, flow-induced vibrations and contact mechanics. Finally, the currently-available numerical tools and techniques for assessing the nonlinear dynamical behaviour of structures are discussed. This review motivates the numerical developments presented in the following chapter, as well as the choice of systems studied in Chapter 3.

Contents

1.1 Vibration Hazard in Steam Generators

Inside a nuclear power plant of the Pressurized Water Reactor (PWR) type, steam generators play the role of liquid-liquid heat exchangers between the coolants in the primary and secondary circuits. The latter of these is destined to be evaporated by absorption of heat from the former, which flows from the reactor core. More precisely, heat exchange takes place across the walls of U-shaped tubes, tightly-packed in a bundle (typically consisting of around 3000 tubes in modern PWRs) inside the steam-generator vessel. A typical design for this device, showing a single tube, is presented in Fig. 1.1.

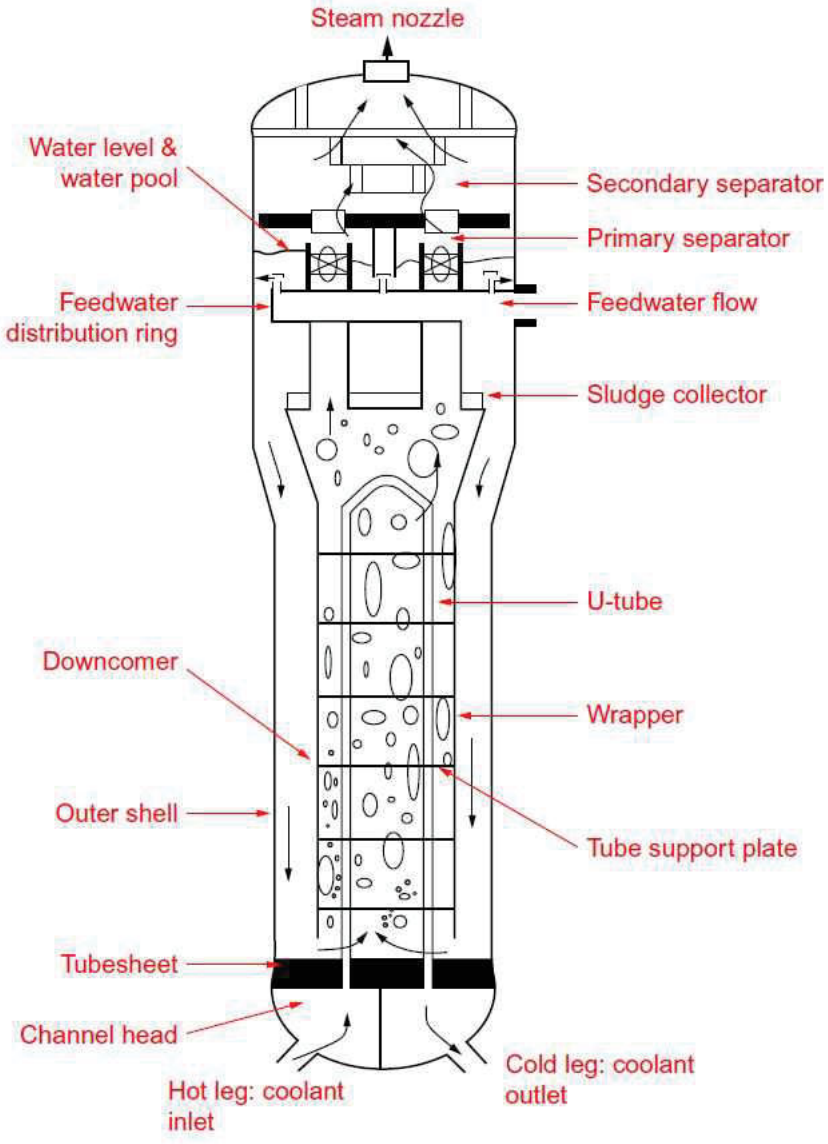

Figure 1.1: Schematic view of a PWR steam generator. From [RIZ 17].

High-temperature coolant from the primary circuit enters a tube via the *hot leg*, flows along the entire span while giving off its heat to the surrounding coolant, and exits at a lower temperature through the *cold leg*. Meanwhile, an upwards two-phase develops inside the inner shell as the secondary coolant evaporates. Steam is filtered by separators and exits the vessel through the uppermost nozzle, while any leftover liquid flows back into the inner shell along with an external water feed. This recirculating flow acts on the tube bundle in two distinct manners: parallelly along the legs (axial flow), and transversally on the U-bends (cross-flow). At several locations, the legs are held in place by support plates.

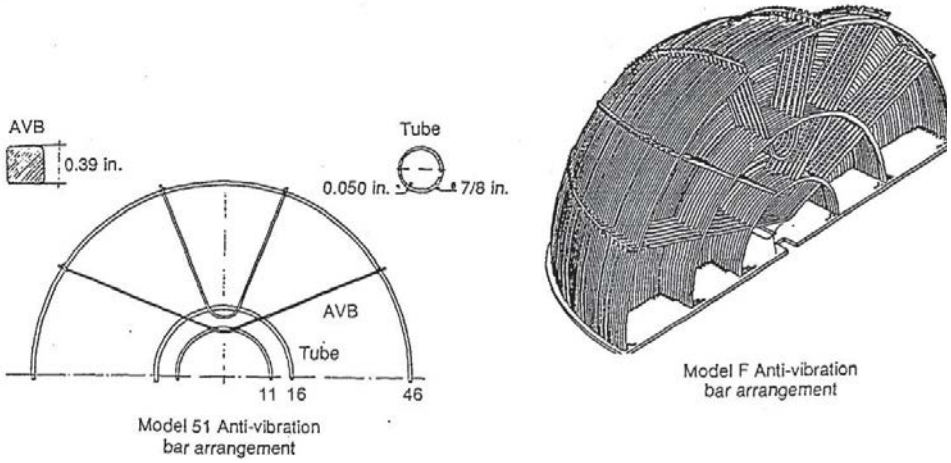

Figure 1.2: Typical recirculating steam generator AVB arrangement. From [MAC 96].

The tube bundles serve a double purpose: on one hand, they act as a barrier between the radioactive, pressurised coolant from the primary cycle; on the other, they ensure efficient steam generation, which renders the production of power possible through the action of a specialized turbine. As such, ensuring their integrity is of vital importance for safe and reliable power plant operation. Indeed, ruptures in the primary coolant circuit are a major practical concern, and were thus the topic of some of the earliest engineering literature published during the early days of nuclear power generation [MEL 65, GAL 66]. Weaver [WEA 08] references works on vibration and noise in steam generators from as far back as 1954. As pointed out in the review by Païdoussis [PAI 81], however, steam-generator problems such as tube failure, which could be brought about by flow-structure interactions, were rarely (if ever) encountered in practice until the seventies. This situation changed drastically as advanced steam generator designs incorporated more compact bundles and higher flow velocities: while this changes led to enhanced efficiency, they come at the price of increasing the overall kinetic energy of the flow. Strong coupling between fluid flow and structural response ensues, which has lead to dramatic economical consequences. As explained in the thesis of Antunes [ANT 86], a 100-hour shutdown of a 1000 MW power plant yields a cost of roughly 3 million US dollars. The 1996 report by the U.S. Nuclear Regulatory Commission [MAC 96] directly cites flow-induced vibrations as the direct precursor of tube failure by fretting

wear. This happens especially at the U-bend region of the tubes, due to tube-to-tube or tube-to-Anti-Vibration Bar (AVB) impacts. As shown in Fig. 1.2, AVBs are installed as a means to prevent high-amplitude, out-of-plane vibration of the tube zones excited by cross-flow. While only narrow gaps are left between tubes and AVBs to allow for thermal expansion of the former under temperature gradients, these can be widened due to misalignment, wear, or other factors, causing abnormal situations in which strong impacts and friction lead to accelerated failure, i.e. a life-span of days rather than years. Improper AVB support has also been reported to lead to high-cycle fatigue [EPR02]. Furthermore, in-plane vibrations have caused tube failures as well, as evidenced by the now-famous malfunction and ultimate total shutdown of the San Onofre Nuclear Generating Station on the Californian coast in 2012, following from a design error which led to abnormally severe thermo-hydraulic conditions [DAP 15].

Besides steam-generator tubes, other components of nuclear reactors are also subjected to flow-induced vibrations, mainly fuel rod assemblies [CHE 72]. Moreover, a great number of applications outside of nuclear power engineering face similar issues: steam condensers [LEE 17], boilers [PAN 12], turbo-compressors [JUN 97] and pipelines [FAA 11], to name but a few. In the present thesis, attention will be focused exclusively on cross-flow excitations, as they lead to the highest response amplitudes and, hence, the greatest vibration risk.

1.1.1 Excitation mechanisms

Fig. 1.3 schematically shows the ideal evolution of response amplitudes for tubes in cross-flow with varying mean transverse velocity.

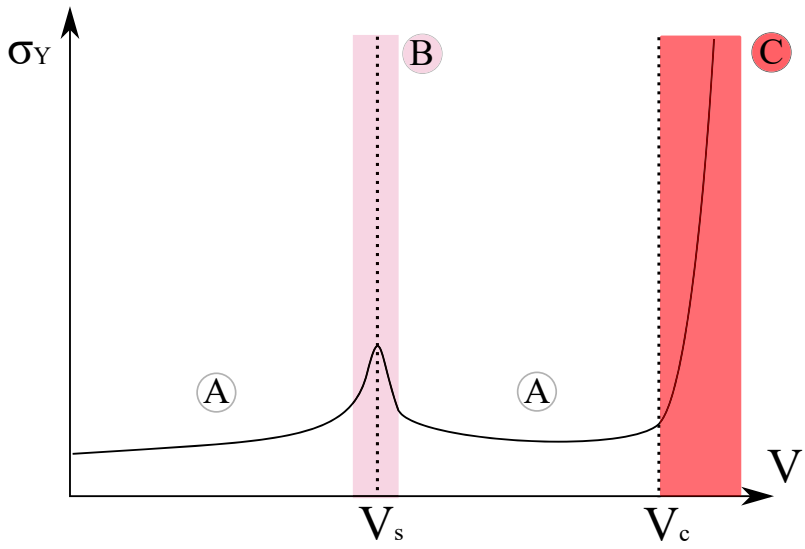

Figure 1.3: Standard deviation of displacement in lift direction for a tube in cross-flow, as a function of mean transverse velocity.

Three regions are immediately evident from this graph, which correspond to distinct fluid-structure interaction mechanisms:

- A) Broadband turbulence (”buffeting”),
- B) Vortex shedding, and
- C) Fluidelastic instability.

Turbulent buffeting is ubiquitous at the high Reynolds numbers which characterise flows inside steam generators, usually in the range: $10^4 \leq Re \leq 10^7$ [AXI 06]. It introduces a random excitation on the tubes which is independent of tube motion and which can be characterized by a broadband frequency spectrum. Axisa et al. [AXI 90] used experimental data from a wide range of tests to propose a dimensionless, 'bi-slope' spectrum that is applicable to single-phase flows. Later on, the two-phase case was tackled by de Langre and Villard [LAN 98] through a similar approach. It should be noted that the latter problem is considerably more complex, as the random spatio-temporal distribution of phases plays a role in the excitation alongside flow turbulence. Consequently, research in this area is still active. Although the methodology of de Langre and Villard has been supported by experimental evidence [ÁLV 18], some authors note its extremely conservative nature, and less restrictive design guidelines have been proposed for steam generator U-tubes [JIA 17]. In recent work, Taylor and Pettigrew [TAY 20] carry out an updated review of experimental data and propose two new, dimensionless upper bounds for random forces in two-phase conditions, spanning different flow regimes. While the capacity to estimate the standard deviation of turbulent efforts is of great importance for long-term wear predictions, their magnitude in practice is quite moderate, for both single and two-phase flows. Hence, this mechanism is not associated to a high vibration hazard in the short term.

Vortex shedding is a well known phenomenon in which a flow detaches from a bluff body as vortices generated at regular intervals. As a result, the structure experiences a periodic forcing at a frequency which depends linearly on mean flow velocity. High-amplitude oscillations can ensue if vortex-shedding is synchronized to one of the structure's natural frequencies, potentially leading to short-term damage. In [LIV 62], the authors study the vibration modes of a row of tubes under excitation by vortex shedding, which they suggest as a potential reason for premature tube failures in steam generators. Chen [CHE 68] studied the vortex-shedding response of an experimental tube bank in a gas flow and proposed design guidelines to prevent vibration and noise in heat exchangers. Gorman [GOR 76] reported resonant responses to vortex shedding in his experiments with tube bundles in liquid cross-flow. These efforts dealt exclusively with simplified configurations in which, most importantly, only single-phase flows were considered. However, as pointed out by Axisa in Chapter 7 of [AXI 06], all experimental investigations on two-phase flow reported an absence of vortex shedding. Furthermore, this fact did not prevent the occurrence of high-amplitude tube oscillations, regardless of bundle geometry or flow composition, for sufficiently high flow velocities, cf. the experiments of Lai

et al. [LAI 19] (transverse a single flexible tube in a rigid array subjected to two-phase cross-flow) or those of Violette et al. [VIO 05] (stream-wise oscillations of a flexible array subjected to two-phase flow), where such a behaviour is observed without vortex shedding. Nowadays, it is clear that the main excitation mechanism behind steam generator tubes failure is of a different nature, and receives the name *fluidelastic instability*. Nevertheless, the study of vortex shedding remains relevant in the context of steam generator design and analysis in relation to acoustic resonance [ZIA 06].

1.1.2 Fluidelastic instability of cylinder arrays

Roberts [ROB 66] was probably the first to have proposed that self-excited oscillations could take place in cylinder arrays. In contrast with buffeting and vortex shedding, which occur even for static cylinders, this mechanism is inherently dependent on structural motions. Fluidelastic instability, as it is now known, started receiving attention following Connors' report of self-excited oscillations in heat-exchanger tube arrays in cross-flow [CON 70]. He postulated a quasi-static, semi analytical model in which oscillations were sustained by energy extracted from the flow, thanks to a specific motion pattern between adjacent tubes. This could only occur for a sufficiently energetic flow, i.e. for flow velocities beyond a critical value (V_c in Fig. 1.3). In his paper, energy-balance considerations were used to derive a formula for predicting the value of V_c, which (along with its variations, such as those proposed by Blevins [BLE 74], Whiston & Thomas [WHI 82], and Price & Païdoussis [PRI 84]) knew a widespread practical use in the following years. However, as evaluated by Price [PRI 01] after a thorough analysis of experimental evidence, even the most refined quasi-static models perform rather poorly at predicting the onset of fluidelastic instability. This fact was recognized in the early eighties and led to the family of unsteady models pioneered by Tanaka & Takahara [TAN 81], as well as the semi-analytical models by Lever & Weaver [LEV 82] for a single flexible cylinder in a rigid bundle and their generalization by Yetisir & Weaver [YET 93a, YET 93b] to the case of multiple flexible cylinders. Price & Païdoussis [PRI 84] found a quasi-steady model by adapting a model for galloping instability to the case of transverse vibrations of tube bundles in cross-flow. An important effect considered by these authors was a time-delay term in the definition of fluidelastic forces. Letting $y(t)$ denote the displacement amplitude of a cylinder of diameter D in the transverse direction upon excitation by a single-phase flow with velocity V and density ρ, the linearised expression for these forces around the static equilibrium position (y_0) takes the form:

$$F_{\text{fe}} = \frac{1}{2}\rho V^2 D \left[\left.\frac{\partial C_L}{\partial y}\right|_{y_0} y(t-\tau) - \frac{1}{V} C_D \dot{y}(t) \right] \tag{1.1}$$

where C_L and C_D are the non-dimensional lift and drag coefficients of the tube profile, respectively. The delay is a mathematical necessity to achieve dynamic instability in this model, and it may be physically justified by arguing that the surrounding flow does not respond immediately to the tube's motions. Different authors, when using variations of quasi-steady models, have conjectured different explanations as to which aspect of the

fluid dynamics is responsible for the delayed term [PAI 13]. While the model of Price & Païdoussis showed a reasonable agreement with experimental data, and was able to predict both stiffness-controlled (depending on the coupling in the motion of two or more tubes) and damping-controlled (requiring only one degree of freedom) stabilities, it failed to capture the physical behaviour of tubes at low values of reduced velocity, defined as:

$$v_r = \frac{fV}{D} \tag{1.2}$$

where f is the frequency of oscillation. This shortcoming is, in fact, shared between this model, the semi-analytical one of Lever-Weaver, and some other well-known ones such as Chen's unsteady model [CHE 83a, CHE 83b]. Granger & Païdoussis [GRA 96] improved on the Price & Païdoussis model by introducing a so-called quasi-unsteady approach. They derived an analytical expression for the fluidelastic coupling forces from the impulsive response of a single flexible tube by requiring continuity and Navier-Stokes (momentum) equations to be satisfied. The physical mechanism behind the negative damping leading to damping-controlled instability is found to be the diffusion of vorticity from the tube boundary layer. The mathematical expression for the fluid forces replaces the discrete delay of Eq. (1.1) by a distributed delay:

$$F_{\text{fe}} = \frac{1}{2}\rho V^2 D \left[\left.\frac{\partial C_L}{\partial y}\right|_{y_0} \int_{-\infty}^{t} \mathbb{D}(\tau) y(t-\tau) d\tau - \frac{1}{V} C_D \dot{y}(t) \right] \tag{1.3}$$

in which the convolution kernel $\mathbb{D}(\tau)$ models the transient decay of disturbances in the flow generated by tube motions. Hidden within this function are constants that must be measured for a given problem, thus making the model a semi-empirical one. When compared to experimental data, the quasi-unsteady model showed a quantitative improvement with respect to its predecessors. Interestingly, this is the case even for systems consisting of several flexible tubes, even though the model considers a unique vibrating tube in a rigid array. This fact supports the claim by Lever & Weaver, who conjectured that a fluidelastic instability analysis of tube arrays may be reduced to the study of a single tube. The model thus provides a description of a destabilizing mechanism which is based on a solid basis of fluid dynamics theory. While this is an important step towards understanding the phenomenon, the model does not consider stiffness-controlled instability and it is unclear whether it may be able to faithfully reproduce the dynamics of tubes for low values of the mass-damping parameter: $m\delta/\rho D^2$, where m is the tube mass and δ its structural damping coefficient.

Even though efforts have not been scarce when it comes to the study of fluidelastic instability, many aspects of the problem remain unanswered to this day, and no available model provides a fully satisfactory predictive (nor descriptive) tool. Indeed, the short exposition presented here barely scratches the surface of a vast scientific literature spanning six decades; comprehensive reviews include the works by Connors [CON 81], Païdoussis [PAI 81, PAI 83, PAI 87, PAI 06], Chen [CHE 75, CHE 84], Pettigrew et al. [PET 91], Price [PRI 95], Gelbe [GEL 95] and Sarpkaya [SAR 03], as well as the books by Axisa

[AXI 06], Gibert [GIB 88] and Païdoussis et al. [PAI 13]. Design guidelines are under constant revision and updating, with the publications by Sun et al. [SUN 19] and Taylor & Pettigrew [TAY 20] being recent examples. Thus, the mechanism rightfully earns the ”elusive” label given to it by Weaver [WEA 08]. In that paper, some potential reasons leading to this fact are: an industrial focus on gathering data for specific equipment rather than on understanding the phenomena, the overwhelming complexity of a multi-physics, strongly coupled problem who is seemingly sensitive to numerous parameters, and the practical difficulty to accurately measure fluidelastic forces. In particular, the latter of these has received considerable attention in past years. Caillaud et al. [CAI 99, CAI 03] have proposed a methodology to measure fluidelastic forces using active control. Bouzidi & Hassan [BOU 15] used CFD computations to find the empirical constants of the Lever-Weaver model for a given tube configuration. In the same vein, investigations of complex fluid-structure interaction problems have been made possible by the advent of high-performance computing. Moulinec et al. [MOU 04a, MOU 04b] used direct numerical simulation to solve the full Navier Stokes equations for a flow through a tube bundle. Sihnde et al. [SHI 14] performed parametric analyses of the coupled fluid-elastic problem in a tube bundle through a mixed RANS-DDES methodology.

1.2 Nonlinear dynamics of unstable tubes

1.2.1 Studies on post-instability behaviour

All the models for fluidelastic instability described above are linear. This is made possible by linearisation of the motion-dependent fluid forces around the equilibrium position of the tubes, which is justified in light of the small vibration amplitudes typical of tube bundles. As such, they can be used to predict the onset of instability but not the tube responses beyond the critical flow velocity, as they unrealistically predict divergent oscillations. In reality, amplitudes remain bounded through the activation of one or more nonlinear mechanisms. For tube bundles, this typically means tube-to-support or tube-to-tube impacts. The interplay between nonlinearity and fluidelastic forces leads to steady-state, limit cycle-like oscillations in which the tubes undergo intermittent contacts. The importance of studying such cycles for tube wear rate estimation and risk assessment has been recognized, and a number[1] of works have been dedicated to this task. Weaver & Schneider [WEA 83] performed wind tunnel experiments on a heat-exchanger U-tube bundle supported by different configurations of AVBs. In the absence of supports, the limit cycles ensuing from fluidelastic instability consisted of essentially motions along the tube’s first out-of-plane bending mode. When the bars were included in such a way as to completely suppress this vibration mode, instability arrived at a larger value of flow velocity and the corresponding limit cycles following the second out-of-plane bending mode instead. This pattern was observed to continue with higher out-of-plane modes as the flow velocity increased. However, no stabilities for in-plane modes were reported. The

[1] A small number, if compared to the bulk of investigations dealing with fluidelastic instability.

effect of an asymmetric clearance was also explored briefly, and was found to provide a stabilizing effect, i.e. to delay the onset of stability to a higher flow velocity. Axisa et al. [AXI 88] present an approach for the numerical investigation of post-instability vibrations. Therein, tube motions are projected onto the unsupported modal basis, with contact forces assumed to be localized at discrete points. Computation of impact forces in the normal direction uses a penalty method in which the cross-section ovalization stiffness, K_c, acts as the penalty coefficient. This quantity can be theoretically estimated through the formula[2]:

$$K_c = 3.8\frac{Ee^2}{D}\sqrt{\frac{e}{D}} \tag{1.4}$$

where e, D, and E are tube thickness, diameter and Young modulus, respectively. The value of K_c is typically on the order of $10^6 N/m$ for steam generator tubes. Tangential forces are computed by using Coulomb's dry friction model, which was later refined by Antunes et al. [ANT 90]. The authors present simulation results for a cross-flow-excited U-tube supported by AVBs, where fluidelastic forces are computed from Connors' model and the equations of motion are integrated in time using De Vogelaere's method [LES 68]: for varying values of flow velocity, a range of dynamical regimes are obtained: periodic (with varying relative contributions of the tube's modes), quasi-periodic and chaotic [OTT 81] vibrations. This behaviour clearly indicates the presence of multiple *bifurcations*, as is typical for nonlinear dynamical systems [GUC 83, KUZ 04]. Païdoussis et al. [PAI 93] studied an analytical, two-degree of freedom model representing the planar motions of a tube in an annular support within a rotated, triangular grid. Fluidelastic coupling forces were provided by the Price & Païdoussis model with experimentally-determined coefficients, and a fourth-order Runge-Kutta algorithm is used to solve for the time histories of motion.

Fig. 1.4, taken from their paper, shows a bifurcation diagram rich in dynamical regimes, ranging from periodic to chaotic and including symmetry-breaking, double-period and quasi-periodic motions. Similarly, the effect of simultaneously varying two parameters was studied (flow velocity and gap size), which resulted in a number of stability boundaries separating different regimes. The same authors investigated a related system, consisting of a clamped-pinned beam subjected to cross-flow, both experimentally [MUR 94a] and analytically [MUR 94b]. While a more complex behaviour is observed, qualitative similarities with the simple two-DOF model are evident. Antunes et al. [ANT 92] performed experiments on a loosely-supported cantilever beam in which fluidelastic forces were simulated by a feedback loop. This provides an effective negative damping, which plays an energy-source role analogous to that of flow velocity in "true" fluidelastic forces. Dynamical regimes of two distinct types were observed, each with different relative modal-to-total response contributions. While one of these was unique for low and high values of negative damping, an intermediate region in which both regimes coexisted was found. Thus, the observed steady state depended on initial conditions. All regimes reported in this study are quasi-periodic, as the motions of the numerous

[2]The original publication reports a coefficient of 1.9 in Eq. (1.4). However, it is nowadays recognized that a factor of two is missing for adequate fit with experimental results.

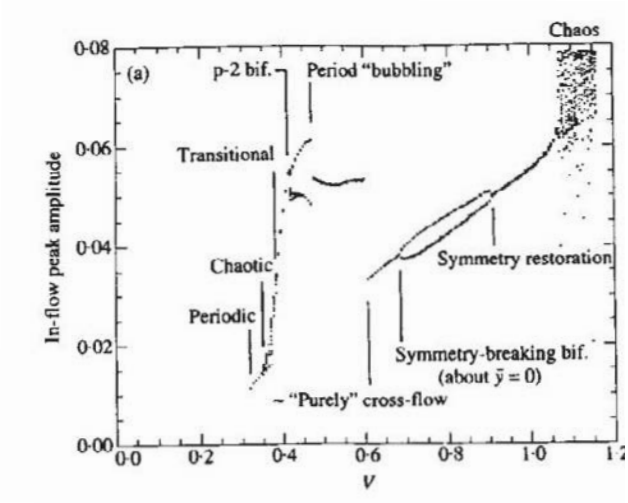

Figure 1.4: Bifurcation diagram for varying flow velocity V, from [PAI 93].

modes involved in the response are unsynchronized but their spectra consist of distinct peaks rather than the broad-band signature of chaos. Piteau et al. [PIT 12] experimentally identified fluidelastic force coefficients and turbulent spectra for a flexible cantilever tube excited by single-phase cross-flow within a rigid, square grid. A numerical model of the system was then shown to be successful in reproducing the experimental results. Recently, the same authors have developed a more advanced test rig which allows for the modal characteristics of the flexible tube to be adjusted [PIT 19]. In a series of conference papers, Borsoi and co-workers investigated different aspects of the dynamics of a 1-DOF model consisting of an autonomous oscillator destabilized by fluidelastic forces, computed by the Granger & Païdoussis quasi-unsteady model with empirical coefficients obtained through active control. The effect of gap size was studied in [BOR 17b], where it was concluded that the relative weight of turbulence in the overall excitation is inversely proportional to this parameter. The distribution of energy between turbulent and fluidelastic forces was discussed in [BOR 17a]. The same paper reported coexisting symmetric (two-sided impacts) and asymmetric (one-sided impacts) periodic cycles for certain values of flow velocity, in the case where turbulence was ignored. Including turbulence, phase-space plots of tube motions were erratic but stayed in the vicinity of said cycles. A parametric study was conducted in [BOR 18]. It was shown that velocity variations led to an amplitude jump, accompanied by a transition from one-sided to two-sided impacts for high-enough values. Prabel et al. [PRA 18] used the quasi-unsteady model to numerically simulate the response of a U-tube in cross-flow with a realistic velocity and density distribution. To this end, the two-phase flow was homogenized into an equivalent single-phase flow. The obtained results showed an increase in the complexity of the responses as the number of modes considered was increased. For three modes (two out-of plane and one in-plane), complementary asymmetrical regimes were observed, similarly to the cantilever beam case. However, only one of these was periodic, while the other was quasi-periodic. Lai et al. [LAI 19] used time-integration to numerically study the

behaviour of a flexible, cantilever beam in a rigid, rotated-triangular grid under the action of a two-phase cross-flow. Fluidelastic forces were computed through the Price & Païdoussis model fitted with experimental data. For increasing flow velocity, transition from steady periodic to quasi-periodic and chaotic motions were observed. The method of multiple scales was employed by Vourganti et al. [VOU 20] to analytically study the stability of a 1-DOF oscillator with a discrete delay to model fluid-elastic forces. As the method requires smooth functions, the impacts in that case where modelled by a cubic spring rather than the usual piecewise-defined functions.

1.2.2 Modelling impacts

The high complexity observed in the studies mentioned above is a result of impacts, which are a particularly strong type of nonlinearity. An ideal, 1-DOF impact oscillator with natural (angular) frequency ω_0 is described by the constrained system:

$$\begin{cases} \ddot{x}(t) + \zeta\dot{x}(t) + \omega_0^2 x(t) = f(t) & , \quad \forall t > 0 \\ \dot{x}(t_c^+) = -r\dot{x}(t_c^-) & , \quad t = t_c \end{cases} \tag{1.5}$$

where t_c is any instant where impact takes place, i.e. when $x(t_c) = g$ for a given gap size g. This model considers an instantaneous change in the sign of velocity, with a potential energy loss given by the restitution coefficient $r \in (0, 1]$, with the limiting case $r = 1$ corresponding to perfectly elastic collisions. The term $f(t)$ accounts for external forcing. Even though the system is linear between impacts, the discontinuity in velocity means that the system is highly-nonsmooth [BRO 99]. This, in itself, represents a challenge to the usual time-stepping integration schemes. As a consequence, specialized methods have been devised to treat such problems [PAO 01, ACA 09]. When a periodic forcing such as $f(t) = \beta\sin(\omega t)$ is applied, transitions from periodic to chaotic behaviour are known to happen for increasing values of β, usually through a sequence of period-doubling bifurcations [GUC 83, HIN 84].
An alternative modelling approach consists in adopting a penalty formulation, in which some penetration of the structure into the support (or elastic deformation of the former due to contact) is allowed. Hence, the impact law from Eq. (1.5) is replaced by a piecewise-continuous function:

$$\ddot{x}(t) + \zeta\dot{x}(t) + \omega_0^2 x(t) + f_c(\delta_1)\hat{H}(\delta_1) = f(t) \tag{1.6}$$

where $\delta_1 = x(t) - g$ is the penetration depth and $\hat{H}$ represents the Heaviside step function. Thus, the support exerts a restoring force on the structure for the duration of contact, which occurs over a finite time interval rather than instantaneously. Typically, linear or exponential functions are used for $f_c(\delta)$. In the case of steam-generator vibrations, the former is adopted [AXI 88], such that:

$$f_c(\delta_1) = K_c\delta_1 \tag{1.7}$$

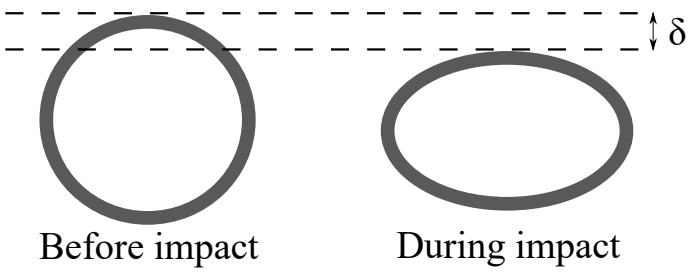

Figure 1.5: Ovalization of tube section at impact.

Besides enhanced ease for numerical simulations, this approach has the advantage of being physically significant, as the parameter K_c is a measurable quantity which represents the cross-section deformation during impact, as schematized in Fig. 1.5.

Eq. (1.6) specifically describes one-sided impacts, but it can be readily extended to other cases. For two-sided impacts:

$$\ddot{x}(t) + \zeta\dot{x}(t) + \omega_0^2 x(t) + f_c(\delta_1)\hat{H}(\delta_1) - f_c(\delta_2)\hat{H}(\delta_2) = f(t) \tag{1.8}$$

where $\delta_2 = -x(t) - \tilde{g}$. Several authors have studied the dynamics of systems similar to Eq. (1.8) for asymmetric gaps, i.e. $g \neq \tilde{g}$. Natsiavas & Gonzalez [NAT 92] used a semi-analytical approach to compute frequency response curves of a forced oscillator with asymmetric impacts. They reported loss of stability through a period-doubling bifurcation, leading to a sub-harmonic resonance peak at roughly twice the excitation frequency of the main resonance. Kim et al. [KIM 05] studied a SDOF torsional system with asymmetric gaps using the harmonic balance method and, similarly, encountered a sub-harmonic resonance peak. Duan & Singh [DUA 08] found branches of double-period solutions isolated from the main response curve, i.e. an *isola*. A connection between asymmetry and period-doubling is evident from these results. This fact is especially interesting in light of the transition to chaos via the successive period-doubling (or *sub-harmonic cascade*) route. De Langre & Lebreton [LAN 96] performed experiments and numerical computations on a forced SDOF system displaying both geometrical nonlinearity and two-sided, soft impacts. For certain combinations of driving amplitude a frequency, chaotic motions were observed, but solely in the asymmetrical configurations. While this aspect is not explored deeply in their paper, it is likely that chaos arrives following a sub-harmonic cascade.

An impact damper may also be included in order to account for energy losses resulting from impacts, which is analogous to the role of a restitution coefficient [HUN 75]. Païdoussis et al. [PAI 93] use a piecewise-linear impact damper to model the dissipation of energy by the response of high-frequency vibration modes of a cylinder not included in the reduced-order model used. This strategy was also employed by Prabel et al. [PRA 18] in their study of U-tube vibrations. Mureithi et al [MUR 94a] used a more refined model in which the impact damping coefficient is a nonlinear function of normal velocity and including a squeeze-film effect. Padmanabhan & Singh [PAD 95] incorporate impact

damping into their model of gear rattle effects in automotive engines. A simple function describing two-sided, linearly damped impacts is given by:

$$f_c(x,\dot{x}) = (K_c(x(t)-g)+C_c\dot{x}(t))^+\hat{H}(x(t)-g) - (K_c(x(t)+\tilde{g})+C_c\dot{x}(t))^-\hat{H}(-x(t)-\tilde{g}) \tag{1.9}$$

where the operators $(\cdot)^+$ and $(\cdot)^-$ denote, respectively, the positive and negative parts of the expressions within parentheses. Fig. 1.6 shows the graphs of Eqs. (1.6) and Eq. (1.8) side by side, for a displacement given by $x(t) = 1.2\sin(t)$ and $K_c = 20, C_c = 6, g = \tilde{g} = 1$.

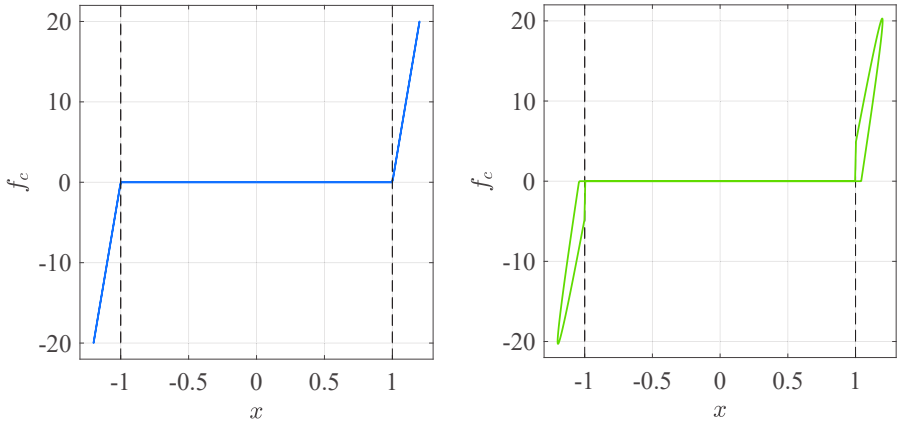

Figure 1.6: Graphs of symmetric impact functions (penalty formulation) with and without impact damping. Left: impact term from Eq. (1.6), right: Eq. (1.8).

Another important energy dissipation mechanism is friction, which plays a central role in many industrial applications, including: tube-to-support contacts in steam generator tubes [AXI 88], brake squeal [COU 09], turbine blade dampers [WAN 93] and violin string models [VIG 18]. The modelling of friction is far from being a task, as described in great detail by the historical review of Feeny et al. [FEE 98]. Indeed, one can not reasonably speak of a universal model, but rather of a group of models with certain applicability margins. For sliding friction between two metallic surfaces in contact, the so-called Coulomb, or dry, friction gives a force in the tangential direction as:

$$f_T = \mu|f_N|\text{sign}\dot{x}_T(t) \tag{1.10}$$

with μ the dimensionless dry friction coefficient, f_N the normal force and $\dot{x}_T(t)$ the tangential velocity. f_N can be given, for instance, by Eq. (1.9) in the case of intermittent contacts, or by the weight of an object in permanent contact. When upon a surface moving at a constant velocity V, an oscillating system may undergo stick-slip oscillations: rapid transitions from a sticking to a sliding state as elastic forces overcome stiction. In that case, the velocity in Eq. 1.10 is replaced by $v_{\text{rel}} = \dot{x}(t) - V$. Furthermore, the dry friction coefficient may be a nonlinear function of v_{rel} [YOS 00]. An issue encountered when using such models for numerical simulation is the fact that the sign function is not uniquely defined for. $\dot{x}_T(t) = 0$. The theory of Fillippov systems [BER 07] can be used to

rigorously study this problem through the formalism of differential inclusions. Another approach, widely used in practice, is to *regularize* the above model by complementing it with a constitutive law for speeds close to zero. Such a model was proposed by Oden & Martins [ODE 85], in which a linear evolution links the positive and negative regions of the sign function over a small interval around $\dot{x}_T(t) = 0$. Tangential force is then non-smooth but completely regular. Antunes et al. [ANT 90] proposed a more refined methodology in which the sticking behaviour was modelled by a fictitious degree of freedom attached to the main one via a spring-damper mechanism. Leine et al. [LEI 98] proposed a so-called switch friction model in which the tangential force varies continuously from sliding to static friction.

1.3 Numerical methods for nonlinear vibration problems

The equations of motion to be solved in structural vibrations result from the finite-element discretization of the continuous expression of dynamical equilibrium. They are sets of nonlinearly-coupled, second-order, ordinary differential equations whose analytical solutions are generally impossible to find. While powerful semi-analytical techniques such as multiple-scale analysis [NAY 79] and normal form transformation [JEZ 91] exist, they are usually limited to systems with *weak* nonlinearities, i.e. those for which the nonlinear terms remain small in comparison to the linear ones. This condition is certainly not met in intermittent contact problems. Hence, as already evidenced from the above discussion, numerical methods are fundamental in investigating their dynamic behaviour. In the context of heat-exchanger tube vibrations, the main focus is on finding steady-state solutions, as these are the ones that determine long-term behaviour. Strictly speaking, the presence of turbulent fluctuations and their corresponding forces renders the system's behaviour unsteady; however, after an initial transient period, turbulent flows become statically steady, in the sense that mean flow features do not vary over time. Consequently, it is reasonable to assume a similar behaviour for structural motions. The search for periodic and quasi-periodic solutions is of particular importance in this respect, as they are common steady-state regimes for vibrating systems.

1.3.1 Time-domain methods

Numerical time-integration techniques are fundamental in capturing transient behaviour of dynamical systems. This is relevant, for instance, in passive vibration control by use of nonlinear energy sinks [GEN 00, LEE 08, GEN 11], or in the numerical study of chaotic motions [NAR 91, CAI 92]. Dokainish & Subbaraj present an extensive survey of common explicit [DOK 89] and implicit [SUB 89] algorithms. Specialized techniques have been developed for the time-integration of nonsmooth dynamical systems [MOR 88, ACA 09]. Strongly-nonlinear restoring forces resulting from non-instantaneous impacts, e.g. Eqs.(1.5,1.6,1.8), can be treated as long as the chosen time

step for the discretization is smaller than the contact duration. In [PIT 18], for instance, the authors use a value of $5 \cdot 10^{-5}$ s for the post-instability study of a loosely-supported, cantilever tube in cross-flow. Explicit algorithms, which avoid the use of a non-linear solver at each time step, are thus preferred in this context. Well-known and widely-used examples are the methods from the Runge-Kutta family, which can also be extended to treat delay differential equations [BAK 00, SHA 09]. Puthanpurayil et al. [PUT 14] proposed a time-domain implementation permitting the computation of a distributed delay term such as the one in Eq. (1.3). Prabel et al. [PRA 18] improved on this approach by using a recurrence relation to compute the distributed delay term during integration with an explicit De Vogelaere algorithm. Nevertheless, all time-integration methods are inefficient when it comes to capturing steady-state solutions, as computations have to be performed over a large-enough interval to ensure that the transient response has faded. Moreover, while a system of nonlinear equations admits both stable and unstable steady-state regimes as solutions, only the former can be observed through numerical integration. The *shooting* technique [NAY 89, SEY 10] is an alternative time-domain approach that finds periodic solutions by replacing the initial-value problem of time-integration by a Boundary-Value Problem (BVP). Through an iterative procedure, the initial conditions which satisfy dynamical equilibrium as well as periodicity are found. This requires the equations of motion to be time-integrated over one period, which can be known in advanced (forced oscillations) or an additional unknown to be found (autonomous oscillations, for example in the case of self-excited motions). Sundararajan & Noah [SUN 97] combine this method with a continuation algorithm to study forced vibrations of rotor systems. A similar approach was undertook by Dimitriadis [DIM 11] to study the parametric behaviour of limit-cycle oscillations in an aeroelastic system. A remarkable feature of this study is the use of additional degrees of freedom to represent unsteady aerodynamic forces, which is equivalent to having a distributed delay, Eq. (1.3), with a sum-of-exponentials type kernel [SMI 11, DIM 17]. Howell & Pernicka [HOW 87] used a shooting method to compute quasi-periodic solutions of the restricted three-body problem.

Collocation methods get rid of time-integration altogether by considering a discrete version of the periodic BVP. The steady-state solution is assumed to be a combination of orthogonal (e.g., Legendre) polynomials. Then, by using a Galerkin projection onto the basis formed by these same polynomials, a set of nonlinear algebraic equations is obtained in which the unknowns are the solution values evaluated at discrete points. This method has been proved to be both efficient and highly robust, and is thus at the heart of numerous software for the analysis of nonlinear dynamics, including: COLSYS [ASC 79], CONTENT [GOV 99, GOV 00] AUTO [DOE 12], MATCONT [DHO 03, DHO 04] , COCO [DAN 10]. The latter was recently used to study families of quasi-periodic solutions in a forced, delayed Duffing oscillator [AHS 19]. DDE-BIFTOOL [ENG 02] specializes in the solution of delay differential equations.

The codes mentioned herein make use of *continuation methods*: once a solution is found, a whole branch of solutions can be unfolded by treating one of the system's parameters as a new unknown and following the equilibrium path. This idea was orig-

inally proposed for the study of equilibria in nonlinear elasticity [CRI 81] and then adapted for the study of periodic solutions. Different approaches for path-following have been employed over the years, with the most popular variants being arc-length continuation [KEL 83, KEL 86, SEY 10] and the Asymptotic Numerical Method (ANM) [DAM 90, COC 94]. The former consists in taking a step along the tangent direction to the path at a given solution, followed by orthogonal corrections until convergence. The latter, on the other hand, uses a series expansion to locally represent the path in the vicinity of the initial solution, iteratively solving for the expansion coefficients. Arc-length continuation can be seen as a first-order truncation of the corresponding series expansion. Continuation software has built-in routines for the stability evaluation of the computed periodic solutions, allowing for a detection of bifurcations as described in Sect. 1.3.3. Hence, they represent a valuable aid at understanding the complex dynamics of nonlinear systems. Nevertheless, codes relying on collocation methods are generally restricted to systems with a few degrees of freedom. Moreover, the frequency content of solutions computed in this way is not directly available and must be obtained in a post-processing stage. Both of these shortcomings are addressed by frequency-domain methods.

1.3.2 Frequency-domain methods

Krylov & Bogoliubov [KRY 50] were probably the first to have proposed a semi-analytic method whose principle was to look for periodic solutions in the form of truncated Fourier series. A Galerkin projection of the differential equations of motion onto a base of trigonometric functions, which are mutually orthogonal, transforms the initial problem into a system of nonlinear algebraic equations whose unknowns are the Fourier coefficients up to a certain harmonic component. As Nayfeh pointed out in his book [NAY 79], an *a priori* estimation of the number of terms required to correctly capture periodic motion is seldom possible, and the use of different approximation techniques was suggested. Nevertheless, this issue would be circumvented by the numerical implementation of the method by Nakhla & Vlach [NAK 76], who used it to find periodic regimes in nonlinear electronic circuits. Dynamical equilibrium is formulated as a minimization problem for an error function, and the number of harmonics is adjusted accordingly. Lau et al. [LAU 82] applied the Harmonic Balance Method (HBM) in a structural dynamics context to study parametrically-excited, linear and geometrically-nonlinear systems with one or several degrees of freedom. They introduce the Incremental Harmonic Balance Method (IHBM), by which continuation of periodic solutions is performed via direct parametrization of the equilibrium by path one of the system's parameters. This approach was followed by Pierre et al. [PIE 85] and Ferri & Dowell [FER 88] for the study of friction-damped systems. An extension of the HBM to capture quasi-periodic responses was first proposed by Chua & Ushida [CHU 81] and later adapted to the IHBM by Lau et al. [LAU 83]. Kim & Choi [KIM 97] use this method to study quasi-periodic oscillations of a forced, nonlinear Jeffcott rotor. A major breakthrough regarding practical implementation was the introduction of the Alternating Frequency-Time (AFT) procedure by Cameron & Griffin [CAM 89], as it allows arbitrary nonlinearities to be treated by the HBM. The main idea

is to compute the corresponding forces in the time domain, where -usually simple- analytical expressions are available, and then to transform back to the frequency domain. Any suitable algorithms, such as the Fourier Transform (FFT) and its inverse, can be used to perform this operation. The principle is illustrated in Fig. 1.7.

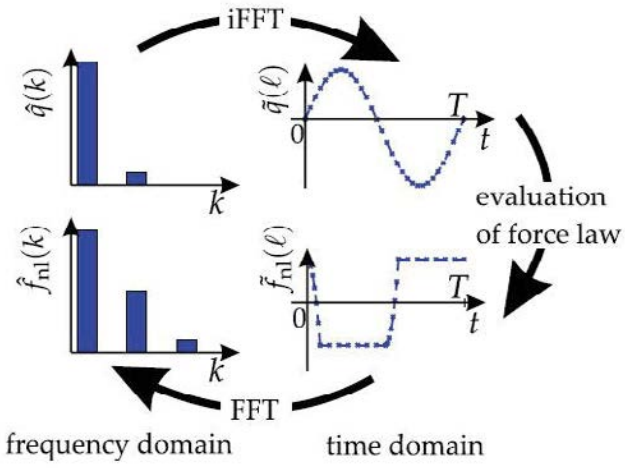

Figure 1.7: Illustration of the AFT procedure, from [KRA 19].

The coupling of AFT-HBM with arc-length continuation was proposed by Von Groll & Ewins [GRO 01]. This approach is much better suited to the analysis of nonlinear systems than IHBM, as the parametrization of the equilibrium path by the so-called *natural* coordinate (i.e. the abscissa along the equilibrium curve) allows for the algorithm to follow the path across folds. Cochelin & Vergez [COC 09] extended the ANM to the continuation of periodic solutions by coupling it with the HBM. This led to the development of the continuation software MANLAB [KAR 13, GUI 19]. In a recent paper, Woiwode et al. [WOI 20] compare both of these techniques for a variety of mechanical systems and conclude that arc-length continuation is better suited to treat regularized nonlinearities like impacts or friction, whereas an outstanding performance can be expected from ANM for inherently smooth systems.
In any case, the potential of HBM-based continuation as a design and analysis tool cannot be understated. Some additional examples of this in mechanical engineering include the nonlinear modal analysis of aerospace structures [KER 13, DET 15b, SAL 16], the response prediction of a tuned mass damper subjected to a multi-frequency excitation with hundreds of terms and stiff impacts [TIL 18], optimization of a nonlinear vibration absorber [DET 15a, GRE 17], the analysis of aeroelastic airfoils [LIU 04, LIU 07, DAI 14], and the study of break squeal [COU 09].

It is relevant to note, at this point, that no studies of steam-generator vibrations have applied continuation methods so far, neither by time-domain nor by frequency-domain approaches. This can be partially explained by the stochastic nature of the observed re-

sponses due to turbulence, which prevents any sustained periodic or quasi-periodic regime to develop. Nevertheless, analysing the behaviour of tubes under the steady-state, mean flow could provide valuable insight into their extremely complex dynamics. In particular, the HBM seems to be ideally suited for the task, as fluidelastic forces involving discrete (Eq. (1.1)) or distributed (Eq. (1.3)) delays can be efficiently computed in the frequency domain. For instance, the time-domain convolution products appearing in the latter become simple products under Fourier transformation as per the convolution theorem [BLA 05].

1.3.3 Stability and Bifurcations

1.3.3.1 Floquet Theory

As mathematical solutions to the equations of motion, periodic solutions can be either stable of unstable in nature. Different definitions of stability are used in nonlinear dynamics literature [GUC 83], and for periodic solutions the focus is on *linear stability*. Let us consider a generic system of the form:

$$\dot{\mathbf{u}}(t) = \mathbf{f}(\mathbf{u}(t), t) \tag{1.11}$$

for a smooth function $\mathbf{f} : \mathbb{R}^n \rightarrowtail \mathbb{R}^n$, and $\mathbf{u}(t) \in \mathbb{R}^n$. Assuming the state of the system to be a slight perturbation from a known periodic solution $\mathbf{u}_0(t)$, i.e. $\mathbf{u}(t) = \mathbf{u}_0(t) + \boldsymbol{\eta}(t)$, a first-order expansion of Eq. 1.11 yields the linear system with periodic coefficients:

$$\dot{\boldsymbol{\eta}}(t) = \mathbf{A}(t)\boldsymbol{\eta}(t) \tag{1.12}$$

where $\mathbf{A}(t) = \left[\dfrac{\partial \mathbf{f}}{\partial \mathbf{u}}\right]_{\mathbf{u}=\mathbf{u}_0}$. The n solutions to Eq. 1.12 make up the fundamental solution matrix $\boldsymbol{\Phi}(t)$, with initial conditions $\boldsymbol{\Phi}(0) = \mathbf{I}_n$. Any two states of $\boldsymbol{\eta}$(t) are related by this matrix and, in particular:

$$\boldsymbol{\eta}(T) = \boldsymbol{\Phi}(T)\boldsymbol{\eta}(0) \tag{1.13}$$

where T is the minimal period of $\mathbf{u}_0(t)$: $\mathbf{u}_0(t+T) = \mathbf{u}_0(t)$. Hence, the eigenvalues of $\boldsymbol{\Phi}(T)$, called the *monodromy matrix*, determine whether the perturbation decays (returns to the underlying cycle $\mathbf{u}_0$) or grows (strays away from $\mathbf{u}_0$) over the course of a period. The eigenvalues, $\mu \in \mathbb{C}$, are called *Floquet multipliers* and yield the criterion:

- Stable solution: $|\mu_j| < 1,\ \forall i = 1, ..., n$,
- Unstable solution otherwise.

Alternatively, one may use the fact that solutions to Eq. 1.12 have the form $\boldsymbol{\eta}(t) = e^{\lambda t}\mathbf{p}(t)$, where $\mathbf{p}(t+T) = \mathbf{p}(t)$, combined with Eq. 1.13 to express the stability criterion in terms of the *Floquet exponents* given by $\mu = e^{\lambda T}$, such that:

- Stable solution: $\Re\left\{\lambda_j\right\} < 0,\ \forall i = 1, ..., n$,

- Unstable solution otherwise.

Numerical methods for stability evaluation of periodic solutions are designed to compute either μ_i or λ_i. A technique for approximating the monodromy matrix with time-integration was proposed by Friedmann et al. [FRI 77]. Shooting techniques yield this matrix as a by-product [SEY 10], and it can be constructed with ease from matrices employed in orthogonal collocation [DOE 91]. On the other hand, frequency-domain methods compute Floquet exponents, following the approach pioneered by Takahashi [TAK 79] and now known as Hill's method. Von Groll & Ewins [GRO 01] proposed a version of this method which is specialized for mechanical systems described by second-order differential equations and which leads to solving a Quadratic Eigenvalue Problem (QEP) in the frequency domain. Their implementation uses a real HBM formulation, such the coefficient matrices involved in the QEP are already available as a by-product of the Newton-Raphson iterations to convergence. Several authors have successfully employed this technique [DET 14, XIE 15, GRE 17, ALC 19]; however, its usual form cannot be used in the case of distributed delays, which are equivalently expressed as additional first-order differential equations [SMI 11]. An alternative method, based on a complex HBM formulation, was proposed by Lazarus & Thomas [LAZ 10], expanded upon by Bentvelsen & Lazarus [BEN 17], and developed alongside ANM-HBM continuation [KAR 13, GUI 20] for the treatment of general systems, i.e. Eq. 1.11.

1.3.3.2 Computing bifurcations

Along the continuation of periodic solutions, Floquet exponents evolve and may have their real parts become positive/negative according to the system's parameters. Such an event is called a *bifurcation*. With respect to the continuation parameter, values before and after bifurcation correspond to a different number of co-existing solutions. This can happen by the equilibrium-path curve turning back on itself (a *fold*, *turning point*, *saddle-node*, or *limit point* bifurcation of cycles), or by a new curve branching out from it. The latter may be of a different dynamical nature than the former, for instance a branch of quasi-periodic (a *secondary Hopf* or *Neimark-Sacker* bifurcation) or double-period solutions bifurcating from a periodic solution curve. Hence, the capacity to detect and characterize bifurcations is extremely important. For time-domain methods, the problem has been extensively tackled, as reviewed in the books by Seydel [SEY 10] and Kuznetsov [KUZ 04]. The main idea consists in monitoring the values of particular test functions during continuation, which change sign when a bifurcation has occurred. After detection, an iterative algorithm precisely localizes the bifurcation by solving for dynamical equilibrium along with additional constraint equations for bifurcation characterization. Details can be found in the works by Doedel et al. [DOE 03], Dhooge at al. [DHO 04], Govaerts [GOV 00, GOV 05] and Witte el al. [WIT 13].

Continuation can be applied to the extended systems defining bifurcations, a technique called *bifurcation tracking*. The curves thus produced serve the role of stability boundaries across which different dynamical behaviours are exhibited either by a varying number of solutions, a change in the nature of these, or both. Their knowledge is thus precious to the understanding of global dynamics. It shall be clear that further Floquet exponents may cross the imaginary axis during bifurcation tracking, indicating a codimension-2 bifurcation (denoted *codim-2*). The term 'codimension' relates to the number of parameters to be tuned in order for such an event to happen, and thus codim-N bifurcations may be observed through recursive tracking, where N is limited by the number of Floquet exponents a system possesses. Fig. 1.8 shows the successive bifurcations that can be encountered when performing continuation of equilibria[3], up to codim-3. The AUTO software supports detection, localization and tracking of codim-2 bifurcations of periodic solutions. Recently, so-called control-based continuation was used by Renson et al.to perform experimental bifurcation tracking [REN 16, REN 17, REN 19].

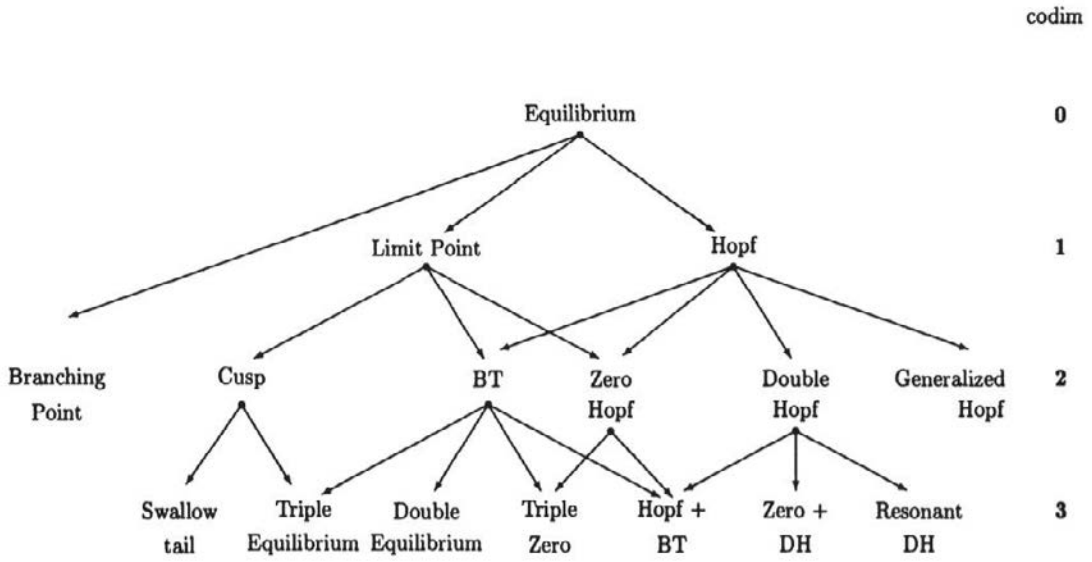

Figure 1.8: Classification of bifurcations with codimensions 0 through 3, from [GOV 00].

In contrast, frequency-domain bifurcation analysis is much more recent. Detroux et al. [DET 15b] proposed extended systems for the characterization of limit point and Neimark-Sacker bifurcations, and performed tracking of the former. This led to the uncovering of isolated resonance curves (or *isolas*) in a forced system. Xie et al. [XIE 16, XIE 17] employed alternative extended systems and tracked bifurcations in rotor dynamics applications. Grenat et al. [GRE 17] use this formalism to develop bifurcations analysis of nonlinear normal modes. Later, the same authors [GRE 19] used recursive tracking of limit points in increasing codimension to optimize a nonlinear tuned vibra-

[3] A similar picture could be drawn for periodic solutions.

tion absorber. Methods to systematically compute higher-codimension bifurcations of arbitrary nature in the frequency domain have yet to be proposed.

1.4 Summary

The numerical prediction of non-linear response to fluidelastic instability in steam-generator tubes is a challenging task. On one hand, no fully-satisfactory model has been found to take into account fluidelastic forces. On the other, the combination of complex geometries, time-delay effects and strong nonlinearities gives rise to an extremely rich behaviour which is fertile in bifurcations. Numerical methods to tackle this issue should be able to handle the efficient continuation of limit cycles induced by the balance between frequency-dependent fluidelastic forces and impacts of beams, perform stability evaluations of converged cycles, carry out bifurcation analyses (detection, localization and tracking) and allow the transition between branches at bifurcation points regardless of their nature (periodic, quasi-periodic, sub-harmonic). While this would not lead to exact predictions of operating behaviour -due to the stochastic character of turbulence-, it would surely shed light on the underlying phenomenology associated with steam-generator tube vibrations. Potentially, this would aid in the creation of optimized design guidelines.

The rest of this thesis is structured in two chapters, with the first one devoted to the development of numerical methods that meet the above requirements, and the second one focused on applications to simplified systems which approximate -in an increasingly realistic way- qualitative aspects of the steam-generator tube vibration problem. Following the bibliographical review presented in this chapter, the formalism of AFT-HBM with arc-length continuation is adopted. From that starting point, the following contributions to numerical analysis of nonlinear vibration problems are presented in Chapter 2:

1. A method to study discrete and distributed-delay systems in the frequency domain which includes, in particular, the stability analysis of the latter by an appropriate reformulation of Hill's method.

2. A practical approach to transitioning from periodic to quasi-periodic branches at a Neimark-Sacker bifurcation, as well as the stability evaluation of quasi-periodic regimes.

3. A systematic methodology to construct extended systems for the characterization of bifurcations in any codimension.

4. A numerical implementation of continuation and bifurcation analysis algorithms into the finite-element software CAST3M, thus permitting such analysis in practical nonlinear vibration problems with arbitrary geometries.

Chapter 2

Bifurcation analysis by Harmonic Balance

This chapter details the numerical methods for general bifurcation analysis in the frequency domain, based on coupling Harmonic Balance (HBM) and Pseudo Arc-length Continuation (PAC). After a brief overview of the well-known general principles and notations, the main contributions are discussed, which are three-fold: quasi-periodic analysis (including stability and branching from a NS bifurcation), the treatment of systems with time delays (particularly distributed delays, i.e. integro-differential equations) and the generalization of bifurcation analysis to arbitrary codimension. The methods are showcased on two example systems: a Jeffcott rotor and a Nonlinear Energy Sink (NES). Finally, the implementation of the presented methods in the finite-element software CAST3M is addressed.

Contents

2.1 Continuation of periodic solutions: an overview

2.1.1 The Harmonic Balance Method (HBM)

Let us consider a discrete, nonlinear dynamical system having n degrees of freedom (DOFs), whose evolution in time is governed by the following equation:

$$\mathbf{M}\ddot{\mathbf{x}}(t)+\mathbf{C}\dot{\mathbf{x}}(t)+\mathbf{K}\mathbf{x}(t)+\mathbf{f}_{\mathrm{NL}}(\mathbf{x}(t),\dot{\mathbf{x}}(t),\ddot{\mathbf{x}}(t))+\mathbf{f}_{\mathrm{I}}(\mathbf{x}(t),\tau)=\mathbf{f}(t) \tag{2.1}$$

If the system is idealized as a collection of lumped masses, as will be done throughout this chapter, this expression can be considered exact and may include full matrices, with $\mathbf{x}(t)\in\mathbb{R}^n$ a vector of generalized displacements. Otherwise, it may represent a discrete approximation to a continuous problem through, e.g., a finite-element spatial discretization or a modal expansion up to the n-th normal mode, in which case the modal displacements $\mathbf{q}(t)$ replace $\mathbf{x}(t)$ in the above equation. In any case, $\mathbf{M},\mathbf{C}$ and $\mathbf{K}$ are the (full or modal) inertia, damping, and stiffness matrices, respectively, whereas $\mathbf{f}_{\mathrm{NL}}$ is the vector of nonlinear forces and $\mathbf{f}(t)$ is the vector of applied external forces. The term $\mathbf{f}_I$ accounts for any potential time-delay terms and will be discussed further in Sect. 2.2.1; for the purposes of this section we will consider $\mathbf{f}_{\mathrm{I}}=\mathbf{0}$.

An approximate solution to Eq. (2.1) is sought in two steps. Firstly, the steady state solution $\mathbf{x}(t)$ is assumed to be representable by a series expansion over a certain basis $\mathbb{B}_1(t)$ of orthonormal functions with particular properties, usually (quasi-)periodicity. Secondly, this expansion is introduced in the equations of motion, which are then projected onto an orthonormal basis $\mathbb{B}_2(t)$ through an adequate scalar product. The classical HBM consists of using a basis of trigonometric functions for both expansion and projection, i.e. performing the Fourier-Galerkin method, such that the time dimension is removed, which results is an algebraic problem for the Fourier coefficients of $\mathbf{x}(t)$. This implies choosing $\mathbb{B}_1(t)=\mathbb{B}_2(t)=\mathbb{F}_H(\omega t)\in\mathbb{R}^L$, with $L=2H+1$, such that:

$$\mathbb{F}_H(\omega t)=\left[\begin{array}{ccccccc}1 & \cos(\omega t) & \sin(\omega t) & \dots & \cos(H\omega t) & \sin(H\omega t)\end{array}\right] \tag{2.2}$$

where ω is the fundamental circular frequency of oscillation and the expansion is truncated at the H-th harmonic. An alternative choice for a basis consists of the complex trigonometric functions:

$$\mathbb{E}_H(\omega t)=\left[\begin{array}{ccccccc}e^{-iH\omega t} & \cdots & e^{-i\omega t} & 1 & e^{i\omega t} & \cdots & e^{iH\omega t}\end{array}\right] \tag{2.3}$$

It is quite simple to derive an isomorphism between $\mathbb{F}_H(\omega t)$ and $\mathbb{E}_H(\omega t)$ by Euler's formula, which leads to the conclusion that both bases are equivalent. Herein, all developments will be based on Eq. (2.2). While lacking the symmetric nature of Eq. (2.3) (which leads to convenient operators and greater overall elegance), this formulation has the advantage of avoiding complex algebra, which is useful in view of the Cast3M implementation of the method.

A generic periodic vector $\mathbf{p}(t)$ can be uniquely expressed in terms of its Fourier coeffi-

cients, $\mathbf{P} \in \mathbb{R}^{nL}$:

$$\mathbf{p}(t) = (\mathbb{F}_H(\omega t) \otimes \mathbf{I}_n)\,\mathbf{P} \tag{2.4}$$

with the following ordering convention:

$$\mathbf{P} = \left[\mathbf{P}_0^T, \mathbf{P}_{c1}^T, \mathbf{P}_{s1}^T, \ldots, \mathbf{P}_{cH}^T, \mathbf{P}_{sH}^T\right]^T \tag{2.5}$$

The symbol $\otimes$ stands for the Kronecker tensor product[1]. Each sub-vector $\mathbf{P}_x \in \mathbb{R}^n$ contains the x-th Fourier coefficient of each DOF, with the subscript x denoting either the static positions (0), or the cosine (cj) and sine (sj) parts of each harmonic, for $j = 1, \ldots, H$. Conversely, thanks to the orthonormality of the Fourier basis, $\mathbf{P}$ is obtained from $\mathbf{p}(t)$ through:

$$\mathbf{P} = \langle \mathbb{F}_H^T(\omega t) \otimes \mathbf{I}_n, \mathbf{p}(t) \rangle \tag{2.6}$$

where the inner product $\langle \cdot, \cdot \rangle$, defined on the space of real, periodic functions over $\left[0, \dfrac{2\pi}{\omega}\right]$, is given by:

$$\langle f(t), g(t) \rangle = \frac{\omega}{2\pi} \int_0^{\frac{2\pi}{\omega}} f(t) g(t) dt \tag{2.7}$$

Time-derivatives of $\mathbf{p}(t)$ are also proportional to $\mathbf{P}$, since only the basis functions are time-dependent. More precisely:

$$\dot{\mathbf{p}}(t) = \omega(\mathbb{F}_H(\omega t)\nabla \otimes \mathbf{I}_n)\mathbf{P} \tag{2.8}$$

The operator $\nabla \in \mathbb{R}^{L \times L}$ applies a permutation to the basis functions (equivalent to a 90-degree rotation), so that the velocity and displacement vectors are orthogonal in the frequency domain:

$$\begin{aligned} \nabla &= \operatorname{diag}(0, \nabla_1, ..., \nabla_H) \\ \forall j = 1, ..., H \quad &: \ \nabla_j = j \begin{bmatrix} 0 & 1 \\ -1 & 0 \end{bmatrix} \end{aligned} \tag{2.9}$$

As every term in Eq. (2.1) must be periodic as well if $\mathbf{x}(t)$ is, we can Fourier-expand them all and use the Galerkin method to obtain:

$$\begin{aligned} \mathbf{R}(\mathbf{X}, \omega) &= \left[\omega^2(\nabla^2 \otimes \mathbf{M}) + \omega(\nabla \otimes \mathbf{C}) + \mathbf{I}_L \otimes \mathbf{K}\right]\mathbf{X} + \mathbf{F}_{\mathrm{NL}}(\mathbf{X}, \omega) - \mathbf{F}(\omega) \\ &= \mathbf{Z}(\omega)\mathbf{X} + \mathbf{F}_{\mathrm{NL}}(\mathbf{X}, \omega) - \mathbf{F}(\omega) \\ &= \mathbf{0} \end{aligned} \tag{2.10}$$

[1] This allows for very compact written expressions of the equations of motion. Nonetheless, a practical implementation would benefit from avoiding the construction and storage of large sparse matrices. A more efficient procedure is to treat each DOF separately, even through parallel computing if possible.

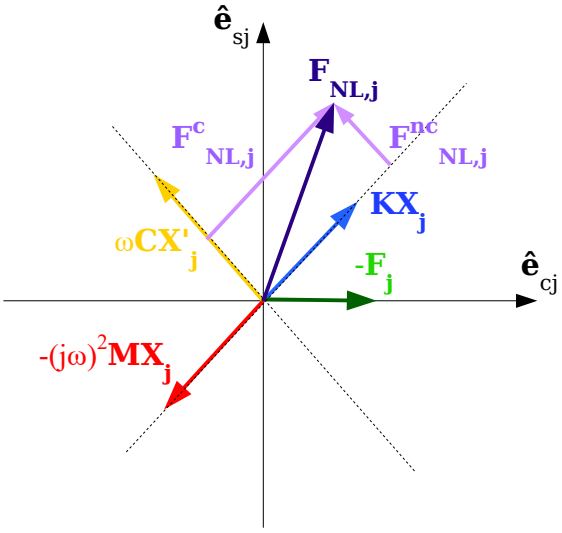

Figure 2.1: Schematic force balance for the j-th harmonic.

Here, the dynamic stiffness matrix $\mathbf{Z}(\omega) \in \mathbb{R}^{nL \times nL}$ has the following structure:

$$\begin{aligned} \mathbf{Z}(\omega) &= \operatorname{diag}\left(\mathbf{K}, \mathbf{Z}_1(\omega), ..., \mathbf{Z}_H(\omega)\right) \\ \forall j = 1, ..., H \quad &: \quad \mathbf{Z}_j(\omega) = \begin{bmatrix} \mathbf{K} - (j\omega)^2\mathbf{M} & j\omega\mathbf{C} \\ -j\omega\mathbf{C} & \mathbf{K} - (j\omega)^2\mathbf{M} \end{bmatrix} \end{aligned} \tag{2.11}$$

Finding an approximate periodic solution to Eq. (2.1), correct up to the H-th harmonic, is therefore equivalent to finding roots of the residue function, $\mathbf{R}(\mathbf{X}, \omega)$, which is a frequency-domain expression of dynamical equilibrium as illustrated in Fig. 2.1. We shall distinguish between the following cases:

Forced response: $\mathbf{C} \neq \mathbf{0}$, $\mathbf{F}(\omega) \neq \mathbf{0}$

The system is damped. The fundamental circular frequency, ω, is fixed and equals that of the forcing term $\mathbf{f}(t)$, which is necessarily periodic. The residue is then a function of $\mathbf{X}$ only and the problem $\mathbf{Y}_F(\mathbf{X}) = \mathbf{R}(\mathbf{X}) = \mathbf{0}$ is well-posed.

Autonomous response: $\mathbf{C} \neq \mathbf{0}$, $\mathbf{F}(\omega) = \mathbf{0}$

The system is damped but unforced. Hence, periodic solutions are possible only if $\mathbf{F}_{\text{NL}}$ contains non-conservative terms which balance damping in such a way that the net dissipated energy over one cycle is zero, i.e.: $\mathbf{F}_{\text{NL}} = \mathbf{F}^{nc}_{\text{NL}} + \mathbf{F}^{c}_{\text{NL}}$, where $\mathbf{F}^{nc}_{\text{NL}} \perp \mathbf{F}^{c}_{\text{NL}}$ and $\mathbf{F}^{nc}_{\text{NL}} = -\omega(\nabla \otimes \mathbf{C})\mathbf{X}$. Furthermore, the circular frequency is unknown a priori and must be found simultaneously with the Fourier coefficients. The problem $\mathbf{R}(\mathbf{X}, \omega) = \mathbf{0}$ is under-constrained and must be completed by an additional equation. This is typically done by introducing a *phase condition* which fixes the initial phase of any given DOF, which is arbitrary since periodic solutions are invariant under time translations in the autonomous

case. Thus, without loss of generality, an initial phase of zero may be chosen for the first DOF:

$$\begin{aligned} &\dot{x}_1(0) = 0 \implies g(\mathbf{X}) = \mathbf{e}_0\mathbf{X} = 0 \\ &\mathbf{e}_0 = [0\,0\,1\,0\,2\,\ldots\,0\,H] \otimes [1\,0\,\ldots\,0] \end{aligned} \tag{2.12}$$

The problem $\mathbf{Y}_{\mathrm{A}}(\mathbf{X},\omega) = \left[\mathbf{R}^T(\mathbf{X},\omega)\;\; g(\mathbf{X})\right]^T = \mathbf{0}$ is well-posed.

Free response: $\mathbf{C} = \mathbf{0}$, $\mathbf{F}(\omega) = \mathbf{0}$

The system is conservative, which implies that $\mathbf{F}_{\mathrm{NL}} = \mathbf{F}^c_{\mathrm{NL}}$ with $\mathbf{F}^c_{\mathrm{NL}}$ collinear to $\left[\mathbf{I}_L \otimes \mathbf{K} - \omega^2\nabla^2 \otimes \mathbf{M}\right]\mathbf{X}$. The solutions $\mathbf{X}$ in this case correspond precisely to the definition of *Nonlinear Normal Modes* (NNMs) in the sense of Rosenberg [ROS 62]: families of periodic orbits of a system's underlying conservative part, parametrized by energy level. Indeed, as no input nor output of energy is present in the conservative equation, solutions exist for arbitrary values of $E = \mathbf{X}^T\mathbf{X}$, which is a measure of total energy in accordance with Parseval's theorem. In other words, the norm of $\mathbf{X}$ is free to vary; this leads to an under-constrained problem which requires the appending of an *energy condition* such as:

$$h(\mathbf{X}) = \mathbf{X}^T\mathbf{X} - E_0 = 0 \tag{2.13}$$

with $E_0 \in \mathbb{R}^+$. In contrast to the linear modes, an implicit relation exists between $\mathbf{X}$ and ω, so these variables must be computed simultaneously. Moreover, as the conservative system is autonomous as well, Eq. (2.12) must be used to choose a particular solution amongst the continuum of possibilities. This means, however, that the system is over-constrained, as $nL+2$ equations are set up for the $nL+1$ unknowns $\mathbf{X}$ and ω. The solution we choose herein, following [ARQ 06], is to relax the system by including an artificial parameter a, which plays the role of a trivial Lagrange multiplier associated with the non-conservative force:

$$\mathbf{F}_a(\mathbf{X}) = a(\nabla \otimes \mathbf{I}_n)\mathbf{X} \tag{2.14}$$

Hence, dynamical equilibrium reads:

$$\mathbf{R}(\mathbf{X},\omega,a) = \left[\omega^2(\nabla^2 \otimes \mathbf{M}) + \mathbf{I}_L \otimes \mathbf{K}\right]\mathbf{X} + a(\nabla \otimes \mathbf{I}_n)\mathbf{X} + \mathbf{F}^c_{\mathrm{NL}}(\mathbf{X},\omega) = \mathbf{0} \tag{2.15}$$

As a non-zero energy level is imposed through Eq. (2.13), the only allowable value is $a = 0$, and one effectively solves the conservative equations. The problem $\mathbf{Y}_{\mathrm{NNM}}(\mathbf{X},\omega,a) = \left[\mathbf{R}^T(\mathbf{X},\omega,a)\;\; g(\mathbf{X})\;\; h(\mathbf{X})\right]^T = \mathbf{0}$ is well-posed.

The Newton-Raphson method is used to find a solution to any of the above problems. To this end, the Jacobian matrices associated to the forced, autonomous or free (NNM) cases must be constructed at each iteration:

$$\mathbf{J}_{\mathrm{F}} = \mathbf{R}_{\mathbf{X}} \tag{2.16}$$

$$\mathbf{J}_{\mathrm{A}} = \begin{bmatrix} \mathbf{R}_{\mathbf{X}} & \mathbf{R}_{\omega} \\ \mathbf{g}_{\mathbf{X}} & 0 \end{bmatrix} \tag{2.17}$$

$$\mathbf{J}_{\mathrm{NNM}} = \begin{bmatrix} \mathbf{R}_{\mathbf{X}} & \mathbf{R}_{\omega} & \mathbf{R}_{a} \\ \mathbf{g}_{\mathbf{X}} & 0 & 0 \\ \mathbf{h}_{\mathbf{X}} & 0 & 0 \end{bmatrix} \tag{2.18}$$

where subscripts denote partial differentiation and dependence on the corresponding variables has been omitted for ease of presentation. It should be noticed that most of the derivatives hereupon can be readily computed from the definitions given in this chapter. However, the terms:

$$\mathbf{R}_{\mathbf{X}}(\mathbf{X},\omega) = \mathbf{Z}(\omega) + \frac{d\mathbf{F}_{\mathrm{NL}}}{d\mathbf{X}} \tag{2.19}$$

$$\mathbf{R}_{\omega}(\mathbf{X},\omega) = [2\omega(\nabla^2 \otimes \mathbf{M}) + (\nabla \otimes \mathbf{C})] + \frac{d\mathbf{F}_{\mathrm{NL}}}{d\omega} \tag{2.20}$$

introduce derivatives of nonlinear forces, which require a special treatment. The same can actually be said of the forces themselves, which are part of the residual vectors $\mathbf{Y}_{\mathrm{pt}}$ since, in all cases, the Newton-Raphson correction to be added to the vector of unknowns, $\boldsymbol{\Upsilon}_{\mathrm{pt}}$, at the k-th iteration is given by:

$$\boldsymbol{\zeta}^{(k)} = -\mathbf{J}_{\mathrm{pt}}^{-1}(\boldsymbol{\Upsilon}_{\mathrm{pt}}^{(k)})\mathbf{Y}_{\mathrm{pt}}(\boldsymbol{\Upsilon}_{\mathrm{pt}}^{(k)}) \tag{2.21}$$

where the sub-index $_{\mathrm{pt}}$ stands for any one of the problem types: {F, A, NNM} and $\boldsymbol{\Upsilon}_{\mathrm{pt}}$ contains the corresponding unknowns. Convergence of the method is considered to be achieved at iteration k if the residual norm falls below a given tolerance $\varepsilon > 0$:

$$\| \mathbf{Y}_{\mathrm{pt}}(\boldsymbol{\Upsilon}_{\mathrm{pt}}^{(k)}) \| < \varepsilon \implies \boldsymbol{\Upsilon}_{\mathrm{pt}}^{(k)} \text{ is a solution} \tag{2.22}$$

2.1.2 Computing nonlinear forces

Determining the Fourier coefficients of nonlinear forces and their derivatives is not a trivial task, as analytical expressions are generally not available in the frequency domain. A wide range of problems, namely those dealing with large displacements or nonlinear damping, involve forces with polynomial forms. For this particular class of functions, an efficient computation can be performed by exploiting the convolution theorem. This is frequently done when a complex formulation of the HBM is used, see e.g. [COC 09], but rarely (if at all) for the real formulation. A method applicable to the latter is presented in Appendix A.1. For all other kinds of nonlinearities, the Alternating Frequency-Time (AFT) method introduced by [GRO 01] is certainly a practical choice.

General terms: AFT

The main idea is to compute the forces (and their derivatives) in the time domain, where their explicit definitions are available and often simple, and to subsequently obtain their Fourier coefficients by projecting them onto the frequency domain, where the harmonic equations are solved. Projections from one domain to the other are made by direct and inverse Fourier transforms, which computationally leads to two variants of the method:

a) DFT-based: Let $\bar{\mathbf{x}} \in \mathbb{R}^{nN\times 1}$ represent an N-sample representation of the periodic solution vector over the uniformly-spaced time grid $\bar{t} = [t_0, ..., t_{N-1}]^T$, where $t_N = \frac{2\pi}{\omega}$ and, $\forall k = 0, ..., N:\ t_k = \frac{k}{N}\frac{2\pi}{\omega}$. Hence, from Eq.(2.4):

$$\bar{\mathbf{x}} = \left(\begin{bmatrix} \mathbb{F}_H(0) \\ \vdots \\ \mathbb{F}_H\left(2\pi\frac{N-1}{N}\right) \end{bmatrix} \otimes \mathbf{I}_n \right) \mathbf{X} = (\mathbf{\Gamma}_H \otimes \mathbf{I}_n)\mathbf{X} \tag{2.23}$$

Multiplication by matrix $\mathbf{\Gamma}_H \in \mathbb{R}^{N\times L}$ thus performs an inverse DFT. The direct transform is given by the pseudo-inverse $\mathbf{\Gamma}_H^{-1}$, such that $\mathbf{\Gamma}_H^{-1}\mathbf{\Gamma}_H = \mathbf{I}_L$ and:

$$\mathbf{X} = (\mathbf{\Gamma}_H^{-1} \otimes \mathbf{I}_n)\bar{\mathbf{x}} \tag{2.24}$$

This is, in particular, true for the vector of nonlinear forces, which is thus given by:

$$\mathbf{F}_{\mathrm{NL}} = (\mathbf{\Gamma}_H^{-1} \otimes \mathbf{I}_n)\bar{\mathbf{f}}_{\mathrm{NL}}(\bar{\mathbf{x}}, \dot{\bar{\mathbf{x}}}, \ddot{\bar{\mathbf{x}}}) \tag{2.25}$$

The sampled velocities and accelerations, if required, are computed by combining Eqs. (2.23) and (2.8):

$$\dot{\bar{\mathbf{x}}} = \ \ \omega((\mathbf{\Gamma}_H\nabla) \otimes \mathbf{I}_n)\mathbf{X} = \ \ \omega(\mathbf{\Gamma}_H \otimes \mathbf{I}_n)\mathbf{V} \tag{2.26}$$

$$\ddot{\bar{\mathbf{x}}} = \omega^2((\mathbf{\Gamma}_H\nabla^2) \otimes \mathbf{I}_n)\mathbf{X} = \omega^2(\mathbf{\Gamma}_H \otimes \mathbf{I}_n)\mathbf{A} \tag{2.27}$$

Differentiation of Eq. (2.25) with respect to ($\mathbf{X}$,ω), minding the chain rule, thus yields:

$$\begin{aligned} \frac{d\mathbf{F}_{\mathrm{NL}}}{d\mathbf{X}} &= (\mathbf{\Gamma}_H^{-1} \otimes \mathbf{I}_n)\left[\frac{\partial\bar{\mathbf{f}}_{\mathrm{NL}}}{\partial\bar{\mathbf{x}}}(\mathbf{\Gamma}_H \otimes \mathbf{I}_n) + \omega\frac{\partial\bar{\mathbf{f}}_{\mathrm{NL}}}{\partial\dot{\bar{\mathbf{x}}}}((\mathbf{\Gamma}_H\nabla) \otimes \mathbf{I}_n) + \omega^2\frac{\partial\bar{\mathbf{f}}_{\mathrm{NL}}}{\partial\ddot{\bar{\mathbf{x}}}}((\mathbf{\Gamma}_H\nabla^2) \otimes \mathbf{I}_n)\right] \\ &= \frac{\partial\mathbf{F}_{\mathrm{NL}}}{\partial\mathbf{X}} + \omega\frac{\partial\mathbf{F}_{\mathrm{NL}}}{\partial\mathbf{V}}(\nabla \otimes \mathbf{I}_n) + \omega^2\frac{\partial\mathbf{F}_{\mathrm{NL}}}{\partial\mathbf{A}}(\nabla^2 \otimes \mathbf{I}_n) \end{aligned} \tag{2.28}$$

$$\begin{aligned} \frac{d\mathbf{F}_{\mathrm{NL}}}{d\omega} &= (\mathbf{\Gamma}_H^{-1} \otimes \mathbf{I}_n)\left[\frac{\partial\bar{\mathbf{f}}_{\mathrm{NL}}}{\partial\omega} + \left(\frac{\partial\bar{\mathbf{f}}_{\mathrm{NL}}}{\partial\dot{\bar{\mathbf{x}}}}((\mathbf{\Gamma}_H\nabla) \otimes \mathbf{I}_n) + 2\omega\frac{\partial\bar{\mathbf{f}}_{\mathrm{NL}}}{\partial\ddot{\bar{\mathbf{x}}}}((\mathbf{\Gamma}_H\nabla^2) \otimes \mathbf{I}_n)\right)\mathbf{X}\right] \\ &= (\mathbf{\Gamma}_H^{-1} \otimes \mathbf{I}_n)\frac{\partial\bar{\mathbf{f}}_{\mathrm{NL}}}{\partial\omega} + \frac{\partial\mathbf{F}_{\mathrm{NL}}}{\partial\mathbf{V}}(\nabla \otimes \mathbf{I}_n)\mathbf{X} + 2\omega\frac{\partial\mathbf{F}_{\mathrm{NL}}}{\partial\mathbf{A}}(\nabla^2 \otimes \mathbf{I}_n)\mathbf{X} \end{aligned} \tag{2.29}$$

Since matrices $\mathbf{\Gamma}_H, \mathbf{\Gamma}_H^{-1}$ depend solely on H and N, they need only be computed once as a preliminary step, and so this method is very easy to implement. For a given H, it

is necessary to choose a number of samples $N \geq 2H+1$ in order to avoid the *aliasing* phenomenon [HES 09, DAI 18]: as the numerical representation of a function is made up of a discrete collection of values, any events occurring between two consecutive samples are unresolved. Hence, high-frequency components are incorrectly interpreted as a combination of lower-frequency ones, artificially distorting the signal.An illustration is shown in Fig. 2.2 with the function $f(t) = sin(3t)$. For $N = 3 < 7$, a discrete Fourier transform 'sees' the function $-sin(t)$, shown in dashed lines. On the other hand, choosing $N = 16 > 7$ leads to an unambiguous representation. This corresponds to the intuition that good resolution requires at least one sample per peak in the corresponding waveform. Respecting the condition above, commonly known as the *sampling theorem*, yields the exact values of Fourier coefficients up to the H-th harmonic through DFT [KRA 19].

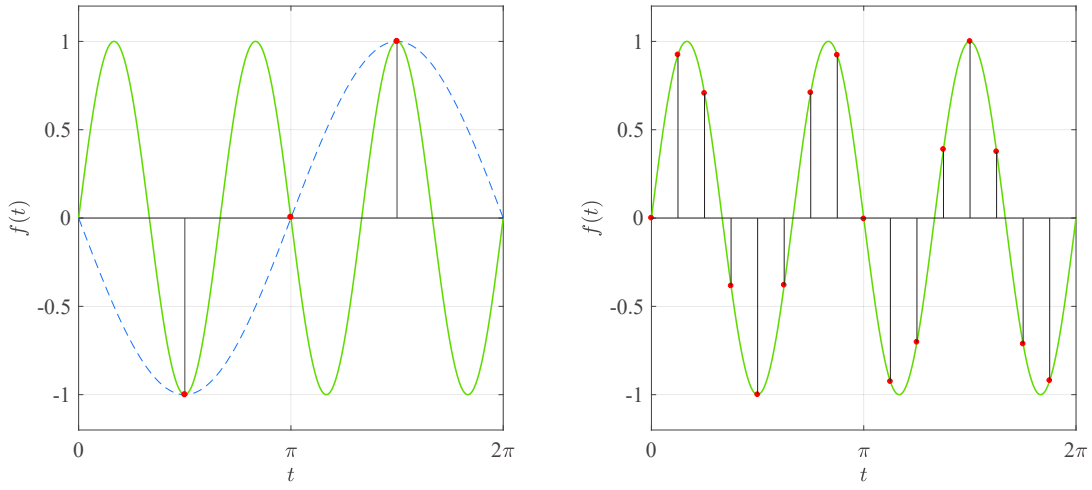

a) $N = 3$ b) $N = 16$

Figure 2.2: Aliasing phenomenon for the representation of $f(t) = sin(3t)$.

b) FFT-based: The main drawback of the DFT method is its computational cost, which grows quadratically with H and N. Indeed, the number of operations involved in one back-and-forth transformation of a vector with length L is $nNL(L+nN)$. Supposing N and L are of the same order of magnitude (a rather optimistic estimation, as discussed in the following paragraph), this means that computing the nonlinear forces demands at least the same computational effort as inverting the Jacobian in Eq. (2.21), and this is still not taking into account the derivatives. A higher efficiency is possible through the replacement of the straightforward products $(\mathbf{\Gamma}_H^{-1} \otimes \mathbf{I}_n)\bar{\mathbf{x}}$ and $(\mathbf{\Gamma}_H \otimes \mathbf{I}_n)\mathbf{X}$ by calls to direct and inverse Fast Fourier Transform (FFT) subroutines, respectively. A FORTRAN implementation, for instance, exists within the open-access linear algebra library FFTPACK [SWA 84], whereas **fft/ifft** are standard commands available in MATLAB. Both of these are based on the algorithm generally attributed to Cooley and Tukey [COO 65], which is based on recursively computing n_1 complex DFTs of size n_2, where $N = n_1 n_2$. Optimal efficiency is thus achieved by choosing N to be as decomposable as possible into small

integer factors, i.e. N should be a power of 2.
The direct FFT of a sampled signal yields complex-valued Fourier coefficients $\hat{\mathbf{X}}_j,\ \forall j = 0,...,H$, from where the real coefficients are computed through:

$$\mathbf{X}_{cj} = \frac{2}{N}\Re\left(\hat{\mathbf{X}}_j\right) \qquad\qquad \mathbf{X}_{sj} = -\frac{2}{N}\Im\left(\hat{\mathbf{X}}_j\right) \tag{2.30}$$

An additional advantage of the FFT over the DFT-based AFT is that it is generalizes to multiple-dimensional Fourier series with relative ease, which is convenient for quasi-periodic analyses. Besides, as in such cases the size of the problem becomes $n(2H+1)^m$, the gain in computational efficiency quickly becomes a necessity rather than a commodity.

2.1.3 Pseudo Arc-length Continuation (PAC)

The equations for dynamic equilibrium generically depend on an arbitrary number of parameters, whose values are fixed when calculating a solution $\boldsymbol{\Upsilon}^0_{\text{pt}}$. Let us consider a parameter α, with initial value α^0. A small variation $\Delta\alpha$ will result in violating the equilibrium conditions, unless a corresponding variation $\Delta\Upsilon_{\text{pt}}$ is introduced such that $\mathbf{Y}_{\text{pt}}(\boldsymbol{\Upsilon}^0_{\text{pt}} + \Delta\boldsymbol{\Upsilon}_{\text{pt}}, \alpha^0 + \Delta\alpha) = \mathbf{0}$. A Taylor expansion around the initial solution can be performed, as the residual $\mathbf{Y}_{\text{pt}}$ depends continuously on the Fourier coefficients and on all of its parameters. To first order, this yields:

$$\mathbf{Y}_{\text{pt}}(\boldsymbol{\Upsilon}^0_{\text{pt}} + \Delta\boldsymbol{\Upsilon}_{\text{pt}}, \alpha^0 + \Delta\alpha) \approx \mathbf{J}^0_{\text{pt}}\Delta\boldsymbol{\Upsilon}_{\text{pt}} + \mathbf{Y}^0_{\alpha}\Delta\alpha \approx \mathbf{0} \tag{2.31}$$

where the super-index denotes evaluation at $\left(\boldsymbol{\Upsilon}^0_{\text{pt}}, \alpha^0\right)$ and the error is $O\left(\max\left(||\Delta\boldsymbol{\Upsilon}_{\text{pt}}||^2, |\Delta\alpha|^2\right)\right)$. The Implicit Function Theorem ensures that a smooth, bijective curve $f(\boldsymbol{\Upsilon}_{\text{pt}}, \alpha) = 0$ exists in the vicinity of the initial solution, under the condition that $\mathbf{J}^0_{\text{pt}}$ is non-singular. The first-order approximation of Eq.(2.31) -which lies on the local tangent line to the initial solution in $(\boldsymbol{\Upsilon}_{\text{pt}}, \alpha)$ space- will generally not belong to this curve. Nevertheless, for sufficiently small variations, it provides a good starting point from where Newton-Raphson iterations may be used to converge to a new solution. The strategy is thus of the *predictor-corrector* type, and consists of two stages:

Prediction An additional equation must be appended to Eq.(2.31) in order to achieve closure. The *pseudo arc-length* equation is used:

$$||\Delta\boldsymbol{\Upsilon}_{\text{pt}}||^2 + \Delta\omega^2 = \Delta s^2 \tag{2.32}$$

where $\Delta s > 0$, which fixes the magnitude of the tangent step. The predicted solution is:

$$\begin{pmatrix} \boldsymbol{\Upsilon}^{1\{0\}}_{\text{pt}} \\ \alpha^{1\{0\}} \end{pmatrix} = \begin{pmatrix} \boldsymbol{\Upsilon}^0_{\text{pt}} \\ \alpha^0 \end{pmatrix} + \begin{pmatrix} \Delta\boldsymbol{\Upsilon}_{\text{pt}} \\ \Delta\alpha \end{pmatrix} \tag{2.33}$$

where the components of the tangent vector satisfy:

$$\begin{bmatrix} \mathbf{J}^0_{\text{pt}} & \left(\mathbf{Y}^0_{pt}\right)_{\alpha} \\ \Delta\boldsymbol{\Upsilon}^T_{\text{pt}} & \Delta\alpha \end{bmatrix} \begin{pmatrix} \Delta\boldsymbol{\Upsilon}_{\text{pt}} \\ \Delta\alpha \end{pmatrix} = \begin{pmatrix} \mathbf{0} \\ \Delta s^2 \end{pmatrix} \tag{2.34}$$

Correction Newton-Raphson iterations are performed in a direction orthogonal to the tangent vector of the predictor step. At the k-th iteration, the corrections are computed as the solution to:

$$\begin{bmatrix} \mathbf{J}_{\mathrm{pt}}^{1\{k\}} & \mathbf{Y}_{\omega}^{1\{k\}} \\ \Delta\boldsymbol{\Upsilon}_{\mathrm{pt}}^{T} & \Delta\alpha \end{bmatrix} \begin{pmatrix} \delta\boldsymbol{\Upsilon}_{\mathrm{pt}} \\ \delta\alpha \end{pmatrix} = - \begin{pmatrix} \mathbf{Y}_{\mathrm{pt}}^{1\{k\}} \\ 0 \end{pmatrix} \tag{2.35}$$

until the magnitude of the residual falls below a given tolerance.

This procedure can be automated so that the implicit curve is computed step-by-step over a given range of α. An efficient algorithm includes automatic step-length adaptation, such that smaller steps are taken in the presence of important local curvature, as evidenced by large deviation from the tangent approximation. The number of required iterations at a given step is an appropriate practical measure of this characteristic, and is thus the foundation of adaptation strategies [SEY 10]. Besides, as the sign of the tangent vector is not inherently prescribed by Eq. (2.32), it is the duty of the algorithm to choose it so that direction of the course is preserved along continuation. Letting $\mathbf{t}_i$ be the tangent vector at the i-th step, the condition to fulfill is simply expressed as: $\mathbf{t}_i^T \cdot \mathbf{t}_{i-1} > 0$.
Fig. 2.3 summarizes the PAC algorithm with tangent prediction, as used throughout this work. It shall be noted that this method works for any system of nonlinear algebraic equations. In particular, it can be used on the defining systems for the wide range of bifurcations encountered in dynamics problems, which are presented in the following sections. This application of continuation methods is termed *bifurcation tracking* [XIE 17, DET 14, PET 16].

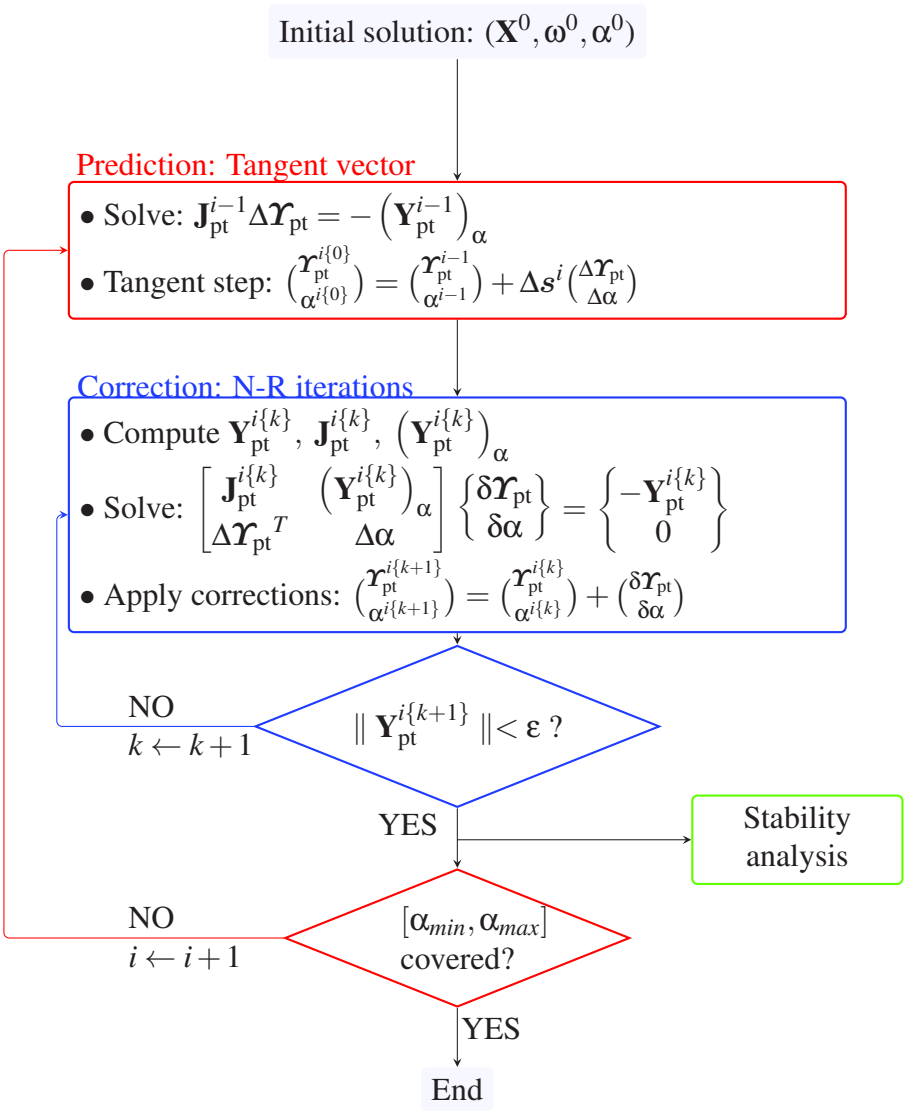

Figure 2.3: Generic HBM-PAC algorithm.

2.1.4 Bifurcation analysis

2.1.4.1 Codimension-1 bifurcations

The numerical computation of Floquet exponents for nonlinear vibration problems can be performed in the frequency domain by employing Hill's method. When pseudo arc-length continuation is used, this amounts to solving the quadratic eigenvalue problem [GRO 01]:

$$\left[\mathbf{R}_{\mathbf{X}} + \lambda \mathbf{D}_1 + \lambda^2 \mathbf{D}_2\right] \bar{\mathbf{P}} = \mathbf{0} \tag{2.36}$$

where $\mathbf{R}_{\mathbf{X}}$ is defined by Eq. (2.19) and:

$$\begin{cases} \mathbf{D}_1 = 2\omega\nabla \otimes \mathbf{M} + \mathbf{I}_L \otimes \mathbf{C} + \dfrac{\partial \mathbf{F}_{\mathrm{NL}}}{\partial \mathbf{V}} \\ \mathbf{D}_2 = \mathbf{I}_L \otimes \mathbf{M} \end{cases} \tag{2.37}$$

Given that Floquet exponents are implicit, continuous functions of the parameters on which a system depends, bifurcations are generically found during the continuation of (quasi-) periodic solutions. Fig. 2.4 summarizes the four well-known bifurcation scenarios in codimension 1, represented by one or two (complex conjugate) *critical* exponents crossing the imaginary axis in the Argand plane. The rigorous detection of bifur-

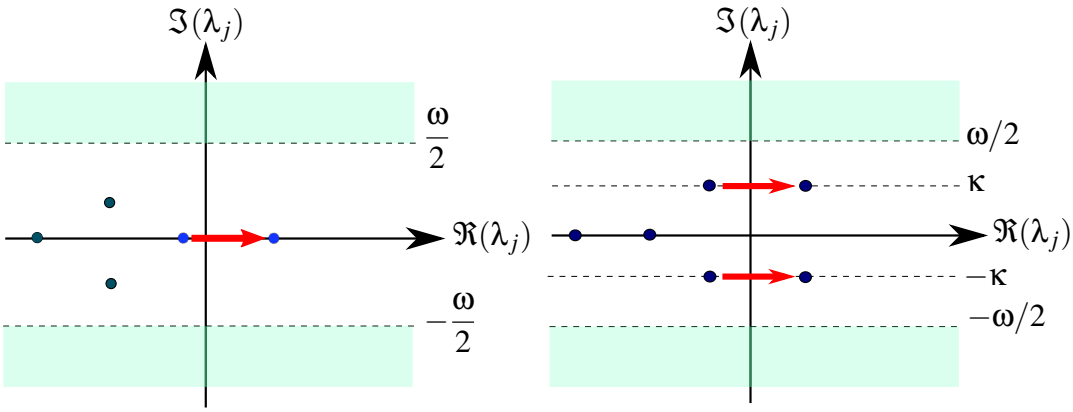

a) Static bifurcation: LP or BP.

b) Dynamic bifurcation: NS or PD.

Figure 2.4: Stability loss at codimension-1 bifurcations.

cations is done by evaluating, at each continuation step, scalar test functions tailored to vanish at a specific bifurcation. Examples can be found in [DOE 03, SEY 10], or even [XIE 17, ALC 19] in the context of HBM. A more efficient methodology for practical implementations consist in keeping track of "unstable exponents", i.e. of exponents with positive real parts, and comparing their number at consecutive steps. For the j-th step, let this number be given by N_u^j. This yields a very simple criterion, as follows:

1. $N_u^j - N_u^{j-1} = 0$: regular point, no bifurcation has occurred.

2. $N_u^j - N_u^{j-1} = 1$: static bifurcation. A critical Floquet exponent crosses the imaginary axis through the origin, corresponding to a singular Jacobian matrix: $\det(\mathbf{R}_\mathbf{X}) = 0$. If this is accompanied by a change in the continuation direction, i.e. $\Delta\omega^j \Delta\omega^{j-1} < 0$, then a point of vertical tangency ($\Delta\omega = 0$) exists on the response curve and the bifurcation at hand is a Limit Point (LP). Else, the singularity is degenerate and translates the non-uniqueness of the tangent vector; in other words, two branches of solutions intersect at the bifurcation, which is thus a Branch Point (BP). As solutions pertaining to distinct branches are qualitatively different, the latter case is associated to the breaking of a certain symmetry (see Sect. 2.2.4).

3. $N_u^j - N_u^{j-1} = 2$: dynamic bifurcation. A pair of complex conjugates crosses the imaginary axis. At the critical value, such that $\Re(\lambda_\pm) = 0$, the imaginary part has magnitude $\Im(\lambda_\pm) = \pm\kappa$. A branch of solutions, whose frequency content includes combinations of ω and $|\kappa| \in \left]0, \frac{\omega}{2}\right]$, emanates from the bifurcation: in the generic case where the ratio ω/κ is irrational, a Neimark-Sacker (NS) bifurcation occurs and the family of branching solutions is quasi-periodic. If, on the other hand, this ratio is an integer, then the minimal period of the branching solutions is multiplied. The most fundamental case, both by its ubiquitousness and its practical implications, is *period doubling* (PD), where $|\kappa| = \omega/2$.

Hereafter, typical fully-extended systems are given for each kind of bifurcation.

$$\mathbf{Y}_{\mathrm{LP}}(\mathbf{X}, \phi, \omega) = \begin{bmatrix} \mathbf{R} \\ \mathbf{R}_\mathbf{X}\phi \\ \phi^T\phi - 1 \end{bmatrix} \tag{2.38}$$

$$\mathbf{Y}_{\mathrm{BP}}(\mathbf{X}, \phi, \omega, \gamma) = \begin{bmatrix} \mathbf{R} + \gamma\phi \\ \phi^T\mathbf{R}_\mathbf{X} \\ \phi^T\mathbf{R}_\omega \\ \phi^T\phi - 1 \end{bmatrix} \tag{2.39}$$

$$\mathbf{Y}_{\mathrm{NS}}(\mathbf{X}, \phi_R, \phi_I, \kappa, \omega) = \begin{bmatrix} \mathbf{R} \\ \left(\mathbf{R}_\mathbf{X} - \kappa^2\mathbf{D}_2\right)\phi_R - \kappa\mathbf{D}_1\phi_I \\ \kappa\mathbf{D}_1\phi_R + \left(\mathbf{R}_\mathbf{X} - \kappa^2\mathbf{D}_2\right)\phi_I \\ \phi_R^T\phi_R - 1 \\ \mathbf{p}^T\phi_R \end{bmatrix} \tag{2.40}$$

$$\mathbf{Y}_{\mathrm{PD}}(\mathbf{X}, \phi_R, \phi_I, \omega) = \begin{bmatrix} \mathbf{R} \\ \left(\mathbf{R}_\mathbf{X} - \left(\frac{\omega}{2}\right)^2\mathbf{D}_2\right)\phi_R - \left(\frac{\omega}{2}\right)\mathbf{D}_1\phi_I \\ \left(\frac{\omega}{2}\right)\mathbf{D}_1\phi_R + \left(\mathbf{R}_\mathbf{X} - \left(\frac{\omega}{2}\right)^2\mathbf{D}_2\right)\phi_I \\ \phi_R^T\phi_R - 1 \end{bmatrix} \tag{2.41}$$

They are presented in a form suitable for forced response analysis, but they are also applicable to autonomous responses as well by systematically including a phase condition

alongside the constraint equations. Moreover, as a trivial zero exponent is always included among the $2n$ Floquet exponents of autonomous periodic solutions, a necessary additional step for computing static bifurcations in that case consists in shifting

In Eq.(2.39), γ is an artificial parameter used to unfold the BP bifurcation, similarly to the relaxation strategy used for NNM computation. Any non-zero value of γ would generate an imperfect bifurcation, i.e. disjoint solution branches, as the dynamical equilibrium equations are perturbed. Thus, imposing $\gamma = 0$ is equivalent to requiring symmetry of the main branch. In addition, it should be noted that the *left* eigenvector is considered in this case. The degeneracy of the zero exponent is equivalent to the singularity of the tangent matrix from Eq.(2.33), which in turn implies that $\mathbf{R}_\omega$ is in the range of $\mathbf{R}_\mathbf{X}$. In other words:

$$\exists \mathbf{v} \in \mathbb{R}^{nL}, \quad \mathbf{R}_\mathbf{X}\mathbf{v} + \mathbf{R}_\omega = \mathbf{0} \tag{2.42}$$

which leads to the third line of Eq.(2.39) upon multiplication by the left eigenvector.

In Eq.(2.40), the last lines are used to normalize vectors ϕ_R and ϕ_I, with $\mathbf{p} \in \mathbb{R}^{nL}$ a constant vector with non-zero projection on $\mathrm{Span}(\phi_R, \phi_I)$. In practice, any two non-contradictory normalization conditions can be used, and those above can be replaced -for instance- by: $\mathbf{p}^T\phi_R = 0$ and $\mathbf{p}^T\phi_I - 1 = 0$. These simplify to the LP system, Eq. (2.38), for $\kappa = 0$, as the lack of amplitude constraint allows for ϕ_R to become nil. The physical reason for the need of two is that, as explained in Sect. 2.2.2, a 2-torus such as the ones on the branch emerging from a NS bifurcation is parametrized by two time-like coordinates. While the total initial phase is imposed by the forcing, the phase of one of the latter can be taken arbitrarily, and a particular value must be chosen by fixing the value of a given component, as is done by the second normalization equation above.

As the second frequency κ is not unknown in this case of Eq.2.41, one of the normalization equations has to be removed. An alternate extended system, which resembles Eq.(2.40) as closely as possible, is obtained by keeping κ variable and replacing the second normalization condition by the phase-locking expression: $\omega - 2\kappa = 0$.
For completeness, details on the computation of the different terms involved in the Jacobian matrices of general extended systems are given in Appendix A.2.

2.1.4.2 Trivial eigenvalue of autonomous systems

A limit cycle solution to conservative systems, such as Eq. (2.1) with $\mathbf{f}(t) = \mathbf{0}$, is never unique, in the sense that a continuous family of associated solutions can be obtained by varying its phase, which is imposed only artificially through a phase condition. This implies the existence of a trivial Floquet exponent with value zero, which has no impact on the actual stability behaviour of the computed solutions. Ideally, this would pose no problem, since one could just isolate this eigenvalue and evaluate stability with the remaining ones. However, given that numerical errors are practically unavoidable, the trivial eigenvalue may fluctuate and cross the stability boundary $\Im(\lambda) = 0$ during continuation, which would be spuriously interpreted as a bifurcation. Therefore, a better strategy is to identify the trivial exponent not by its value, but rather through a formal characterisation. This may be achieved by finding an analytical expression of its associated eigenvector, as follows.

Consider a periodic solution of Eq. 2.86 with an arbitrary initial phase: $\mathbf{X}(t+b_0), b_0 \in \mathbb{R}$. Its Fourier expansion can be expressed in two equivalent ways, either in terms of the coefficients associated with zero phase shift, $\mathbf{X}_0$, or by considering a new vector $\mathbf{X}_{b_0}$:

$$\mathbf{x}(t+b_0) = [\mathbb{F}(\omega(t+b_0)) \otimes \mathbf{I}_n]\,\mathbf{X}_0 = [\mathbb{F}(\omega t) \otimes \mathbf{I}_n]\,\mathbf{X}_{b_0} \tag{2.43}$$

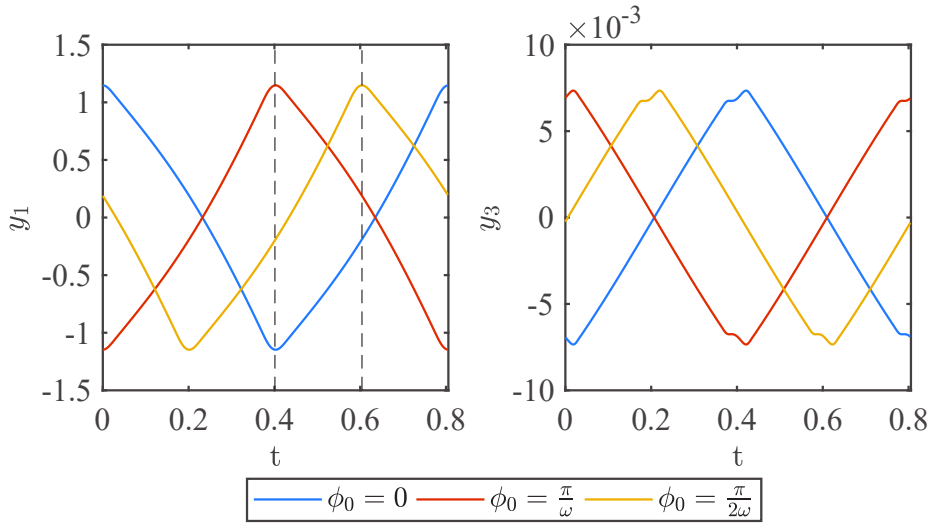

Figure 2.5: Translation invariance. The three time series shown all satisfy Eq. (1), with the phase condition $\dot{y}_1(\omega b_0) = 0$ imposed on the first mode.

This relation simply states the known fact that a phase shift equates to a rotation of the harmonic coefficients by an angle b_0 in the frequency domain, while their amplitudes are kept constant. Indeed, by using trigonometric identities, it is straightforward to deduce: $\mathbb{F}(\omega(t+b_0)) = \mathbb{F}(\omega t)\mathbf{G}(\omega b_0)$, where :

$$\mathbf{G}(\omega b_0) = \mathrm{diag}\left(1, \begin{bmatrix} \cos(\omega b_0) & \sin(\omega b_0) \\ -\sin(\omega b_0 & \cos(\omega b_0) \end{bmatrix}, \ldots, \begin{bmatrix} \cos(H\omega b_0) & \sin(H\omega b_0) \\ -\sin(H\omega\, b_0) & \cos(H\omega b_0) \end{bmatrix}\right) \tag{2.44}$$

$$\Longrightarrow \mathbf{X}_{b_0} = (\mathbf{G}(\omega b_0) \otimes \mathbf{I}_n)\mathbf{X}_0 \tag{2.45}$$

Fig. 2.5 illustrates this on a periodic solution to an autonomous equation, rotated to satisfy different phase conditions. Now, if $\mathbf{X}_0$ satisfies dynamical equilibrium, the invariance property implies that $\mathbf{X}_{b_0}$ must do the same for any b_0. Hence: $\mathbf{R}(\mathbf{X}_{b_0}) = \mathbf{0}$ and, moreover:

$$\frac{d\mathbf{R}(\mathbf{X}_{b_0})}{db_0} = \frac{\partial \mathbf{R}}{\partial b_0} + \mathbf{R}_{\mathbf{X}}(\mathbf{X}_{b_0})\frac{d\mathbf{X}_{b_0}}{db_0} = \mathbf{0} \tag{2.46}$$

As the equilibrium residual does not depend explicitly on b_0, the first term is identically zero. Furthermore, from Eq. (2.45), $\frac{d\mathbf{X}_{b_0}}{db_0} = \omega(\nabla\mathbf{G}(\omega b_0)\otimes\mathbf{I}_n)\mathbf{X}_0 = \omega(\nabla\otimes\mathbf{I}_n)\mathbf{X}_{b_0}$, which implies:

$$\mathbf{R}_\mathbf{X}(\mathbf{X}_{b_0})\left[(\nabla\otimes\mathbf{I}_n)\mathbf{X}_{b_0}\right] = \mathbf{0} \tag{2.47}$$

The term within brackets is a vector which belongs to the null space of $\mathbf{R}_\mathbf{X}$ for any given b_0. Thus, regardless of the phase condition used to fix the value of this quantity, the corresponding eigenvector for the zero eigenvalue of $\mathbf{R}_\mathbf{X}$ is always given by Eq. (2.47). This is true, in particular, for $b_0 = 0$:

$$\mathbf{R}_\mathbf{X}(\nabla\otimes\mathbf{I}_n)\mathbf{X}_0 = \mathbf{0} \tag{2.48}$$

This proves that the invariant nature of limit cycles is reflected by a zero eigenvalue of its Jacobian matrix. Now, let us consider once more the eigenvalue problem of Eq. (2.36). The trivial Floquet exponent is sought by imposing $\lambda = 0$. We find:

$$\mathbf{R}_\mathbf{X}\bar{\mathbf{P}} = \mathbf{0} \tag{2.49}$$

Any nil Fourier exponents thus coincide with zero eigenvalues of the Jacobian. Only one such eigenvalue exists for a regular periodic solution if the system is autonomous. This implies that, necessarily,

$$\bar{\mathbf{P}} = (\nabla\otimes\mathbf{I}_n)\mathbf{X} \tag{2.50}$$

is the eigenvector associated to the trivial Floquet exponent.
Coming back to the static bifurcations of autonomous systems, the Jacobian matrix $\mathbf{R}_\mathbf{X}$ appearing in extended systems Eqs. (2.38) and (2.39) can be replaced by:

$$\mathbf{R}_{\mathbf{X}s} = \mathbf{R}_\mathbf{X} - \frac{\bar{\mathbf{P}}\bar{\mathbf{P}}^T}{||\bar{\mathbf{P}}||^2} \tag{2.51}$$

whose spectrum is the same as that of the original Jacobian, with except that the trivial exponent has been shifted to -1. In this way, any null exponent found along the continuation procedure can be unambiguously identified as either a LP or a BP and then localized by using Newton-Raphson iterations on a slightly modified form of Eqs. (2.38,2.39):

$$\mathbf{Y}_{\mathrm{LPA}}(\mathbf{X},\phi,\omega,\alpha) = \begin{bmatrix} \mathbf{R} \\ g(\mathbf{X}) \\ \mathbf{R}_{\mathbf{X}s}\phi \\ \phi^T\phi - 1 \end{bmatrix} \tag{2.52}$$

$$\mathbf{Y}_{\mathrm{BPA}}(\mathbf{X},\phi,\omega,\alpha,\gamma) = \begin{bmatrix} \mathbf{R}+\gamma\phi \\ g(\mathbf{X}) \\ \mathbf{R}_{\mathbf{X}s}\phi \\ \phi^T\mathbf{R}_\omega \\ \phi^T\phi - 1 \end{bmatrix} \tag{2.53}$$

For the case of NS and PD bifurcations, no change to the corresponding extended systems is necessary. It should be noted, however, that stability evaluation itself requires the trivial eigenvalue to be shifted from the quadratic problem, Eq (2.36). This can be accomplished by using the technique proposed in [MEI 13], or by using a typical shift on the double-size, equivalent linear system:

$$\begin{bmatrix} \mathbf{0} & \mathbf{I}_L \\ -\mathbf{D}_2^{-1}\mathbf{R}\mathbf{x} & -\mathbf{D}_2^{-1}\mathbf{D}_1 \end{bmatrix} \begin{bmatrix} \bar{\mathbf{P}} \\ \lambda\bar{\mathbf{P}} \end{bmatrix} = \lambda \begin{bmatrix} \bar{\mathbf{P}} \\ \lambda\bar{\mathbf{P}} \end{bmatrix} \tag{2.54}$$

In the latter case, the eigenvector used to shift the trivial zero of the left-hand matrix is clearly equal to $\left[(\nabla \otimes \mathbf{I}_n)\mathbf{X}^T \;\; \mathbf{0}^T\right]^T$. Moreover, it shall be noted that these expressions imply the geometric and algebraic multiplicities of the zero exponent to be identically equal to two, in such a way that each zero is associated to a different eigenvector, thus enabling $\bar{\mathbf{P}}^T\phi = 0$. Shall this condition not be verified, as may be the case in practice, ϕ is sought as a generalized eigenvector by using the alternative systems presented in Appendix A.2.

2.2 Contributions to the numerical analysis of nonlinear vibration problems

2.2.1 Delayed systems

In this section, the following time-delayed term $\mathbf{f}_\mathrm{I}$ of Eq. 2.1 is considered:

$$\mathbf{f}_\mathrm{I} = \mathbf{A}\mathbf{x}(t-\tau) + \mathbf{B}\dot{\mathbf{x}}(t-\tau) + a\int_{-\infty}^{t} \mathbf{D}(\tau)\mathbf{x}(t-\tau)d\tau \tag{2.55}$$

where $a \in \mathbb{R}$, is considered. Each of the terms in the above expression is a linear function of lagged displacements/velocities, i.e. evaluated at a previous state characterized by the time lag $\tau \in \mathbb{R}^+$. Likewise, the nonlinear force vector is allowed to depend on the delayed variables: $\mathbf{f}_\mathrm{NL}(\mathbf{x},\dot{\mathbf{x}},\tau) \equiv \mathbf{f}_\mathrm{NL}(\mathbf{x}(t),\dot{\mathbf{x}}(t),\mathbf{x}(t-\tau),\dot{\tilde{\mathbf{x}}}(t-\tau))$. If $a = 0$ and $\mathbf{A}$,$\mathbf{B}$ are not both nil (*discrete delay*), the system's characteristic equation is transcendental rather than polynomial, and so Hill's method leads to a nonlinear eigenvalue problem for its Floquet exponents, which are infinite. The stability evaluation in such cases has been addressed by several authors (e.g. [WAN 19]) and is not considered within the scope of the present work. Nonetheless, the computation and continuation of periodic solutions through the HBM is straightforward, and so it is detailed next for completeness. On the other hand, if $a \neq 0$ and $\mathbf{A} = \mathbf{B} = \mathbf{0}$ (*distributed delay*), certain types of kernel functions allow for the integro-differential equations of motions to be recast into an equivalent, purely differential form to which a set of additional first-order equations has been appended. In the context of pseudo arc-length continuation, Floquet exponents are then obtainable through a particular variant of Hill's method which is introduced in this section.

2.2.1.1 Discrete delays

The delayed term is given by: $\mathbf{f}_{\mathrm{I}} = \mathbb{A}\mathbf{x}(t-\tau) + \mathbf{B}\dot{\mathbf{x}}(t-\tau)$. Let $\mathbf{X}_\tau$ represent the Fourier coefficients of a delayed periodic solution to Eq.(2.1), say $\mathbf{x}(t-\tau)$, with angular frequency ω. Relative to the coefficients of the current-time solution, $\mathbf{X}$, $\mathbf{X}_\tau$ is rotated in the frequency domain by an angle $-\omega\tau$ due to the time lag. Hence, using the rotation matrix of Eq. (2.44):

$$\begin{aligned} &\mathbf{X}_\tau = (\mathbf{G}(-\omega\tau)\otimes\mathbf{I}_n)\,\mathbf{X} \\ \Longrightarrow &\begin{cases} \mathbf{x}(t-\tau) = (\mathbb{F}_H(\omega t)\mathbf{G}(-\omega\tau)\otimes\mathbf{I}_n)\,\mathbf{X} \\ \dot{\mathbf{x}}(t-\tau) = \omega\,(\mathbb{F}_H(\omega t)\nabla\mathbf{G}(-\omega\tau)\otimes\mathbf{I}_n)\,\mathbf{X} \end{cases} \end{aligned} \tag{2.56}$$

The Fourier-Galerkin projection of the equations of motion yields a residual analogous to Eq. (2.10), where additional terms are included in the dynamic stiffness matrix:

$$\mathbf{Z}_\tau(\omega) = \omega^2\nabla^2\otimes\mathbf{M} + \omega\,(\nabla\otimes\mathbf{C} + \nabla\mathbf{G}(-\omega\tau)\otimes\mathbf{B}) + \mathbf{I}_L\otimes\mathbf{K} + \mathbf{G}(-\omega\tau)\otimes\mathbf{A} \tag{2.57}$$

A successful convergence of the Newton-Raphson algorithm towards a periodic solution must take into account the ω-dependence of matrix $\mathbf{G}(-\omega\tau)$. Moreover, the AFT-computation of derivatives also has to be adapted in the case of nonlinear functions of $\mathbf{x}(t-\tau)$ and $\dot{\mathbf{x}}(t-\tau)$. Denoting the sampled representation of these two vectors by, respectively, $\bar{\mathbf{x}}_\tau$ and $\bar{\mathbf{v}}_\tau$:

$$\begin{aligned} \frac{d\mathbf{F}_{\mathrm{NL}}}{d\mathbf{X}} = (\boldsymbol{\Gamma}_H^{-1}\otimes\mathbf{I}_n)\Bigg[&\frac{\partial\bar{\mathbf{f}}_{\mathrm{NL}}}{\partial\bar{\mathbf{x}}}(\boldsymbol{\Gamma}_H\otimes\mathbf{I}_n) + \frac{\partial\bar{\mathbf{f}}_{\mathrm{NL}}}{\partial\bar{\mathbf{x}}_\tau}((\boldsymbol{\Gamma}_H\mathbf{G}(-\omega\tau))\otimes\mathbf{I}_n) \\ &+\omega\frac{\partial\bar{\mathbf{f}}_{\mathrm{NL}}}{\partial\bar{\mathbf{v}}_\tau}((\boldsymbol{\Gamma}_H\nabla\mathbf{G}(-\omega\tau))\otimes\mathbf{I}_n)\Bigg] \end{aligned} \tag{2.58}$$

where, without loss of generality, it has been assumed that nonlinear forces dependent only on $\mathbf{x}(t), \mathbf{x}(t-\tau)$ and $\dot{\mathbf{x}}(t-\tau)$. It shall be noted that frequency dependence is also introduced here through the rotation matrix; this must be considered when computing the term $\mathbf{R}_\omega$.

Example: A self-excited Duffing oscillator with feedback control Consider the following SDOF system:

$$\ddot{x}(t) + 2\zeta\dot{x}(t) + x(t) + k_{\mathrm{NL}}x^3(t) - c_{\mathrm{NL}}\dot{x}^3(t) + ax(t-\tau) + b\dot{x}(t-\tau) = p\cos(\omega t) \tag{2.59}$$

with $(k_{\mathrm{NL}}, c_{\mathrm{NL}}, \tau, p) \geq (0,0,0,0)$ and $(a,b)\in\mathbb{R}$. Eq. (2.59) serves as a toy model to study the dynamics of a mechanical system undergoing large displacements and self-excited oscillations (due, in this case, to a cubic negative-damping term), as one could encounter when studying fluid-structure interaction problems. Control of the system's dynamics is

sought through delayed state feedback. With the values $\zeta = 0.05, p = 0.5, k_{\mathrm{NL}} = 0.05$ fixed, the frequency-response curve is computed with $H = 5, n_{FFT} = 2^9$ for varying time-lag τ in four different scenarios:

- Case 1: Displacement feedback, no nonlinear damping: $a = -0.1, b = 0, c_{\mathrm{NL}} = 0$
- Case 2: Displacement feedback, nonlinear damping: $a = -0.1, b = 0, c_{\mathrm{NL}} = 0.01$
- Case 3: Full state feedback, no nonlinear damping: $a = -0.1, b = -a, c_{\mathrm{NL}} = 0$
- Case 4: Full state feedback, nonlinear damping: $a = -0.1, b = -a, c_{\mathrm{NL}} = 0.01$

Results are summarized in Figs. 2.6 a) through d). Four values were chosen for τ: $\{0.000, 0.086, 0.286, 0.786\}$. Besides frequency responses, bifurcation tracking of LPs is shown as well. This can be achieved even in the absence of stability information, as this particular bifurcation is detected by monitoring the component of the tangent vector related to the continuation parameter, $\Delta\omega$ in this case. Furthermore, it can be shown (see Appendix A.2) that extended systems for the static bifurcations retain their forms when delays are considered, the only differences occurring during the computation of the extended Jacobian matrix. Once the LPs were localized, they were tracked with τ as continuation parameter, yielding the stability boundaries of Fig.2.7. For this simple example, it can be observed that an increased lag has a stabilizing effect in the absence of nonlinear damping, i.e. Cases 1 and 3, as seen on the overall decrease of peak amplitude whether a displacement-only or a full feedback are used. The latter is notoriously more effective, as these curves possess no LPs at all and the response is rendered almost linear. For the longest time lag, the curve in Case 1 also loses its bi-stability zone. This can be explained by bifurcation tracking, as the LP curves remarkably coalesce at a cusp point for $\tau = 0.7141$. Thus, choosing a delay superior to this value ensures the suppression of an unstable branch and the associated amplitude jumps. On the other hand, comparing these two cases further reveals that the feedback has a softening effect on the response curve of Case 1, while the opposite is true for Case 3.
With the addition of negative nonlinear damping, a displacement feedback alone (Case 2) can be thought to have the reverse effect, as Fig. 2.6 b) clearly shows an increase of peak amplitude with increasing τ. While this is true for the chosen values, the projection of stability boundaries on the $\omega - ||\mathbf{X}||$ plane are closed loops, so that amplitudes lower to those of the non-delayed case are reachable for larger values of τ. However, the two LP curves are disjoint and transcendental with respect to τ in this case, so a bi-stable region is unavoidable if the other parameters remain unchanged. A similar behaviour is observed when a full state feedback is used, Case 4.

An optimal tuning of the controller is possible by choosing (a, b, τ) such that features of the curve (e.g. maximum response amplitude, bi-stability region width, quasi-periodic responses) are either amplified or hindered, subjected to variation of the external parameters (c_{NL}, p). The generalized bifurcation analysis exposed in Sect. 2.2.3 is ideally suited

to tackle this interesting problem; nevertheless, as this requires stability computations - which have not been implemented here in the case of discrete delays-, this study is left for future work.

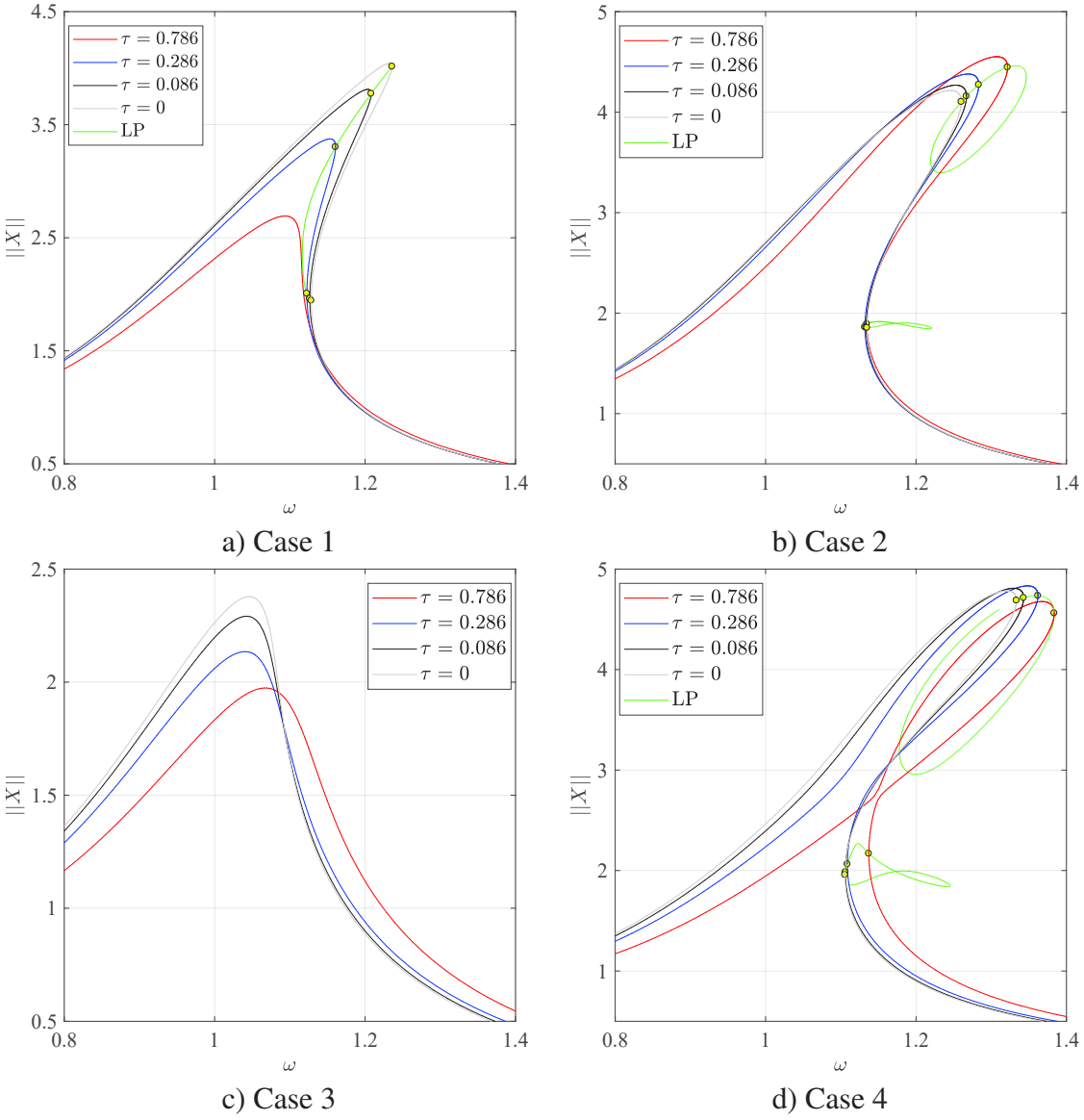

Figure 2.6: Time-lag effect on the FRC of a self-excited Duffing oscillator, Eq. (2.59).

2.2.1.2 Distributed delays

The term $\mathbf{f}_{\mathrm{I}} = \mathbf{y}_d(t)$ is given by a convolution between displacements[2] and a certain kernel function $\mathbb{D}(t)$, say:

[2]Convolutions involving velocities are treated in exactly the same way.

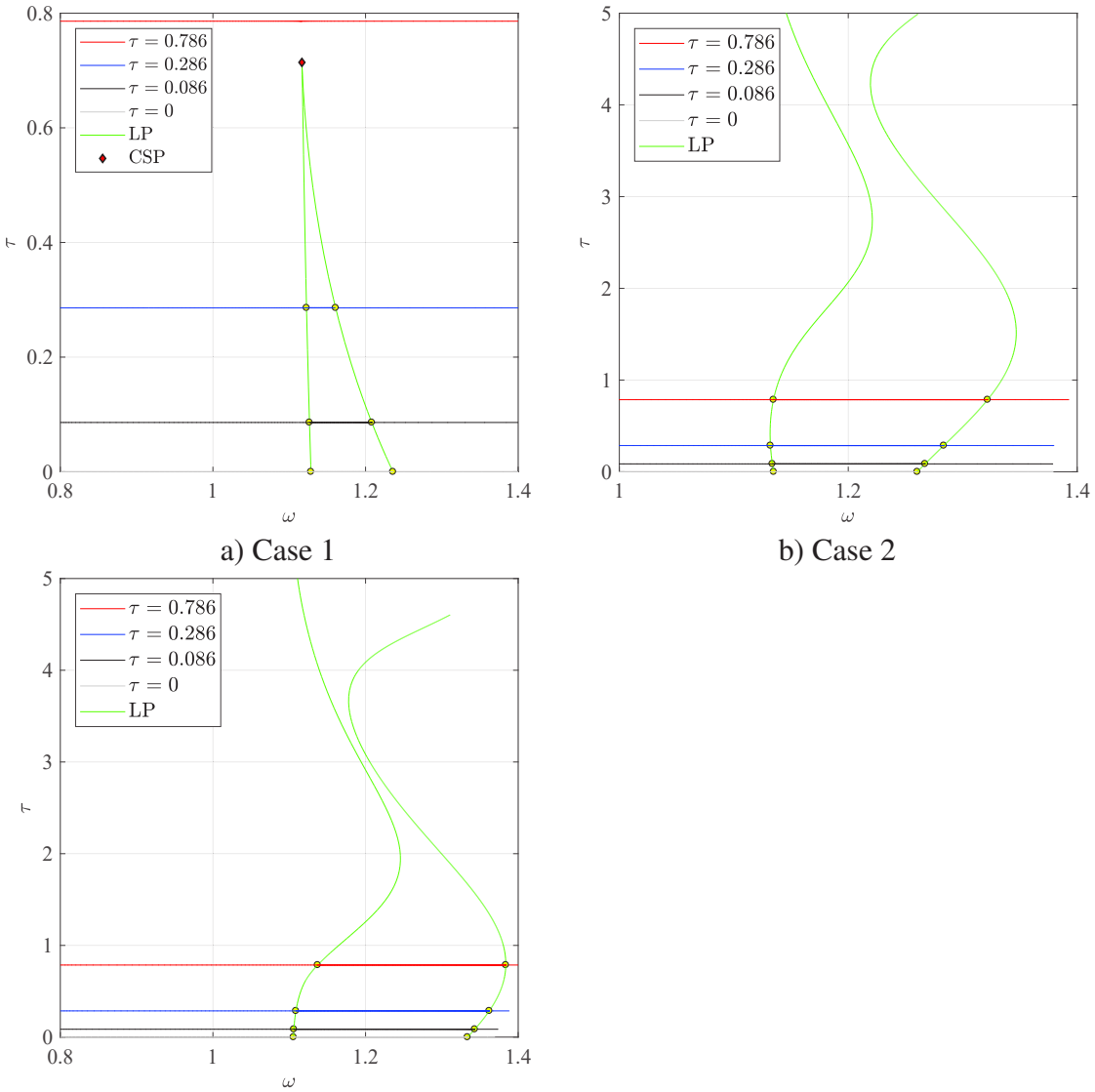

a) Case 1

b) Case 2

d) Case 4

Figure 2.7: LP bifurcation tracking.

$$\mathbf{y}_d(t) = \int_{-\infty}^{t} \mathbb{D}(\tau)\mathbf{x}(t-\tau)d\tau \tag{2.60}$$

We require the kernel function to be continuously differentiable on $]0, 2\pi/\omega]$ and to have a bounded delay, i.e. to respect causality: $\mathbb{D}(t) = 0, \forall t < 0$. While the mechanical systems under study consist of a finite number of modes, the introduction of convolutions with generic kernels leads to an infinite-dimensional system of equations, just as in the case of discrete delays. In particular, this means that the characteristic equations defining the Floquet exponents will be transcendental rather than polynomial. However, in the special case where the kernel is defined by a sum of *exponential* terms, the integro-

differential equations can be shown to be equivalent to a system of ODEs with dimension $N_a = n(1+n_e)$, where n_e is the number of exponentials in $\mathbb{D}(t)$. This fact stems from the particular behaviour of the exponential function under the derivative operator, as can be seen by replacing $\mathbb{D}(t) = \bar{H}(t)e^{-at}$ in Eq. (2.60) and taking its derivative with respect to t, with $\bar{H}(t)$ the Heaviside step function. The result, applying Leibniz's rule, is:

$$\dot{\mathbf{y}}_d(t) = \mathbf{x}(t) - a\mathbf{y}_d(t) \tag{2.61}$$

This is an inhomogeneous, first-order differential equation for $\mathbf{y}_d(t)$, which can be treated as an internal variable whose dynamics describe a memory effect. By noticing that Eq. (2.60) imposes $\mathbf{y}_d(0) = \mathbf{0}$, we conclude that the following two equations (and their corresponding initial value problems) are strictly equivalent:

$$\mathbf{M}\ddot{\mathbf{x}}(t) + \mathbf{C}\dot{\mathbf{x}}(t) + \mathbf{K}\mathbf{x}(t) + \sum_{i=1}^{n_e} \mathbf{L}_i \int_0^t e^{-a_i\tau}\mathbf{x}(t-\tau)d\tau + \mathbf{f}_{NL}(\mathbf{x}(t),\dot{\mathbf{x}}(t)) = \mathbf{f}(t) \tag{2.62}$$

$$\Longleftrightarrow \begin{cases} \mathbf{M}\ddot{\mathbf{x}}(t) + \mathbf{C}\dot{\mathbf{x}}(t) + \mathbf{K}\mathbf{x}(t) + \sum_{i=1}^{n_e} \mathbf{L}_i\mathbf{y}_{di}(t) + \mathbf{f}_{NL}(\mathbf{x}(t),\dot{\mathbf{x}}(t)) = \mathbf{f}(t) \\ \dot{\mathbf{y}}_{d1}(t) = \mathbf{x}(t) - a_1\mathbf{y}_{d1}(t) \\ \vdots \\ \dot{\mathbf{y}}_{dn_e}(t) = \mathbf{x}(t) - a_{n_e}\mathbf{y}_{dn_e}(t) \end{cases} \tag{2.63}$$

Other integral terms, e.g. the integrals of instantaneous (non-delayed) displacements involved in PID controllers, may be substituted using the same procedure. What follows can certainly be applied to such systems as well (with slight adjustments), although hereafter our attention will be centred around Eqs. (2.62) and (2.63). Indeed, these arise quite naturally in fluid-induced vibration problems, in the form of Wagner's function for unsteady aerodynamics [DIM 17] or the quasi-unsteady model of fluid-elastic instability of tube bundles in cross-flow [GRA 96], for instance, as a decreasing exponential has the meaningful physical interpretation of recent events having more impact on the present state than those far behind in the past. Let us remark that, by linearity, equations for the internal variables will be periodic -once a steady state is reached- if the vector function $\mathbf{x}(t)$ is periodic as well. Hence, this is assumed to be the case and the Fourier-Galerkin projection is applied on every line of Eq. (2.63), which gives:

$$\begin{cases} \mathbf{Z}(\omega)\mathbf{X} + \sum_{i=1}^{n_e} \mathbf{L}_i\mathbf{Y}_{di} + \mathbf{F}_{NL}(\mathbf{X}) - \mathbf{P} = \mathbf{0} \\ [a_1\mathbf{I}_L \ + \omega(\nabla\otimes\mathbf{I}_n)]\,\mathbf{Y}_{d1} \ = \mathbf{X} \\ \vdots \\ [a_{n_e}\mathbf{I}_L + \omega(\nabla\otimes\mathbf{I}_n)]\,\mathbf{Y}_{dn_e} = \mathbf{X} \end{cases} \tag{2.64}$$

Eq.(2.64) could be solved directly by Newton-Raphson iterations, treating the $\mathbf{Y}_{di}$ as additional unknowns. However, this is unnecessary, as the Fourier coefficients of the internal variables are proportional to $\mathbf{X}$ (this is evident from Eq.(2.64), as well as from the convolution theorem). For all $a_i \neq 0$, the matrices $[a_i\mathbf{I}_L + \omega(\nabla\otimes\mathbf{I}_n)]$ admit the inverses:

$$\mathbf{S}_i(\omega) = (\mathbf{B}_i(\omega)\otimes\mathbf{I}_n)\,[a_i\mathbf{I}_L - \omega\nabla\otimes\mathbf{I}_n] \tag{2.65}$$

where:

$$\mathbf{B}_i(\omega) = \text{diag}\left(1/a_i^2, \frac{1}{a_i^2+\omega^2}\begin{bmatrix}1 & 0\\ 0 & 1\end{bmatrix}, ..., \frac{1}{a_i^2+(H\omega)^2}\begin{bmatrix}1 & 0\\ 0 & 1\end{bmatrix}\right)$$

Eq. (2.65), actually, describes nothing more than the Laplace transform of a decaying exponential function evaluated at the discrete values $\{0, \omega, ..., H\omega\}$, with the real parts along the diagonal and the imaginary parts as the elements of a skew-symmetric matrix. Respectively, these contribute additional stiffness and (negative) damping terms to the equations of dynamical equilibrium, which read:

$$\mathbf{R}(\mathbf{X},\omega) = \left[\mathbf{Z}(\omega) + \sum_{i=1}^{n_e}\left(\mathbf{B}_i(\omega)\otimes\mathbf{L}_i\right)\left[a_i\mathbf{I}_L - \omega\nabla\otimes\mathbf{I}_n\right]\right]\mathbf{X} + \mathbf{F}_{NL}(\mathbf{X}) - \mathbf{P} = \mathbf{0} \quad (2.66)$$

2.2.1.3 Hill's method revisited

Our goal is to determine the local stability of a periodic solution $\mathbf{x}_0(t)$ to Eq.(2.66) by studying the evolution of a small applied perturbation $\boldsymbol{\eta}(t)$, i.e. by letting $\mathbf{x}(t) = \mathbf{x}_0(t) + \boldsymbol{\eta}(t)$ in the equations of motion. A linear system is thus obtained for the perturbation, whose asymptotic behaviour characterizes the attractive (stable) or repulsive (unstable) nature of the underlying cycle, $\mathbf{x}_0(t)$. Stability calculations for pseudo arc-length continuation algorithms in the frequency domain usually follow [GRO 01] and are based on the quadratic eigenvalue problem of Eq. (2.36). However, as shown next, this approach is not directly applicable to cases with integral terms, i.e. $\mathbf{f}_\text{I}(t) \neq \mathbf{0}$, or any other system in which some terms are described by additional differential equations. An alternative methodology is proposed hereafter which generalizes this version of Hill's method.

Memoryless vibrations: $\mathbf{f}_\text{I}(t) = \mathbf{0}$

Replacing the perturbed solution in Eq. (2.1) and keeping only the tangent (first-order) terms in the Taylor expansion of the nonlinear forces leads to:

$$\mathbf{M}\ddot{\boldsymbol{\eta}}(t) + \left[\mathbf{C} + \left(\frac{\partial \mathbf{f}_\text{NL}}{\partial \dot{\mathbf{x}}}\right)_{\dot{\mathbf{x}}_0(t)}\right]\dot{\boldsymbol{\eta}}(t) + \left[\mathbf{K} + \left(\frac{\partial \mathbf{f}_\text{NL}}{\partial \mathbf{x}}\right)_{\mathbf{x}_0(t)}\right]\boldsymbol{\eta}(t) = \mathbf{0} \quad (2.67)$$

As the tangent stiffness and damping matrices are evaluated at the converged cycle, they are periodic functions with frequency equal to ω. Eq.(2.67) is then a linear, autonomous system of equations with periodic coefficients, whose study can be performed through Floquet theory. As a preliminary step, however, we will recast it into an equivalent first-order form of double size by introducing the state vector $\mathbf{z}(t) = [\boldsymbol{\eta}^T(t), \dot{\boldsymbol{\eta}}^T(t)]^T$. Hence:

$$\dot{\mathbf{z}}(t) = \mathbf{A}(t)\mathbf{z}(t) \quad (2.68)$$

with the coefficient matrix given by:

$$\mathbf{A}(t) = \begin{bmatrix} \mathbf{0}_n & \mathbf{I}_n \\ -\mathbf{M}^{-1}\left[\mathbf{K} + \left(\frac{\partial \mathbf{f}_{\mathrm{NL}}}{\partial \mathbf{x}}\right)_{\mathbf{x}_0(t)}\right] & -\mathbf{M}^{-1}\left[\mathbf{C} + \left(\frac{\partial \mathbf{f}_{\mathrm{NL}}}{\partial \dot{\mathbf{x}}}\right)_{\dot{\mathbf{x}}_0(t)}\right] \end{bmatrix} \tag{2.69}$$

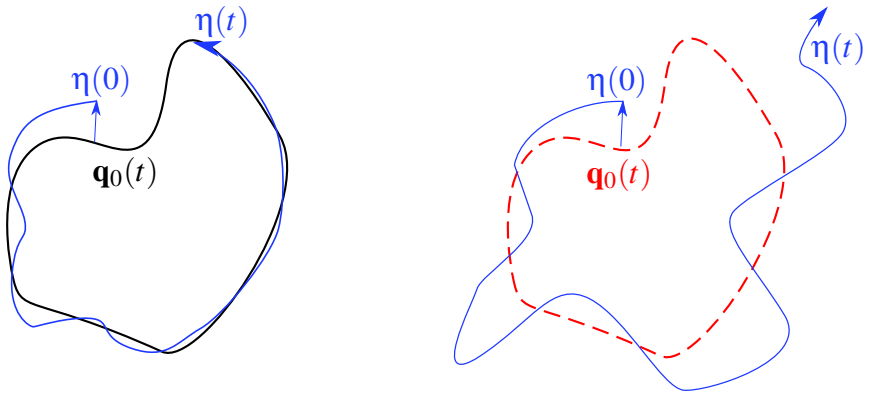

Figure 2.8: Notion of local (asymptotic) stability for a cycle $\mathbf{q}_0(t)$. Left: stable cycle, right: unstable cycle.

The $2n$ solutions of Eq.(2.68) are known as the *Floquet forms*, which play a role analogous to normal modes for systems with periodic coefficients and are expressed in the general form $\mathbf{z}_j(t) = e^{\lambda_j t}\mathbf{p}_j(t)$, with $\mathbf{p}_j(t+2\pi/\omega) = \mathbf{p}_j(t)$. Clearly, the time evolution of the perturbation is determined by the real part of the exponents λ_j: if there exists at least one j such that $\Re\{\lambda_j\} > 0$, the associated mode's amplitude grows exponentially and the underlying cycle is thus unstable, as depicted in Fig. 2.8. Furthermore, in the case of unforced systems, there exists at least one trivial exponent equal to zero. This is due to the invariance of periodic solutions with respect to time translations, which equates to the existence of a direction in phase space along which perturbations have no effect. This particular direction is given by $\dot{\mathbf{v}}(t) = [\dot{\mathbf{x}}_0^T(t), \ddot{\mathbf{x}}_0^T(t)]^T$, and the demonstration of this fact is a classical result shown in numerous textbooks, see e.g. [SEY 10]. Substituting the Floquet form ansatz in Eq. (2.68) and factoring out the exponentials from both sides yields an equation for the λ_j purely in terms of periodic functions:

$$\dot{\mathbf{p}}_j(t) + \lambda_j \mathbf{p}_j(t) = \mathbf{A}(t)\mathbf{p}_j(t) \tag{2.70}$$

Eq. (2.70) has been used in [LAZ 10, BEN 17], where a Fourier expansion of the coefficient matrix and of vector $\mathbf{p}_j(t)$ was introduced. Then, using harmonic balance, a linear eigenvalue problem is obtained from which the characteristic (Floquet) exponents are found as the eigenvalues of a truncated *Hill's matrix*. The right-hand side, being a product of two time series, leads to a convolution in the frequency domain which is represented by a Toeplitz matrix if a complex formulation of harmonic balance is employed (and a more complicated matrix otherwise). Hereafter we adopt a different approach, which has the advantage of exploiting information already available from the AFT-HBM

solution of the equations of motion to efficiently construct a real Hill's matrix. Conceptually, vectors $\mathbf{p}_j(t)$ consist of the state representation of some periodic solution, i.e. the vertical concatenation of, say, a "displacement part" and a "velocity part". Thus, each half can be expressed as a separate Fourier series, here denoted with the previously-introduced DFT operators:

$$\mathbf{p}_j(t) = \begin{bmatrix} (\boldsymbol{\Gamma}_H \otimes \mathbf{I}_n)\mathbf{P} \\ (\boldsymbol{\Gamma}_H \otimes \mathbf{I}_n)\mathbf{P}' \end{bmatrix} = \begin{bmatrix} (\boldsymbol{\Gamma}_H \otimes \mathbf{I}_n) & \mathbf{0}_{nL} \\ \mathbf{0}_{nL} & (\boldsymbol{\Gamma}_H \otimes \mathbf{I}_n) \end{bmatrix} \boldsymbol{\phi} \tag{2.71}$$

Eq. (2.70) is then projected row-wise onto the frequency domain through left-multiplication by the inverse transformation matrix $\mathbf{I}_2 \otimes \left(\boldsymbol{\Gamma}_H^{-1} \otimes \mathbf{I}_n\right)$, which yields the eigenvalue problem:

$$\mathbb{H}\boldsymbol{\phi} = \lambda\boldsymbol{\phi} \tag{2.72}$$

where Hill's matrix is explicitly given by:

$$\mathbb{H} = \begin{bmatrix} -\omega\nabla \otimes \mathbf{I}_n & \mathbf{I}_{nL} \\ \mathbf{H}_K & \mathbf{H}_C \end{bmatrix} \tag{2.73}$$

$$\mathbf{H}_{\mathrm{K}} = -(\mathbf{I}_L \otimes \mathbf{M}^{-1})\left[\mathbf{I}_L \otimes \mathbf{K} + \frac{\partial \mathbf{F}_{\mathrm{NL}}}{\partial \mathbf{X}}\right]$$
$$\mathbf{H}_{\mathrm{C}} = -\omega\nabla \otimes \mathbf{I}_n - (\mathbf{I}_L \otimes \mathbf{M}^{-1})\left[\mathbf{I}_L \otimes \mathbf{C} + \frac{\partial \mathbf{F}_{\mathrm{NL}}}{\partial \mathbf{X}'}\right]$$

It should be noted that the derivatives appearing in Eq. (2.73) have already been computed during the iteration process for the converged cycle, so that no further computations are necessary to assemble this matrix for sufficiently compliant systems[3]. While this formulation of the Hill matrix is a novelty, it is straightforward to demonstrate its equivalence with the well-known quadratic eigenvalue problem introduced by Von Groll and Ewins. Indeed, the first line of Eq. (2.72) states: $\bar{\mathbf{P}}' = (\lambda\mathbf{I}_{nL} + \omega\nabla \otimes \mathbf{I}_n)\bar{\mathbf{P}}$. Introducing this expression in the second line leads exactly to Eq. (2.36).

Moreover, and most importantly, this approach is readily generalisable to the case of systems with memory, which is not an obvious task if the traditional QEP, Eq. (2.36), is taken as a starting point.

In the same way as before, an evaluation of local stability around a cycle $\mathbf{q}_0(t)$ is sought by applying a perturbation $\boldsymbol{\eta}(t)$ to Eq. (2.62). The resulting equation for the perturbation is similar to Eq. (2.67):

[3]While an accurate computation of the Fourier coefficients of cycles can be achieved through AFT with moderate sampling, highly stiff systems may require a re-evaluation of these terms with a higher sampling rate in order to ensure convergence of the Floquet exponents; this aspect is discussed more in detail in Chapter 3.

$$\mathbf{M}\ddot{\boldsymbol{\eta}}(t)+\left[\mathbf{C}+\left(\frac{\partial \mathbf{f}_{\mathrm{NL}}}{\partial \dot{\mathbf{x}}}\right)_{\dot{\mathbf{x}}_0(t)}\right]\dot{\boldsymbol{\eta}}(t)+\left[\mathbf{K}+\left(\frac{\partial \mathbf{f}_{\mathrm{NL}}}{\partial \mathbf{x}}\right)_{\mathbf{x}_0(t)}\right]\boldsymbol{\eta}(t)+\sum_{i=1}^{n_e}\mathbf{L}_i\int_0^t e^{-a_i\tau}\boldsymbol{\eta}(t-\tau)d\tau=\mathbf{0} \tag{2.74}$$

Let us define the state vector $\mathbf{z}(t)=[\boldsymbol{\eta}^T(t),\dot{\boldsymbol{\eta}}^T(t),\boldsymbol{\zeta}_1^T(t),...,\boldsymbol{\zeta}_{n_e}^T(t)]^T$, where each of the $\boldsymbol{\zeta}_j^T(t)$ vectors $(j=1,...,n_e)$ stands for the j-th convolution term for the perturbation. The state representation of the above equation is then, after recast in extended-ODE system form, exactly the same as Eq. (2.68), with the periodic coefficient matrix:

$$\mathbf{A}(t)=\begin{bmatrix} \mathbf{0}_n & \mathbf{I}_n & \mathbf{0}_n & \cdots & \mathbf{0}_n \\ -\mathbf{M}^{-1}\left[\mathbf{K}+\left(\frac{\partial \mathbf{f}_{\mathrm{NL}}}{\partial \mathbf{x}}\right)_{\mathbf{x}_0(t)}\right] & -\mathbf{M}^{-1}\left[\mathbf{C}+\left(\frac{\partial \mathbf{f}_{\mathrm{NL}}}{\partial \dot{\mathbf{x}}}\right)_{\dot{\mathbf{x}}_0(t)}\right] & -\mathbf{M}^{-1}\mathbf{L}_1 & \cdots & -\mathbf{M}^{-1}\mathbf{L}_{n_e} \\ \mathbf{I}_n & \mathbf{0}_n & -a_1\mathbf{I}_n & \cdots & \mathbf{0}_n \\ \vdots & \vdots & \vdots & \ddots & \vdots \\ \mathbf{I}_n & \mathbf{0}_n & \mathbf{0}_n & \cdots & -a_{n_e}\mathbf{I}_n \end{bmatrix} \tag{2.75}$$

The application of Floquet theory, followed by harmonic balance, leads once again to the linear eigenvalue problem of Eq. (2.72), where Hill's matrix is now given by:

$$\mathbb{H} \quad = \quad \begin{bmatrix} -\omega\nabla\otimes\mathbf{I}_n & \mathbf{I}_{nL} & \mathbf{0}_{nL} & \cdots & \mathbf{0}_{nL} \\ \mathbf{H}_{\mathrm{K}} & \mathbf{H}_{\mathrm{C}} & -\mathbf{I}_L\otimes(\mathbf{M}^{-1}\mathbf{L}_1) & \cdots & -\mathbf{I}_L\otimes(\mathbf{M}^{-1}\mathbf{L}_{n_e}) \\ \mathbf{I}_{nL} & \mathbf{0}_{nL} & -\omega\nabla\otimes\mathbf{I}_n-a_1\mathbf{I}_{nL} & \cdots & \mathbf{0}_{nL} \\ \vdots & \vdots & \vdots & \ddots & \vdots \\ \mathbf{I}_{nL} & \mathbf{0}_{nL} & \mathbf{0}_{nL} & \cdots & -\omega\nabla\otimes\mathbf{I}_n-a_{n_e}\mathbf{I}_{nL} \end{bmatrix} \tag{2.76}$$

The advantages of using the formulation described above are evident when one attempts to apply the Floquet-Fourier approach on the second-order Eq. (2.74), which leads to the system:

$$\mathbf{M}\left(\ddot{\mathbf{p}}+2\lambda\dot{\mathbf{p}}+\lambda^2\mathbf{p}\right)+\mathbf{C}(t)\left(\dot{\mathbf{p}}+\lambda\mathbf{p}\right)+\mathbf{K}(t)\mathbf{p}+\sum_{i=1}^{n_e}\mathbf{L}_i\int_0^t e^{-(a_i+\lambda)\tau}\mathbf{p}(t-\tau)d\tau=\mathbf{0} \tag{2.77}$$

Here, the total stiffness and damping matrices have been replaced by the symbols $\mathbf{K}(t)$ and $\mathbf{C}(t)$, respectively, to denote their time-dependence. The extended differential system is obtained afterwards by defining the internal variables:

$$\mathbf{s}_i(t)=\int_0^t e^{-(a_i+\lambda)\tau}\mathbf{p}(t-\tau)d\tau \;\;,\;\; \forall i=1,...,n_e$$

$$\Longrightarrow \begin{cases} \mathbf{M}\left(\ddot{\mathbf{p}}+2\lambda\dot{\mathbf{p}}+\lambda^2\mathbf{p}\right)+\mathbf{C}(t)\left(\dot{\mathbf{p}}+\lambda\mathbf{p}\right)+\mathbf{K}(t)\mathbf{p}+\sum_{i=1}^{n_e}\mathbf{L}_i\mathbf{s}_i(t)=\mathbf{0} \\ \dot{\mathbf{s}}_i(t)+(\lambda+a_i)\mathbf{s}_i(t)=\mathbf{p}(t) \;\;,\;\; \forall i=1,...,n_e \end{cases} \tag{2.78}$$

The following quadratic problem is obtained for the eigenvalues λ and their associated eigenvectors $\psi = \left[\mathbf{P}^T, \mathbf{S}_1^T, ..., \mathbf{S}_{n_e}^T\right]^T$:

$$\left[\bar{\mathbf{D}}_0 + \lambda\bar{\mathbf{D}}_1 + \lambda^2\bar{\mathbf{D}}_2\right]\psi = \mathbf{0} \tag{2.79}$$

with the coefficient matrices given by:

$$\bar{\mathbf{D}}_2 = \begin{bmatrix} \mathbf{D}_2 & \mathbf{0}_{nL} & \cdots & \mathbf{0}_{nL} \\ \mathbf{0}_{nL} & \mathbf{0}_{nL} & \cdots & \mathbf{0}_{nL} \\ \vdots & \vdots & \ddots & \vdots \\ \mathbf{0}_{nL} & \mathbf{0}_{nL} & \cdots & \mathbf{0}_{nL} \end{bmatrix} \quad , \quad \bar{\mathbf{D}}_1 = \begin{bmatrix} \mathbf{D}_1 & \mathbf{0}_{nL} & \cdots & \mathbf{0}_{nL} \\ \mathbf{0}_{nL} & \mathbf{I}_{nL} & \cdots & \mathbf{0}_{nL} \\ \vdots & \vdots & \ddots & \vdots \\ \mathbf{0}_{nL} & \mathbf{0}_{nL} & \cdots & \mathbf{I}_{nL} \end{bmatrix}$$

$$\bar{\mathbf{D}}_0 = \begin{bmatrix} \mathbf{R}_{\mathbf{X}} & \mathbf{I}_L \otimes \mathbf{L}_1 & \cdots & \mathbf{I}_L \otimes \mathbf{L}_{n_e} \\ -\mathbf{I}_{nL} & \omega\nabla \otimes \mathbf{I}_n + a_1\mathbf{I}_{nL} & \cdots & \mathbf{0}_{nL} \\ \vdots & \vdots & \ddots & \vdots \\ -\mathbf{I}_{nL} & \mathbf{0}_{nL} & \cdots & \omega\nabla \otimes \mathbf{I}_n + a_{n_e}\mathbf{I}_{nL} \end{bmatrix}$$

A problem immediately appears, as $\bar{\mathbf{D}}_2$ is singular and the same is true for its double-size first-order form. This does not immediately imply that Eq. (2.79) is not solvable, but infinite roots will appear amongst its solutions, which is not the case for the well-posed matrix $\mathbb{H}$ from Eq. (2.76). Furthermore, the accuracy of eigenvalue solvers is compromised when dealing with such singular, leading to erroneous results (especially when the systems at hand are stiff). An alternative approach is to directly express the Fourier coefficients of the internal variables as a function of $\mathbf{P}$ by using the second line of Eq. (2.78), which leads to a regular system. However, this involves matrices similar to Eq. (2.65) but which include rational functions of λ, and thus defines a nonlinear eigenvalue problem. The difficulty is then much higher when compared to Eq. (2.72), which is linear and stands out as the most convenient formulation within the present framework of the HBM.

The eigenvalues of matrix $\mathbb{H}$, which are in the number of $(2+n_e)nL$, contain the $(2+n_e)n$ Floquet exponents of the system. These are identified by selecting, amongst all solutions, those whose imaginary parts lie within the elementary cell $[-\frac{\omega}{2}, \frac{\omega}{2}]$, i.e. those with the smallest imaginary parts in magnitude, as first suggested in [MOO 05]. Stability assessments are then possible by inspection of the real parts. This is true regardless of whether the original system is forced or autonomous, the only difference being that a trivial zero eigenvalue is present in the latter case. Regarding bifurcations, the usual extended systems for LPs and BPs remain unchanged; furthermore, those for the PD and NS bifurcations have exactly the same form, upon addition of corrective terms to the usual matrices $\mathbf{D}_1$ and $\mathbf{D}_2$. Details and the proof of this claim are presented in Appendix A.3.

2.2.2 Quasi-periodic analysis

The HBM can be readily extended to compute quasi-periodic solutions of Eq. (2.1), by assuming $\mathbf{q}(t)$ to be a M-periodic function, i.e. one which is periodic with respect to each of its M arguments independently. As such, it may be expressed as an M-dimensional Fourier series, which we write compactly as:

$$\mathbf{x}(t) = (\mathbb{F}_H(\boldsymbol{\theta}) \otimes \mathbf{I}_n)\mathbf{X} \tag{2.80}$$

where hyper-time vector $\boldsymbol{\theta} = [\omega_1 t, ..., \omega_M t] = [\theta_1, ..., \theta_M]$ groups the independent time scales associated with each basic frequency. The requisite imposed on the frequencies is that they are incommensurable; in other words:

$$\forall (i,j) \in \{1, ..., M\}, i \neq j \implies \frac{\omega_i}{\omega_j} \notin \mathbb{Q} \tag{2.81}$$

since otherwise the elements of $\boldsymbol{\theta}$ are linearly dependant and the formulation reduces to a lower-dimensional Fourier series. The vector $\mathbb{F}^H(\boldsymbol{\theta})$ contains the harmonic functions forming an orthonormal basis for the sought solutions, which are approximated up to the H-th harmonic, while the associated Fourier coefficients make up the vector $\mathbf{X}$.
Orthogonality is defined through the following inner product on continuous, M-periodic functions:

$$\langle f(t), g(t) \rangle = \left(\prod_{i=1}^{M} \frac{\omega_i}{2\pi} \right) \int_0^{\frac{2\pi}{\omega_M}} ... \int_0^{\frac{2\pi}{\omega_1}} f(\boldsymbol{\theta}) g(\boldsymbol{\theta}) d\theta_1 ... d\theta_M \tag{2.82}$$

As an immediate consequence of this definition:

$$\langle \mathbb{F}_H(\boldsymbol{\theta}), \mathbb{F}_H(\boldsymbol{\theta}) \rangle = \mathbf{I}_L \tag{2.83}$$

where $L = (2H+1)^M$ is the size of the system for each DOF. As time only appears in the elements of $\boldsymbol{\theta}$, velocity and acceleration terms are also proportional to $\mathbf{X}$ in the frequency domain. Hence:

$$\dot{\mathbf{x}}(t) = \left(\frac{d}{dt} \mathbb{F}_H(\boldsymbol{\theta}) \otimes \mathbf{I}_n \right) \mathbf{X} = \left[\left(\sum_{i=1}^{M} \omega_i \frac{\partial \mathbb{F}_H(\boldsymbol{\theta})}{\partial \theta_i} \right) \otimes \mathbf{I}_n \right] \mathbf{X} \tag{2.84}$$

$$\ddot{\mathbf{x}}(t) = \left(\frac{d^2}{dt^2} \mathbb{F}_H(\boldsymbol{\theta}) \otimes \mathbf{I}_n \right) \mathbf{X} = \left[\left(\sum_{j=1}^{M} \sum_{i=1}^{M} \omega_j \omega_i \frac{\partial^2 \mathbb{F}_H(\boldsymbol{\theta})}{\partial \theta_j \partial \theta_i} \right) \otimes \mathbf{I}_n \right] \mathbf{X} \tag{2.85}$$

Replacing all variables in Eq. (2.1) by their frequency-domain expressions and taking the product of the resulting equations with the basis functions $\mathbb{F}_H(\boldsymbol{\theta})$ yields the general form of the algebraic problem to be solved for the Fourier coefficients of the solution and the basic frequencies:

$$\mathbf{R}(\mathbf{X}, \boldsymbol{\omega}) = \mathbf{Z}(\boldsymbol{\omega})\mathbf{X} + \mathbf{F}_{\mathrm{NL}}(\mathbf{X}) - \mathbf{F}(\boldsymbol{\omega}) = \mathbf{0} \tag{2.86}$$

Through the forcing term $\mathbf{f}(t)$, some or all of the basic frequencies may be imposed. Let $m \leq M$ be the number of 'free' frequencies of the problem. The total number of unknowns is thus $nL+m$, whereas the system given in (2.86) consists of merely nL equations. Closure is achieved by appending m additional phase conditions to the system. A robust way of doing this is by exploiting the invariance with respect to translation along certain directions in hyper-time, which correspond to the velocity vectors associated to each 'free' time scale. Thus, assigning a value to any component of each of these vectors uniquely fixes a phase for the solution and effectively closes the system of equations; letting $\mathbf{e}_k$ denote the unit vector for the k-th coefficient, we may write:

$$\begin{aligned} &\forall i = 1,...,m \;\; \mathbf{e}_k^* \cdot ((\nabla_i \otimes \mathbf{I}_n)\mathbf{X}) = 0 \\ &\nabla_i = \left\langle \mathbb{F}_H(\boldsymbol{\theta}), \frac{\partial \mathbb{F}_H(\boldsymbol{\theta})}{\partial \theta_i} \right\rangle \end{aligned} \tag{2.87}$$

As will be shown later on, the vectors in parentheses are actually eigenvectors of the system's Jacobian associated with zero eigenvalues. Invariance along these particular directions comes from the fact that they span the null-space: perturbations along any of them has no effect on the solution other than shifting its phase.
The dynamic stiffness matrix in Eq. (2.86) can be explicitly written as:

$$\mathbf{Z}(\boldsymbol{\omega}) = \nabla^2 \otimes \mathbf{M} + \nabla \otimes \mathbf{C} + \mathbf{I}_L \otimes \mathbf{K} \tag{2.88}$$

where a total derivative has been introduced:

$$\nabla = \sum_{i=1}^{M} \omega_i \nabla_i \tag{2.89}$$

Bi-dimensional time case
The implementation details will now be discussed by considering the particular case where $M = 2$.
Let the vectors $\mathbf{X}_{\mathrm{x}(i,j)}$ group the n Fourier coefficients for a given combination $i\omega_1 + j\omega_2$ of the basic frequencies, where the subindex x identifies the cosine (real) part ($x = c$) or the sine (imaginary) part ($x = s$). Thus, for a H-harmonic approximation:

$$\mathbf{X} = \begin{bmatrix} & & \mathbf{X}^T_{(0,0)} & & \cdots & \mathbf{X}^T_{\mathrm{c}(H,0)} & \mathbf{X}^T_{\mathrm{s}(H,0)} \\ \mathbf{X}^T_{\mathrm{c}(-H,1)} & \mathbf{X}^T_{\mathrm{s}(-H,1)} & \cdots & \mathbf{X}^T_{\mathrm{c}(0,1)} & \mathbf{X}^T_{\mathrm{s}(0,1)} & \cdots \mathbf{X}^T_{\mathrm{c}(H,1)} & \mathbf{X}^T_{\mathrm{s}(H,1)} \\ & & \cdots & & & & \\ \mathbf{X}^T_{\mathrm{c}(-H,H)} & \mathbf{X}^T_{\mathrm{s}(-H,H)} & \cdots & \mathbf{X}^T_{\mathrm{c}(0,H)} & \mathbf{X}^T_{\mathrm{s}(0,H)} & \cdots \mathbf{X}^T_{\mathrm{c}(H,H)} & \mathbf{X}^T_{\mathrm{s}(H,H)} \end{bmatrix}^T \tag{2.90}$$

It should be noted that, because of the symmetry properties of the Fourier transform, it is sufficient to consider only positive values of the second subindex. This is illustrated in Fig. 2.9, which shows the distribution of Fourier coefficients for a quasi-periodically forced Duffing oscillator.

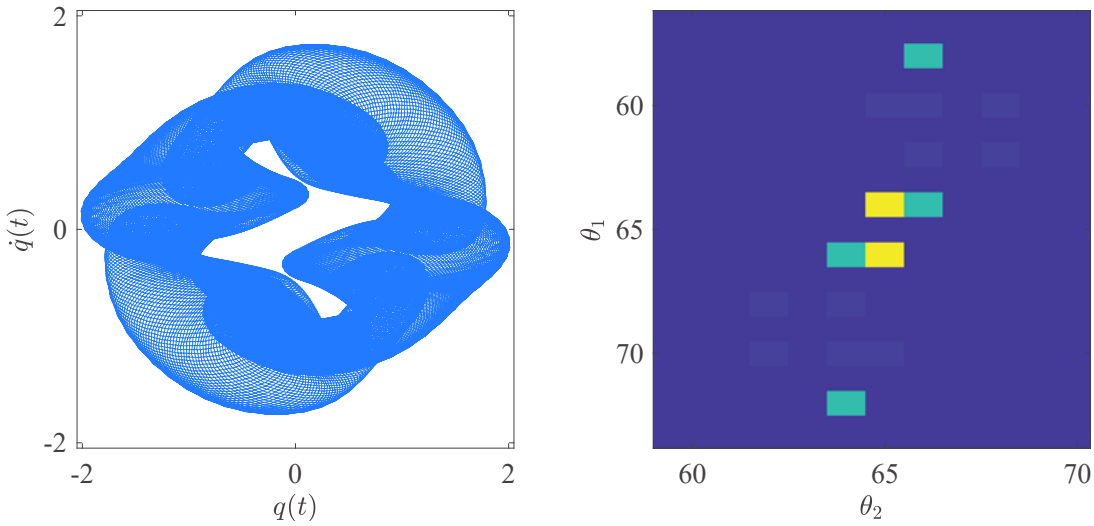

Figure 2.9: Response of a Duffing oscillator to two-frequency QP forcing, with 64^2 sampling points for the FFT2 algorithm. Left: phase space plot, right: frequency content (centered DFT2). Harmonics (1,0), (1,1) and (1,7) are dominant.

Furthermore, by inspecting the terms of this depiction, it is clear that the basis $\mathbb{F}_2^H(\boldsymbol{\theta})$ is nothing more than the frequency-domain convolution corresponding to the product of bases $\mathbb{F}_1^H(\omega_1 t)$ and $\mathbb{F}_1^H(\omega_2 t)$ (which can be observed in the first "row" and the centre "column", respectively). Thus, both of these can be viewed as sub-spaces of the full toroidal space, a fact that proves to be useful for branch switching.
The total derivative is given by:

$$\nabla = \omega_1 \nabla_1 + \omega_2 \nabla_2 \tag{2.91}$$

with the partial derivatives being block-diagonal matrices.
The two-dimensional direct and inverse Fourier transforms are used to go back and forth between time and frequency domains for the practical computation of the nonlinear terms $\mathbf{F}_{\mathrm{NL}}(\mathbf{X})$. More specifically, the direct and inverse Discrete Fourier Transform algorithms (DFT2 and IDFT2, respectively) are implemented. To this end, the real Fourier coefficients (2.90) are expressed in complex form through the formula:

$$\widehat{\mathbf{X}}_{(0,0)} = \frac{1}{2}\mathbf{X}_{(0,0)} \; ; \; \widehat{\mathbf{X}}_{(\pm a,b)} = \frac{1}{2}\left[\mathbf{X}_{\mathrm{c}(\pm a,b)} \mp i\mathbf{X}_{\mathrm{s}(\pm a,b)}\right] \text{ for } a,b = 1,\ldots,H \tag{2.92}$$

Next, the complex coefficients are re-arranged in matrix form. This includes a zero-padding operation in order to have an adequate number of sampling points n_f for the time-domain signal. The transformation mapping the real Fourier coefficient vector to the complex coefficient matrix $\mathbf{Mat}\widehat{\mathbf{X}} \in \mathbb{R}^{n_f \times n_f \times n}$ is thus simply expressed by introducing the operator $\mathbf{T}_{\mathbb{C}}$:

$$\mathbf{Mat}\widehat{\mathbf{X}} = \mathbf{T}_{\mathbb{C}}\mathbf{X} \tag{2.93}$$

For practical purposes, the matrix $\mathbf{Mat}\widehat{\mathbf{X}}$ is a three-dimensional array, with one two-dimensional "layer" attributed to each DOF. Thus, the following operations are performed independently on each of these and may be parallelized to enhance computational efficiency.
Let $\mathbf{D}_{n_f}^n$ denote the n-dimensional transition tensor composed of n instances of the n_f-point DFT matrix. The two-dimensional Fourier transform is carried out by inverse Fourier-transforming each row of $\mathbf{Mat}\widehat{\mathbf{X}}$ and subsequently applying this same operation to each column of the obtained tensor:

$$\widehat{\mathbf{x}}(\theta_1,\theta_2) = \mathbf{D}_{n_f}^n \left[\mathbf{D}_{n_f}^n \mathbf{Mat}\widehat{\mathbf{X}}^T\right]^T = \left[\mathbf{D}_{n_f}^n \mathbf{T}_{\mathbb{C}}\mathbf{X}\right]\mathbf{D}_{n_f}^{nT} \tag{2.94}$$

If the time-domain velocities and/or accelerations are involved in the nonlinear forces, they can be obtained in exactly the same fashion by using the corresponding formulas. Afterwards, the time-domain expressions for these forces are evaluated and the associated Fourier coefficients are found by applying the inverse operations to those described above:

$$\mathbf{F}_{\mathrm{NL}}(\mathbf{X}) = \mathbf{T}_{\mathbb{C}}^{-1}\left(\mathbf{D}_{n_f}^{n*}\left[\mathbf{D}_{n_f}^{n*}\widehat{\mathbf{f}}_{\mathrm{NL}}^T(\widehat{\mathbf{x}},\widehat{\dot{\mathbf{x}}})\right]^T\right) = \mathbf{T}_{\mathbb{C}}^{-1}\left(\mathbf{D}_{n_f}^{n*}\left[\widehat{\mathbf{f}}_{\mathrm{NL}}(\widehat{\mathbf{x}},\widehat{\dot{\mathbf{x}}})\mathbf{D}_{n_f}^{nT*}\right]\right) \tag{2.95}$$

From this expression, the frequency-domain derivatives[4] can also be expressed as a function of their time-domain counterparts:

$$\frac{\partial \mathbf{F}_{\mathrm{NL}}}{\partial \mathbf{X}} = \frac{\partial \mathbf{F}_{\mathrm{NL}}}{\partial \widehat{\mathbf{f}}_{\mathrm{NL}}}\frac{\partial \widehat{\mathbf{f}}_{\mathrm{NL}}}{\partial \widehat{\mathbf{x}}}\frac{\partial \widehat{\mathbf{x}}}{\partial \mathbf{X}} + \frac{\partial \mathbf{F}_{\mathrm{NL}}}{\partial \widehat{\mathbf{f}}_{\mathrm{NL}}}\frac{\partial \widehat{\mathbf{f}}_{\mathrm{NL}}}{\partial \widehat{\dot{\mathbf{x}}}}\frac{\partial \widehat{\dot{\mathbf{x}}}}{\partial \mathbf{X}}$$

$$\frac{\partial \mathbf{F}_{\mathrm{NL}}}{\partial \mathbf{X}} = \mathbf{T}_{\mathbb{C}}^{-1}\left(\mathbf{D}_{n_f}^{n*}\mathbf{D}_{n_f}^{nT*}\right)\left\{\frac{\partial \widehat{\mathbf{f}}_{\mathrm{NL}}}{\partial \widehat{\mathbf{x}}}\left[\mathbf{D}_{n_f}^n \mathbf{T}_{\mathbb{C}}\mathbf{D}_{n_f}^{nT}\right] + \frac{\partial \widehat{\mathbf{f}}_{\mathrm{NL}}}{\partial \widehat{\dot{\mathbf{x}}}}\left[\mathbf{D}_{n_f}^n \mathbf{T}_{\mathbb{C}}(\nabla \otimes \mathbf{I}_n)\mathbf{D}_{n_f}^{nT}\right]\right\} \tag{2.96}$$

Stability

The definition of asymptotic stability remains unchanged for quasi-periodic solutions to Eq. (2.67). Thus, application of a perturbation η leads once again to the autonomous Eq. (2.67), with the difference that the damping and stiffness matrices are now quasi-periodic functions. For an M-dimensional hyper-time, one may thus consider a solution to be of the general form:

$$\boldsymbol{\eta}(t) = \boldsymbol{\eta}(\theta_1,...,\theta_M) = e^{\lambda t}\mathbf{p}(\theta_1,...,\theta_M)$$

An equation analogous to Eq. (2.70) is thus obtained through first-order recast, with the time derivative now expressed in terms of partial derivatives with respect to each time scale:

$$\sum_{i=1}^{M}\omega_i\frac{\partial \mathbf{p}_j(t)}{\partial \theta_i} + \lambda_j \mathbf{p}_j(t) = \mathbf{A}(t)\mathbf{p}_j(t) \tag{2.97}$$

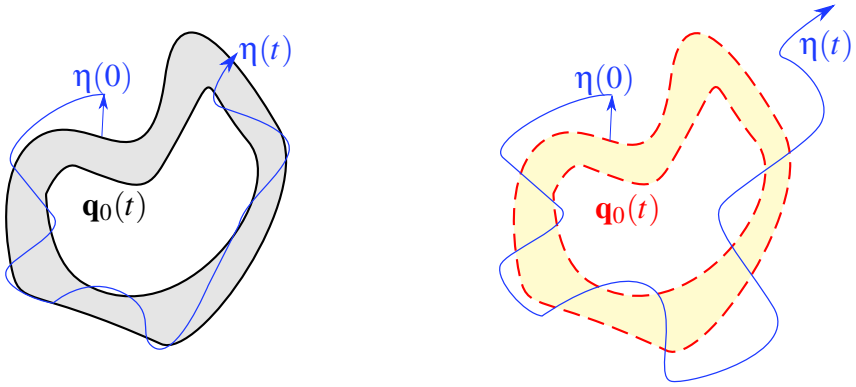

Figure 2.10: Local stability for a quasi-periodic solution $\mathbf{q}_0(t)$. Left: stable cycle, right: unstable cycle.

Projection onto the frequency domain leads once again to Eq. (2.72), where the total derivative, Eq. (2.89), is employed.

Mediating the computational strategies for the computation of the required terms, Hill's methods remains unchanged for quasi-periodic solutions, as the number of Floquet exponents for a given system does not depend on the nature of its solutions. However, it is important to realize that any free phase will lead to a trivial eigenvalue, just as in the case of autonomous systems discussed in Sect. 2.1.4.2. In fact, an analogous invariance argument may be advanced for quasi-periodic solutions, as follows. Consider a periodically-forced system driven at a frequency ω_1, which acts as continuation parameter; let one of its solutions be $\mathbf{x}(\theta_1,\theta_2)$, belonging to a bifurcated branch born at a NS point. As the forcing prescribes only a phase with respect to the first hyper-time coordinate, the total phase is free: in other words, time-translations purely along the second time coordinate result in rotations along the torus surface, which is invariant. A good geometric picture, represented in Fig. (2.11) is the following: a Poincaré section of the solution in phase space taken at $t = 0$ yields a closed curve, such that an infinite family of solutions describe the same torus, each one corresponding to a different starting point on this curve.

Let us express the partially time-shifted Fourier coefficients as:

$$\begin{aligned}\mathbf{x}(\theta_1,\theta_2+\Delta\theta_2) &= [\mathbb{F}(\theta_1,\theta_2+\Delta\theta_2)\otimes\mathbf{I}_n]\,\mathbf{X} = [\mathbb{F}(\theta_1,\theta_2)\mathbf{G}_2(\Delta\theta_2)\otimes\mathbf{I}_n]\,\mathbf{X}\\ &= [\mathbb{F}(\theta_1,\theta_2)\otimes\mathbf{I}_n]\,\mathbf{X}_{\Delta\theta_2}\end{aligned} \tag{2.98}$$

where the matrix $\mathbf{G}_2$ operates a partial rotation along the second hyper-time coordinate. Owing to invariance, the first variation of the equilibrium equations with respect to $\Delta\theta_2$ must be nil for any given ω_1 and ω_2. Hence:

[4] Alternatively, one can compute this term using finite differences, which is much simpler to code but also quite inefficient.

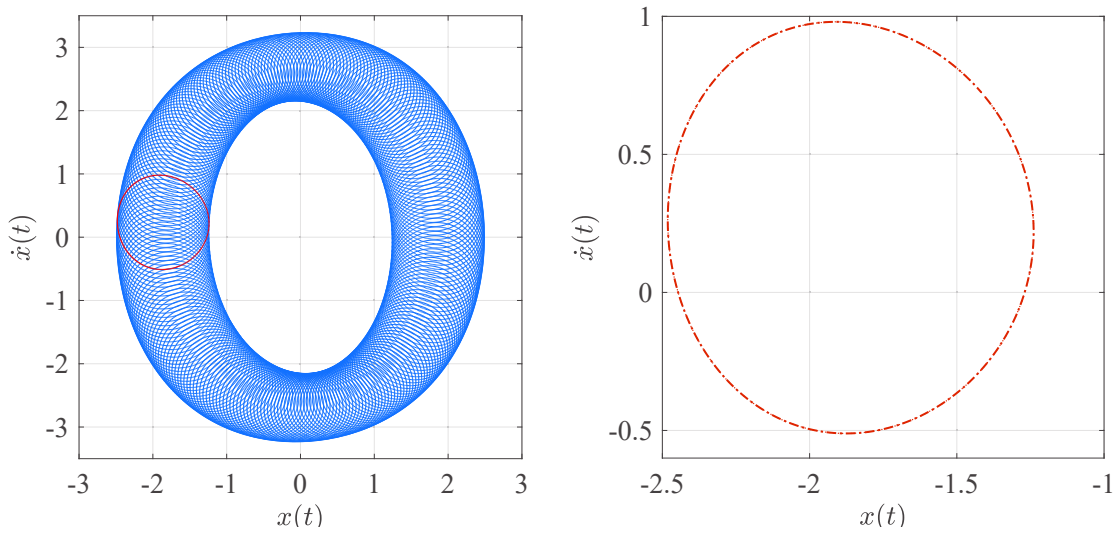

Figure 2.11: A forced quasi-periodic solution. The time history is probed at regular intervals equal to the forcing period $T = 2\pi/\omega_1$. Left: phase-space representation; right: Poincaré section.

$$\begin{aligned}\frac{d\mathbf{R}(\mathbf{X}_{\Delta\theta_2},\Delta\theta_2)}{d(\Delta\theta_2)} &= \frac{\partial\mathbf{R}}{\partial(\Delta\theta_2)} + \mathbf{R}_{\mathbf{X}}(\mathbf{X}_{\Delta\theta_2})\frac{\partial\mathbf{X}_{\Delta\theta_2}}{\partial(\Delta\theta_2)} \\ &= \mathbf{R}_{\mathbf{X}}(\mathbf{X}_{\Delta\theta_2})\,(\nabla_2\otimes\mathbf{I}_n)\,\mathbf{X}_{\Delta\theta_2} = \mathbf{0}\end{aligned} \tag{2.99}$$

This proves that, regardless of the chosen phase condition, the Jacobian (and thus the Hill matrix) possesses a trivial eigenvalue with an associated null-space spanned by the vector $(\nabla_2\otimes\mathbf{I}_n)\,\mathbf{X}_{\Delta\theta_2}$.

2.2.3 Generalized bifurcation analysis

Special points on bifurcation curves can be detected, precisely localized and tracked in an analogous manner to codim-1 bifurcations on response curves. Hence, by recursive application of tracking, an understanding of the global bifurcation behaviour of the system -i.e., over the full parameter space- is attainable. Evidently, this has great potential as a functional optimization technique, as certain aspects of the dynamics may be enhanced or suppressed altogether by adequate parameter choices. This was recently done in [GRE 19] to ensure safe operation of a nonlinear vibration absorber by avoiding high-amplitude isolated solutions. In that case, a recursive tracking of LPs was proposed; in this section, the same idea is generalized to all kinds of bifurcations.

Consider any one of the extended systems presented in Sect. 2.1.4.1, which we will denote generically as $\mathbf{Y}_1(\mathbf{W})$, with all the corresponding variables (Fourier coefficients

$\mathbf{X}$, frequency ω, and potentially eigenvectors/eigenvalues characterizing a particular bifurcation) being grouped into the vector $\mathbf{W}$. Without loss of generality, let us assume that ω was used as the initial continuation parameter and that a second one, α, is freed and used to track bifurcations with pseudo arc-length continuation. The tangent matrix at the i-th continuation step is thus given by:

$$\mathbf{J}_{\mathbf{Y}_1}(\mathbf{W},\alpha) = \begin{bmatrix} (\mathbf{Y}_1)_{\mathbf{W}} & (\mathbf{Y}_1)_{\alpha} \\ \Delta\mathbf{W}_{i-1}^{T} & \Delta\alpha_{i-1} \end{bmatrix} \tag{2.100}$$

where the derivatives are evaluated at $(\mathbf{W}_i,\alpha_i)$. Following the constraint equations appended to dynamical equilibrium in $\mathbf{Y}_1(\mathbf{W},\alpha)$, each solution along the computed curve possesses a certain number of fixed Floquet exponents which have a null real part up to the chosen tolerance of the NR algorithm: one for LPs and BPs, two for PDs and NSs (plus an additional one in the autonomous case). Let the number of these free exponents be given by d. The remaining $2n-d$ ones evolve as a function of ω and α, such that one of the three following scenarios might be encountered between two consecutive continuation steps i and $i+1$:

1. **Pseudo-regular point**: the number of exponents with negative real parts among the $2n-d$ free ones does not change from one step to the other. Likewise, the continuation direction is preserved. This last statement is equivalent to either of the following: $\det((\mathbf{Y}_1)_{\mathbf{W}}|_i)\det((\mathbf{Y}_1)_{\mathbf{W}}|_{i+1}) > 0$, or $\Delta\alpha_i\Delta\alpha_{i+1} > 0$.

2. **Generalized turning point**: The continuation direction changes, as evidenced by $\det((\mathbf{Y}_1)_{\mathbf{W}}|_i)\det((\mathbf{Y}_1)_{\mathbf{W}}|_{i+1}) < 0$, or $\Delta\alpha_i\Delta\alpha_{i+1} < 0$. Meanwhile, the number of Floquet exponents with negative real parts stays the same.

3. **Codim-2 bifurcation**: one or more of the free Floquet exponents cross the imaginary axis, while the continuation direction is preserved.

It should be noted that a linear stability analysis, as given by Hill's method, yields sufficient information to distinguish between cases 1 and 3, under the condition that all d eigenvalues on the imaginary axis are shifted away or ignored during stability evaluation while performing bifurcation tracking. This operation can be achieved with great ease, since the associated eigenvectors of the Hill matrix are solved for at each step. Formally, one detects hybrid bifurcations by evaluating the real parts of Floquet exponents issued from the artificially-hyperbolic system:

$$\widetilde{\mathbb{H}}\phi = \left(\mathbb{H} - \sum_{i=1}^{d} \mathbf{v_i}\mathbf{v_i^T}\right)\phi = \lambda\phi \tag{2.101}$$

For a practical implementation, shifting Hill's matrix is not required, as the critical Floquet exponents can simply be identified with the aid of their eigenvectors. Extended systems for any codim-k bifurcations identified in this manner, with k being an arbitrary

integer greater than 1, are then constructed in a modular fashion, using constraint equations for the codim-1 case as building blocks. The codim-2 case, for which an exhaustive list has been established by Kuznetsov and co-workers [KUZ 04, WIT 13], is used here for illustration purposes. Two qualitatively different situations, which transpose exactly to the codim-k case, have to be considered:

Strong resonances

They correspond to a pair of Floquet multipliers crossing the unit circle through one of the first four roots of unity:

$$\mu_{1,2}^k = 1 \tag{2.102}$$

with $k = 1,2,3,4$ and $\mu \in \mathbb{C}$. Although, in practice, crossings through higher roots of unity is evidently possible, these four cases are special in the sense that they lead to high-order terms which cannot be eliminated in the associated normal forms [HAL 91], a trait absent for the *weak* resonances ($k > 4$). In turn, this results in extremely complex dynamics in their vicinity. Reasoning in terms of Floquet exponents $\lambda_{1,2}$, the conditions of Eq. (2.102) are equivalent to:

$$\begin{cases} \text{1:1 resonance } (R1) : & \lambda_{1,2} = 0 \\ \text{1:2 resonance } (R2) : & \lambda_{1,2} = \pm i\frac{\omega}{2} \\ \text{1:3 resonance } (R3) : & \lambda_{1,2} = \pm i\frac{\omega}{3} \\ \text{1:4 resonance } (R4) : & \lambda_{1,2} = \pm i\frac{\omega}{4} \end{cases} \tag{2.103}$$

While these bifurcations are not generic in codim-1, they are readily found along NS curves in codim-2 as the ratio ω/κ becomes rational, implying phase-locked (resonant) tori. It should be noted that the condition for a $R2$ resonance is exactly the same as that for a PD bifurcation, Eq. (2.41). However, we distinguish between the two on the basis of their codimension.

1:1 resonance **(R1)** $\lambda_1 = \lambda_2 = 0$

Also known as a *double-zero*, *fold-fold*, or *Bogdanov-Takens* bifurcation of cycles. This is an instance of a bifurcation with geometric multiplicity 1 but algebraic multiplicity $k > 1$, i.e. a k-fold repeated root for the eigenvalue problem given by Eq. (2.72), associated to a single eigenvector ϕ_1. The null subspace of $\mathbb{H}$ has thus a rank deficiency of order $k-1$, and a complete basis for it may be constructed by finding $k-1$ generalized eigenvectors $\phi_2, ..., \phi_k$ that constitute the links of a Jordan chain alongside ϕ_1 [TIS 01].
The following relations thus hold for $P(\lambda) = \mathbf{A}_0 + \lambda\mathbf{A}_1 + ... + \lambda^p\mathbf{A}_p$, a generic matrix

polynomial of order $p > k$:

$$\begin{aligned} &P(\lambda_0)\phi_1 = \mathbf{0} \\ &P(\lambda_0)\phi_2 = -P'(\lambda_0)\phi_1 \\ &\qquad\vdots \\ &P(\lambda_0)\phi_k = -P'(\lambda_0)\phi_{k-1} - \ldots - \frac{1}{(k-1)!}P^{(k-1)}(\lambda_0)\phi_1 \end{aligned} \tag{2.104}$$

This form is suitable for the quadratic eigenvalue problems such as the standard Hill method, Eq. (2.79). If the equivalent linear recast is rather considered, i.e:

$$\begin{bmatrix} \mathbf{0} & \mathbf{I} \\ -\mathbf{D}_2^{-1}\mathbf{R}_\mathbf{X} & -\mathbf{D}_2^{-1}\mathbf{D}_1 \end{bmatrix} \begin{bmatrix} \phi \\ \lambda\phi \end{bmatrix} = \mathbf{A} \begin{bmatrix} \phi \\ \lambda\phi \end{bmatrix} = \lambda \begin{bmatrix} \phi \\ \lambda\phi \end{bmatrix} \tag{2.105}$$

then the above equations still hold by introducing the following matrix polynomial: $\hat{P}(\lambda, \phi) = (\mathbf{A} - \lambda\mathbf{I}) \left[\phi^T, \lambda\phi^T\right]^T$. For a root with multiplicity 2, this leads to:

$$\begin{aligned} &\hat{P}(\lambda_0, \phi_1) = \mathbf{0} \\ &\hat{P}(\lambda_0, \phi_2) = -\hat{P}'(\lambda_0, \phi_1) \end{aligned} \tag{2.106}$$

The alternate form of Hill's method proposed in this thesis, with $\mathbb{H}$ as described in Eqs.(2.73,2.76), is treated in the exact same fashion, hence all the following developments apply to reducible integro-differential systems as well. Eq. (2.106) together with the constraint equations for codim-1 bifurcations provides the required tool to construct extended systems for multiple roots, of which 1:1 resonance is the sole codim-2 example. Let φ denote the generalized eigenvector. Thus, by introducing $\lambda_0 = 0$ into Eq. (2.106), one finds the constraint equation $\mathbf{R}_\mathbf{X}\varphi + \mathbf{D}_1\phi = \mathbf{0}$, which leads to the following extended system:

$$\mathbf{Y}_{\mathrm{R1}}(\mathbf{X}, \phi, \omega, \varphi, \alpha) = \begin{bmatrix} \mathbf{R} \\ \mathbf{R}_\mathbf{X}\phi \\ \phi^T\phi - 1 \\ \mathbf{R}_\mathbf{X}\varphi + \mathbf{D}_1\phi \\ \phi^T\varphi \end{bmatrix} \tag{2.107}$$

where the last equation is a normalisation condition on φ, derived as follows. While the vector ϕ in the equation $\mathbf{R}_\mathbf{X}\varphi + \mathbf{D}_1\phi = \mathbf{0}$ is uniquely defined through the normalization in the LP extended system, it is not the same for φ, since it can be replaced by $\tilde{\varphi} = \varphi + a\phi$ for any $a \in \mathbb{R}$ and yield the same result. Nevertheless it is always possible, since ϕ and φ cannot be collinear, to choose $a = a_0$ such that ϕ and $\tilde{\varphi}$ are orthogonal, as illustrated in Fig. 2.12. This is the vector chosen among the family of possible solutions, whose initial approximation for the Newton-Raphson method can be found by solving for a_0 and φ:

$$\begin{bmatrix} \mathbf{R}_\mathbf{X} & \mathbf{0} \\ \phi^T & ||\phi||^2 \end{bmatrix} \begin{bmatrix} \varphi \\ a_0 \end{bmatrix} = \begin{bmatrix} -\mathbf{D}_1\phi \\ 0 \end{bmatrix} \tag{2.108}$$

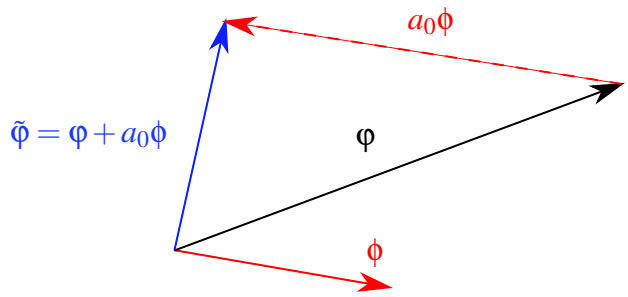

Figure 2.12: Eigenvectors spanning the null subspace associated to a multiple root.

The R1 bifurcation is relevant in quasi-periodic analysis, since it marks the branching, i.e. the birth or end, of a NS curve out a LP one. As its name suggests, it is a consequence of the coincidence between natural frequencies of two different vibration modes of the system, triggered by the detuning introduced by nonlinear effects. For instance, two modes with initially close linear frequencies can intersect due to stress stiffening. In the vicinity of an R1 point, the closeness between these frequencies results in a beating phenomenon, i.e. modulated oscillations. Conversely, this bifurcation can also be detected along NS tracking, where it is self-evident from the fact that eigenvalues $\pm i\kappa$ tend to zero.

1:n resonance **(Rn)** $\lambda_{1,2} = \pm i\dfrac{\omega}{n}, n \in \mathbb{N}$

Extended systems for the other strong resonances are found by appending the required phase-locking condition to the NS system, Eq. (2.40), as follows:

$$\mathbf{Y}_{\mathrm{Rn}}(\mathbf{X}, \phi_R, \phi_I, \omega, \kappa, \alpha) = \begin{bmatrix} \mathbf{R} \\ \left(\mathbf{R}_{\mathbf{X}} - \kappa^2 \mathbf{D}_2\right)\phi_R - \kappa \mathbf{D}_1 \phi_I \\ \kappa \mathbf{D}_1 \phi_R + \left(\mathbf{R}_{\mathbf{X}} - \kappa^2 \mathbf{D}_2\right)\phi_I \\ \mathbf{p}^T \phi_R - 1 \\ \mathbf{p}^T \phi_I \\ \omega - n\kappa \end{bmatrix} \tag{2.109}$$

At an Rn point, branches of nT-periodic sub-harmonic solutions bifurcate and can be followed by applying the techniques introduced in the following section.

Hybrid bifurcations

Critical Floquet exponents in this case are of different nature, i.e. each root has simple multiplicity. Thus, extended systems are built by straightforwardly appending the constraint equations for the corresponding codim-1 bifurcations one after the other. Regarding nomenclature, here the choice is made to borrow from the bifurcations of equilibria. Thus, the words "of cycles" shall be understood to be systematically, albeit implicitly, present. For instance, the word *Hopf* refers to a Hopf bifurcation *of cycles*, i.e. a NS bifurcation.

Zero-Hopf **(ZH)** $\lambda_1 = 0, \lambda_{2,3} = \pm i\kappa$

In contrast with the R1 case, a NS curve does not start/end at a ZH bifurcation. Rather, a curve of LP and one of NS intersect transversely at this point. Letting ϕ be the eigenvector corresponding to the zero exponent and $\varphi = \varphi_R \pm i\varphi_I$ the complex eigenvector associated to the incommensurate frequency κ:

$$\mathbf{Y}_{\mathrm{ZH}}(\mathbf{X}, \phi, \omega, \varphi_R, \varphi_I, \kappa, \alpha) = \begin{bmatrix} \mathbf{R} \\ \mathbf{R_X}\phi \\ \phi^T\phi - 1 \\ \left(\mathbf{R_X} - \kappa^2\mathbf{D_2}\right)\varphi_R - \kappa\mathbf{D}_1\varphi_I \\ \left(\mathbf{R_X} - \kappa^2\mathbf{D_2}\right)\varphi_I + \kappa\mathbf{D}_1\varphi_R \\ \mathbf{p}^T\varphi_R - 1 \\ \mathbf{p}^T\varphi_I \end{bmatrix} \tag{2.110}$$

Locating a ZH bifurcation is useful for branching from a curve of LP to either a NS curve or a quasi-periodic response branch.

Hopf-Hopf **(HH)** $\lambda_{1,2} = \pm i\kappa, \lambda_{2,3} = \pm i\xi$

As a last example, the case where a second pair of complex-conjugate Floquet exponents crosses the imaginary along NS tracking is considered. It should be noted that, although the *Hopf-Hopf* bifurcation strictly denotes the case where ω, κ and ξ are all incommensurate, other cases such as *flip-Hopf* ($\lambda_{1,2} = \pm i\kappa, \lambda_{2,3} = \pm i\omega/2$) can be derived easily from the following system by fixing one of the frequencies to the appropriate value and removing one of the normalisation equations. Considering two complex-conjugate eigenvalue pairs ϕ and φ, the HH extended system reads:

$$\mathbf{Y}_{\mathrm{HH}}(\mathbf{X}, \phi_R, \phi_I, \kappa, \omega, \varphi_R, \varphi_I, \xi, \alpha) = \begin{bmatrix} \mathbf{R} \\ \left(\mathbf{R_X} - \kappa^2\mathbf{D_2}\right)\phi_R - \kappa\mathbf{D}_1\phi_I \\ \left(\mathbf{R_X} - \kappa^2\mathbf{D_2}\right)\phi_I + \kappa\mathbf{D}_1\phi_R \\ \mathbf{p}^T\phi_R - 1 \\ \mathbf{p}^T\phi_I \\ \left(\mathbf{R_X} - \xi^2\mathbf{D_2}\right)\varphi_R - \xi\mathbf{D}_1\varphi_I \\ \left(\mathbf{R_X} - \xi^2\mathbf{D_2}\right)\varphi_I + \xi\mathbf{D}_1\varphi_R \\ \mathbf{p}^T\varphi_R - 1 \\ \mathbf{p}^T\varphi_I \end{bmatrix} \tag{2.111}$$

Generalized turning points

Let $\mathbf{Y}(\mathbf{V}, \alpha)$ denote a set of l nonlinear algebraic equations depending on an arbitrary set of variables, grouped in vector $\mathbf{V} \in \mathbb{R}^l$, and tracked with respect to the scalar parameter α. An implicit curve in the $(l+1)$-dimensional solution space is defined by $\mathbf{Y}(\mathbf{V}, \alpha) = \mathbf{0}$ together with an appropriate arc-length equation. The components $(\Delta\mathbf{V}, \Delta\alpha)$ of the tangent vector at any given point on this curve thus satisfy:

$$\mathbf{Y_V}\Delta\mathbf{V} + \mathbf{Y}_\alpha\Delta\alpha = \mathbf{0} \tag{2.112}$$

Just as in the case of a LP, the curve exhibits a fold whenever $\Delta\alpha = 0$. Thus, the $\mathbf{V}$-increment is none other than an eigenvector ψ spanning the null-space of $\mathbf{Y}_\mathbf{V}$, whose magnitude can be fixed to any non-zero value to yield an extended system analogous to a codim-1 LP:

$$\mathbf{Y}^G(\mathbf{V},\psi,\alpha) = \begin{bmatrix} \mathbf{Y} \\ \mathbf{Y}_\mathbf{V}\psi \\ \psi^T\psi - 1 \end{bmatrix} \tag{2.113}$$

Replacing $\mathbf{Y}^G$ with the LP extended system, Eq. (2.38), in the above expression leads to a characterization of the well-known *cusp* bifurcation (CSP). The Chenciner (CH) and Generalized Period Doubling (GPD) are the analogous points on NS and PD curves, respectively. Serving as organizing centres for the global dynamics of a given system, generalized turning points mark the appearance or vanishing of attractors. This, in particular, is true of isolas. Certain cusp bifurcations have been shown to indicate isola birth/death as well as detaching from/attaching to a main response branch. In [ALC 19], whose results are presented in Chapter 3 of this thesis, a similar phenomena is observed in relation to GPD bifurcations.

Fig. 2.13 summarizes the discussion of the present subsection. Even though the tree-like structure of this diagram branches out and becomes complicated when codimension increases -as the number of possible cases widens-, the first two 'levels' are the foundation on which the most general scenarios can be constructed.

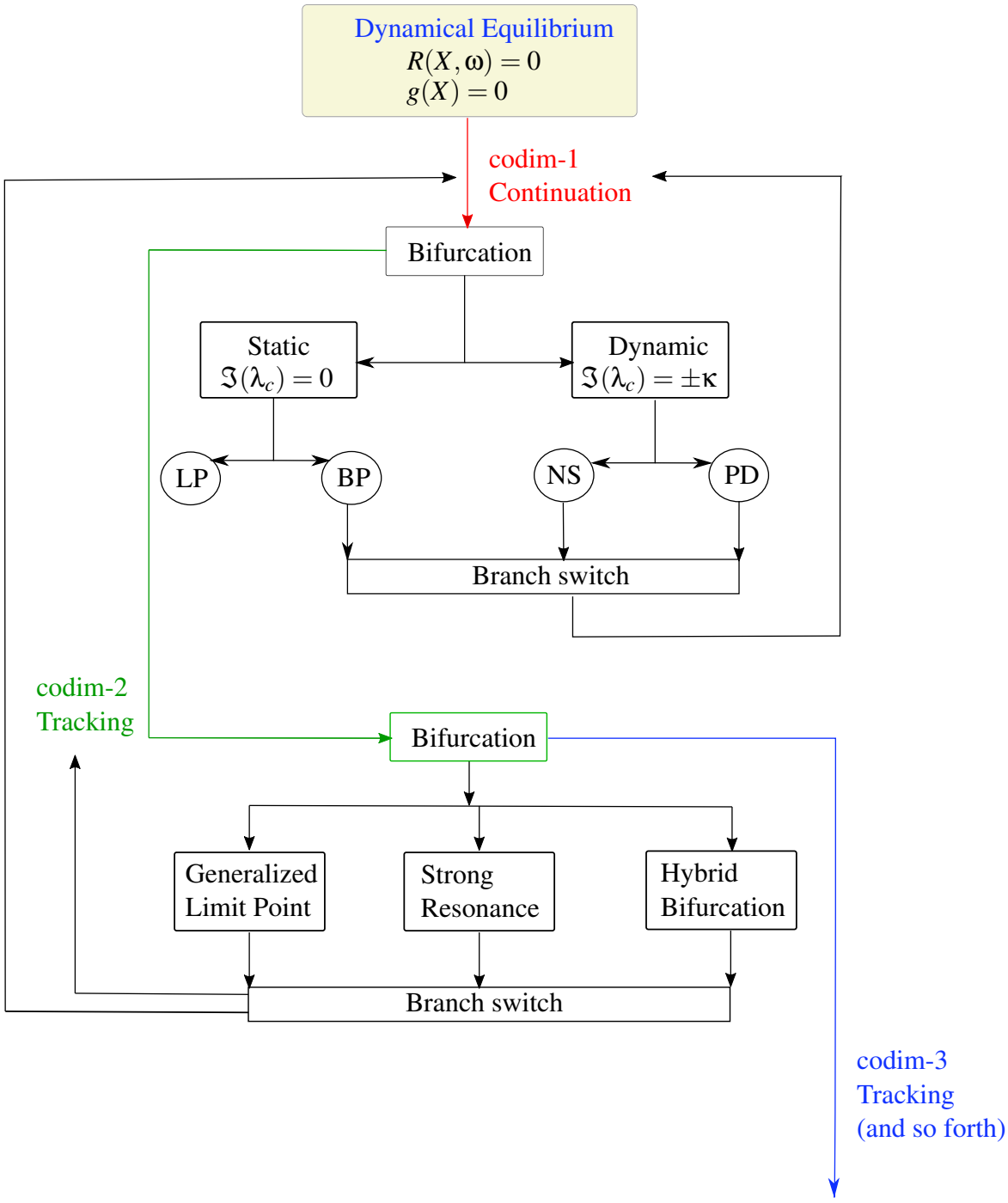

Figure 2.13: Summary of numerical bifurcation analysis.

2.2.4 Branch switching

Periodic branches

With the exception of LPs, all codim-1 bifurcations exist at the intersection of (at least) two branches of qualitatively-different solutions. BPs are frequently referred to as *symmetry-breaking* bifurcations since cycles on one of the branches are *half-wave symmetric*, i.e.:

$$\mathbf{x}\left(t+\frac{T}{2}\right) = -\mathbf{x}(t) \tag{2.114}$$

whereas those on the bifurcating branch do not. In the context of the HBM, this means that even harmonics are inactive in the former branch but not in the bifurcating one, a fact that is easily proven by considering:

$$\begin{cases} \cos\left(j\omega\left(t+\dfrac{T}{2}\right)\right) = \cos(j\omega t)\cos(j\pi) - \sin(j\omega t)\sin(j\pi) = (-1)^j\cos(j\omega t) \\ \sin\left(j\omega\left(t+\dfrac{T}{2}\right)\right) = \sin(j\omega t)\cos(j\pi) + \cos(j\omega t)\sin(j\pi) = (-1)^j\sin(j\omega t) \end{cases} \tag{2.115}$$

Comparing Eqs. (2.114) and (2.115), it is clear that only a signal whose spectrum contains exclusively odd harmonics verifies half-wave symmetry, see Fig. 2.14. Moreover, any signal can be decomposed into its odd and even harmonics: $\mathbf{X} = \mathbf{X}_o + \mathbf{X}_e$ where the first right-hand side vector contains non-zero terms only on its components associated to odd harmonics, and vice-versa. Thus, clearly $\mathbf{X}_o^T\mathbf{X}_e = 0$. Let us formalize this by stating that $\mathbf{X}_o \in \mathbb{U}_o \subset \mathbb{R}^{nL}$ and $\mathbf{X}_e \in \mathbb{U}_e \subset \mathbb{R}^{nL}$, where any two elements -taken one from each subset- are orthogonal.

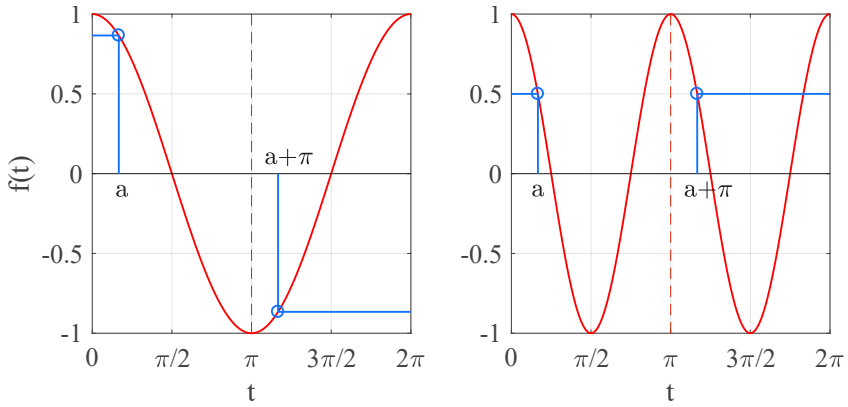

Figure 2.14: 2π-periodic functions. Left: $\cos(t)$, exhibiting half-wave symmetry. Right: $\cos(2t)$, an antisymmetric function.

Following a symmetric branch means that, at the j-th continuation step, the tangent vector $\mathbf{t}_j \in \mathbb{U}_o$. Assuming a BP to occur precisely at the j-th step, the emerging non-symmetric tangent $\mathbf{t}_{\text{BP}}$ has a non-zero projection on both $\mathbb{U}_o$ and $\mathbb{U}_e$, which implies that:

$\mathbf{t}_{\text{BP}} = a\mathbf{t}_j + b\mathbf{v}_e, \mathbf{v}_e \in \mathbb{U}_e, (a,b) \in \mathbb{R}^2$. This last vector can be identified with the eigenvector ϕ associated to the nil eigenvalue of the Jacobian $\mathbf{R}_{\mathbf{X}}$. This observation is at the heart of the *parallel search* algorithm for branch switching [HEN 05, DOE 12], whose principle is to take a step along ϕ from a BP and then converge onto the bifurcating branch through orthogonal Newton-Raphson corrections. The other well-known alternative is to compute the coefficients (a,b) through the use of the *Algebraic Branching Equation* (ABE) [KEL 86].
It is important to note that half-wave symmetry, as described above, is not the only way in which BPs can occur. For instance, along the FRC of a 2-DOF system of which only one mode is excited by an external force, a branch of bi-modal solutions can bifurcate from the main curve due to modal interactions. The argument advanced herein still holds by considering a decomposition $\mathbf{X} = \mathbf{X}_1 + \mathbf{X}_2$, where the vectors respectively contain the (odd and even) coefficients of the first and second mode, so that $\mathbf{X}_1^T \mathbf{X}_2 = 0$.

Sub-harmonic branches

Recall that the Fourier basis $\mathbb{F}_H(\omega t)$ includes only terms whose frequencies are multiples of the fundamental frequency ω. This means, first of all, that sub-harmonic responses can not be computed with this basis alone, but also that PD and Rn bifurcations can be readily identified as such. Indeed, consider the alternative basis:

$$\mathbb{F}_{nH}(\omega t) = \left[1, \cos(\frac{\omega}{n}t), \sin(\frac{\omega}{n}t), \cos(\omega t), \sin(\omega t), ...\right] \tag{2.116}$$

Since $\mathbb{F}_H(\omega t) \subset \mathbb{F}_{nH}(\omega t)$, any T-periodic solution to the equations of motion can be constructed in this new basis. However, the addition of sub-harmonic functions means that the minimal period is now nT. As a consequence, the period-multiplying bifurcation is not associated with a change in period any more: instead, it identifies a BP, as a branch emerges on which the solutions have components orthogonal to those of the branch being followed. The operation $\omega \leftarrow \frac{\omega}{n}$ transforms $\mathbb{F}_H(\omega t)$ into $\mathbb{H}_{nH}(\omega t)$. In practice, this implies extending the size of vector $\mathbf{X}$ in order to not neglect the higher harmonics while including sub-harmonics.
The most practical way to switch branches, upon detection of a sub-harmonic bifurcation, is thus to extend the original Fourier basis and compute the eigenvector ϕ verifying $\mathbf{R}_{\mathbf{X}}\phi = \mathbf{0}$. Afterwards, the ABE or parallel switching can be applied.

Quasi-periodic branches

Branches of quasi-periodic solutions emerging from a NS bifurcation on a periodic branch can be reached through a similar switching technique as that concerning asymmetrical periodic or sub-harmonic branches. Once again, the key idea is to exploit the symmetry-breaking nature of the bifurcation. A root of the system Eq. 2.40 yields $[\mathbf{Q}, \omega, \phi_R, \phi_I, \kappa]$, where a perturbation applied to the marginally stable cycle at $(\mathbf{Q}, \omega)$ is described by the relation:

$$\boldsymbol{\eta}_{\pm}(t) = \left[\mathbb{F}_H(\omega t) \otimes \mathbf{I}_n\right](\phi_R \pm i\phi_I)\, e^{\pm i\kappa t} \tag{2.117}$$

The general form of $\boldsymbol{\eta}(t)$ is a linear combination of the eigenvalue/eigenvector pairs corresponding to the positive and negative values of κ. Considering this and grouping terms yields:

$$\boldsymbol{\eta}(t) = [\mathbb{F}_H(\omega t) \otimes \mathbf{I}_n] \left\{ (e^{i\kappa t} + e^{-i\kappa t})\boldsymbol{\phi}_R + i(e^{i\kappa t} - e^{-i\kappa t})\boldsymbol{\phi}_I \right\} \tag{2.118}$$

From Euler's formula, the terms in parentheses correspond, respectively, to $2\cos(\kappa t)$ and $2i\sin(\kappa t)$. Thus, since the frequencies ω and κ are incommensurate, the resulting product of trigonometric functions gives rise to two-frequency quasi-periodic motions. The extended HBM formalism of Sect. 2.2.2 with a bi-dimensional hyper-time accounts for this type of solutions by introducing the basis $\mathbb{F}_H(\omega t, \kappa t)$. It should be noted that $\mathbb{F}_H(\omega t) \subset \mathbb{F}_H(\omega t, \kappa t)$, such that we may consider the decomposition $\mathbf{X} = \mathbf{X}_{\mathrm{P}} + \mathbf{X}_{\mathrm{QP}}$, where the first right-hand side vector has as non-zero components those which are included in the periodic basis $\mathbb{F}_H(\omega t)$. The perturbation $\boldsymbol{\eta}(t)$ can be expressed in terms of the new basis functions, as follows:

$$\boldsymbol{\eta}(t) = [\mathbb{F}_H(\omega t, \kappa t) \otimes \mathbf{I}_n] \boldsymbol{\psi} \tag{2.119}$$

where the coefficients of the real eigenvector $\boldsymbol{\psi}$ depend on those of $\boldsymbol{\phi}_R$ and $\boldsymbol{\phi}_I$. Indeed, by distributing the $\cos(\kappa t)$ and $\sin(\kappa t)$ terms over the components of $\mathbb{F}_H(\omega t)$ and applying trigonometric product identities, it can be shown that $\boldsymbol{\psi}$ consists entirely of terms involving combinations of harmonics of ω and the fundamental frequency κ. Moreover, the explicit expressions of the corresponding coefficients are given by:

$$\begin{cases} \boldsymbol{\psi}_{\mathrm{c}(a,1)} = \boldsymbol{\phi}_{R(\mathrm{c}a)} - \mathrm{sign}(a)\boldsymbol{\phi}_{I(\mathrm{s}a)} \\ \\ \boldsymbol{\psi}_{\mathrm{s}(a,1)} = \mathrm{sign}(a)\boldsymbol{\phi}_{R(\mathrm{s}a)} - \boldsymbol{\phi}_{I(\mathrm{c}a)} \ , \ \forall a = -H, ..., -1, 1, ..., H \\ \\ \left[\boldsymbol{\psi}_{\mathrm{c}(0,1)}, \boldsymbol{\psi}_{\mathrm{s}(0,1)}\right] = \left[\boldsymbol{\phi}_{R(0)}, -\boldsymbol{\phi}_{I(0)}\right] \end{cases} \tag{2.120}$$

For practical implementations, a specific arrangement must be defined for the coefficients $\mathbf{X}_{\mathrm{y}(a,b)}$ of arbitrary vectors spanned by the quasi-periodic basis, where the sub-index y can stand for c or s (cosine or sine terms, respectively) and $b = 0, ..., H$. It is important to note that, regardless of the chosen arrangement, the vector $\boldsymbol{\psi}$ is always orthogonal to the response curve at a NS bifurcation. This is necessarily the case because any non-zero coefficients of a periodic solution must correspond to the "0-th harmonic" of κt in vector $\boldsymbol{\psi}$, i.e. $\boldsymbol{\psi}_{y(|a|,0)}$. Hence, this situation is analogous to symmetry-breaking of periodic solutions and to period multiplying. Indeed, as in the latter case, extending the original basis to include the new time scale has the effect of 'transforming' a NS bifurcation into a standard branch point[5]. The classical ABE could thus be used to robustly follow the emerging branch. Alternatively, parallel search can be applied. The approach taken herein is to use Eq.(2.120) to transform the complex eigenvector found from NS localization into a real eigenvector in terms of the quasi-periodic basis $\mathbb{F}_H(\omega t, \kappa t)$, and to use parallel switching afterwards. This is simpler to code -as it avoids the numerical computation of second derivatives- but more likely to encounter convergence issues as compared to the ABE.

[5]The analogy is actually imperfect, as a phase condition must also be appended to the initial system of equations to fix the phase along the second hyper-time direction. Nevertheless, this is the only difference.

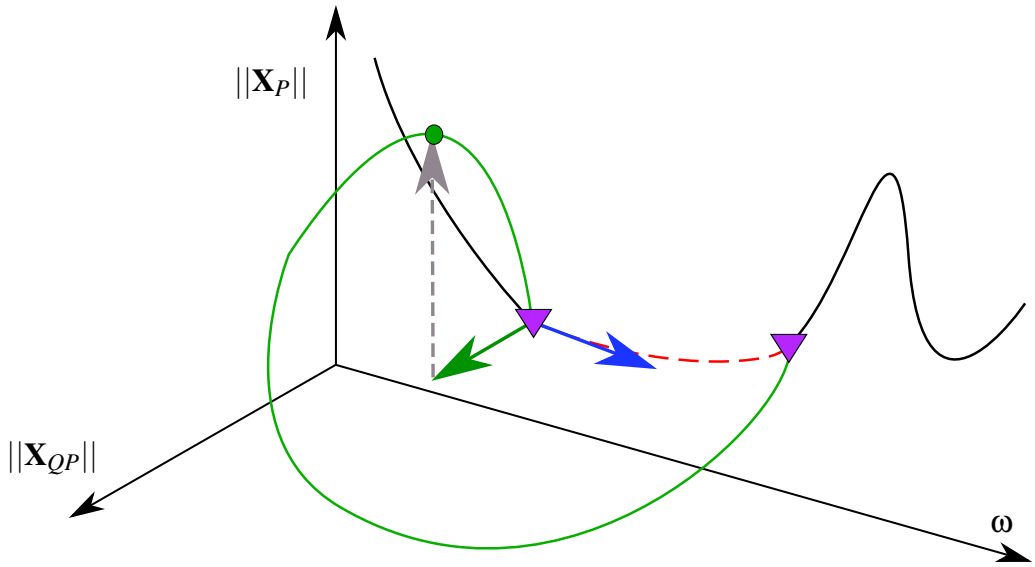

Figure 2.15: QP branch between two NS bifurcations. Dashed arrow (in grey) shows the direction of parallel search. Blue and green arrows represent, respectively, the tangent vector along the periodic codim-1 space and eigenvector ψ.

2.2.5 Benchmark examples

2.2.5.1 Isolas of the Jeffcott rotor

Consider the following simple model of a symmetrically-supported, nonlinear Jeffcott rotor:

$$m\begin{bmatrix}\ddot{x}\\ \ddot{y}\end{bmatrix}+c\begin{bmatrix}\dot{x}\\ \dot{y}\end{bmatrix}+k\begin{bmatrix}x\\ y\end{bmatrix}+\frac{g(r)}{r}\begin{bmatrix}1 & -f_T\\ f_T & 1\end{bmatrix}\begin{bmatrix}x\\ y\end{bmatrix}=f\omega^2\begin{bmatrix}\cos(\omega t)\\ \sin(\omega t)\end{bmatrix} \tag{2.121}$$

This equation describes the planar motions of a disk of radius R and with a mass unbalance f, rotating within an annular support with an angular speed ω. Notice that mass, damping and stiffness properties are the same along both directions, owing to the symmetry of the system. The last term in the left-hand side describes the contact forces, both in the normal and tangential directions, projected on the x and y-directions. Dry Coulomb friction is assumed for the tangential force, such that: $||\mathbf{F}_T|| = ||\mathbf{F}_N|| = f_T||\mathbf{F}_N||$, whereas the magnitude of the normal force is given by the function $g(r)$ in non-dimensional form:

$$g(r)=\frac{1}{2}\left[(r-1)+\sqrt{(r-1)^2+4\eta}\right] \tag{2.122}$$

where $r(t)=\sqrt{x^2(t)+y^2(t)}$ is the radial displacement. It should be noted that these equations make use of non-dimensional variables such that both contact stiffness and support radius are unitary. Similarly, f_T is a regularized function of relative velocity:

$$f_T(v_{rel})=\mu\frac{v_{rel}}{\sqrt{v_{rel}^2+\varepsilon}} \tag{2.123}$$

with:

$$v_{rel}(x, y, \dot{x}, \dot{y}, \omega) = \frac{x\dot{y} - y\dot{x}}{r} + R\omega \tag{2.124}$$

Let $H = 5$ and $n_{FFT} = 2^8$. Fig. 2.16 shows frequency response curves for two different values of forcing amplitude, with other parameters taking the following values: $m = 1$, $c = 0.1$, $k = 0.04$, $R = 20$, $\mu = 0.125$, $\eta = \varepsilon = 1E-5$. For $f = 0.4$, the mass unbalance alone does not generate contact between rotor and stator, represented by the dashed line, and so the well-known linear response is obtained. On the other hand, for $f = 0.9524$, contact is established for $\omega > 0.153$ and a fully nonlinear response results over a wide range of forcing frequencies, delimited by LPs. Furthermore, stability of the periodic branch is lost through a NS bifurcation at $\omega_{NS} = 0.59$. This is a consequence of friction forces, which manifest as cross-coupling terms in the equations of motion and oppose damping in the tangential direction at contact. Thus, for high-enough amplitudes, damping is overcome by friction and a backward whirl regime begins at an angular speed non-synchronous to ω. In the unstable region following this bifurcation, quasi-periodic motions thus occur, and even coexist with a linear, synchronous periodic response over the range delimited by the two LPs at $\omega_{LP1} = 0.89$ and $\omega_{LP2} = 0.99$. Moreover, by zooming in at this later point, it can be seen that a second NS bifurcation occurs in its vicinity, as shown in Fig. 2.16 c). Indeed, the closeness of these two points hints at the presence of a coalescence frequency ω_{ZH}, i.e. a ZH bifurcation, for a different, albeit nearby, parameter set.

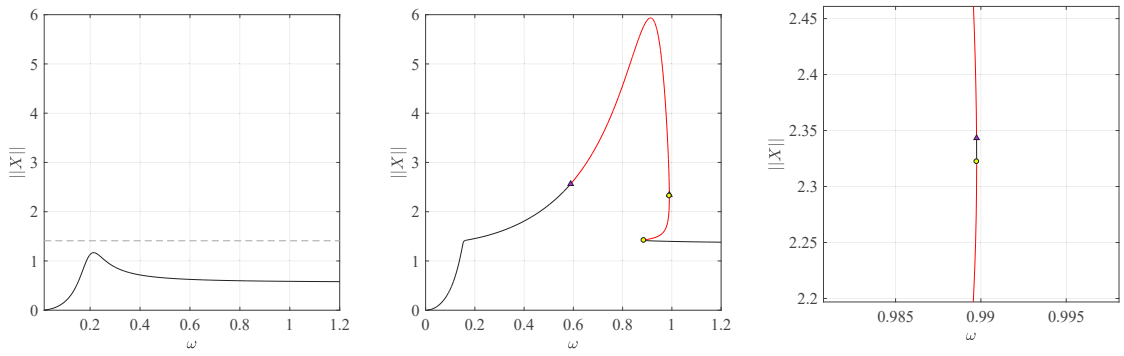

a) f = 0.4 b) f = 0.9524 c) f = 0.9524, zoom

Figure 2.16: Forced response of Jeffcott rotor, Eq. (2.121). ○: LP, △: NS

Bifurcation tracking with respect to f has been performed and the resulting stability boundaries are shown in Fig. 2.17. As discussed in Sect. 2.2.3, the Floquet exponents with null real parts are shifted by exploiting their corresponding eigenvectors, thus allowing codim-2 bifurcations to be detected by a standard stability analysis (Hill's method); generalized turning points, which in this case are cusps, are detected by monitoring the sign of Δf. Solutions with unstable modes besides those associated to the codim-1 bifurcation are represented as cyan lines in this diagram: in this case, they are delimited by two zero-hopf bifurcations, ZH1 and ZH2, marked by cyan circles. The Floquet exponents associated with the LP curve are shown in Fig. 2.18. It should

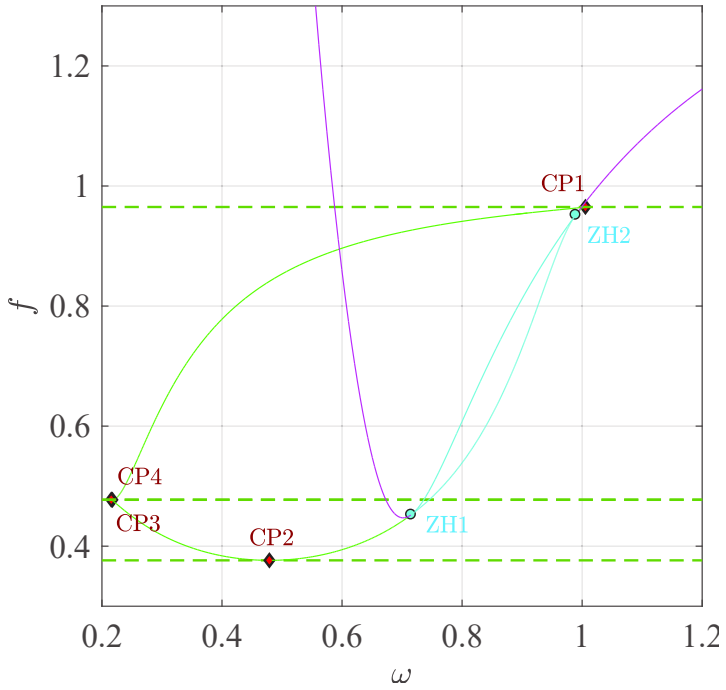

Figure 2.17: Jeffcott rotor bifurcations tracked with respect to parameter f. Green: LP curve. Magenta: NS curve. Cyan: 'unstable' bifurcations.

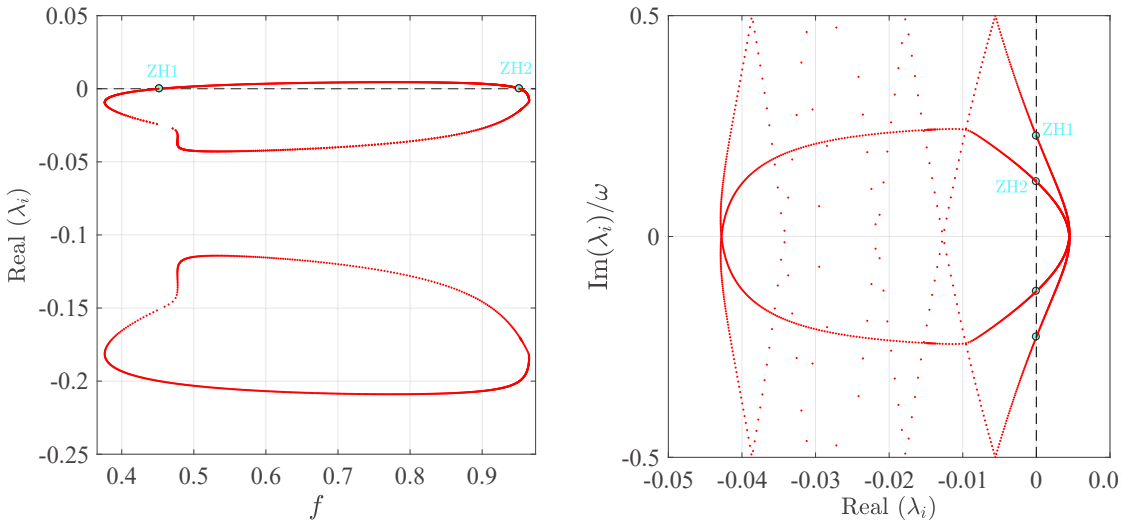

a) $f - \Re(\lambda_i)$ b) $\Re(\lambda_i) - \Im(\lambda_i)/\omega$

Figure 2.18: Floquet exponents of LP solutions for the Jeffcott rotor with $\mu = 0.125$.

be noted that only three out of the system's four exponents are represented, as the one associated to the singular Jacobian has been shifted to -1.

Tracking of NSs and LPs both yield the exact same locations for the ZH bifurcations, as expected. Even if only one of the curves is computed, for instance the LP one, such a point can be used to easily transition to the NS curve by using it as an initial solution and then employing continuation on the associated extended system. An interesting observation, is that an 'unstable' LP or NS bifurcation happens within an unstable branch with no stability change, whereas a 'stable' one separates a stable and an unstable periodic branch.

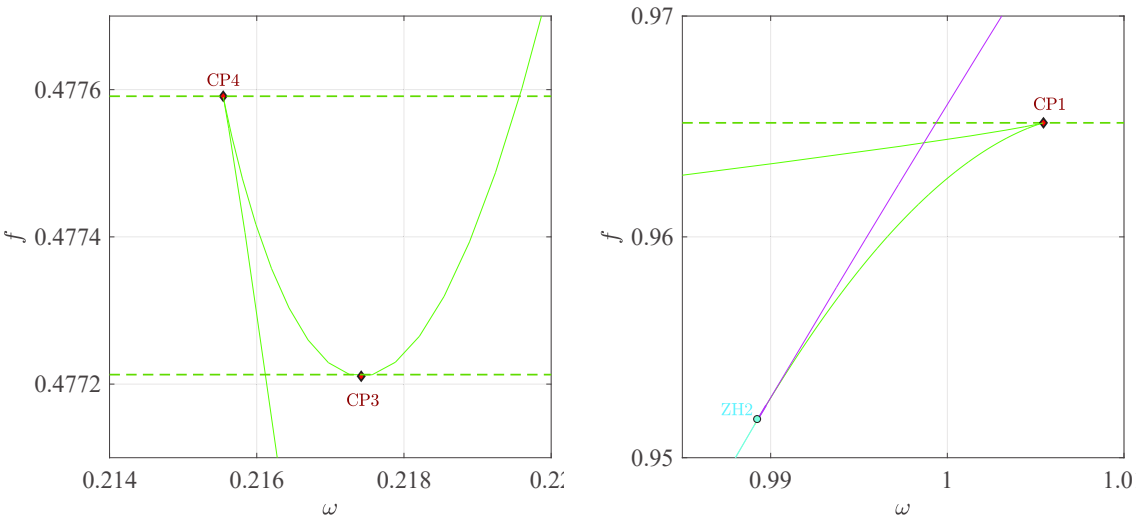

a) CP3 and CP4 b) CP1

Figure 2.19: Close-up view of cusp bifurcations for the Jeffcott rotor with $\mu = 0.125$.

Similarly, four cusp bifurcations have been detected by monitoring the sign of Δf and subsequently localized, as marked by red diamonds in Figs. 2.17 and 2.19, the latter showing more details around the outermost points. While these bifurcations are all characterized as local extrema of the LP curve, they have different interpretations in terms of the system's dynamics. As the magnitude of f is increased, the following phenomena are encountered:

- $f < f_{CP2}$: Absence of any LP. The system's response is strictly linear.
- $f = f_{CP2}$: The cusp is an isola centre.
- $f_{CP2} < f < f_{CP3}$: The center splits into two LPs which bound a closed response curve composed of a stable and an unstable branch. Solutions on the isola are high-amplitude and thus nonlinear, whereas the main response curve remains linear. Moreover, for $f > f_{ZH1}$, quasi-periodic solutions are born from NS bifurcations on the isola.
- $f = f_{CP3}$ Isola merging. The cusp point is a BP which connects the isola and the main response curve.

- $f_{CP3} < f < f_{CP4}$: The BP splits into two LPs, for a total of four. Each pair borders an unstable branch, the first one in the narrow region $\omega \in [\omega_{CP4}, \omega_{CP3}]$ and the second one in the wide bi-stability region for $\omega > \omega_{CP3}$.
- $f = f_{CP4}$: the low-amplitude unstable branch disappears as the two LPs which enclose it coalesce at the cusp.
- $f_{CP4} < f < f_{CP1}$: overall response amplitude increases. The two remaining LPs move closer together. For the narrow region between f_{ZH1} and f_{CP1}, both NS bifurcations are now accompanied by stability changes in the response curve.
- $f = f_{CP1}$: The two LPs meet at a cusp.
- $f > f_{CP1}$: Absence of LPs, and thus of amplitude jumps (for periodic solutions). With increasing f, the two NS bifurcations enclose a wider range of forcing frequencies and quasi-periodic motions become the norm.

Fig 2.2.5.1 shows once again the FRC at $f = 0.4 < f_{CP3}$, where both the low-amplitude linear response and the isola are visible. To compute the latter, the point with the lowest ω at the intersection of the LP curve and the horizontal line $f = 0.4$ on Fig 2.17 was used as a starting point for the continuation algorithm.

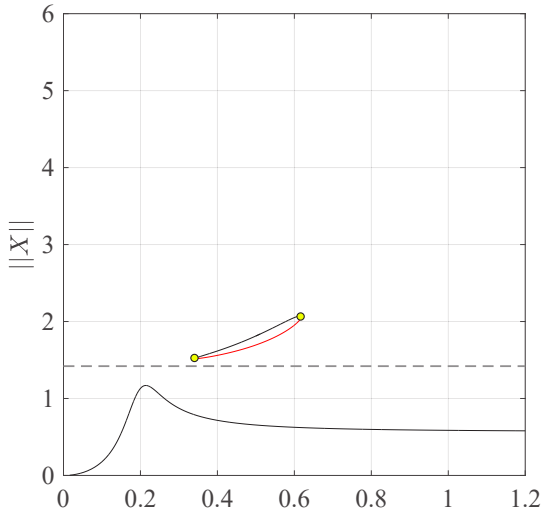

Figure 2.20: Forced response at $f = 0.4$, with isola.

Changes in response curve topology as f is increased from f_{CP3} to beyond f_{CP4} are shown Fig. 2.21. Also noticeable in these graphs are two NS bifurcations, out of which one belongs to the unstable branch of what was formerly the isola. This is to be expected, as $f > f_{ZH1}$. Interestingly, a visual inspection of Figs. 2.17 and 2.19 reveals that cusp points CP2 and CP3 -corresponding to the birth and merging of the isola, respectively- appear as parabolic extrema on the $w - f$ plane, whereas CP1 and CP4 -which mark the

disappearance of an unstable branch- are seen as sharp wedges. While this is purely an effect of the projection employed, it hints at the possibility of distinguishing between both cases through a well-defined criterion. Such a characterization of cusps, with its numerical implementation, is left as an open problem for future work.

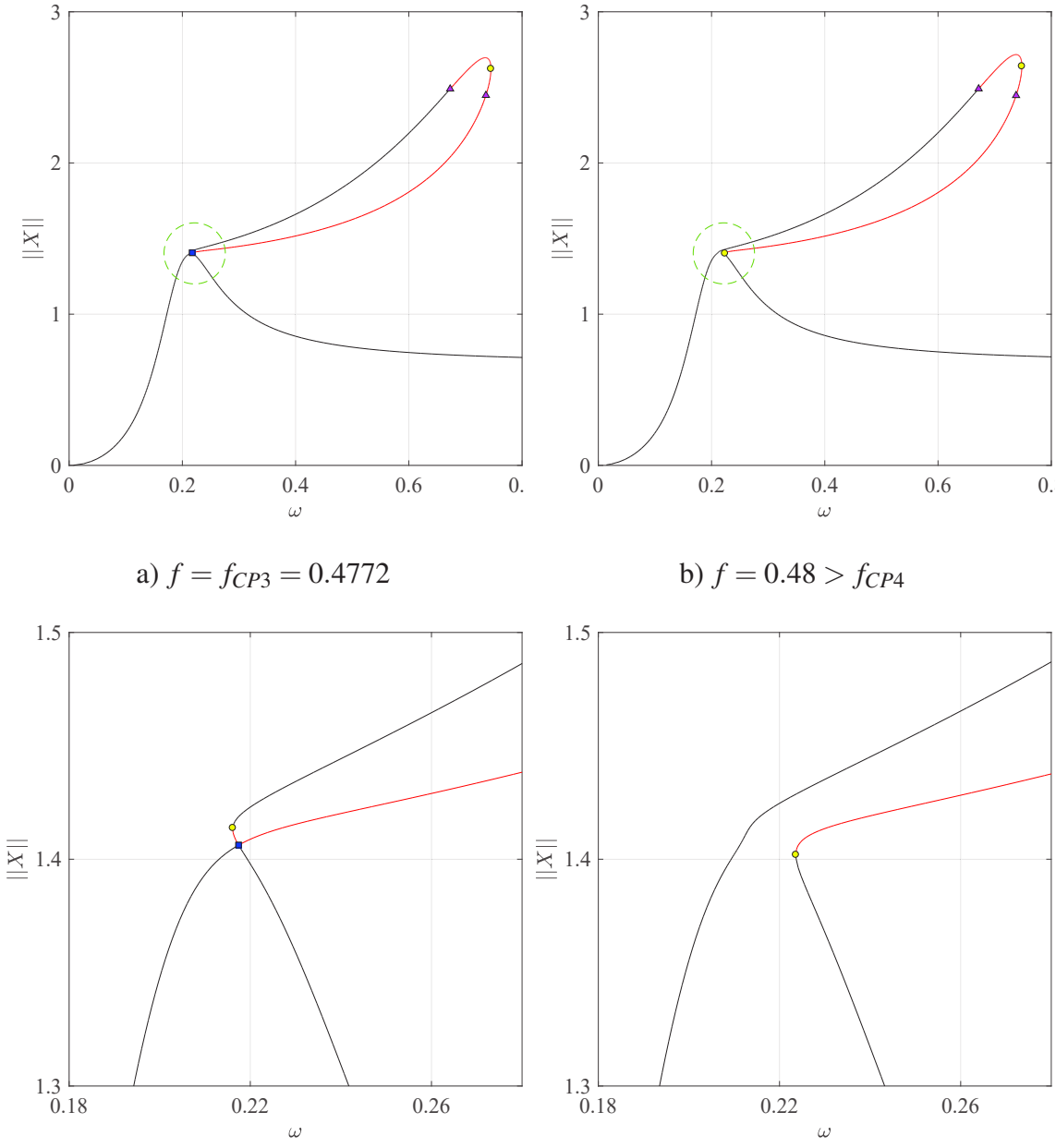

a) $f = f_{CP3} = 0.4772$ b) $f = 0.48 > f_{CP4}$

c) $f = f_{CP3}$, zoom d) $f = 0.48$, zoom

Figure 2.21: Evolution of response curve in the vicinity of cusp points CP3 and CP4.

2.2.5.2 Quasi-periodic solutions & Strong resonances of a Nonlinear Energy Sink (NES)

The dynamics of an essentially nonlinear element with mass e_{NES} attached to a main structure is described by Eq. (2.125):

$$\begin{bmatrix} 1 & 0 \\ 0 & e_{\text{NES}} \end{bmatrix} \begin{bmatrix} \ddot{x}_1 \\ \ddot{x}_2 \end{bmatrix} + \begin{bmatrix} c & -c \\ -c & c \end{bmatrix} \begin{bmatrix} \dot{x}_1 \\ \dot{x}_2 \end{bmatrix} + \begin{bmatrix} 1 & 0 \\ 0 & 0 \end{bmatrix} \begin{bmatrix} x_1 \\ x_2 \end{bmatrix} + k_{NL} \begin{bmatrix} (x_1 - x_2)^3 \\ (x_2 - x_1)^3 \end{bmatrix} = \begin{bmatrix} f\cos(\omega t) \\ 0 \end{bmatrix} \tag{2.125}$$

This configuration offers great potential in passive vibration control applications, as an irreversible energy transfer from the main system to the NES is efficient over a wide range of frequencies and without the need for tuning, as a consequence of the NES having no natural frequency. Here, parameter values are fixed at: $k_{\text{NL}} = 0.5, c = 0.04, e_{\text{NES}} = 0.1$. The forced response curve is computed with an initial forcing amplitude $f = 0.03$, yielding curves of Fig. 2.22. For all the results presented here, a five-harmonic approximation was used. Two NS bifurcations are found surrounding the linear resonance frequency, and the quasi-periodic FRC was computed as well by branching from the lowest-frequency NS. For illustration purposes, the coexisting (stable) quasi-periodic and (unstable) periodic regime are shown in Fig. 2.23 for $\omega = 1$.

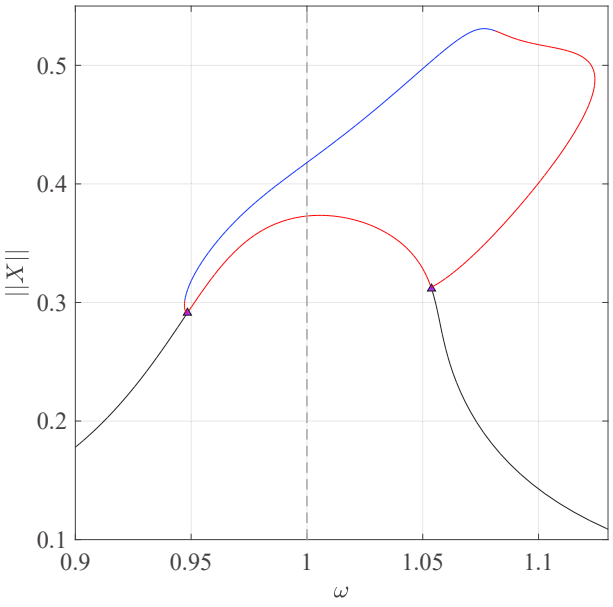

Figure 2.22: Frequency response for NES at $f = 0.03$. Black: stable periodic, blue: stable quasi-periodic, red: unstable.

Next, the forcing amplitude f was used as a tracking parameter within the interval $[0, 0.5]$. The result of this operation is shown in Fig. 2.24, superimposed to the previous FRC. The NS curve loses stability at a ZH point, which was then used as a starting point to track LP bifurcations. Moreover, two R4 and one R3 strong resonances were localized in this interval.

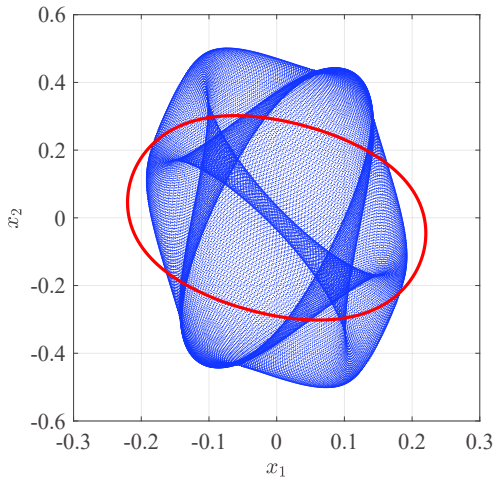

Figure 2.23: NES: coexisting regimes at $\omega = 1$.

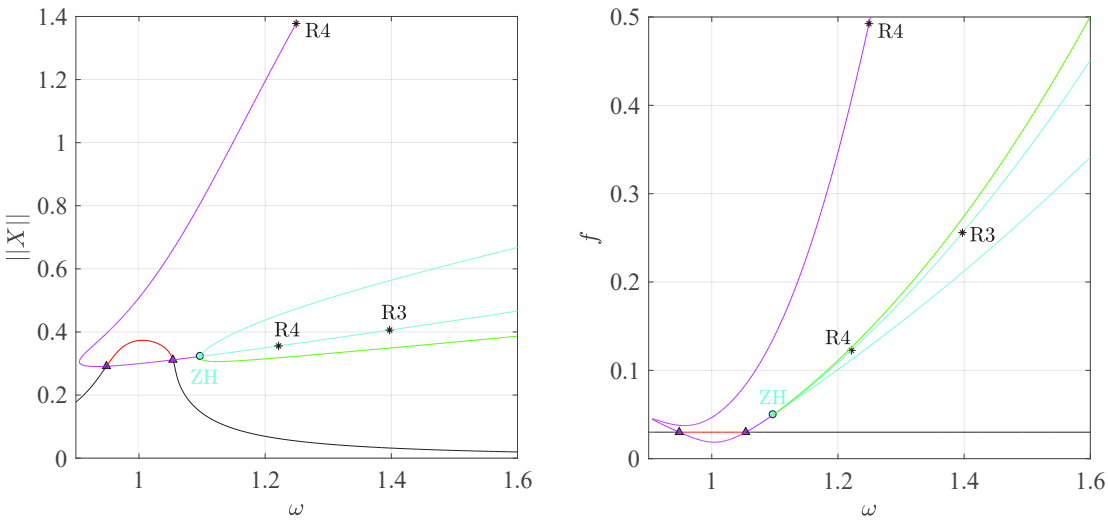

$\omega - ||\mathbf{X}||$ plane. $\omega - f$ plane.

Figure 2.24: NES: NS/LP tracking with respect to f. Magenta: NS curve, green: LP curve, cyan: 'unstable' bifurcations.

Using extended sub-harmonic bases, branches of $4T$ and $3T$-periodic solutions were computed starting from the respective bifurcations on the unstable NS curve: $(\omega, f) = (1.2213, 0.1226)$ for R4 and $(\omega, f) = (1.3973, 0.2559)$ for R3. Fig. 2.25 groups continuation results around each bifurcation and shows one example of converged cycle for each one. Black dots in the latter indicate values of x_1, x_2 sampled at the forcing period $T = 2\pi/\omega$. It can be noted that two distinct sub-harmonic branches emerge from the strong resonance points, and also that these curves are fully unstable.

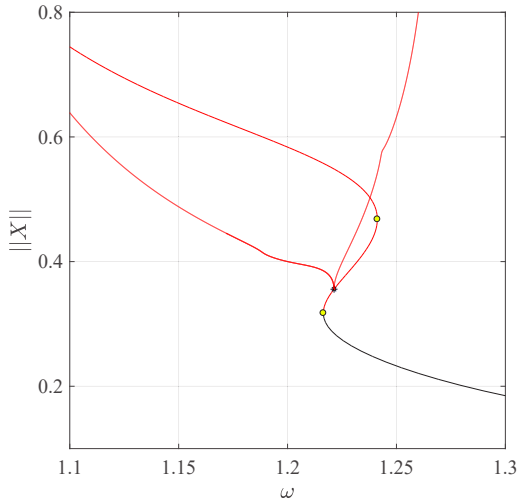

$4T$-periodic FRC, $f = 0.1226$.

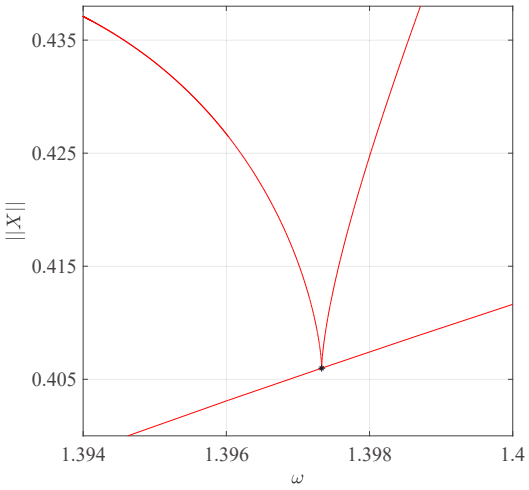

$3T$-periodic FRC, $f = 0.2559$.

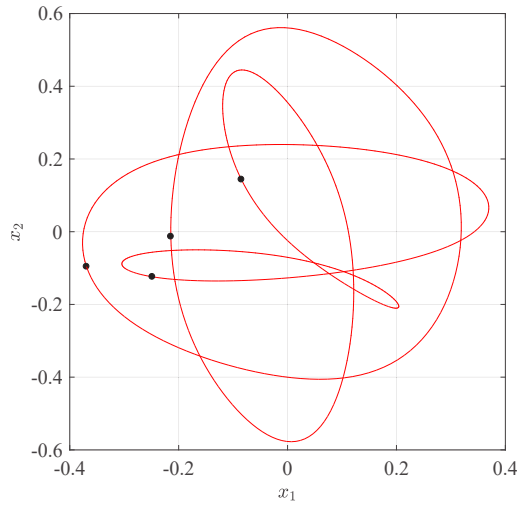

$4T$-periodic cycle, $\omega = 1.2375$.

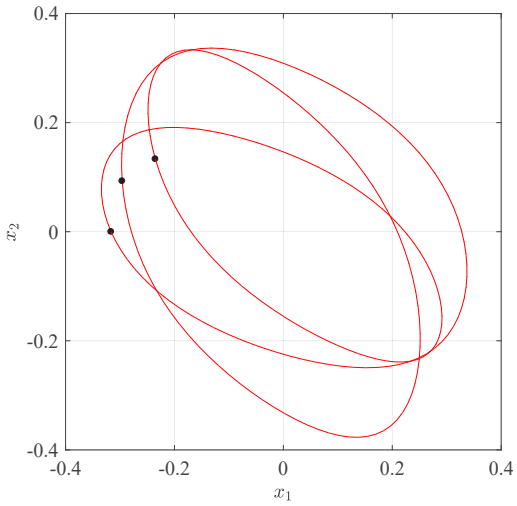

$3T$-periodic cycle, $\omega = 1.3982$.

Figure 2.25: NES: Sub-harmonic responses at strong resonances R4 and R3.

2.3 CAST3M Implementation

The methods described above have been implemented in the form of an operator, called **DYNC** (for DYNamic Continuation), in the most recent version of Cast3M. In this way, not only can systems of arbitrarily complicated geometries be studied, but one also benefits from the wide library of non-linear forces (*linkages*) which is already present in the software. As an illustration, Fig 2.26 shows the computational model of the steam-generator U-tube studied Chapter 3.

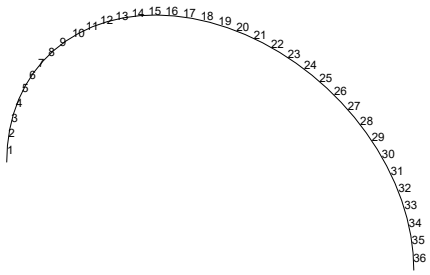

Line element model.

3D-element model.

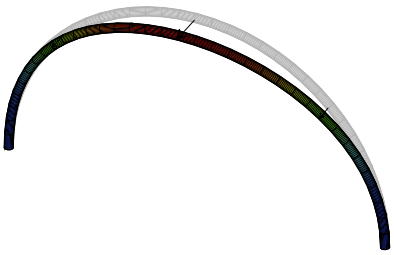

First out-of-plane bending mode.

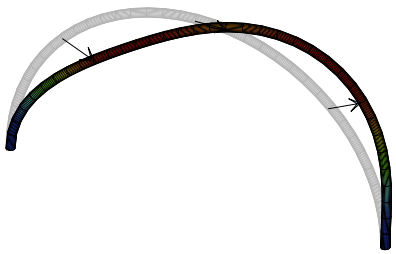

First in-plane bending mode.

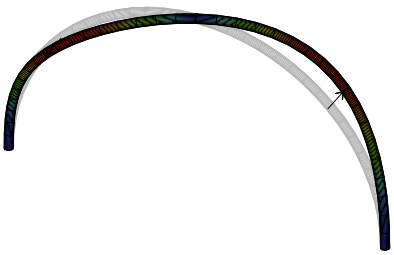

Second out-of-plane bending mode.

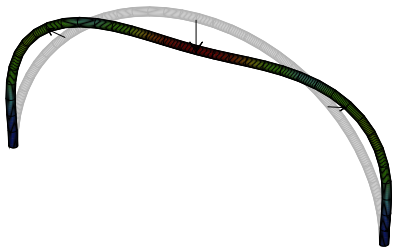

Second in-plane bending mode.

Figure 2.26: Cast3M model of upper U-tube region in stagnant fluid.

The modal basis shown is computed for the tube in with stagnant fluid with a non-uniform density distribution, so the added mass effect is directly incorporated into the system and leads to slightly asymmetrical out-of-plane modes. This complicated scenario is treated without difficulties in CAST3M. Continuation and bifurcation methods

can then be applied on the reduced, modal representation of the system with the inclusion of forcing terms and nonlinear forces.

Scope The objective is to find periodic solutions of the discrete equations of motion:

$$\mathbf{M}\ddot{\mathbf{q}}(t) + a\mathbf{C}\dot{\mathbf{q}}(t) + \mathbf{K}\mathbf{q}(t) = \mathbf{f}_{\mathrm{NL}}(\mathbf{q}(t), \dot{\mathbf{q}}(t)) + a\mathbf{f}_{\mathrm{e}}(t) \tag{2.126}$$

obtained by projecting a full finite-element model onto a basis consisting of the first n linear eigenmodes, and to study their parametric evolution through continuation methods and bifurcation analysis. Here, $\mathbf{q} \in \mathbb{R}^n$ is the vector of modal displacements, while the physical displacements $\mathbf{d}$ of any given point $\mathbf{p} = (x, y, z)$ on the structure are obtained by linear combination:

$$\mathbf{d}(\mathbf{p}, t) = \mathbf{\Phi}(\mathbf{p})\mathbf{q}(t) \tag{2.127}$$

with $\mathbf{\Phi}(\mathbf{p}) \in \mathbb{R}^{s \times n}$ a matrix containing the eigenvectors evaluated at $\mathbf{p}$. $\mathbf{M}$, $\mathbf{C}$ and $\mathbf{K}$ are, respectively, the (modal) mass, damping, and stiffness matrices, while the vectors $\mathbf{f}_{\mathrm{e}}$, $\mathbf{f}_{\mathrm{NL}}$ contain the modal contributions of applied external loads and nonlinear forces. Depending on whether the parameter a is nil or not, the computed solutions may correspond to the forced, autonomous, or free response curves. This is, in every aspect, analogous to the discussion of the present chapter, the only difference being the back-and-forth transformations required between modal and physical coordinates to compute contact forces.

Linkages

Nonlinear forces defined in terms of modal displacements and velocities are referred to as *base-A linkages* in Cast3M jargon. They are straightforwardly computed by AFT. On the other hand, nonlinear forces defined in terms of physical displacements and velocities are called *base-B linkages*, and their computation requires two additional steps. Firstly, the physical displacements at the N_c contact points must be computed through Eq. (2.127), thus yielding $\mathbf{d}_i = \mathbf{d}(\mathbf{p}_i, t), \forall i = 1, ..., N_c$, so that the forces in physical space, $\hat{\mathbf{f}}_{\mathrm{NL}}(\mathbf{d}_i, \dot{\mathbf{d}}_i)$, can be evaluated. Secondly, these forces must be projected to modal basis. Looping over all linkages, the total force vector is given by:

$$\begin{aligned} \mathbf{f}_{\mathrm{NL}}(\mathbf{q}, \dot{\mathbf{q}}) &= \sum_{i=1}^{N_c} \mathbf{\Phi}^T(\mathbf{p}_i) \left[\hat{\mathbf{f}}_{NL}(\mathbf{d}_i, \dot{\mathbf{d}}_i) \right] + \mathbf{f}^A_{\mathrm{NL}}(\mathbf{q}, \dot{\mathbf{q}}) \\ &= \mathbf{f}^B_{\mathrm{NL}}(\mathbf{q}, \dot{\mathbf{q}}) + \mathbf{f}^A_{\mathrm{NL}}(\mathbf{q}, \dot{\mathbf{q}}) \end{aligned} \tag{2.128}$$

where the second terms groups all base-A linkages. As the contact points are specified beforehand in most situations, the matrices $\mathbf{\Phi}(\mathbf{p}_i)$ are computed and stocked during the pre-processing stage. This makes the treatment of localized non-linearities extremely efficient.

Problem setup

In Cast3M, a structural dynamics problem is defined by writing a text file with *.dgibi* extension, containing a series of statements in the OOP-language GIBIANE[6]. This leads to the definition of several *Table* objects which can be read and exploites by operators. In our case, the call to DYNC has the syntax:

TAB1 = **DYNC** TMOD TCHR TLIA TAMOR TINI TNUM NHBM NFFT;

where NHBM and NFFT are two integers indicating, respectively, the desired number of harmonics and FFT samples, while the remaining inputs are the following Table objects:

1. TMOD: modal basis.
2. TCHR: external loadings (if forced response).
3. TLIA: linkages.
4. TAMOR: damping (if forced response).
5. TINI: approximation to the first solution (optional).
6. TNUM: setting for the numerical continuation, including: problem type, max./min. step-size, among others.

Remarks: The modal basis table TMOD is simply computed by a call to the Cast3M operator VIBR. A detailed description of all currently-supported linkages is included in the *Manual Pages* page of the website, under the tag DYNE[7]. The output table TAB1 consists of two sub-tables: the first one stocks the Fourier coefficients, frequencies, Floquet exponents, and stabilities at each continuation step, while the second one stocks the bifurcations found along the response curves.

Examples

This section briefly presents example calculations performed with DYNC. The *.dgibi* files corresponding to the test cases herein are available under the *Examples* page of the Cast3M website, and described succinctly in Tab. 2.1. A summary of the main parameters is as follows:

1. Duffing oscillator: NHBM $= 5$, NFFT $= 2^8$, $n = 1$, point mass, base-A linkage.
2. Jeffcot rotor: NHBM $= 7$, NFFT $= 2^8$, $n = 2$, point mass, base-B linkage.
3. Cantilever beam: NHBM =15, NFFT $= 2^{10}$, system modelled with 50 beam elements, base-B linkage. The case $n = 3$ is shown for NNM computation.

[6]Detailed explanations, tutorials and examples can be found on the Cast3M website. While most commands in the GIBIANE language use French words, documentation is available both in French and English.

[7]DYNE is the explicit time-integration operator in Cast3M, which uses the same library of nonlinear forces.

Note: The inherently non-smooth impact forces involved in the last examples have been replaced by a smooth approximation in order to enhance the performance of pseudo arc-length continuation. This is not strictly necessary if contact stiffness is moderate (which is not the case of the *dync03.dgibi* test case). The option to smooth contact forces is supported by the current version of the program.

*.dgibi	System	Cast3M Linkage	Force
dync01	Duffing oscillator	COUPLAGE_DEPLACEMENT	Geometric nonlinearity
dync02	Jeffcott rotor	POINT_CERCLE_FROTTEMENT	Frictional (annular) contact
dync03	Cantilever beam	POINT_PLAN	Bilateral elastic impacts

Tableau 2.1: Cast3M test cases.

Fig. 2.27 shows the superposition of the frequency-response and backbone curves for a single Duffing oscillator. The well-known bi-stability region characterized by an unstable branch delimited by two LPs is clearly visible. As the system is lightly damped, the resonant (highest-amplitude) response coincides with a cycle on the NNM curve.

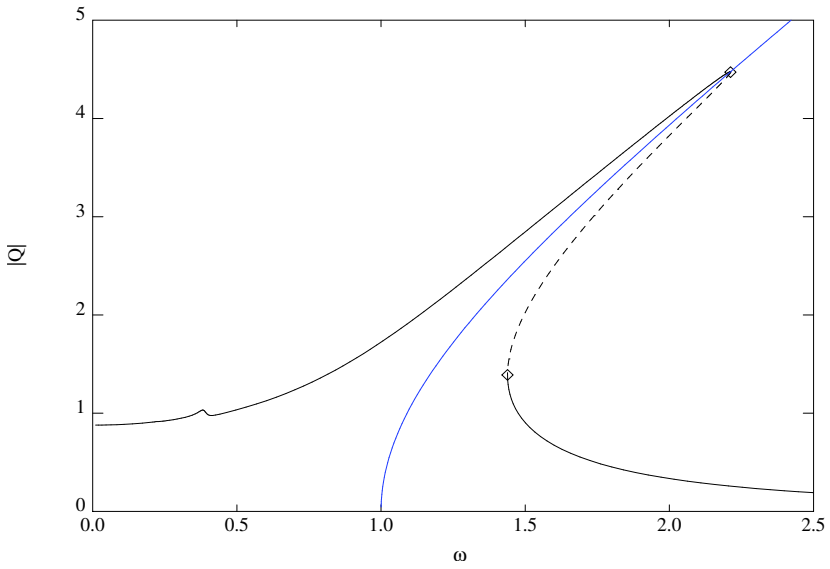

Figure 2.27: Duffing oscillator: frequency response (black) and backbone curve (blue). Notice the limit points (diamonds).

The frequency response of a Jeffcott rotor model, identical to the one presented in Sect 2.2.5, is shown in Fig. 2.28. As before, the presence of friction leads to de-synchronization and thus to the onset of quasi-periodic motions, as evidenced by a NS bifurcation. The LP on the unstable branch has also been computed.

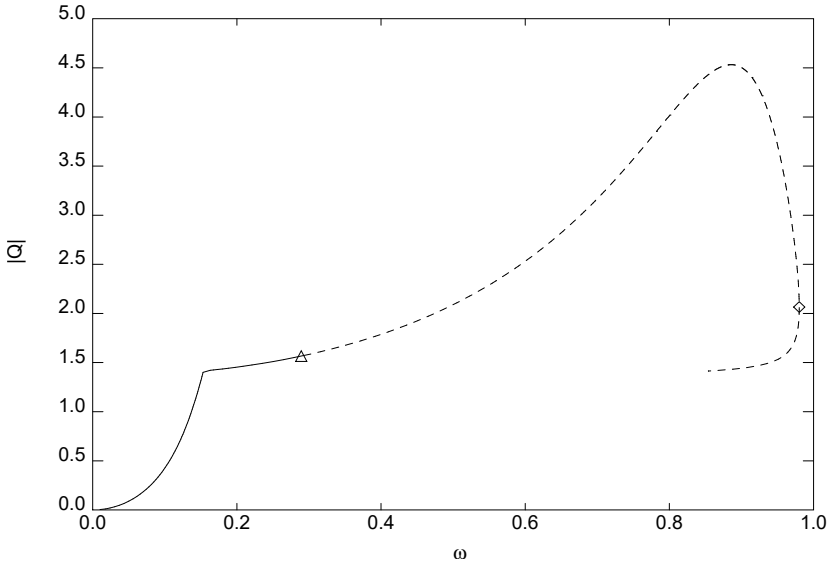

Figure 2.28: Jeffcott rotor: frequency response; notice the Neimark-Sacker (triangle) and limit point (diamond) bifurcations.

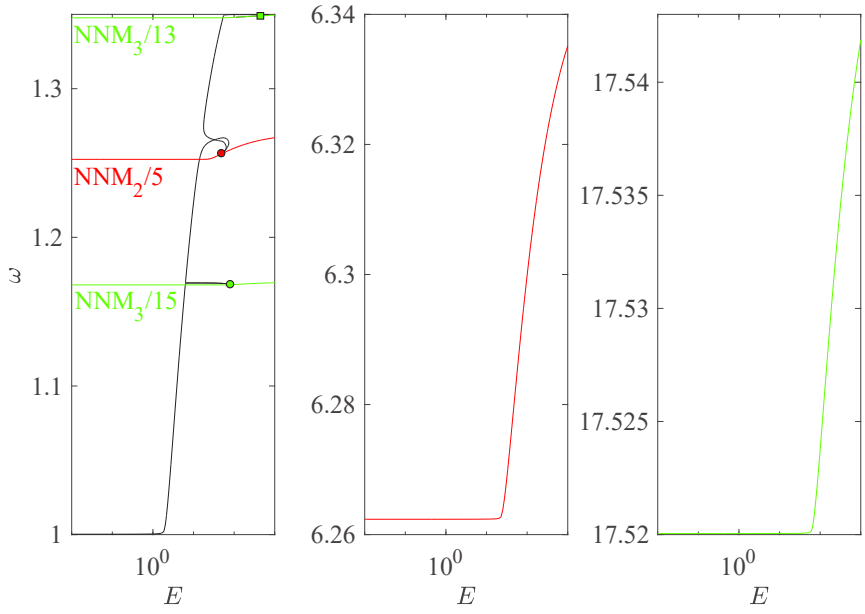

Figure 2.29: Frequency-energy plot of cantilever beam with bilateral elastic stops. Left to right: first NNM (internal resonances labelled by markers), second NNM, third NNM.

Fig. 2.29 shows the backbone curves for the first three NNMs of the cantilever beam with symmetrical stops. While the second and third modes have monotonous evolutions with increasing energy level, interaction tongues appear along the backbone curve of the first mode. This corresponds to modal interactions: due to nonlinear coupling, a higher

mode can become active when the frequency of the first one, or one of its harmonics, is close to its own. By plotting scaled version of the second and third NNMs in the same graph as the first mode, the curves are seen to intersect at specific points. Therein, an internal resonance occurs: there is exact coincidence between a harmonic of the first-mode frequency and that of the second or third modes. In the case of the present example, 1:15 and 1:13 resonances are found between the third and first modes, as well as a 1:5 resonance between second and first. This means that, around internal resonance frequencies, a response consisting of a combination of modes is obtained even if a mono-modal excitation is applied. It should be noted that resonances beyond 1:15 can not be observed with the present setup, as a 15-harmonic expansion is used.

2.4 Conclusion

In this chapter, several contributions to the numerical, frequency-domain analysis of nonlinear vibration problems are presented. The stability of quasi-periodic solutions, as well as a branch switching technique to follow them from a NS bifurcation, is introduced. A formulation for time-delay problems is also proposed for the case of discrete and continuous delays. For the latter, stability evaluation and bifurcations are addressed. The procedure to track bifurcations of all types and in arbitrary codimension is described. Finally, the implementation of these methods in the finite element software CAST3M -which allows for the treatment of complex structures- is reported. Numerous brief examples are provided for illustration purposes. In following chapters, these techniques and concepts are applied to study the phenomenology of steam-generator vibrations.

Chapter 3

Applications: Towards an understanding of steam-generator vibrations

This chapter presents the study of three simplified models which represent, in a broad sense, certain key aspects of steam-generator tube vibrations. Firstly, the tube's first bending mode is assimilated to a SDOF oscillator with bilateral contacts and cubic stiffness. It is shown how the symmetry (and loss thereof) of the system greatly impacts the resulting dynamics and leads to complex bifurcation scenarios, such as the period-doubling route to chaos and the formation of sub-harmonic isolas. As an intermediate approximation, a cantilever tube subjected to single-phase cross-flow is considered next. The quasi-unsteady model is used to compute fluidelastic forces in the frequency domain and the dynamics are explored by through continuation for an increasing number of modes. In particular, a pattern of super-harmonic resonances is observed for the higher modes, to which the linearly-unstable first one transfers energy via impacts. Finally, a more realistic system representing a U-tube vibrating in non-uniform flow is studied.

Contents

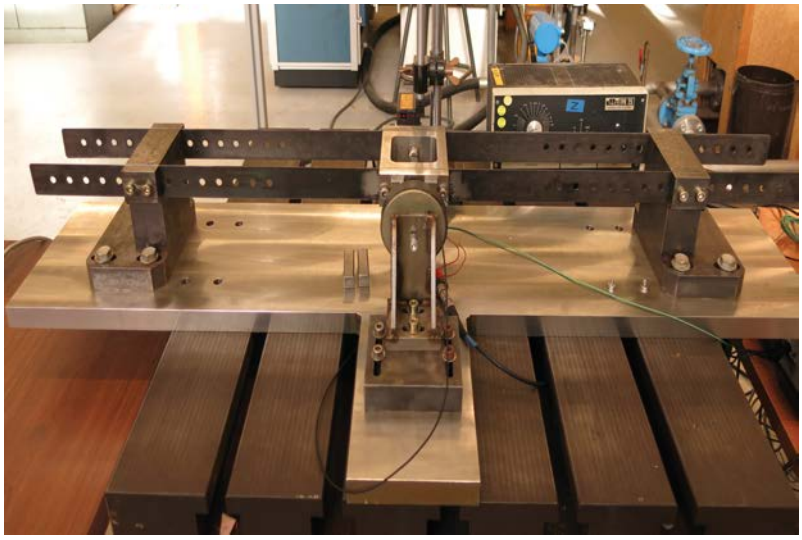

Figure 3.1: Experimental apparatus

3.1 The KOALA model

The techniques and concepts discussed previously are applied to an example system, shown in Fig. 3.1.
The apparatus in this photograph was first studied by de Langre et al. in [LAN 91]. It was conceived as a simple mechanism which exhibits chaos, with the purpose of validating time integration algorithms. In that paper, it was observed that both measured and calculated chaotic regimes had a rich sub-harmonic spectrum, i.e., frequencies below that of the external forcing, and thus a sub-harmonic cascade was suggested as the likely route to chaos. However, a detailed bifurcation analysis was deemed out of the scope of their study. This is, in turn, the objective of this section.

3.1.1 Modelling

Fig. 3.2(a) shows a schematic representation of our system. It consists of a heavy concrete block supported by two clamped, slender steel bars on its sides. A mono-harmonic external excitation $p(t) = p\cos(\omega t)$ is provided by a fixed electromagnet whose oscillating magnetic field drives a coil, attached to the main block, sinusoidally. In this configuration, the system is constrained to move in only one direction. Displacement amplitude, denoted by $x(t)$, is measured relative to the rest position of the block's centre of mass, which coincides with the location of a rigid stop. One elastic spring lies on each side of the stop, so that the mass undergoes intermittent contacts when the displacement amplitude is greater in magnitude than at least one of the gaps, which are adjustable and allowed to be asymmetrical: contacts happen for $x(t) > j_2$ or $x(t) < -j_1$. In this study, we limit ourselves to the clearance-type system, where both j_1 and j_2 are positive, as opposed to the pre-loaded type. The springs are chosen to have a stiffness K_c which is larger

than the stiffness k of the linear system's first bending mode. As explained in [LAN 96],

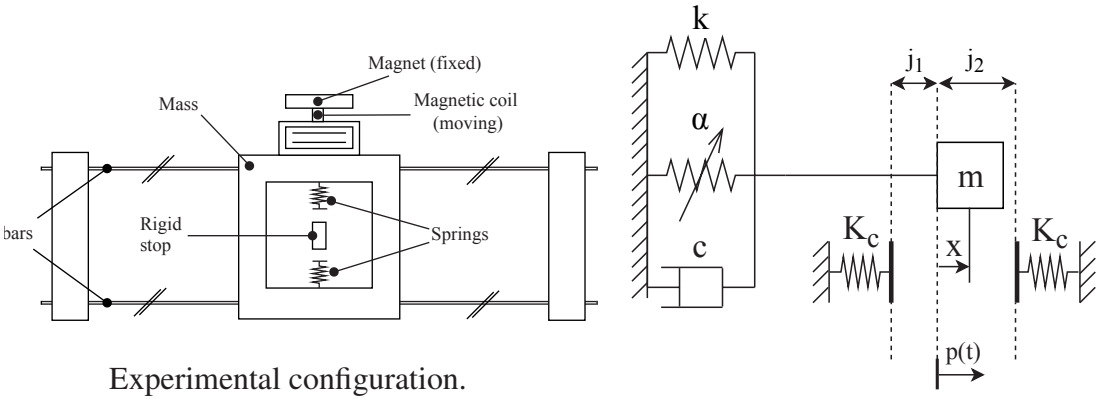

Experimental configuration.

SDOF model.

Figure 3.2: Idealized system

the geometrical and material parameters were carefully chosen so that the system's first natural frequencies were far apart on the spectrum. Indeed, for the first bending mode, $f_1 = 5$ Hz and $f_3 = 80$ Hz for the third mode, whereas the second one has no contribution on the motion of the mass. Thus, if the frequencies associated to both the external forcing and the contact stiffness are kept low enough we can consider the motion to be largely dominated by the first mode. The limited parameter ranges used later in this paper are chosen to verify this constraint. As a consequence, the system is modelled by a forced SDOF oscillator of the form:

$$m\ddot{x}(t) + c\dot{x}(t) + kx(t) + f_{\mathrm{NL}}(x) = p\cos(\omega t) \tag{3.1}$$

and depicted in Fig. 5 b).
Nonlinear terms, included in f_{NL}, come from two distinct effects:

1. During vibration, the clamped bars are bent perpendicularly to their length, which produces tension. The projection of this force onto the direction of motion gives rise to a cubic stiffness term $f_{\mathrm{NL,g}} = \alpha x^3$, where α is a constant depending on the geometry of the bars and their Young modulus.

2. A piecewise-linear stiffness induced by the clearances:
   $f_{\mathrm{NL,c}} = K_c\left[(x + j_1)H(x + j_1) + (x - j_2)H(x - j2)\right]$.
   $H(\cdot)$ represents the Heaviside step function.

Note that, in general, some amount of dissipation can be expected due to contact, which would require the inclusion of a piecewise-linear damping force in the model as was done in [NAT 92]. However, a combination of force measurements and free-oscillation tests revealed this effect to be negligible compared to modal damping, and thus it was omitted.

Before proceeding further, equation (3.1) is recast into non-dimensional form. Introducing the following dimensionless quantities:

$$\begin{array}{cccccc} x(t) = j_1\bar{x}(t), & \omega_0 = \sqrt{\frac{k}{m}}, & \tau = \omega_0 t, & c = 2\omega_0 m\zeta, & \omega = \bar{\omega}\omega_0, \\ p = kj_1\bar{p}, & j_2 = j_1\bar{j}, & \alpha = \bar{\alpha}\frac{k}{j_1^2}, & K_c = \bar{K}_c k & \end{array} \tag{3.2}$$

the equation of motion is written as:

$$\bar{x}''(\tau) + 2\zeta\bar{x}'(\tau) + \bar{x}(\tau) + \bar{\alpha}\bar{x}^3(\tau) + \bar{F}_c(\bar{x}(\tau)) = \bar{p}\cos(\bar{\omega}\tau) \tag{3.3}$$

where $(\cdot)'$ represents derivation with respect to τ and the restoring force from the clearances is:

$$\bar{F}_c(\bar{x}(\tau)) = \bar{K}_c\left[(\bar{x}(\tau)+1)H(\bar{x}(\tau)+1) + (\bar{x}(\tau)-\bar{j})H(\bar{x}(\tau)-\bar{j})\right] \tag{3.4}$$

The choice of using j_1 rather than j_2 as a reference length is arbitrary and would not change the results if reversed. It is, however, convenient to introduce the ratio of clearances $\bar{j}$ as a parameter, since this provides a way to quantify the symmetry of the system. As shown next, this symmetry factor has a defining influence on the system's bifurcation behaviour.
As a final preliminary step before analysis, we replace the non-smooth contact force (3.4) by a regularized approximation. This is not strictly necessary for the HBM-based continuation to succeed, as the AFT technique is perfectly capable to converge in such cases. However, for stiff springs, convergence issues were found for bifurcation localization. To get rid of this inconvenience, the following smooth definition is used instead:

$$\bar{F}_{c,r}(\bar{x}(\tau)) = \bar{K}_c\left[\bar{x}(\tau) + \frac{1}{\pi}\left(f^- - f^+ + \frac{1}{2\sigma}f^L + a_c\right)\right] \tag{3.5}$$

where:

$$f^+ = (\bar{x}(\tau)+1)\tan^{-1}(\sigma(\bar{x}(\tau)+1))$$

$$f^- = (\bar{x}(\tau)-\bar{j})\tan^{-1}(\sigma(\bar{x}(\tau)-\bar{j}))$$

$$f^L = \log\left[\frac{1+(\sigma(\bar{x}(\tau)+1))^2}{1+(\sigma(\bar{x}(\tau)-\bar{j}))^2}\right]$$

$$a_c = \left[\tan^{-1}(\sigma) - \bar{j}\tan^{-1}(-\sigma\bar{j}) - \frac{1}{2\sigma}\log\left(\frac{1+\sigma^2}{1+(\sigma\bar{j})^2}\right)\right]$$

The function $\bar{F}_{c,r}$ from (3.5) tends to the non-smooth contact force as $\sigma \to \infty$. In the case of the results presented hereafter, $\sigma = 3\cdot 10^3$ was fixed. The choice of this value was made after numerical tests, which showed that further increasing σ beyond this point had a negligible effect on the position of bifurcations.

3.1.2 Numerical results

3.1.2.1 Period-doubling cascades

The values of parameters used in this study are summarized in Table 3.1. Based on the simple error estimation technique proposed by Ferri [FER 09], it was found through numerical tests that choosing H=15 was enough to guarantee that higher harmonics had a negligible effect on even the most nonlinear responses for the present system, which correspond to the strongly forced, asymmetric configuration. For the sake of simplicity, the same number of harmonics (H=15) was used for all tested cases, with $N_s = 2^8$ sampling points used for the AFT algorithm. It should be stressed that using such a high number of harmonics is not needed for frequency intervals away from resonances, where the response amplitudes (and thus the magnitudes of nonlinear forces) are small. However, this does not substantially increase computation times for a SDOF system.

Tableau 3.1: Koala: Parameter values for Sect. 3.1.2.1.

ζ	$\bar{\alpha}$	$\bar{\omega}$	$\bar{p}$	$\bar{K}_c$	$\bar{j}$
0.03	0.16	[1.3 ; 4.0]	[0.0 ; 2.0]	[0.0 ; 6.0]	[0.0 ; 1.0]

Following [LAN 96], the main focus is on the post-resonant ($\bar{\omega} > 1$) behaviour of the system as a function of the forcing frequency.

Frequency-response curves

The contact stiffness is initially set to $\bar{K}_c = 4.7$. Figure 3.3 shows two frequency response curves, corresponding to perfect symmetry ($\bar{j} = 1$) and "maximum" asymmetry ($\bar{j} = 0$), for a weak forcing case: $\bar{p} = 0.55$. The results are quite different: while they have comparable peak amplitudes and both show a bi-stable zone between two LP bifurcations, the locations of these points differ. More importantly, an additional unstable region appears in the asymmetric case for excitation frequencies beyond twice the natural frequency. Two period doubling bifurcations, which are absent in the symmetric case, border this region, where the system enters a sub-harmonic vibration regime. This new branch has also been computed using the branching algorithm of Sect. 2.2.4, and it can be observed that it contains no bifurcations at this forcing level. The same qualitative behaviour as the main resonance is displayed, with a bi-stable zone generated by a hardening effect.

Now we consider the case of a strong forcing: $\bar{p} = 1.7$. As the symmetric case showed no qualitative changes with respect to the former case, it is not presented here. On the other hand, as seen in figure 3.4, the sub-harmonic branch of the system with asymmetric gaps contains two additional PD bifurcations. Between them, the 2T-periodic solutions are unstable, giving rise to 4T-periodic motions.

The cycles corresponding to the points labelled **A** and **B** in Fig. 3.4 (respectively before and after the lowest-frequency PD bifurcation) are shown in phase space in Fig. 3.5. The latter can be seen to contain an additional loop when compared to the former.

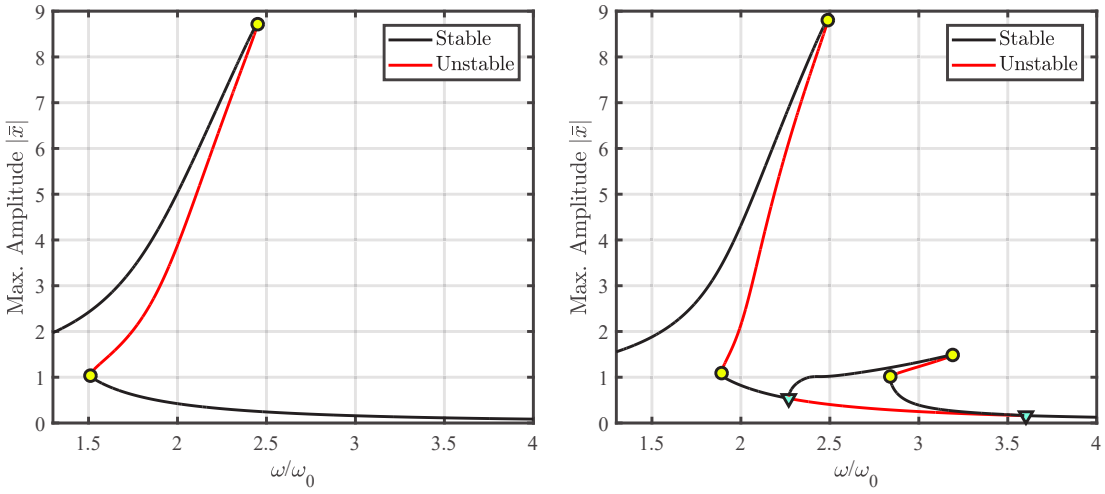

Symmetric case ($\bar{j} = 1$) Asymmetric case ($\bar{j} = 0$)

Figure 3.3: Frequency-response curves, weak forcing.(○: Limit Point; ▽: Period-Doubling bifurcation point)

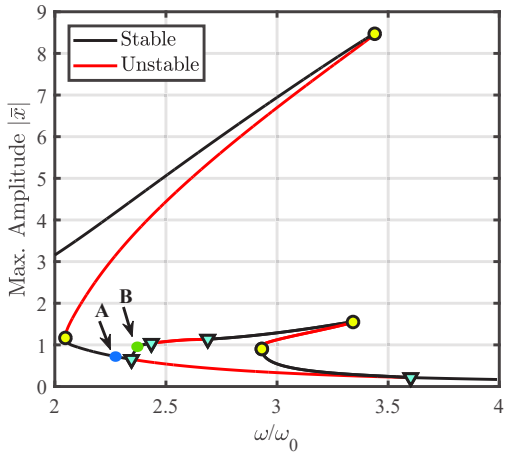

Figure 3.4: Successive PD bifurcations in the asymmetric configuration, strong forcing.

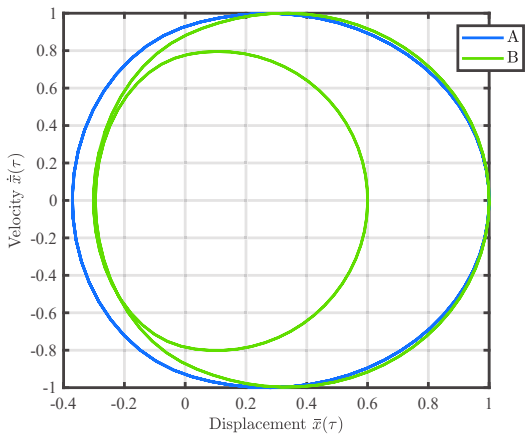

Figure 3.5: Phase space plots of cycles **A** and **B** from Fig. 3.4.

Thus, in the span of one forcing period, the whole of cycle **A** is described, whereas only half of **B** is. This provides visual evidence of a double-period response. The evolution of Floquet exponents as a function of forcing frequency can be seen in Figs. 3.7 and 3.7 when a T-periodic or 2T-periodic Fourier basis is used by the HBM, respectively. On the region between two PD bifurcations, the former has a pair of complex conjugate eigenvalues with magnitude $\omega/2$, while the corresponding exponents in the latter are purely real, thus characterizing a symmetry-breaking BP.

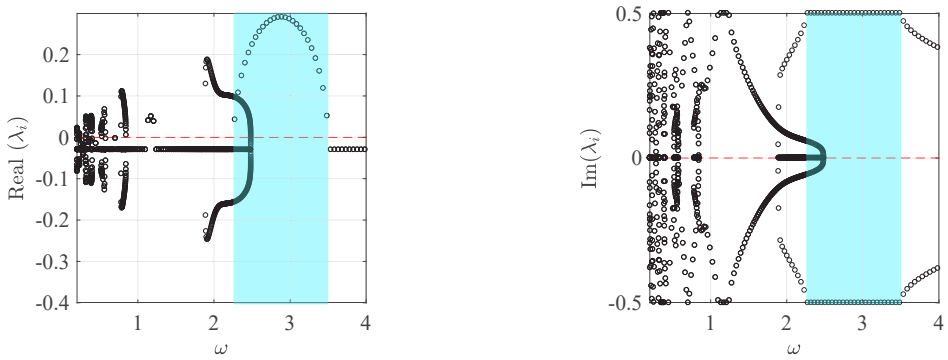

a) Real part. b) Imaginary part.

Figure 3.6: Floquet exponents near period-doubling bifurcations: T-periodic basis.

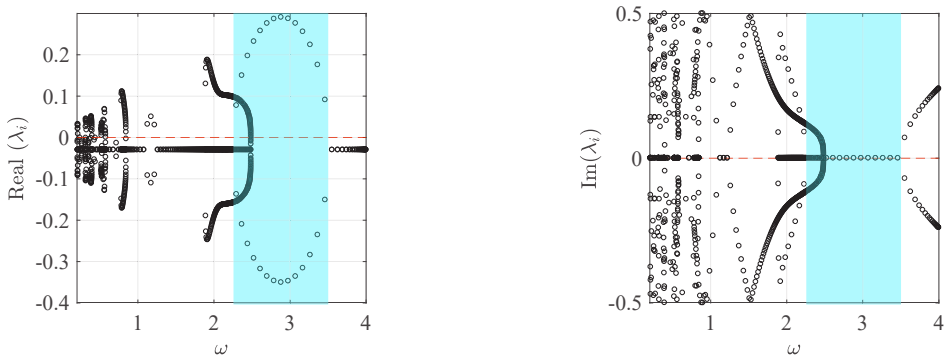

a) Real part. b) Imaginary part.

Figure 3.7: Floquet exponents near period-doubling bifurcations: 2T-periodic basis.

Forcing amplitude

The PD bifurcations presented above for $(\bar{j} = 0)$ were tracked with respect to the forcing amplitude $\bar{p}$. The resulting curves, as well as their projection on the codimension-2 plane $(\bar{\omega}, \bar{p})$, are presented in Fig. 3.8. For visualization purposes, response curves at different values of $\bar{p}$ are included as well.

It can be seen that the first pair of PD points happens independently of the forcing amplitude over the considered range, thus implying that this phenomenon is not driven by external forcing. On the contrary, the stability boundary corresponding to the second stage of the cascade, labelled "4T+" (solutions whose period is at least 4T), only exists for high forcing amplitudes.

Contact stiffness

While varying the contact stiffness in a continuous fashion is evidently infeasible in

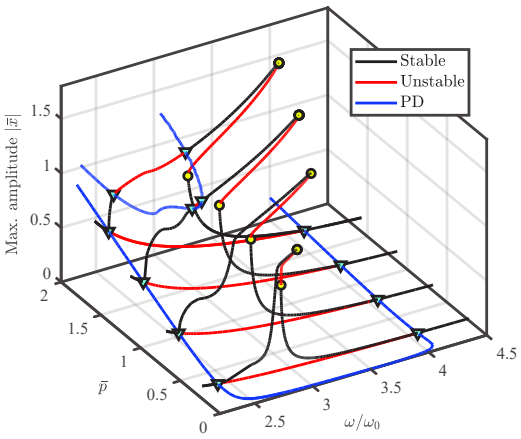

PD bifurcation tracking.

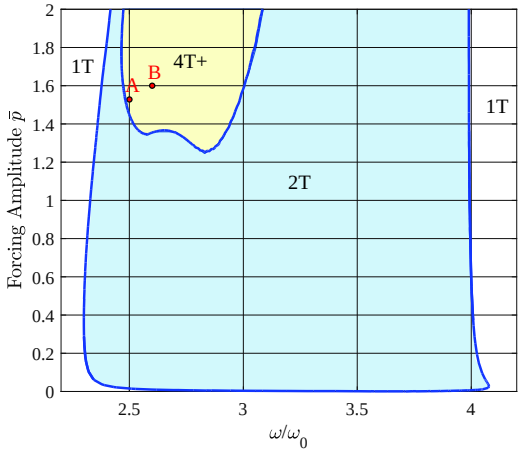

Period doubling boundaries on $(\bar{\omega}, \bar{p})$ plane. Labels indicate the periodicity of solutions in each zone.

Figure 3.8: Forcing amplitude as tracking parameter.

practice, this can be done with ease by continuation methods. The four PD bifurcations from Fig. 3.4 were tracked with respect to the contact stiffness $\bar{K}_c$, as shown in Fig. 3.9, with forcing amplitude $\bar{p} = 1.7$.

From these curves, it is easily seen that the first period doubling is quite sensitive to contact stiffness, in contrast with the case of forcing amplitude, since the location of bifurcation points changes significantly as this parameter is varied. Nonetheless, consider the local extremum close to null contact stiffness. From physical grounds, a value of zero simply indicates an absence of springs, and the system reduces to a typical, symmetrical Duffing oscillator in such a case. It is seen here that the boundary folds back shortly before reaching the ω-axis, but we can state that period doubling occurs over practically the whole interval of contact stiffness values, and so this parameter is also not the main trigger for bifurcation in this case.

Chaos

So far, we have confirmed the well-understood fact that high inputs of energy by external forcing, as well as increasingly stiff contacts, have a tendency to promote bifurcation. Successive sub-harmonic branching such as the one observed here hints to the presence of a sequence of PD bifurcations leading to chaos. It is, of course, not possible to use harmonic balance to compute chaotic regimes, since these are aperiodic by definition. Nonetheless, the search for parameter regions associated with chaos can be limited to those in the neighborhood of high-period boundaries. An example of this can be seen in Fig. 3.10. Here, the values $(\bar{p}, \bar{K}_c) = (1.6, 4.2)$ were fixed and a constant-acceleration Newmark scheme was used to numerically integrate the equation of motion over a range of frequency excitation values. A Poincaré map was then established by sampling the response signal (amplitudes and velocities) at intervals equal to the excitation period.

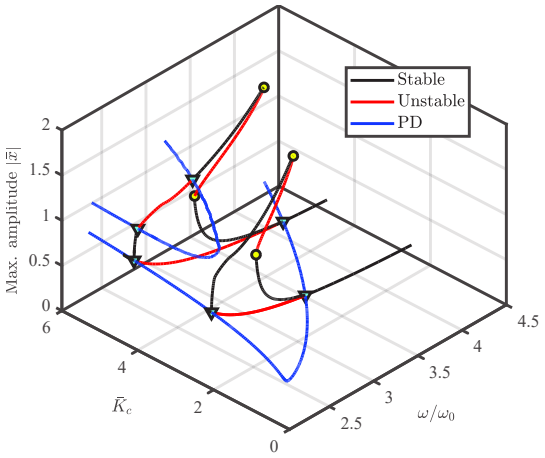

PD bifurcation tracking.

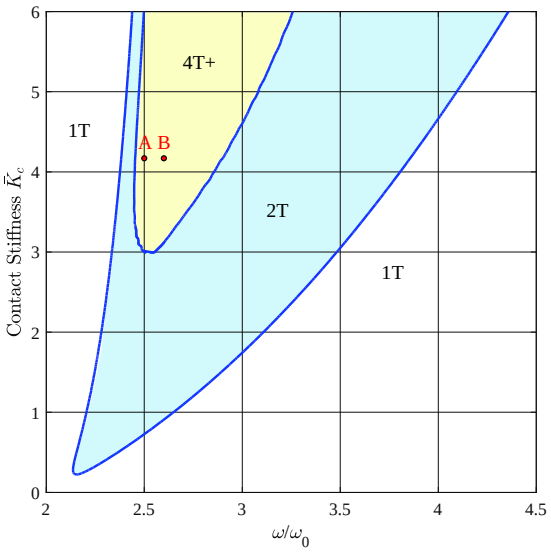

Period doubling boundaries on $(\bar{\omega}, \bar{K}_c)$ plane. Labels indicate the periodicity of solutions in each zone.

Figure 3.9: Contact stiffness as tracking parameter.

Integration was carried out over 1000 periods to ensure that the steady state had been reached, and the amplitudes of the last 100 samples are plotted as a function of frequency.

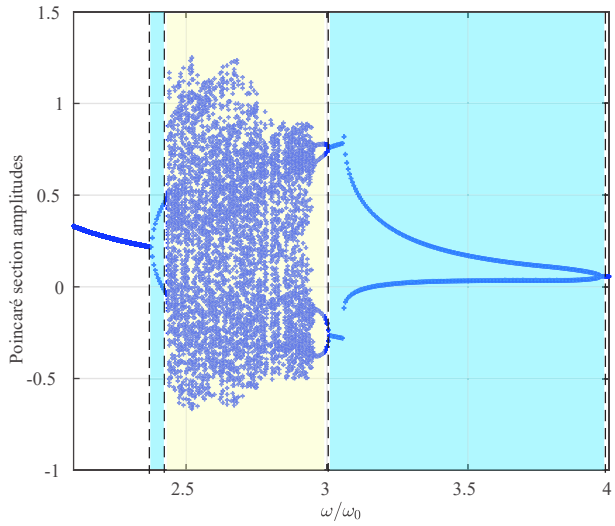

Figure 3.10: Bifurcation diagram. Blue and yellow zones correspond to predicted 2T and 4T-periodic regimes, respectively.

The results observed in this figure match the predictions from Figs. 3.8 and 3.9 in terms of bifurcation behaviour. Moreover, regions of erratic responses can be found within

the predicted 4T+ frequency interval. It can be noted that, while 4T-periodic responses are clearly visible, the transition to chaos is rather abrupt, and thus additional steps in the period-doubling cascade (8T, 16T...) can only be observed over extremely narrow ranges of forcing frequency.

Fig. 3.11 shows the region of predicted and experimentally observed chaos for the same system from de Langre & Lebreton's paper [LAN 96], with respect to forcing amplitude. It can be seen that the main boundary is both quantitatively and qualitatively similar to the 4T+ boundary of Fig. 3.8 (b), which once again suggests a rapid transition once the period doubling sequence is triggered. Furthermore, this highlights the usefulness of bifurcation tracking as a predictive tool, as it yields results close to those obtained with the more computationally intensive method employed in the cited paper.

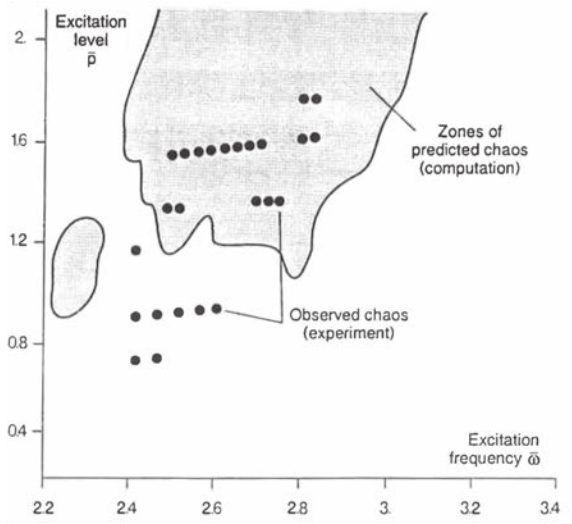

Figure 3.11: Region of predicted chaos, from [LAN 96].

The point labelled **A** in Figs. 3.8 and 3.9, for which a fractal attractor was reported in [LAN 96], is included in this zone as well. Other points inside this boundary also exhibit aperiodic motion, an example of which is seen in Fig. 3.12. These results were obtained by fixing parameter values to those of point **B**: $(\bar{\omega}, \bar{p}, \bar{K}_c) = (2.6, 1.6, 4.2)$.

The pattern formed on the Poincaré section of Fig. 3.12 (b) strongly suggests a chaotic nature, as the orbit is confined to a specific region in phase space (implying the presence of an attractor) and no periodicity is evident. To verify that this response is indeed chaotic, its leading Lyapunov exponent, λ_L, was computed. As explained e.g. in [STR 94], a positive value of this quantity indicates that two initially close trajectories diverge exponentially fast, which is a signature of chaos. Thus, letting $\delta(\tau)$ represent the instantaneous distance between these in phase space, we may write:

$$\delta(\tau) \simeq \delta(0) e^{\lambda_L \tau} \tag{3.6}$$

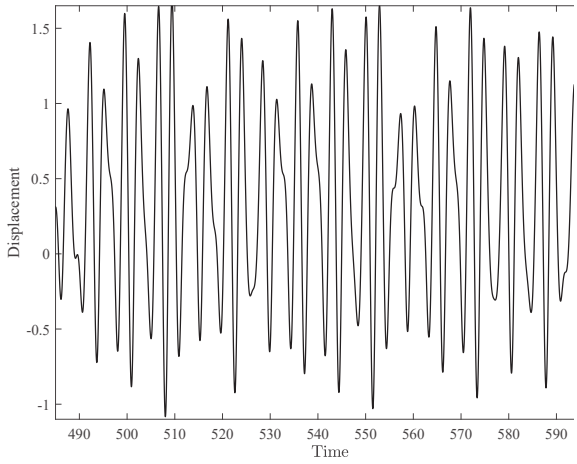

Time series over 50 excitation periods.

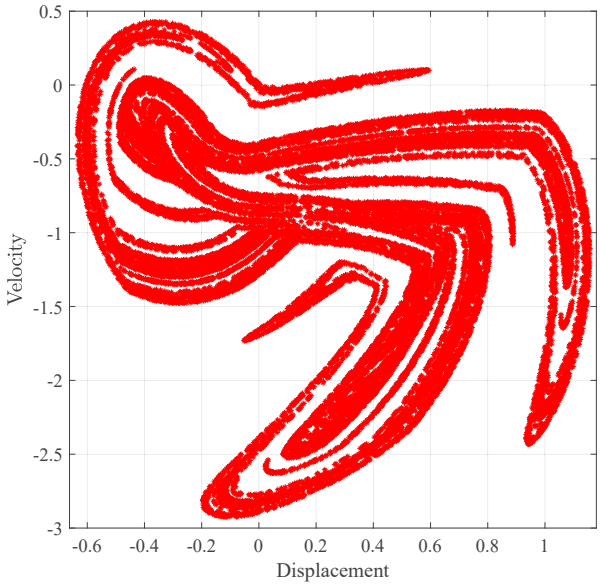

Poincaré section with 5000 samples.

Figure 3.12: Response at point **B** in Figs. 3.8 and 3.9.

Fig. 3.13 shows the time history of $\delta(\tau)$ as obtained from two response signals: the first one, corresponding to Fig. 3.12, was computed for null initial conditions (position and velocity equal to 0), whereas a perturbation of magnitude 10^{-14} was added to initial position for the second one. Sensitivity to initial conditions is clearly evidenced by the exponential growth of the distance with time at a rate approximately equal to $\lambda_L = 0.1918$. On the other hand, the distance can be seen to saturate, since the trajectories pertain to an attractor of fixed length and thus cannot separate indefinitely.

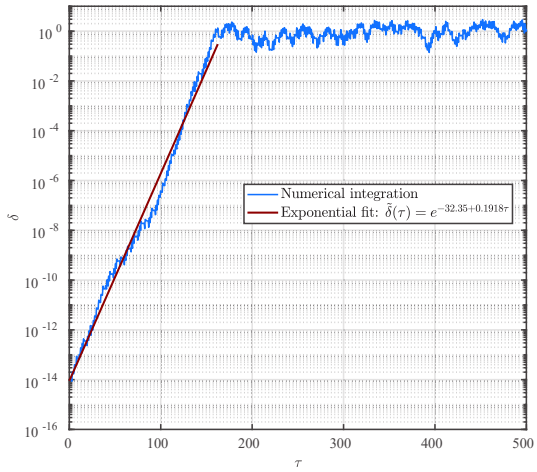

Figure 3.13: Distance between two signals with close initial conditions.

3.1.2.2 Sub-harmonic isolas

Previous studies of this system focused on the two extreme cases $\bar{j} = 1$ and $\bar{j} = 0$. There are two reasons for this: firstly, from an experimental perspective, they are the simplest configurations to implement. Fine-tuning the value of $\bar{j}$ in practice is quite a delicate task, and extreme values are thus more convenient. Secondly, from a phenomenological point of view, it is well-known fact that asymmetry has the tendency to promote bifurcation. Hence, if the objective is solely to observe chaotic motions, it is the "most asymmetric" configuration which offers the optimal conditions. Yet, as observed in the Sect. 3.1.2.1, even the first period doubling of the cascade is absent in the symmetric case, and so no chaos at post-harmonic excitation frequencies may be observed by this route. Therefore, asymmetry is a necessary condition for period doubling. It should be noted that, generally speaking, initially symmetric systems can have their symmetry broken through a regular BP and then undergo period doubling along the asymmetric branches. However, for the parameter intervals considered in this study, this behaviour was not observed. An interesting question which immediately arises is then: how asymmetric must the clearances be in order for period doubling to be possible?

Tableau 3.2: Koala: Parameter values for Sect. 3.1.2.2.

ζ	$\bar{\alpha}$	$\bar{p}$	$\bar{K}_c$
0.15	0.03	0.55	2.48

The following results use the parameter values in Table 3.2, which correspond to the characteristics of the current experimental setup of the Koala test bench at CEA. Figure 3.14 shows PD bifurcation tracking with respect to the symmetry factor, starting from $\bar{j} = 0$, while Fig. 3.15 shows a projection of this curve on the parameter plane $(\bar{\omega}, \bar{j})$.

It is clear that $\bar{j}$ has a very strong influence on period doubling, since the first stability boundary is only defined over a limited range of values: the bifurcation curve has a single local extremum $(\bar{\omega}, \bar{j}) = (\bar{\omega}_{\text{det}}, \bar{j}_{\text{det}})$, whose concavity is opposite to those observed while tracking PD bifurcations with respect to other parameters. At this point, two PD bifurcations coalesce, but the associated sub-harmonic resonance peak does not disappear: rather, it forms a closed loop which is tangent to the main branch. A further increase in $\bar{j}$, towards symmetry, causes the loop to detach and form an isola. Of course, one can also see the situation in the reverse way: as the system strays further away from symmetry, an isola approaches the main branch until merging at a codim-2 local extremum of the PD stability boundary, i.e. a Generalized Period Doubling (GPD) bifurcation (shown as a red diamond), which was precisely localized by using an extended system constructed as per Sect. 2.2.3.

Theoretically, as shown by de Witte et al. [WIT 13], a curve of double-period LPs can be expected to emerge from the GPD point. Thus, the LP tracking algorithm was launched with this bifurcation as a starting point, This LP tracking shows that, for any $\bar{j}$ larger than the critical value $\bar{j}_{\text{det}}$, the sub-harmonic branch detaches and continues to exist

as an isola over a certain range of $\bar{j}$. The existance of LPs on the isolas allows the use of bifurcation tracking, which in turn reveals the presence a codim-2 local extremum at $\bar{j} = \bar{j}_{\max}$ where the two branches coalesce and the isola collapses into a point corresponding to a sub-harmonic isola centre. At this state, the system is "critically symmetric", so that

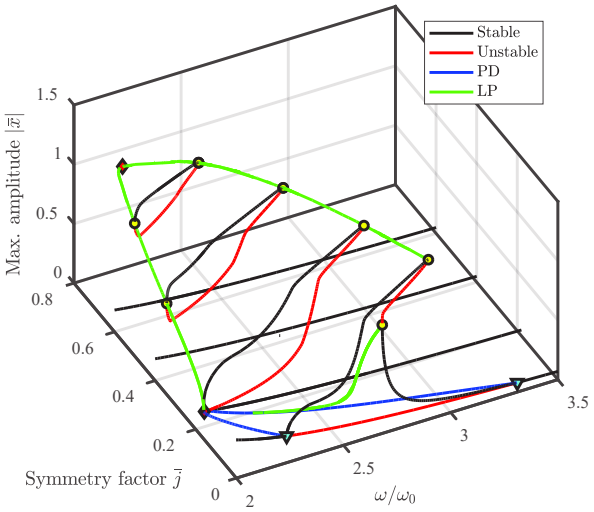

Figure 3.14: Symmetry factor as tracking parameter.

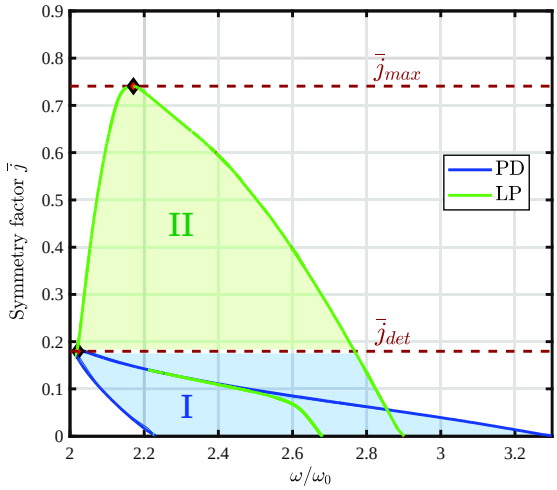

Figure 3.15: Tracking of limit points from an isola merging point. Region I (blue): 2T-periodic solutions. Region II (green): 2T-isolas.

the contribution of the asymmetric harmonics from the nonlinear forces is just important enough to induce bifurcation. For $\bar{j} > \bar{j}_{\max}$, the isola no longer exists.

3.1.2.3 Global dynamics

Isolated sub-harmonic resonances have been shown to exist for system (3.3) for certain parameter combinations and over determined ranges of excitation frequency. Moreover, since they contain a stable branch, they can theoretically be reached by choosing appropriate initial conditions or by adding a perturbation to a stable solution on the main branch. However, in practice, the basin of attraction associated to the isola can be small compared to that of the T-periodic solution, in which case it would be difficult to observe them experimentally. To assess the robustness of the isolas, we have numerically computed basins of attraction for fixed $(\bar{\omega}, \bar{j})$ pairs within their predicted range of existence, i.e. for $\bar{j} \in [\bar{j}_{\text{det}}, \bar{j}_{\text{max}}]$ as shown in Fig. 3.15. For (non-dimensional) initial conditions $[x_0, \dot{x}_0] \in [-2,2] \times [-2,2]$, the equation of motion (3.3) was integrated over several excitation periods until a steady state was established. Using the absolute norm:

$$x_{max} = \|\bar{x}(\tau)\| = \max_{\tau=0,\ldots,2\pi} \{|\bar{x}(\tau)|\} \tag{3.7}$$

contour plots $x_{max} = f(x_0, \dot{x}_0)$ were constructed. Fig. 3.16 shows the results obtained for $(\bar{\omega}, \bar{j}) = (2.09, 0.5)$.

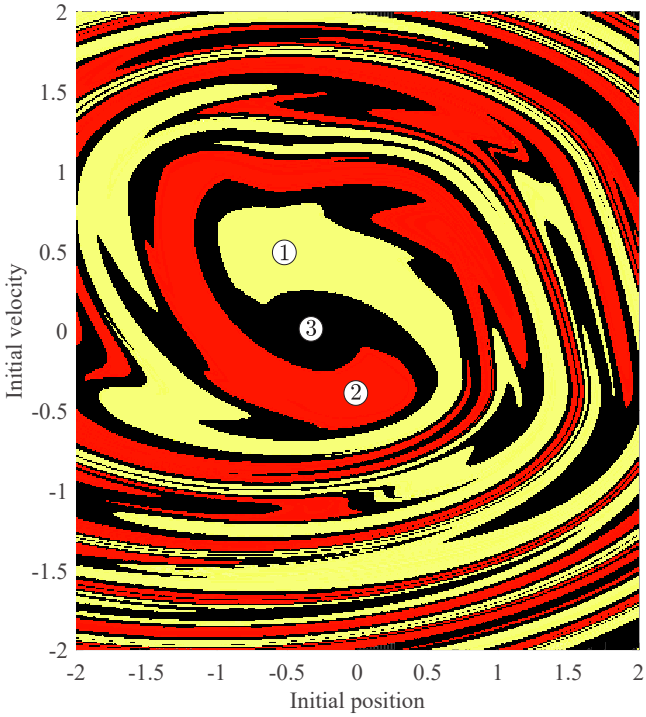

Figure 3.16: Basins of attraction, showing coexistence of three regimes for $\omega/\omega_0 = 2.09$

Three basins are clearly visible, two of which correspond to the low and high-amplitude regimes in the bi-stable zone of the main resonance as in a typical Duffing-like oscillator. The remaining basin is associated with the sub-harmonic regime on the isola,

as illustrated by Fig. 3.17. No attractor seems to be particularly dominant, i.e., for random initial conditions, the chances of finding any one of this regimes are roughly equally likely, which means that these isolas must be robust, thus observable. For completeness, Fig. 3.18 shows the harmonic content of the three numerically calculated solutions. As expected, the low-amplitude (non-resonant and non-impacting) regime is mono-harmonic, the isolated one is predominantly sub-harmonic and the large-amplitude, nonlinear resonant response shows slight harmonic distortion as well as a static component due to asymmetry.

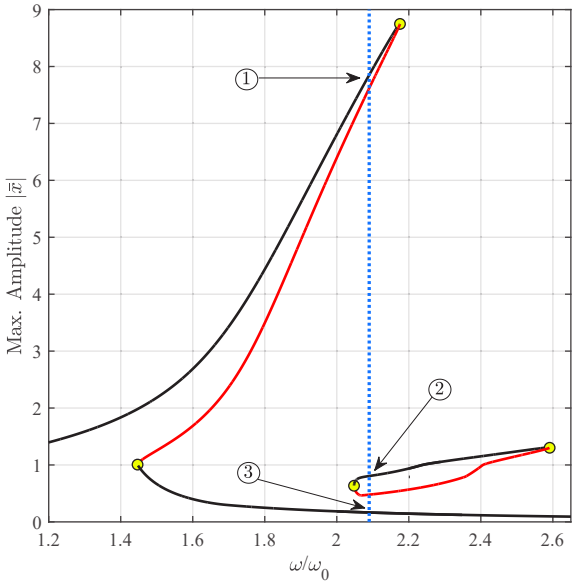

Figure 3.17: Frequency-response curve for $\bar{f} = 0.5$

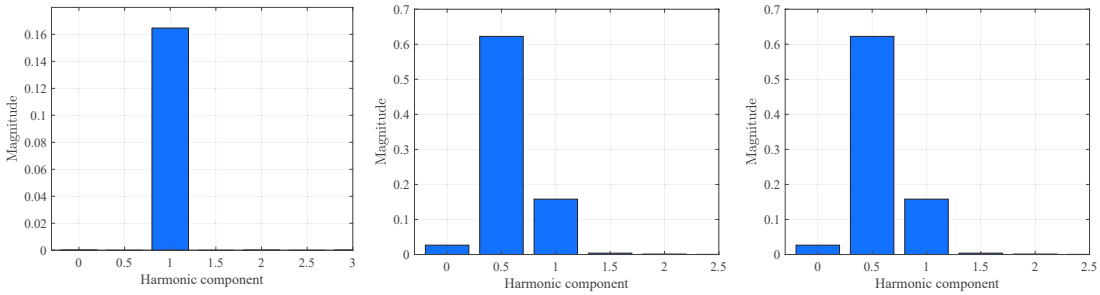

a) Low amplitude, T-periodic.

b) Isolated response, 2T-periodic.

c) Large amplitude, T-periodic.

Figure 3.18: Frequency content for $\omega/\omega_0 = 2.09$.

3.2 A mathematical model for fluid-elastically unstable tubes

3.2.1 Generalities

It is currently recognized that tube arrays in cross-flow undergo instabilities by two distinct mechanisms: stiffness-controlled instability results from the coupled motions of two or more adjacent tubes and leads to buckling, while damping-controlled instability is a consequence of an excess input of energy from the incoming flow, resulting in negative net damping and thus flutter through a Hopf bifurcation at a critical flow velocity. The latter can occur for even a single flexible tube in an otherwise rigid array, as would be the case if the clearance at any one support became abnormally wide as a result of, for instance, misalignment or wear. The focus of this chapter will be on damping-controlled fluid-elastic instability, in particular by employing the *quasi-unsteady* (QU) model of Granger and Païdoussis [GRA 96] to compute the resulting forces exerted on the structure, as described in this section.

The tubes considered satisfy the hypotheses of Euler-Bernoulli beam theory, and thus can be aptly modelled by using 1D beam elements, constituting a n-point mesh $\mathfrak{D} \subset \mathbb{R}^3$. Given boundary conditions, the flow-induced, out-of plane[1] vibrations at any point $\mathbf{x} \in \mathfrak{D}$ -denoted by the vector $\mathbf{Y}(\mathbf{x},t) \in \mathbb{R}^n$- satisfy the dynamical equilibrium statement:

$$\mathbf{M}_s\ddot{\mathbf{Y}} + \mathbf{C}_s\dot{\mathbf{Y}} + \mathbf{K}_s\mathbf{Y} + \mathbf{F}_f + \mathbf{F}_t + \mathbf{F}_c = \mathbf{0} \tag{3.8}$$

where the different force terms correspond to:

- $\mathbf{F}_f(\mathbf{x},t)$: damping-controlled fluid-elastic coupling.
- $\mathbf{F}_t(\mathbf{x},t)$: excitation by broadband turbulence.
- $\mathbf{F}_c(\mathbf{x},t)$: reaction at contact points.

The latter contains the modal projections of impact forces at all n_c contact points along the tube's span, which are computed by a regularized form of Eq. (1.9) given in dimensionless form by:

$$f_c(y) = \frac{1}{2}\left[K_c(y-1) + \sqrt{(K_c(y-1)+C_c\dot{y})^2 + 4K_c\eta}\right. \\ \left. + K_c(y+1) + \sqrt{(K_c(y+1)+C_c\dot{y})^2 + 4K_c\eta} + 2C_c\dot{y}\right] \tag{3.9}$$

where η is an adjustable regularization parameter.
The term $\mathbf{F}_t$ is random by nature, and thus warrants the impossibility of (periodic or otherwise) steady-state vibratory regimes. In what follows, it will be neglected under the

[1] Only this type of motion is considered here for simplicity, as the generalization to arbitrary, three-dimensional motions is straightforward.

assumption that *fluctuations from turbulent fields introduce perturbations on the limit cycles of the system, without altering its underlying dynamics*. This means that, for fixed parameter values, the number and nature of coexisting attractors is unchanged by turbulence. While this idea is intuitively reasonable, it is not backed by solid theoretical arguments and must be, in practice, verified *a posteriori* for a particular configuration. Indeed, no claim is made here on the universal validity of such an assumption, which is itself an open problem and is considered out of scope for the present work. Finally, the QU model gives the following expression for the fluid-elastic forces on the structure:

$$\mathbf{F}_f(\mathbf{x},t) = \frac{1}{2}\rho_f V D \left(C_D \dot{\mathbf{Y}} - \frac{V^2}{D^2}\frac{\partial C_L}{\partial \bar{Y}}(\bar{g} * \mathbf{Y}) \right) \tag{3.10}$$

The first term in Eq. (3.10) represents added damping, whereas the second introduces a memory effect through convolution with the kernel function:

$$\bar{g}(\tau) = \sum_{k=1,2} \alpha_k \delta_k e^{-\delta_k \frac{V_M}{D}\tau} \hat{H}(\tau) + \frac{D}{V}\alpha_0 \hat{\delta}(\tau) \tag{3.11}$$

with $\alpha_0 = 1 - (\alpha_1 + \alpha_2)$, and where $\hat{H}(\tau)$ and $\hat{\delta}$ are, respectively, the Heaviside step function and the Dirac distribution. These effectively hardwire causality into the model, as they ensure that any event prior to the onset of motion at $t = 0$ has no contribution to the tube's dynamics. The second term in Eq. (3.11) leads to an instantaneous restoring force which is linear in $\mathbf{q}(t)$ but dependent on the square of flow velocity, thus making it akin to lift. It shall be noted that array geometries with a positive lift coefficient slope[2] may lead to static divergence for fast flows. As explained in [PAI 13], this condition is not met for industrial cylinder arrays and is actually in conflict with the appearance of dynamic instabilities. As for the remaining parameters appearing in Eqs. (3.10) and (3.11), D is the tube diameter, C_D is the drag coefficient, $V(\mathbf{x})$ and $\rho_f(\mathbf{x})$ are the velocity and density distributions of the flow, respectively, V_M is the maximum velocity, and $(\alpha_1, \alpha_2, \delta_1, \delta_2)$ are empirical constants. More precisely, convolution of displacements with the first term of Eq. (3.11) physically corresponds to the re-organisation of the flow field through convection and diffusion of vorticity layers following every change in tube velocity, a process which lags behind the tube motion and is associated to the time scales:

$$T_k = \frac{D}{V_M \delta_k} \tag{3.12}$$

In the QU model, the whole time history of motion is considered in the computation of instantaneous forces, thus leading to a distributed delay within the mathematical framework of Sect. 2.2.1.2. Any number of terms can be included in the kernel function, but a two-term sum as presented above has been successfully used to gain insight into the phenomenology of steam-generator vibrations through both experimental and numerical investigations [BOR 17a, PIT 18, PIT 12]. For the examples presented in later sections of

[2] I.e., $\frac{\partial C_L}{\partial \bar{Y}} > 0$.

this chapter, the empirical data measured by Piteau et al. in [PIT 19] for a rotated-square grid in a water flow was used to fit the alpha and delta coefficients, leading to the values reported in Table 3.3. As already seen from the two-term case presented here, the value of δ_k increases dramatically with k, which translates the fact that each increasing order resolves events decaying at faster rates. Higher-order terms decay too fast to have a measurable impact if their corresponding time-scales, from Eq. (3.12), are small when compared to the natural period of the structure's first oscillation mode.

	$k=1$	$k=2$
α_k	1.2581	-2.2583
δ_k	0.2209	32.1219

Tableau 3.3: Empirical coefficients for the QU model with two-term memory.

3.2.2 Model reduction

Eq. (3.10) is readily expanded to yield the following expression:

$$\mathbf{F}_f(\mathbf{x},t) = \frac{1}{2}\rho_f V D C_D \dot{\mathbf{Y}} - \frac{1}{2}\rho_f V^2 \frac{\partial C_L}{\partial \bar{Y}}\alpha_0 \mathbf{Y} - \frac{1}{2}\frac{V^3}{D}\frac{\partial C_L}{\partial \bar{Y}}\sum_{k=1,2}\alpha_k\delta_k \int_0^t e^{-\delta_k \frac{V_M}{D}\tau}\mathbf{Y}(\mathbf{x},t-\tau)d\tau \tag{3.13}$$

As all terms in Eq.(3.13) are linear in $\mathbf{Y}$, it is clear that fluid-elastic forces are uncoupled upon projection of the governing equations, Eq. (3.8), onto an orthonormal basis. Thus, consider the modal decomposition:

$$\mathbf{Y}(\mathbf{x},t) = \mathbf{\Phi}(\mathbf{x})\mathbf{q}(t) \tag{3.14}$$

where $\mathbf{\Phi}(\mathbf{x}) = [\phi_1 ... \phi_m] \in \mathbb{R}^{n\times m}$ is the matrix of normalized eigenvectors solutions of: $\left[\mathbf{K}_s - \omega_i^2 \mathbf{M}_s\right]\phi_i = \mathbf{0}$. Before proceeding further, let us re-write the density and velocity distributions as:

$$\rho_f(\mathbf{x}) = \bar{\rho} r(\mathbf{x}) \qquad \bar{\rho} = \frac{1}{L}\int_0^L \rho_f(\mathbf{x})d\mathbf{x} \tag{3.15}$$

$$V(\mathbf{x}) = V_M \nu(\mathbf{x}) \qquad V_M = \max_{\mathbf{x}}\left(|V(\mathbf{x})|\right) \tag{3.16}$$

where L is the total length of the tube span exposed to cross-flow. The modal projection of fluid-elastic forces is thus:

$$\mathbf{f}_f(t) = \mathbf{C}_f\dot{\mathbf{q}} + \mathbf{K}_f\mathbf{q} + \sum_{i=1,2}\mathbf{L}_i(\hat{g}_i * \mathbf{q}) \tag{3.17}$$

with the coefficient matrices given by:

$$\mathbf{C}_f = \frac{1}{2}\bar{\rho}V_M D C_D \mathbf{L}_C \quad = \quad \frac{1}{2}\bar{\rho}V_M D C_D \left[\frac{1}{L}\int_0^L r(\mathbf{x})\nu(\mathbf{x})\boldsymbol{\Phi}^T(\mathbf{x})\boldsymbol{\Phi}(\mathbf{x})d\mathbf{x}\right] \tag{3.18}$$

$$\mathbf{K}_f = -\frac{1}{2}\bar{\rho}V_M^2\frac{\partial C_L}{\partial \bar{Y}}\alpha_0 \mathbf{L}_K \quad = \quad -\frac{1}{2}\bar{\rho}V_M^2\frac{\partial C_L}{\partial \bar{Y}}\alpha_0 \left[\frac{1}{L}\int_0^L r(\mathbf{x})\nu^2(\mathbf{x})\boldsymbol{\Phi}^T(\mathbf{x})\boldsymbol{\Phi}(\mathbf{x})d\mathbf{x}\right] \tag{3.19}$$

$$\mathbf{L}_i = -\frac{1}{2}\bar{\rho}\frac{V_M^3}{D}\frac{\partial C_L}{\partial \bar{Y}}\alpha_i\delta_i\hat{\mathbf{L}}_i = -\frac{1}{2}\bar{\rho}\frac{V_M^3}{D}\frac{\partial C_L}{\partial \bar{Y}}\alpha_i\delta_i \left[\frac{1}{L}\int_0^L r(\mathbf{x})\nu^3(\mathbf{x})\boldsymbol{\Phi}^T(\mathbf{x})\boldsymbol{\Phi}(\mathbf{x})d\mathbf{x}\right] \tag{3.20}$$

Eqs. (3.18-(3.20)) take into account arbitrary distributions of fluid density and velocity along the tube. Regardless of the former, it is clear that matrices $\mathbf{L}_C$, $\mathbf{L}_K$ and $\hat{\mathbf{L}}_i, i = 1,2$ will all be equal in uniform flow, i.e. $\nu(\mathbf{x}) = 1$. This very idealized scenario is explored in Sect. 3.3, while a more realistic distribution is considered in Sect. 3.4. Moreover, the above expressions imply that, even if all the mode shapes kept in the m-mode approximation are symmetric, this symmetry can be broken by virtue of unsymmetrical velocity and-or density distributions. As has been shown so far in the present text, this leads to disjoint response curves and thus requires special attention during parametric analyses. The full equations of motion in the truncated modal basis read:

$$\mathbf{M}\ddot{\mathbf{q}} + \mathbf{C}\dot{\mathbf{q}} + \mathbf{K}\mathbf{q} + \left[\mathbf{C}_f\dot{\mathbf{q}} + \mathbf{K}_f\mathbf{q} + \sum_{k=1,2}\mathbf{L}_k\left(\hat{g}_k * \mathbf{q}\right) + \mathbf{f}_c(\mathbf{q},\dot{\mathbf{q}})\right] = \mathbf{0} \tag{3.21}$$

where the brackets group all the terms additional to the dynamics of the damped linear structure. It is clear that the quantities $||\mathbf{q}(t)||$, ω (the as-yet unknown limit cycle frequency) and V_M are of dissimilar orders of magnitude; indeed, the first of these is about the size of the smallest gap (typically a fraction of a millimetre), the second can be expected to be of the order of the tube's first natural frequency ($\sim 10^2$ rad/s), and the latter -which will take the role of the main continuation parameter- is between 1 and 7 m/s. Thus, to facilitate continuation, the following non-dimensional displacements and time are introduced: $\mathbf{q}(t) = \bar{\mathbf{q}}(t)h_{\min}$, $t = \bar{t}/\omega_1$, where the latter makes use of the first-mode natural frequency. This leads to all quantities of interest being of the same order. Moving forward, it shall be noted that the original notations $\mathbf{q}(t)$ and t will, nevertheless, be kept in order to simplify the presentation. Likewise, we let $V \equiv V_M$.

3.2.3 Hopf bifurcation

From Sect. 2.2.1.2, Eq. (3.21) is equivalent to the mixed-order dynamical system:

$$\begin{cases} \mathbf{M}\ddot{\mathbf{q}} + \mathbf{C}\dot{\mathbf{q}} + \mathbf{K}\mathbf{q} + \left[\mathbf{C}_f\dot{\mathbf{q}} + \mathbf{K}_f\mathbf{q} + \sum_{k=1,2}\mathbf{L}_k\mathbf{y}_k + \mathbf{f}_c(\mathbf{q},\dot{\mathbf{q}})\right] = \mathbf{0} \\ \dot{\mathbf{y}}_1 + b_1\mathbf{y}_1 = \mathbf{q} \\ \dot{\mathbf{y}}_2 + b_2\mathbf{y}_2 = \mathbf{q} \end{cases} \tag{3.22}$$

with $b_k = \delta_k V/D$, which in turn can be written in state form:

$$\dot{\mathbf{z}}(t) = \mathbf{A}\mathbf{z}(t) + \mathbf{f}_{\mathrm{NL}}(\mathbf{z}) \tag{3.23}$$

This latter form is useful in determining the onset of fluid-elastic instability, by studying the eigenvalues of matrix $\mathbf{A}$ with varying V. This information dictates the behaviour of Eq.(3.23) linearised about the trivial fixed point $\mathbf{z}_0(t) = \mathbf{0}$. For low values of V, the fixed point is stable and the only existing attractor. As this parameter is increased, a threshold value V_c is exceeded such that the origin loses its stability by a pair of conjugate eigenvalues crossing the imaginary axis, i.e. a Hopf bifurcation which gives birth to a stable limit cycle. This is due to the structural and added damping of the first mode being cancelled by the destabilizing, non-conservative terms introduced via memory effects. Indeed, the consideration of additional modes in the approximation has no effect on the value of V_c, which exists even for a single mode when using the QU model. At higher velocities, however, it is possible for other modes to become unstable as well.

3.3 Cantilever beam in cross-flow

The system depicted in Fig. 3.19 has been studied by Pitteau and co-workers in a series of papers, both experimentally and numerically [BOR 17a, PIT 18, PIT 19, PIT 15]. A single flexible tube in a rigid square array is subjected to single-phase, spatially uniform, liquid water cross-flow. Its geometry is designed to allow motions in the lift direction only. Symmetrical stops are located at the coordinate $x_c = 0.624L$, where L is the total tube length. On each side, the gaps have the value: $g = 1.5E-3$ m, but the numerical model is scaled so that they correspond to a value of $y_c = 1$, where y_c is the non-dimensional transverse displacement at the stop location. A finite-element representation was set up using CAST3M, and the properties corresponding to the first five modes in absence of the stops are collected in Table 3.4.

Mode	1	2	3	4	5
Frequency (non-dimensional)	1.0	11.67	42.20	73.86	130.92
Mass (kg)	0.15682	0.27256	0.15608	0.16551	0.17557

Tableau 3.4: Modal properties for the cantilever tube.

Eigenfrequencies have been scaled by the first-mode angular frequency, $\omega_1 = 120.4110$ rad/s. In this section, the behaviour of the one-mode approximation is explored by continuation, leading to a global picture of its dynamics that was lacking from previous studies. Furthermore, the effect of including additional modes is investigated. A fixed number of 50 harmonics with $N_s = 2^{12}$ AFT samples was used throughout, with $\eta = 5 \cdot 10^{-5}$ for the regularization of impacts.

3.3.1 1-mode model

The stability analysis of fixed points shows that $V_c = 2.079$ m/s. At this point, a branch of neutrally-stable periodic solutions emerges, with fixed frequency and steadily-growing

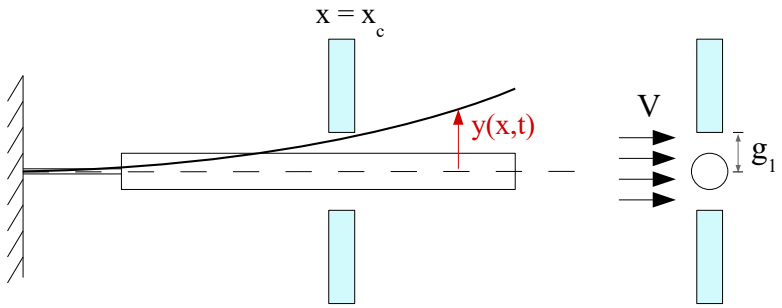

Figure 3.19: Cantilever tube in loose support.

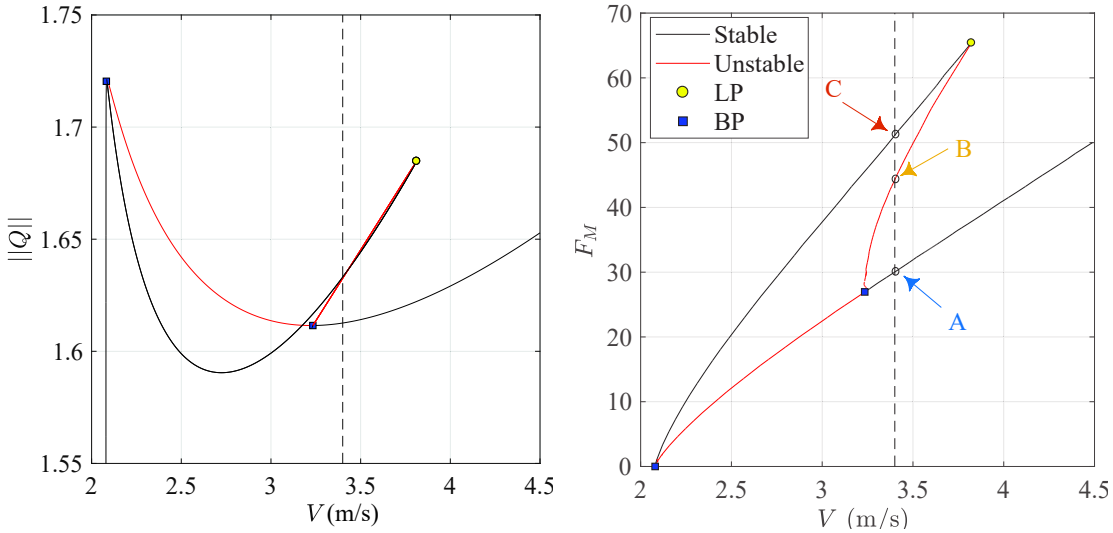

a) $||Q|| - V$ plane b) $F_M - V$ plane

Figure 3.20: Continuation of periodic solutions for one-mode model.

amplitude until impacts start happening, as shown in Fig. 3.20 a). An alternate representation is presented in Fig. 3.20 b), where the maximal (non-dimensional) impact force over one cycle is plotted instead of the norm of Fourier coefficients, $||\mathbf{Q}||$.

Three branches of periodic solutions bifurcate from the starting point of impact. The lower branch (in terms of the associated contact forces) consists of symmetric solutions and is unstable for low flow velocities, up until the BP at $V_{\mathrm{BP}} = 3.239$ m/s. Meanwhile, the upper branches are stable and consist of asymmetric solutions. Moreover, these branches are mirror images of one another: only difference between them is a negative sign in their Fourier coefficients; this comes from the fact that the symmetry of the system can be broken in either the positive or the negative direction, similarly to a buckled beam or plate. Hence, these branches overlap in the projection shown in this figure and only one

curve is visible.

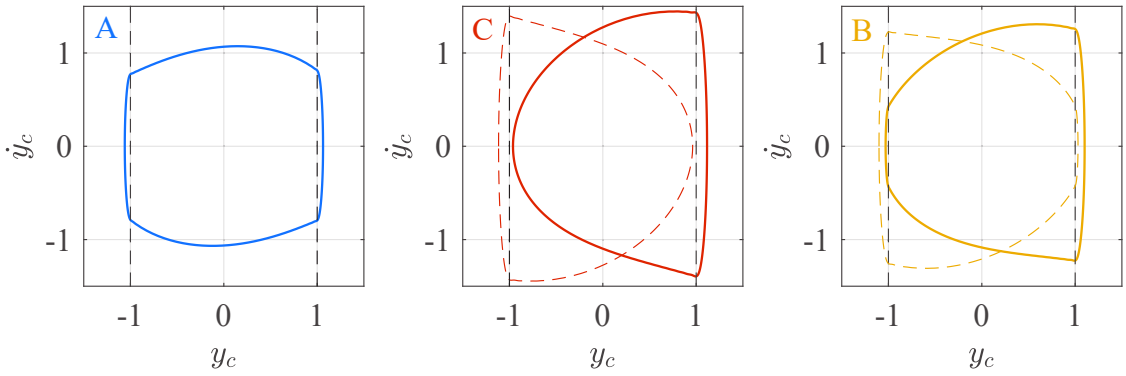

Figure 3.21: Phase-space representation of converged cycles for $V = 3.4$ m/s, at the support location x_c. Letters are associated with points on Fig. 3.3.1. Dashed cycles in the two right-most diagrams correspond to the solutions on the twin asymmetric branches.

Interestingly, stable cycles of both kinds coexist between V_{BP} and $V_{\mathrm{LP}} = 3.822$ m/s. In this region, the symmetric and asymmetric solutions are linked by two entirely unstable transition branches, which ensure a smooth evolution from one behaviour to the other, as could be expected from an equation with continuous dependence on the parameter V. Solutions in the symmetric branch undergo two impacts per period, whereas there is only one in the symmetric branches. Thus, transition cycles are both two-impacts-per-period and asymmetric. Examples of solutions are presented in Fig. 3.21, showing all five coexisting regimes for $V = 3.4$ m/s. For $V > V_{\mathrm{LP}}$, only symmetric cycles exist; this is due to the energy input from the flow being so high that the tube's motion inevitably attains both supports.

Fig 3.22 portrays the evolution of cycle frequency. A first remark to be made is that, at same flow velocity, symmetric regimes have higher frequencies. The difference between them is maximal at V_{LP} and amounts to roughly 8% (or 2.2 Hz, in dimensional terms). Secondly, the cycle frequency at the onset of fluidelastic instability (0.901, non-dimensional value) is lower than the first-mode eigenfrequency of the tube in stagnant fluid. This shift is due to an important added damping effect. As the frequency of impacts, their number per period, and the associated forces change from one branch to another, the interval $V \in [V_{\mathrm{BP}}, V_{\mathrm{LP}}]$ must be studied with great care if a wear and fatigue analysis was expected to be reliable. To this end, for instance, one could compute attraction basins using time-integration methods and assess probabilities of landing in one branch or another by comparing their relative sizes.

A note on stability computation From the fact that K_c is large with respect to the system's stiffness, the contact duration is small compared to the oscillation period. Impacts

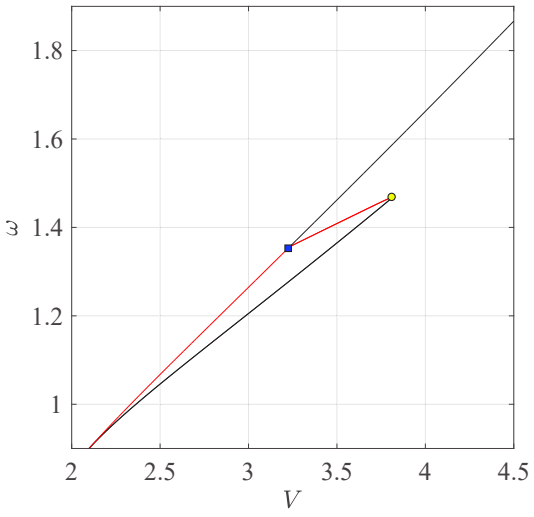

Figure 3.22: Evolution of (non-dimensional) cycle frequency with flow velocity, one-mode model.

are thus localized events in time, which demand an appropriate number of samples N_s in the AFT procedure to be correctly resolved. However, while this certainly affects the accuracy of the computed forces, this effect is much more dramatic on the derivatives of impact forces, which tend to step functions as $\eta \to 0$. Consequently, the appearance of the Gibbs phenomenon is to be expected. This is very relevant for stability evaluation, since these derivatives directly intervene in the computation of the Hill matrix. Figure 3.23 shows how the real parts of the Floquet exponents, along the continuation of the symmetric branch, vary with N_s. The moderate choice $N_s = 2^8$ leads to unusable results, as two exponents spuriously cross the stability boundary in an oscillatory fashion. Increasing to $N_s = 2^{10}$ attenuates this problem, but the trivial Floquet exponent is not exactly zero due to numerical errors, and sign changes still occur without physical meaning. This demonstrates the importance of not only using enough samples, but also of filtering out this particular exponent by using its associated eigenvector according to Sect. 2.1.4.2: the results of doing so are shown in Fig. 3.3.1, where a correct and unambiguous stability evaluation can be performed, followed by bifurcation analysis. It should be noted, nonetheless, that asymmetric solutions are seemingly more sensitive to the Gibbs phenomenon, as evidenced by Fig. 3.24. On these branches, spurious oscillations in the Floquet exponents persist for $N_s = 2^{12}$, but this sampling rate made them sufficiently small to allow for a proper stability evaluation.

3.3.1.1 Choosing a regularization coefficient

The impact function given in Eq. (3.9) depends continuously on all its parameters, including η. This implies that numerical continuation can be used to assess the evolution of a given cycle upon its variation. The idea is to choose the largest possible value for η -thus yielding a smoother function- without changing the value of a certain measure beyond

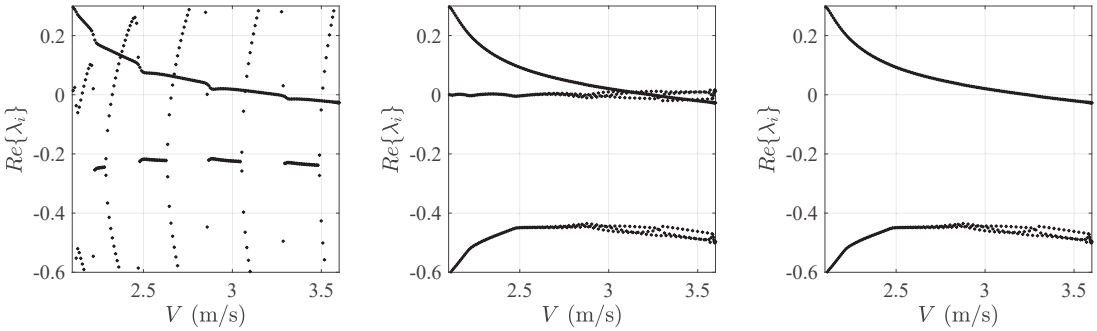

a) $N_s = 2^8$. b) $N_s = 2^{10}$. c) $N_s = 2^{10}$, filtered.

Figure 3.23: Real part of Floquet exponents (symmetric cycles) for different numbers of AFT samples, with trivial exponent shifted to -1.

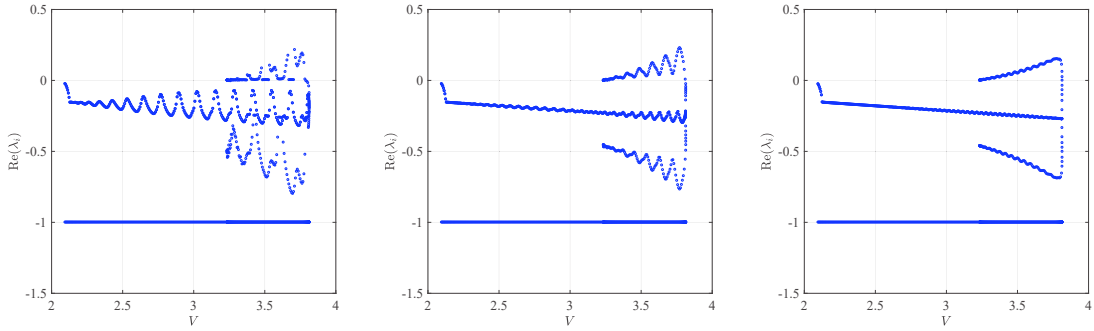

a) $N_s = 2^{10}$. b) $N_s = 2^{11}$. c) $N_s = 2^{12}$.

Figure 3.24: Real part of Floquet exponents (asymmetric cycles) for different numbers of AFT samples.

some threshold, e.g. 5 per cent relative error. Here we have chosen the maximal value of impact force over the cycle, denoted F_M, as this quantity is physically meaningful. Fig. 3.25 shows an example for the one-mode cantilever beam, where it is clear that choosing an overly low value of η leads to completely erroneous results, with the asymmetric branch disappearing altogether at a LP. This graph justifies the choice $\eta = 5 \cdot 10^{-5}$ chosen in this section.

3.3.1.2 Symmetry-breaking perturbation

In practical situations, whether they be experimental models or industrial steam generators, it is unlikely that a tube would be perfectly centred between its surrounding stops. This is particularly true for the latter case, as there is no guarantee that long-term mechanisms such as wear would open the gaps isotropically. Furthermore, as evidenced by the KOALA model, varying degrees of asymmetry potentially have major effects on global dynamics. Hence, the bifurcations observed above are tracked with respect to a parameter $\delta \leq 1$, which replaces one of the clearances. The results of this operation can be seen in

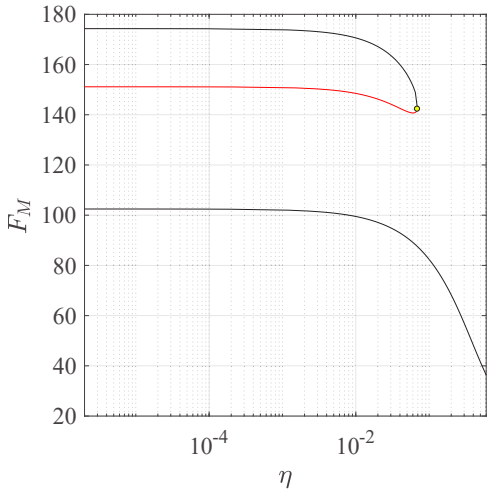

Figure 3.25: Continuation of coexisting cycles with respect to η for a one-mode approximation of the cantilever beam, given $V = 3.6$ m/s.

Fig. 3.26.

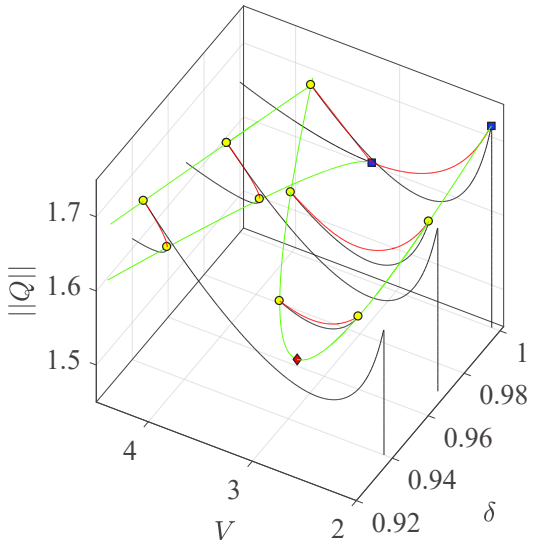

Figure 3.26: LP tracking with respect to left clearance δ.

The effect of asymmetry is immediately seen in the splitting of the original curve ($\delta = 1$). Rather than two qualitatively-different branches connected by BPs, the main curve originating from the Hopf bifurcation coexists with an isola for $\delta < 1$. Furthermore, the curve containing the low-amplitude LPs of the main curve ends up joining one of the BPs of the symmetric system, which has thus been perturbed into an imperfect bifurcation as $\delta \neq 1$. A stability analysis along the LP curve does not reveal any codim-2 bifurcations. However, a cusp point was localized at $(V_{CSP}, \delta_{CSP}) = (2.656, 0.925)$, which indicates

isola formation. A projection of the LP curves onto the parameter plane (δ, V), as in Fig. 3.27, yields stability boundaries between regions with varying numbers of stable solutions, which are all periodic in the present case.

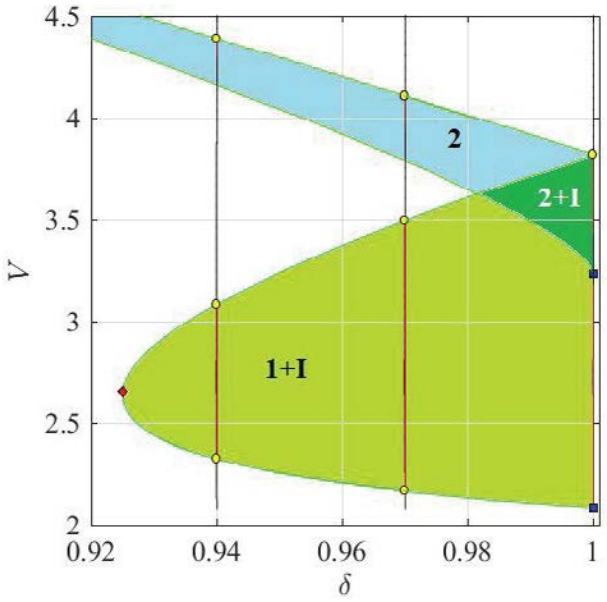

Figure 3.27: Stability chart for varying V and left clearance δ. Numbers in each region indicate stable solutions on the main branch, and 'I' stands for an isolated solution. Outside of the coloured regions, there is one unique solution.

3.3.2 2-mode model

It is immediately evident from Fig. 3.28 that this approximation presents much richer dynamics, compared to the previous one. As before, representations in the $||Q|| - V$ and $F_M - V$ planes are shown. Right after the onset of fluidelastic instability, a similar behaviour is observed: two stable asymmetric and one unstable symmetric branch emerge. At a higher velocity, the branches meet at a BP. In between these points, however, both curves undergo a series of folds. Fig. 3.28 b) shows a clearer view of the pattern. Furthermore, a new BP appears at $V_{BP2} = 4.593$, but its emerging branch is not shown in this figures.

Another interesting result obtained from continuation is the fact that most cycles on both branches are unstable. Periodic solutions are thus rare, with the oscillations of modal coordinates not synchronized in most cases. The responses are then expected to be mostly quasi-periodic, a hypothesis supported by the high number of NS bifurcations found along continuation. These are shown on the $F_M - V$ plane in Fig. 3.29. Simulation by time-integration using the Runge-Kutta scheme of MATLAB's ode45 function were used to confirm the existence of quasi-periodic solutions on the unstable portions of the response curve, with an example shown in Fig. 3.30. Here, two of the HBM-predicted solutions on

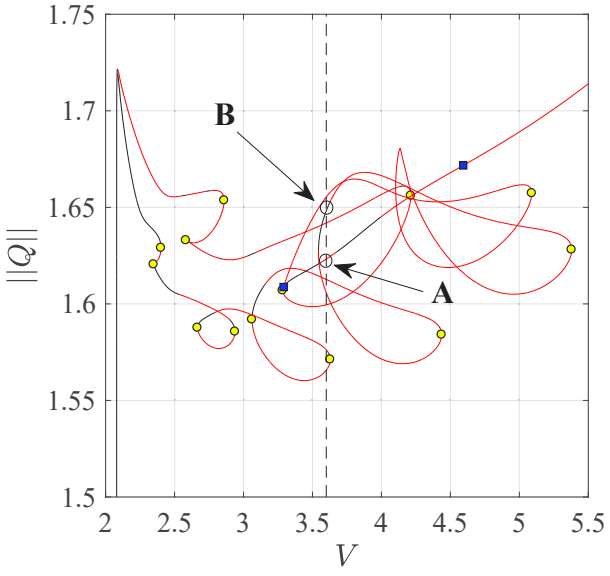

a) $||Q|| - V$ plane

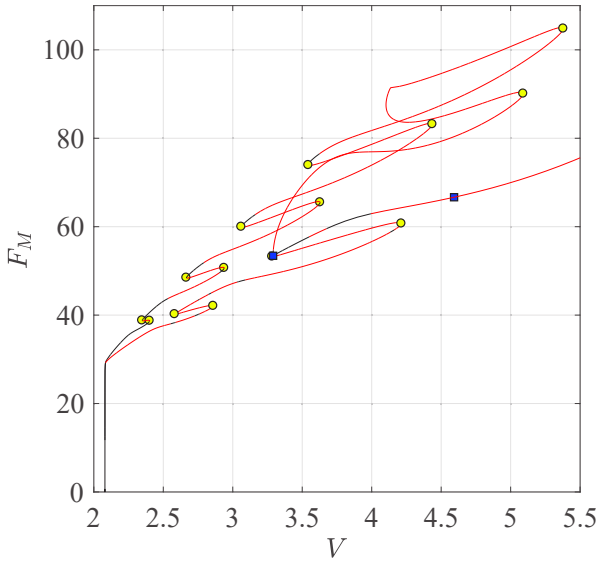

b) $F_M - V$ plane

Figure 3.28: Continuation of periodic solutions for two-mode model.

the symmetric and asymmetric branches, respectively labelled **A** and **B** in Fig. 3.28 a), are compared to ode45's solution for $V = 3.6$ m/s and represented in the configuration space of modal displacements, (q_1, q_2). Cycle **A**, judged unstable by the HBM, was indeed impossible to find; however, a symmetric quasi-periodic regime exists nearby. As clearly seen in this figure, the unstable periodic solution seems to be a backbone for the stable, quasi-periodic motion, i.e. averaging the latter over time would approximately yield the

former. On the other hand, HBM-computed stable cycle **B** is indistinguishable from its time-integration counterpart.

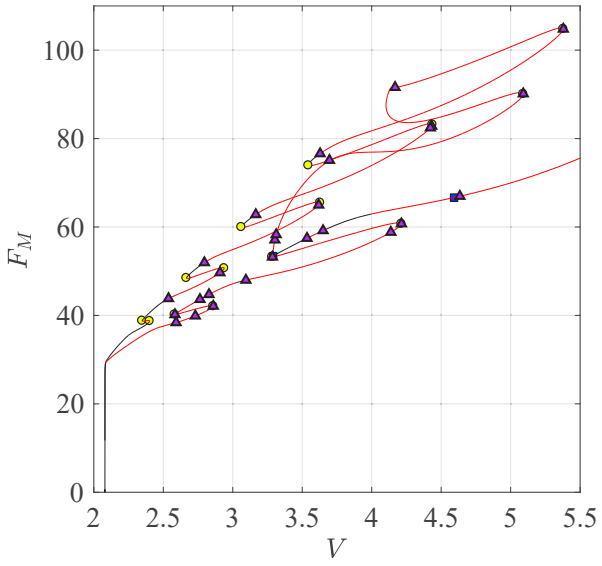

Figure 3.29: Continuation of periodic solution for two-mode model, showing NS bifurcations.

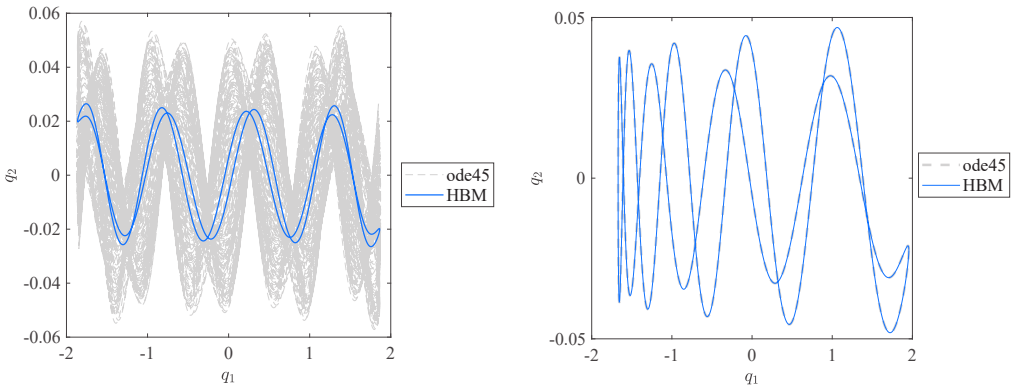

A: Symmetric cycle. **B**: Asymmetric cycle.

Figure 3.30: Comparison of cycles obtained by HBM and time-integration (MATLAB's ode45), for $V = 3.6$ m/s.

To understand the pattern of folds appearing on the aforementioned continuation curves, the frequency content of each mode needs to be analysed. This is practically automatic when using HBM, and leads to the evolutions shown in Fig. 3.31 for the symmetric branch. Therein, each curve corresponds to the norm of an individual frequency component. For instance, $||Q_3^1|| = \sqrt{(Q_{c3}^1)^2 + (Q_{s3}^1)^2}$ represents the amplitude of

the third-harmonic component of the first mode. This figure explains the above pattern as a signature of energy redistribution due to impacts: the linearly-unstable first mode attains a limit cycle thanks to the nonlinearity and acts as an excitation source for the second mode, whose frequency evolves as an increasing function of V. This leads to a series of super-harmonic resonances of the second mode, as seen in the right side of the figure. In particular, the first peak to appear corresponds to the 11-th harmonic of the second mode; this is logical given that its linear eigenfrequency is slightly above 11 times that of the first mode. Furthermore, it should be noted that only odd harmonics respond, which is a direct consequence of the solutions' symmetry. This fact explains the higher number of interactions loops observed on the asymmetric branch in Fig 3.28.

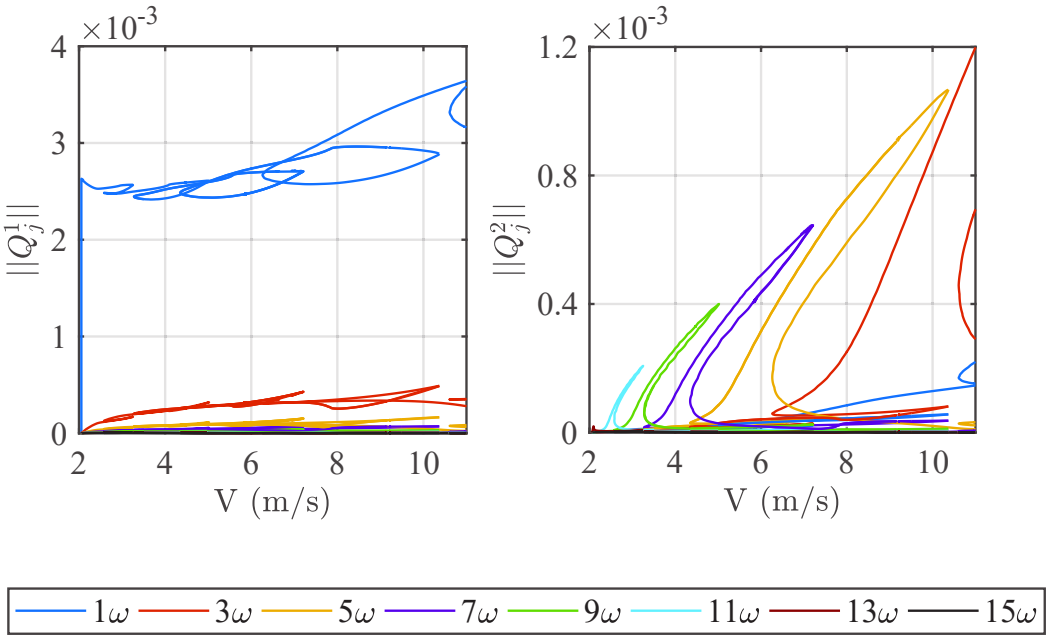

Figure 3.31: Evolution of (dimensional) harmonic amplitudes with flow velocity for the symmetric branch of two-mode model. Left: first mode, right: second mode.

3.3.3 A word on 3-mode and further models

The pattern observed above continues with the addition of a third mode. Symmetric and asymmetric branches are represented in the $||Q|| - V$ plane in Fig. 3.32 (without stability computation). Since this is a system made up of three autonomous oscillators, the solutions in time are expected to be quasi-periodic with two or three incommensurate frequencies.
Qualitatively, the curves share their basic features with their two-mode predecessors (Fig. 3.3.2 a)), although a number of additional, smaller loops and peaks make their appearance.

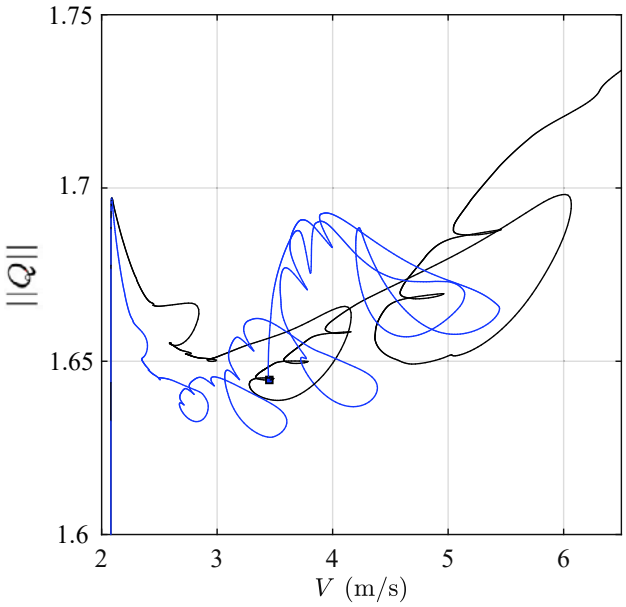

Figure 3.32: Continuation of periodic solutions for three-mode model. Black: symmetric branch; blue: asymmetric branch.

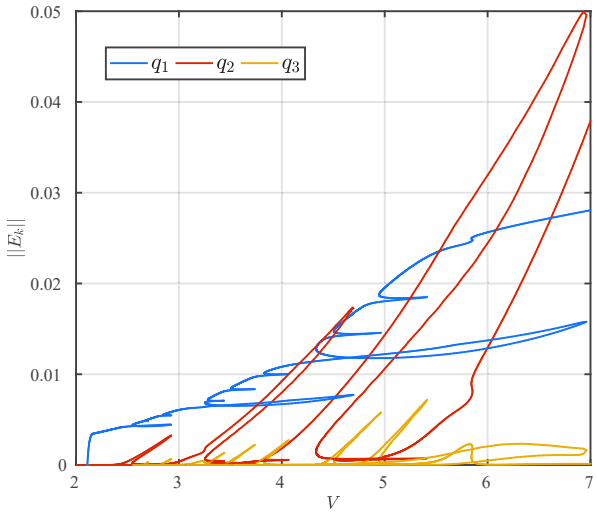

Figure 3.33: Modal kinetic energy, symmetric branch of three-mode cantilever beam model.

This is a consequence of interactions between the first and the third mode, as explicitly shown for the symmetric branch in Fig. 3.33. Here, the modal kinetic energy is plotted for varying V, and super-harmonic resonant peaks on the higher modes are seen to coincide

with those of the first. For the third mode in particular, the first resonance corresponds to the 43rd harmonic, and the associated energies are low in comparison to the other two modes. Close to $V = 5.8$ m/s, an interaction between the three modes can be observed. The pattern of modal interactions extrapolates with the addition of further modes. From the fourth mode onwards, however, the associated modal displacements are negligibly small for practically all the velocity ranges considered.

3.4 Heat-exchanger arc

A more realistic configuration is now considered, as shown in Fig 3.34. The U-like structure has its legs pinned at a number of locations by support plates, while the uppermost arc is free but surrounded by 12 Anti-Vibration Bars (AVBs). Six of these are disposed on each side of the tube, allowing for six symmetrical, bilateral contact points with gap size $g_k = 0.24$ *mm*. Within the hydraulic circuit of a steam generator, high-temperature pressurised water flows from the hot to the cold leg of the tube, exchanging heat with the surrounding fluid along its path. Temperature and density gradients thus generate a flow of the latter in the direction x_2. This cross-flow excitation on the arc induces vibrations of the structure in the direction x_3, normal to the plane (x_1, x_2), through fluid-elastic instability, for maximum flow velocities exceeding a critical value.

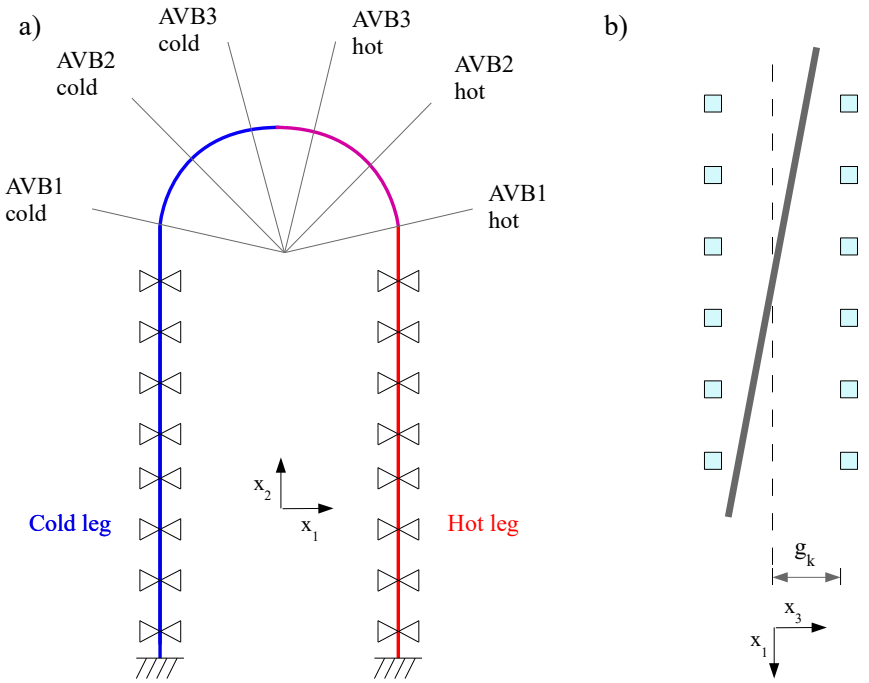

Figure 3.34: Heat exchanger tube. a) Frontal view, b) top view.

3.4.1 Numerical model

As in the previous case study, a finite-element representation of the system described above was set up in CAST3M using linear pipe elements (*TUYE* in CAST3M). A total of 310 three-dimensional elements was used, thus yielding 1860 degrees of freedom. The main characteristics of the model are summarized in Table 3.5.

Radius (m)	1.577
Leg height	9.915
Number of tube support plates	9
Distance between adjacent support plates (m)	1.074
Angle from apex of AVBs (°)	76/48/20
Tube diameter (mm)	19.05
Tube thickness (mm)	1.09
Tube density (kg.m^{-3})	8320
Nominal gap (mm)	$\pm$0.024
Impact stiffness (N/m)	4.10^5
Impact damping (Ns/m)	200
Tube density (kg.m^{-3})	8320

Tableau 3.5: Heat-exchanger tube and AVB characteristics.

Rather than considering uniform spatial distributions of transverse velocity and fluid density, as in the previous example, here we use thermo-hydraulic data representative of that expected to be encountered in an actual steam generator. Specifically, the distributions shown in Fig. 3.35 are used, which were obtained by full thermo-hydraulic simulations and first presented in [PRA 18]. In reality, the tubes are subjected to a two-phase flow consisting of liquid water and steam. For the purposes of the present work, the flow is homogenized, and so the distributions presented correspond to those for the equivalent one-phase flow. As these distributions represent the non-fluctuating (mean) components of the respective fields, it is reasonable to assume that their shapes are invariant and scalable by $(V \equiv V_{max}, \bar{\rho}_f)$ The former is used hereafter as the continuation parameter.

For the following continuation analyses, the full model was reduced by projection onto the eigenbasis of the tube in stagnant fluid and in open-gap condition. The mass matrix thus includes a contribution from the presence of fluid. It should be noted that, while the system is geometrically symmetric, the same is not true for its mode shapes. This is a consequence of the non-uniform and non-symmetric spatial distribution of equivalent density. Table 3.6 groups the modal properties of the first 5 out-of-plane (OP) modes.

For all calculations presented, a 50-harmonic Fourier approximation was used, with a $N_s = 10^{11}$-point sampling. As with the previous system, $\eta = 5 \cdot 10^{-5}$. The results include phase-space diagrams of motion at the six contact points along the tube, which

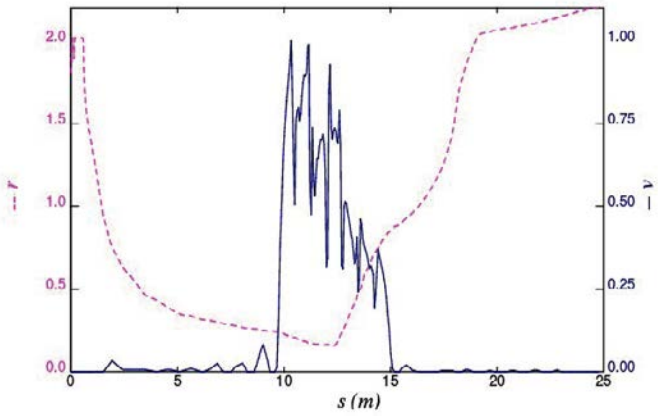

Figure 3.35: Distribution of normalized density r and transverse velocity ν along the tube's abscissa, s, from [PRA 18].

Mode	1	2	3	4	5
Frequency (non-dimensional)	1.0	2.9984	6.4630	11.3844	17.0094
Mass (kg)	1.5306	1.7832	1.7315	1.8251	3.1440

Tableau 3.6: Modal properties for the U-tube model.

are identified by different colours according to the diagram shown in Fig. 3.36.

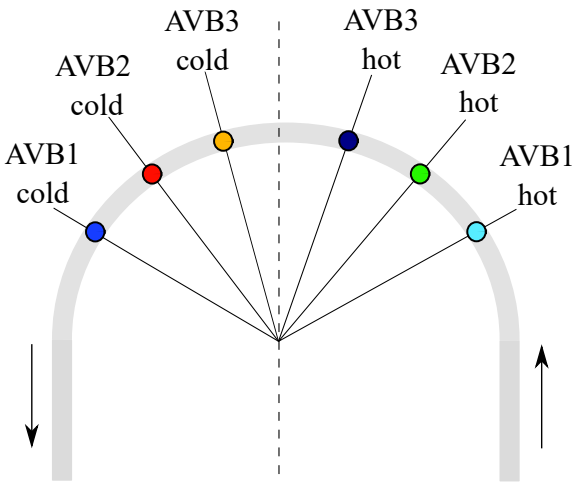

Figure 3.36: U-tube: colour-coding for identification of tube motions.

3.4.2 Continuation results

3.4.2.1 Results for 1 OP mode

The curve shown in Fig. 3.37 represents the evolution of Fourier coefficient amplitude for the one-mode model. All of the solutions are stable and homothetic to the regime depicted in Fig. 3.38 a) for $V = 5$ m/s, in which at all contact points follow a similar trajectory in phase space. The effect of impact damping is clearly seen in Fig. 3.38 b), obtained at the same flow velocity.

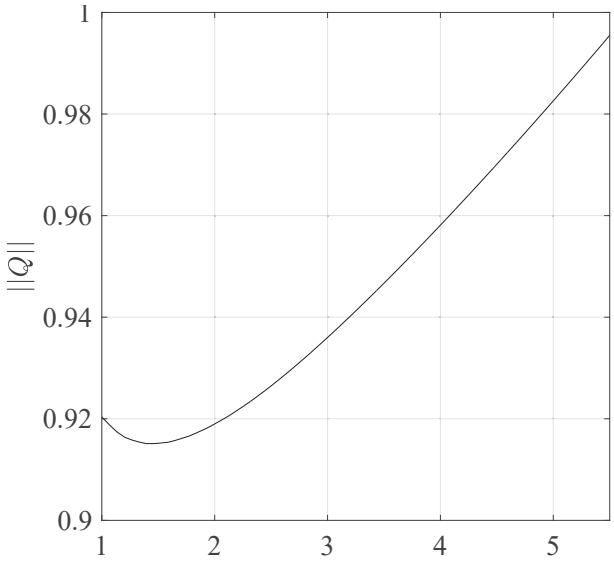

Figure 3.37: U-tube: Continuation for a one-OP-mode model.

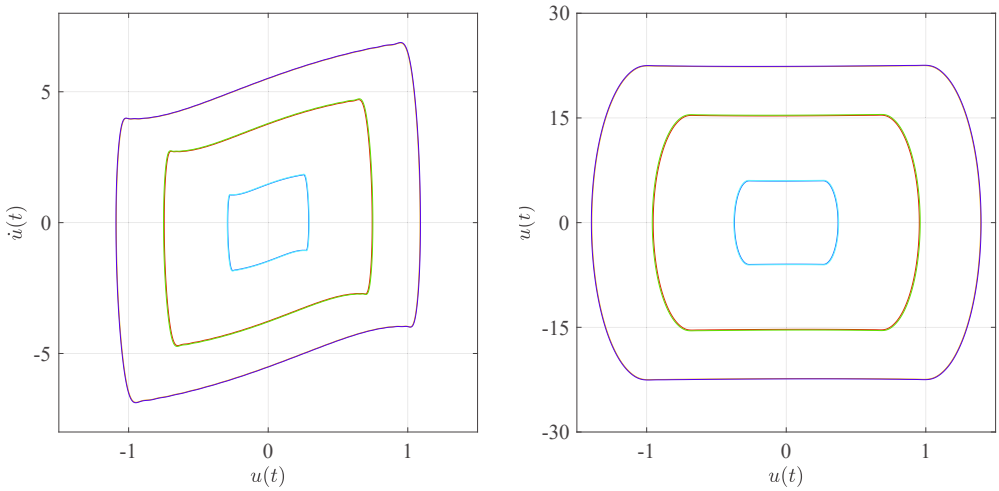

a) $C_c = 200$ b) $C_c = 0$

Figure 3.38: Stable regime at $V = 5$m/s, 1-mode model.

3.4.2.2 Results for 2 OP modes

When a second OP mode is included, continuation reveals the response curves of Fig. 3.39. The lower branch coincides exactly with the 1-mode response, but is mostly unstable. At $V = 2$ m/s, a new branch seems to bifurcate from the first. However, a closer look reveals two disjoint curves, as evidenced in Fig. 3.40. Regimes belonging to this curves show an increasing contribution of the second mode, which goes from virtually non-responsive on the lower branch to dominant on the upper one. Moreover, two regimes at same norm are mirrored images of each other. Hence, this behaviour is perfectly analogous to the transition branches between two and one-sided asymmetrical impacts of Sect. 3.3 with the exception that it is the Fourier coefficients of the second mode, and not those of even harmonics, that become non-zero. The fact that the branches are separated rather than overlapping and connected at a BP is a consequence of the non-uniform density distribution, which perturbs the system in a symmetry-breaking way and leads to an imperfect bifurcation.

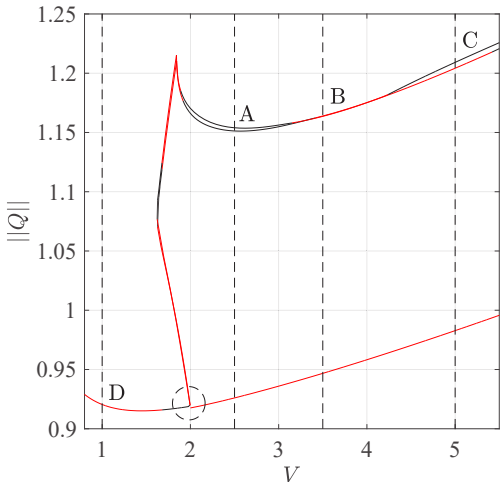

Figure 3.39: U-tube: Continuation for two-OP-mode model.

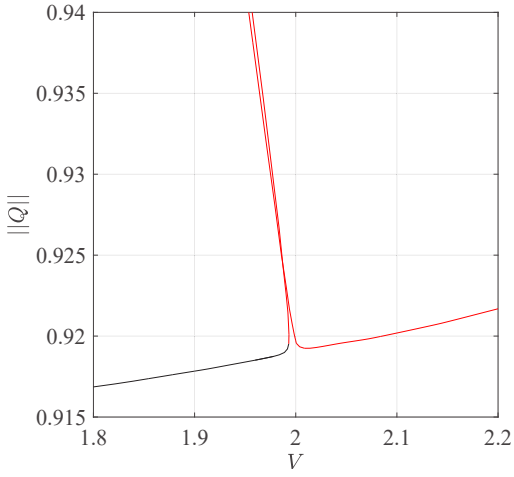

Figure 3.40: Close-up on the imperfect bifurcation.

The regimes obtained at the points A,B,C on the upper branches in Fig. 3.39, respectively corresponding to $V = 2.5, 3.5, 5$ m/s, are explored next. For completeness, the same is done for the dynamics at the low-velocity point D, $V = 1$ m/s. For ease of identification, the names *left branch* and *right branch* are used to refer to the branches starting at values lesser and greater than $V = 2$ m/s on Fig. 3.40, respectively. The transverse displacements at contact points are labelled $u(t)$.

Point A

The qualitative similarity of the cycles on both branches is evident from 3.41. Indeed, besides small differences that are a consequence of system asymmetry,

the same six phase-space trajectories are observed in both images. However, the roles of points symmetrical with respect to the dotted line in Fig. 3.36 is reversed. This results directly from having different signs in the leading (first-harmonic) Fourier coefficient of the second mode. More precisely, for the right-branch cycle: $(Q^1_{c1}, Q^2_{c1}, Q^1_{s1}, Q^2_{s1}) = (0.9527, -0.0028, -0.1135, -0.6344)$ whereas $(Q^1_{c1}, Q^2_{c1}, Q^1_{s1}, Q^2_{s1}) = (0.9537, 0.0046, -0.1320, 0.6241)$ for its left-branch analogue.

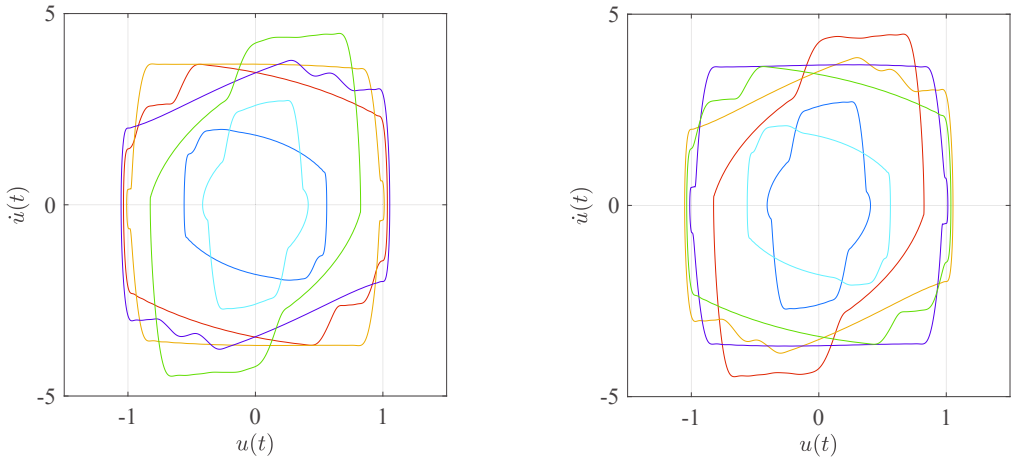

a) Right branch. b) Left branch.

Figure 3.41: Stable cycles at point **A**, $V = 2.5$ m/s.

Point B

Fig. 3.42 shows the the same qualitative features as its predecessor, but in this case the cycles on both branches are unstable.

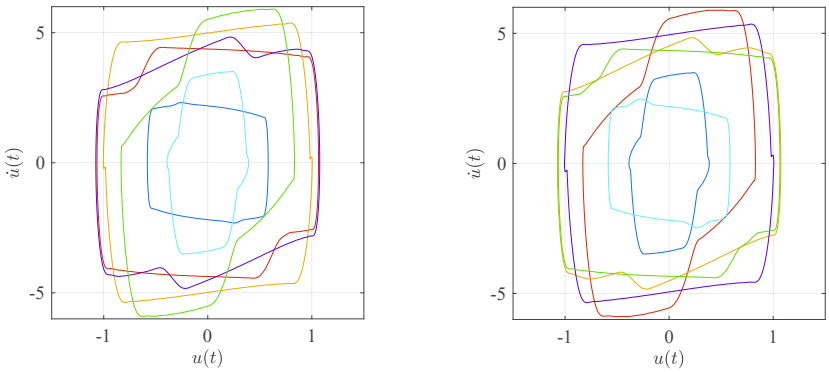

a) Right branch. b) Left branch.

Figure 3.42: Unstable cycles at point **B**, $V = 3.5$ m/s.

The Floquet exponents around this zone indicate loss of stability through 0, i.e. a static bifurcation akin to a BP, as exemplified in Fig. 3.43 for the right branch[3]. However, the HBM was not able to localize the corresponding bifurcations, nor to find any periodic solutions beside the ones on the unstable branches.

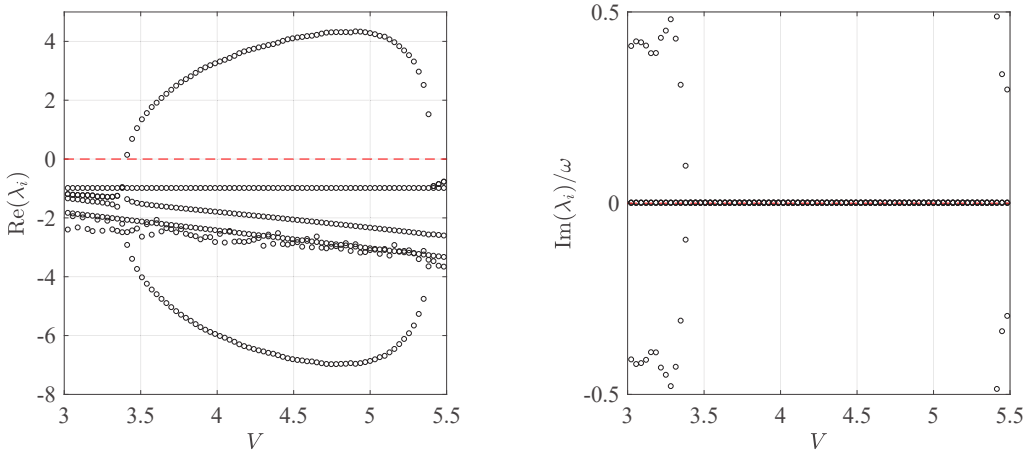

a) Real part. b) Imaginary part.

Figure 3.43: Floquet exponents of right branch as a function of V.

This hints at a transition to an aperiodic regime which is not quasi-periodic either, thus probably chaotic. This hypothesis seems to be supported by the time-histories and phase-space diagram depicted in Fig. 3.44, obtained by time integration.

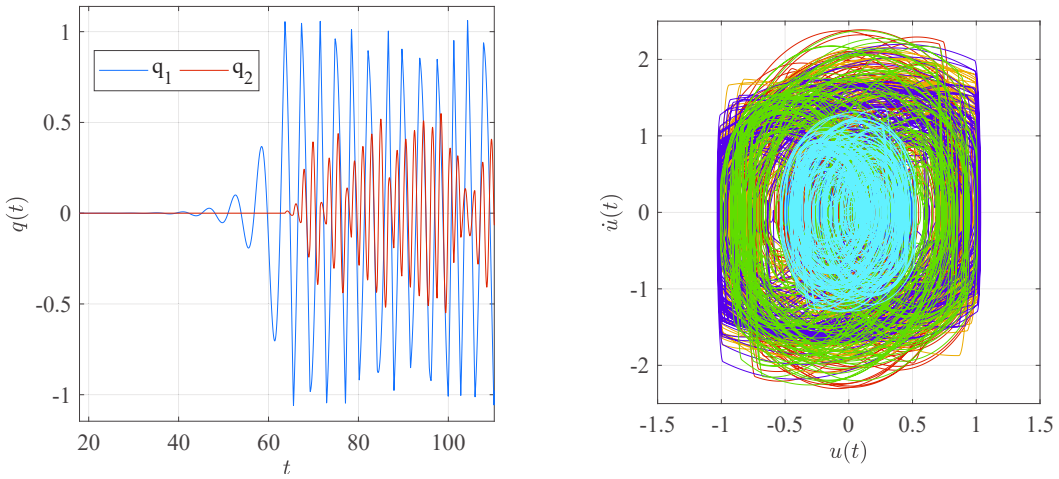

a) Modal displacements. b) Physical displacements.

Figure 3.44: Aperiodic regime at $V = 3.5$ m/s.

[3]The same behaviour is exhibited by the left branch.

The transition from a dynamically divergent, linear regime to a bounded, nonlinear one is evident. Once contacts start (when $q_1(t) = 1$), a chaotic-looking transient motion ensues. Nevertheless, long-time integration over a 1000 time-unit interval shows that this regime does not stabilize to a limit cycle. Further evidence is provided by the corresponding Power Spectral Density (PSD) diagrams, Fig. 3.45, which show a broadband spectre. It should ne noted that the dominant non-dimensional frequency of the first-mode PSD ($f = 0.2875$), marked by a dotted line in Fig. 3.45 a), corresponds approximately to one third of the HBM-predicted unstable cycle frequency.

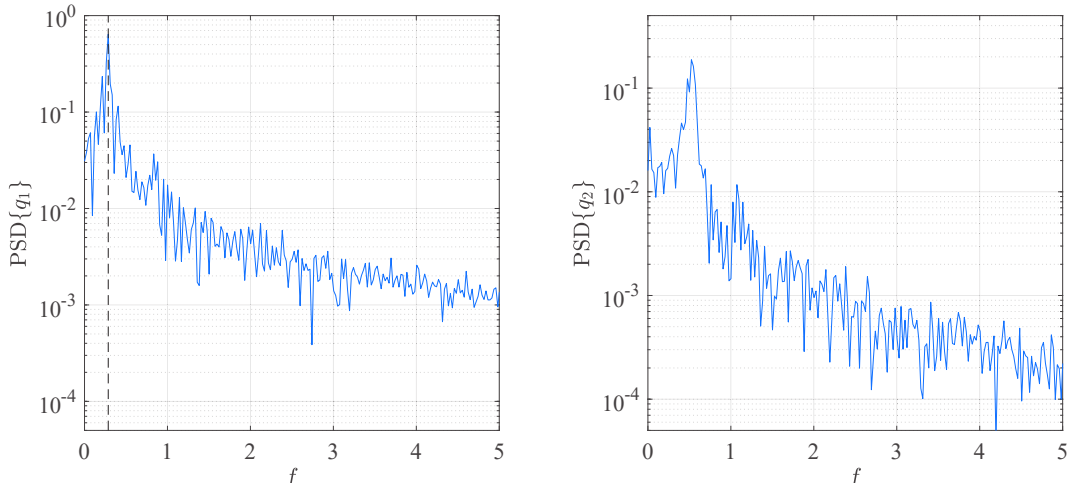

a) First mode, q_1. b) Second mode, q_2.

Figure 3.45: PSD of modal displacements at $V = 3.5$ m/s.

Point C

At this point, one branch is stable and the other is not.

Inspired by the closing remark of last paragraph, a Fourier basis including 3T-periodic sub-harmonics was employed. In this manner, the HBM successfully captured a stable cycle with triple period in coexistence with the branches depicted in Fig. 3.39. Fig. 3.46 shows phase-space representations of stable regimes. The same trend as before, i.e. the fact that both regimes are mutually antisymmetric, is observed here, with one of them additionally being sub-harmonic.

In [PRA 18], the authors report a quasi-periodic cycle which is close to being 3T-periodic. Nevertheless, a verification through time integration yields only the stable cycles depicted in Fig. 3.46. Among the reasons that could explain this discrepancy in results, two of them seem most likely: the inclusion of in-plane modes in the aforementioned paper (which are absent from the present model, for HBM as well as for time-integration), or quasi-periodicity being a numerical artifice introduced by the specific integrator.

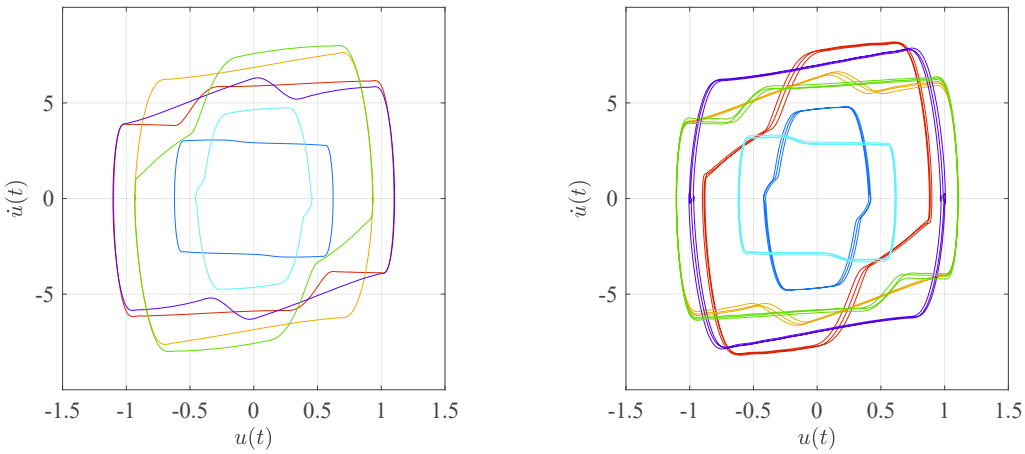

a) Right branch, T-periodic. b) Isolated branch, 3T-periodic.

Figure 3.46: Stable cycles at point **C**, $V = 5$ m/s.

Point D

The Floquet exponents of the left branch for low values of V are pictured in Fig. 3.47. Just as in the case of point **B**, loss of stability occurs by a Floquet exponent crossing the imaginary axis through 0, and no periodic solutions other than the one on the unstable branch would be found. Rather, an aperiodic regime was observed, whose spectre is broadband as shown in Fig. 3.48. In contrast to the previous aperiodic regime, here the dominant frequency coincides exactly with that of the unstable HBM cycle.

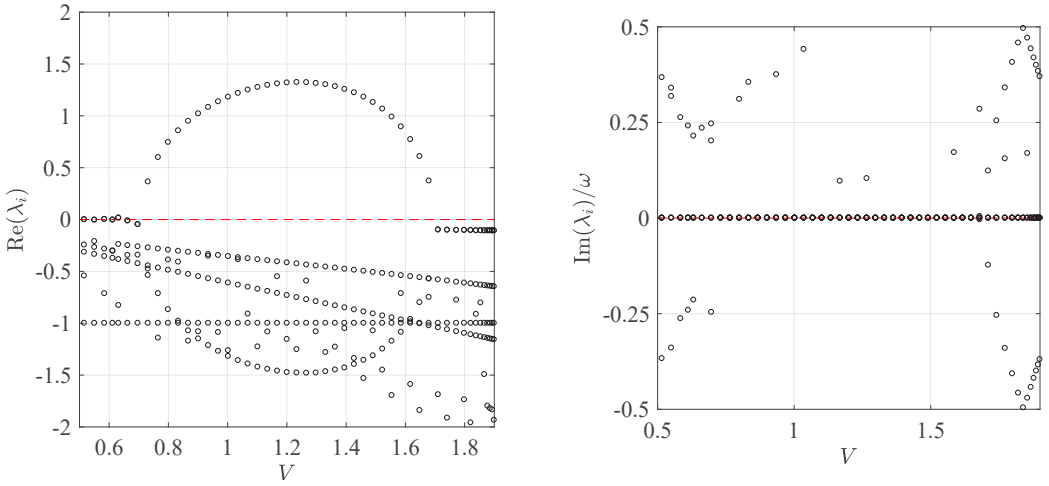

a) Real part. b) Imaginary part.

Figure 3.47: Floquet exponents of left branch as a function of V, low velocities.

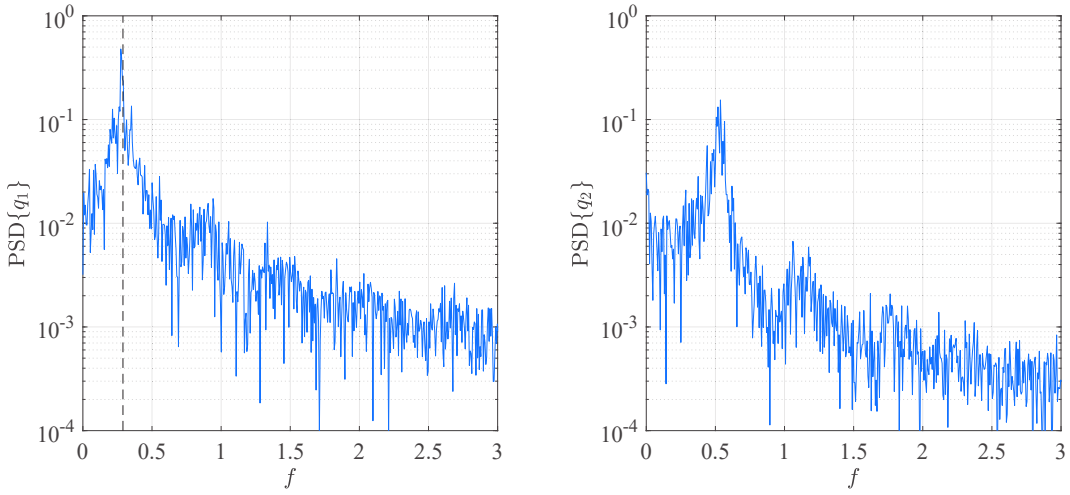

b) Second mode

Figure 3.48: Power spectral density of unsteady regime at $V = 1$ m/s.

Conclusions and Further Work

General conclusion

The present work was motivated by the industrial problem of steam-generator tubes subjected to cross-flow. These structures undergo fluidelastic instability when traversed by a flow with mean velocity beyond a critical value, a complex phenomenon for which no completely satisfying model exists to date. Nonetheless, the associated scientific literature agrees on the frequency-dependent nature of fluidelastic forces. Nonlinearities render the unstable motions bounded but also open the way to coexisting regimes, with some potentially more hazardous than others in terms of long or middle-term structural integrity. Prediction of dynamical behaviour is thus at once crucial and quite complicated.

This issue was addressed by developing robust, efficient computational routines based on the Alternating Frequency-Time Harmonic Balance Method (AFT-HBM). This choice is three-fold advantageous in the context of the present problem: it allows for a straightforward treatment of the delay terms (both discrete and distributed) appearing in most fluid-elastic force models, it has been proven to be well-suited for the study of geometrically-complex industrial systems (with potentially a large number of degrees of freedom) and it offers an extremely fast way of computing periodic solutions, thus rendering it efficient for parametric analyses. The latter, in particular, is achieved by an implementation of pseudo arc-length continuation, through which the evolution of steady-state solutions with respect to parameter variations is readily obtained. All stability changes along continuation are monitored by use of Hill's method and any bifurcations encountered are localized, then tracked.

These methods all existed previously, but were not coupled to a finite-element software which made their use straightforward for practical engineering applications. Thus, in this thesis the aforementioned numerical methods were integrated into the most recent version of CAST3M. Thus, vibration problems with localized nonlinearities can be tackled efficiently. Moreover, contributions were made in the form of numerical methods to extend the existing capabilities of AFT-HBM continuation. The choice of these developments was once again inspired by the steam-generator vibration problem, although their applicability is clearly not limited to it.

The treatment of generic systems with time-delay terms was considered. Using HBM, discrete delays are computed by the use of a frequency-dependent rotation matrix. A demonstration on a toy model is done, which included tracking limit point bifurcations with respect to the delay parameter. A similar treatment is introduced for systems with memory (distributed delays), for which additionally a method for stability calculation is proposed. An eigenvalue problem is thus formed from terms available from the nonlinear root finding algorithm, whose solution leads to Floquet exponents. The advantage of this approach is that is allows for the stability of mechanical systems with internal variables described by additional equations to be evaluated in a convenient way.

Quasi-periodic solutions of forced and autonomous systems were considered. In particular, the application of Hill's method to assess stability is discussed. This requires the identification and shifting of trivial eigenvalues to be performed, which is explained. Moreover, a practical way to transit from a Neimark-Sacker bifurcation of cycles to a branch of quasi-periodic solutions is proposed. This method is tested briefly on a Nonlinear Energy Sink system.

Systems with several degrees of freedom can be expected to undergo numerous bifurcations. Hence, generalized bifurcation tracking in arbitrary codimension was proposed. This involves the presentation of extended systems to characterize well-known bifurcations (in particular, no extended system for codim-1 period doubling had been published for the HBM), but mostly a comprehensive strategy to build such systems of equations in all possible cases.

Three examples are presented which explore the phenomenological aspects of steam-generator vibrations. Firstly, a single-degree-of-freedom system subjected to periodic forcing and two-sided stops is considered. Transitions to chaos through a sub-harmonic cascade was explored as a function of forcing level, and the birth/death of isolated, sub-harmonic response curves for varying asymmetry was evidenced by tracking period-doubling bifurcations and 2T-periodic limit points. Next, two autonomous systems consisting of beams with self-excited oscillations induced by cross-flow were presented. In the first, idealized case, numerous bifurcations occurred as a series of super-harmonic resonances of higher modes came to be for increasing values of flow velocity. It was also shown that, just as in the previous system, isolated response curves are easily created by breaking the system's symmetry. Lastly, a more realistic representation of a steam-generator tube was presented which included non-uniform spatial distributions of density and mean transverse velocity as well as the characteristic U-shape. Carrying over from the two previous systems, the effect of asymmetry is once again seen to have a major role, and the transition from a one-mode to a two-mode model comes about with a remarkable increase in richness of dynamical regimes. For as little as two modes, periodic, sub-harmonic and chaotic motions can be observed. Besides the interesting phenomena brought out by the study of these simplified systems, this work shows the robustness and usefulness of continuation methods when dealing with such complex industrial problems.

On the other side, the limitations of such methods also arise through the results shown herein: fluidelastically-excited impacting systems tend to exhibit non-periodic motions as a norm rather than an exception. Hence, continuation of periodic solutions (through HBM or otherwise) must be seen as a qualitative tool used to identify potentially interesting/dangerous zones in parameter space and not one for high-fidelity simulation, and the fine study of results through time integration methods remains -albeit in a lower extent- an unavoidable task.

Further work

The results from this work open the following research paths:

- CAST3M implementation of geometric nonlinearities. Beyond the scope of the present thesis, large-amplitude vibrations are nevertheless important in a wide range of applications. Thus, introducing computation of the corresponding forces from finite-element models is an interesting perspective.

- Performance enhancement of quasi-periodic AFT-HBM. While the algorithm presented herein is robust and general, no effort was made to optimize it. Hence, as the number of unknowns is large, there is ample room for improvement in terms of performance. This can be done, for instance, by incorporating harmonic selection techniques as well as parallel computing.

- Automatization of high-codimension tracking. Currently, extended systems for bifurcation detection in increasing codimension are programmed in separate files and called upon when required after local stability evaluation. However, all of these are built from the same basic components, i.e. the codim-1 constraints. Recursive programming could then be implemented to automatically track arbitrary bifurcations by using only calls to the codim-1 functions.

- Basin of attraction estimators. Since real-life heat exchanger tubes will inevitably be subjected to turbulent forces, the state of the system in time can be expected to alternate between the coexisting underlying orbits. Thus, fine predictive analyses would benefit from a technique to estimate the time spent around each regime.

- Dynamic modelling of misalignment. In this thesis, it was shown that global dynamics of systems with impacts are affected greatly by the configuration of the latter. While a symmetry-quantifying parameter was used and varied freely, asymmetry and misalignment are bound to happen over time in real systems due to effects such as wear, which are themselves a consequence of impacts. This suggests the investigation of a coupled problem whose objective is to model long-term behaviour with dynamically evolving gaps.

- Consider the uncertainty introduced by turbulence on the steady-state periodic solutions by using, e.g., chaos polynomial expansion [DID 13, PAN 15]. This could lead to bounds for response amplitudes, impact forces and other important quantities.

Appendices

Appendix A

A.1 Fourier coefficients of polynomial forces

For any $(r,s) \in \mathbb{N}^2$, the function $\varphi(u,w) = u^r(t)w^s(t)$, where $u(t)$ and $w(t)$ are periodic functions defined on the interval $\left[0, \frac{2\pi}{\omega}\right]$, can evidently be though of as a product operation iterated $(r+s-1)$ times:

$$\varphi(u,w) = u \cdot (u^{r-1}w^s) = u \cdot \ldots \cdot u \cdot w^s = u \cdot \ldots \cdot u \cdot w \cdot \ldots \cdot w = \text{prod}(u, \text{prod}(\text{prod}(\ldots, w)))$$

Clearly, φ has the same periodicity as its arguments. Let $\mathbf{U}, \mathbf{W}$ and $\mathbf{\Phi}$ represent the discrete Fourier coefficients of u, w and ϕ, respectively. Thus, from the convolution theorem, the product operator in time transforms into circular convolution (denoted conv hereafter) under the Discrete Fourier Transform (DFT) of φ, and the following relation formally holds:

$$\mathbf{\Phi} = \text{conv}(\mathbf{U}, \text{conv}(\text{conv}(\ldots, \mathbf{W}))) \tag{A.1}$$

Thus, given a practical algorithm to compute convolutions of real Fourier series is available, any force expressed as a combination of monomials can be computed by recursive operation. Let us consider $y(t) = u(t)w(t)$. The Fourier coefficients $\mathbf{Y}$ of $y(t)$ are then given in terms of $\mathbf{U}$ and $\mathbf{W}$ by:

$$\begin{cases} Y_0 = \dfrac{1}{2}\mathbf{U}^T\mathbf{W} \\ Y_{c,k} = \dfrac{1}{2}\left\{ \displaystyle\sum_{j=0}^{H}\sum_{l=0}^{H} \left[U_{cj}W_{cl} - U_{sj}W_{sl}\right] \hat{\delta}_{(j+l),k} + \left[U_{cj}W_{cl} + U_{sj}W_{sl}\right] \hat{\delta}_{(j-l),k} \right\} \\ Y_{s,k} = \dfrac{1}{2}\left\{ \displaystyle\sum_{j=0}^{H}\sum_{l=0}^{H} \left[U_{cj}W_{sl} + U_{sj}W_{cl}\right] \hat{\delta}_{(j+l),k} + \left[U_{sj}W_{cl} - U_{cj}W_{sl}\right] \hat{\delta}_{(j-l),k} \right\} \end{cases} \tag{A.2}$$

for all $k = 1, \ldots, H$, where the symbol $\hat{\delta}_{a,b}$ denotes the Dirac delta function, equal to 1 for $a = b$ and to zero else. While seemingly complicated, Eq. (A.2) is nothing more than the

product between a matrix $\mathbf{matU} \in \mathbb{R}^{L\times L}$, constructed from the Fourier coefficients of $\mathbf{U}$, and $\mathbf{W}$. For instance, considering H = 3:

$$\mathbf{matU} = \frac{1}{2}\begin{bmatrix} U_0 & U_{c1} & U_{s1} & U_{c2} & U_{s2} & U_{c3} & U_{s3} \\ 2U_{c1} & U_0 & 0 & U_{c1} & -U_{s1} & U_{c2} & -U_{s2} \\ 0 & 0 & U_0 & -U_{s1} & U_{c1} & -U_{s2} & U_{c2} \\ 2U_{c2} & U_{c1} & -U_{s1} & U_0 & 0 & U_{c1} & -U_{s1} \\ 0 & -U_{s1} & U_{c1} & 0 & U_0 & -U_{s1} & U_{c1} \\ 2U_{c3} & U_{c2} & -U_{s2} & U_{c1} & -U_{s1} & U_0 & 0 \\ 0 & -U_{s2} & U_{c2} & -U_{s1} & U_{c1} & 0 & U_0 \end{bmatrix} \tag{A.3}$$

Remark: it shall be noted, from Eq. (A.2), that $(\mathbf{matU})\mathbf{W} = (\mathbf{matW})\mathbf{U}$. Moreover, the structure of $\mathbf{matU}$ is rather simple, as its first row and column border a symmetric matrix.

A.2 Numerical computation of derivatives

Once detected, bifurcations are localized by Newton-Raphson corrections, given by Eq. (2.21) and recalled hereafter:

$$\boldsymbol{\zeta}^{(k)} = -\mathbf{J}_{\text{pt}}^{-1}(\boldsymbol{\Upsilon}_{\text{pt}}^{(k)})\mathbf{Y}_{\text{pt}}(\boldsymbol{\Upsilon}_{\text{pt}}^{(k)})$$

where $\mathbf{Y}_{\text{pt}}$ is a given extended system depending on the set of variables $\boldsymbol{\Upsilon}_{\text{pt}}$, and $\mathbf{J}_{\text{pt}}$ is the corresponding Jacobian matrix. In this section, the numerical computation of the latter is addressed.

A.2.1 Static bifurcations

As they are characterized by a null Floquet exponent, an important practical distinction must be made between the autonomous and non-autonomous (forced) cases for static bifurcations. Indeed, as discussed in Sect. 2.1.4.2, the spectrum of matrix $\mathbf{R}_{\mathbf{X}}$ for autonomous systems contains a trivial zero exponent with associated eigenvector $\boldsymbol{\psi} = (\nabla \otimes \mathbf{I}_n)\mathbf{X}$. Successful bifurcation detection requires shifting the trivial exponent away from zero, and localization should consider the shifted matrix as well.

A.2.1.1 Forced systems

The Jacobian matrices corresponding to the extended systems (2.38) and (2.39) characterizing LP and BP bifurcations are, respectively:

$$\mathbf{J}_{\text{LP}} = \begin{bmatrix} \mathbf{R}_{\mathbf{X}} & \mathbf{0} & \mathbf{R}_{\alpha} \\ (\mathbf{R}_{\mathbf{X}}\boldsymbol{\phi})_{\mathbf{X}} & \mathbf{R}_{\mathbf{X}} & \mathbf{R}_{\mathbf{X}\alpha}\boldsymbol{\phi} \\ \mathbf{0}^T & 2\boldsymbol{\phi}^T & 0 \end{bmatrix} \tag{A.4}$$

and:

$$\mathbf{J}_{\mathrm{BP}} = \begin{bmatrix} \mathbf{R}_{\mathbf{X}} & \mathbf{0} & \mathbf{R}_{\alpha} & \phi \\ (\mathbf{R}_{\mathbf{X}}\phi)_{\mathbf{X}} & \mathbf{R}_{\mathbf{X}} & \mathbf{R}_{\mathbf{X}\alpha}\phi & 0 \\ \phi^T\mathbf{R}_{\mathbf{X}\alpha} & \mathbf{R}_{\alpha}^T & \mathbf{R}_{\alpha\alpha}^T\phi & 0 \\ \mathbf{0}^T & 2\phi^T & 0 & 0 \end{bmatrix} \tag{A.5}$$

Here, α is the continuation parameter, which may or may not be equal to the forcing frequency ω. All of the terms appearing in the above expressions are found in the autonomous case as well, so a discussion of their practical computation is left for the next paragraph.

A.2.1.2 Autonomous systems

Consider a phase condition $g(\mathbf{X}) = 0$. Hill's matrix $\mathbb{H}$ has a double zero eigenvalue, from which one is the arbitrary Floquet exponent of $\mathbf{R}_{\mathbf{X}}$ and associated to the vector φ. The algebraic multiplicity of $\lambda_0 = 0$ is then equal to two. However, depending on the *geometric* multiplicity (m_0) of λ_0, two distinct cases may arise in practice, as follows.

Case 1: $m_0 = 2$

The null-space of $\mathbb{H}$ has full rank, and is thus spanned by φ and ϕ, with the latter an eigenvector to be determined that corresponds to the unique zero eigenvalue of the shifted Jacobian matrix:

$$\mathbf{R}_{\mathbf{Xs}} = \mathbf{R}_{\mathbf{X}} - \frac{\psi\psi^T}{||\psi||^2} \tag{A.6}$$

the extended system for the LP bifurcation reads:

$$\mathbf{Y}_{\mathrm{LPA}}(\mathbf{X}, \omega, \phi, \alpha) = \begin{bmatrix} \mathbf{R} \\ g(\mathbf{X}) \\ \mathbf{R}_{\mathbf{Xs}}\phi \\ \phi^T\phi - 1 \end{bmatrix} \tag{A.7}$$

where α is the chosen continuation parameter. The corresponding Jacobian is thus:

$$\mathbf{J}_{\mathrm{LPA}} = \begin{bmatrix} \mathbf{R}_{\mathbf{X}} & \mathbf{R}_{\omega} & \mathbf{0} & \mathbf{R}_{\alpha} \\ \mathbf{g}_{\mathbf{X}} & 0 & \mathbf{0} & 0 \\ (\mathbf{R}_{\mathbf{Xs}}\phi)_{\mathbf{X}} & \mathbf{R}_{\mathbf{X}\omega}\phi & \mathbf{R}_{\mathbf{Xs}} & \mathbf{R}_{\mathbf{X}\alpha}\phi \\ \mathbf{0}^T & 0 & 2\phi^T & 0 \end{bmatrix} \tag{A.8}$$

The terms $\mathbf{R}_{\mathbf{X}}$ and $\mathbf{R}_{\omega}$ are already given in Eqs. (2.19) and (2.20), respectively. $\mathbf{g}_{\mathbf{X}}$ is a constant vector, and $\mathbf{R}_{\alpha}$ can be computed either by AFT:

$$\mathbf{R}_{\alpha} = (\Gamma_H^{-1} \otimes \mathbf{I}_n)\frac{\partial \mathbf{f}_{\mathrm{NL}}}{\partial \alpha} \tag{A.9}$$

or finite differences, for instance:

$$\mathbf{R}_\alpha = \frac{\mathbf{R}(\alpha+\varepsilon)-\mathbf{R}(\alpha)}{\varepsilon} \tag{A.10}$$

where the perturbation must be taken small relative to the norm of α: $\varepsilon = |\alpha| \times 10^{-6}$. $(\mathbf{R}_{\mathbf{X}\mathbf{s}}\phi)_{\mathbf{X}}$ consists of two terms:

$$(\mathbf{R}_{\mathbf{X}\mathbf{s}}\phi)_{\mathbf{X}} = (\mathbf{R}_{\mathbf{X}}\phi)_{\mathbf{X}} + \frac{1}{||\psi||^2}\left[\left(\mathbf{I}-\frac{2}{||\psi||^2}\psi\psi^T\right)(\psi^T\phi)+\psi\phi^T\right]\psi_X \tag{A.11}$$

of which the second results from the dependence of the trivial eigenvector on $\mathbf{X}$. On the other hand, the first one may be computed through finite differences, as follows:

$$(\mathbf{R}_{\mathbf{X}}\phi)_{\mathbf{X}} = \frac{\mathbf{R}_{\mathbf{X}}(\mathbf{X}+\varepsilon\phi)-\mathbf{R}_{\mathbf{X}}(\mathbf{X})}{\varepsilon} \tag{A.12}$$

To see why this is true, let us consider an arbitrary, constant vector $\mathbf{v} \in \mathbb{R}^{nL}$. The product $(\mathbf{R}_{\mathbf{X}}\phi)_{\mathbf{X}}\mathbf{v}$ is, by definition, the directional derivative of $(\mathbf{R}_{\mathbf{X}}\phi)$ in the direction of $\mathbf{v}$. Moreover, $\mathbf{R}_{\mathbf{X}}\phi$ itself is a directional derivative of $\mathbf{R}$ following the direction of ϕ. Assuming the vector function $\mathbf{R}$ to be twice continuously differentiable, the order of derivation can be inverted by Schwartz's theorem, and so:

$$(\mathbf{R}_{\mathbf{X}}\phi)_{\mathbf{X}}\mathbf{v} = \frac{\partial(\mathbf{R}_{\mathbf{X}}\phi)}{\partial\mathbf{v}} = \frac{\partial(\mathbf{R}_{\mathbf{X}}\mathbf{v})}{\partial\phi} = \frac{\mathbf{R}_{\mathbf{X}}(\mathbf{X}+\varepsilon\phi)\mathbf{v}-\mathbf{R}_{\mathbf{X}}(\mathbf{X})\mathbf{v}}{\varepsilon}+O(\varepsilon^2)$$

Equating the outermost terms in this series of equivalences and noting that $\mathbf{v}$ is arbitrary yields the desired result. The perturbation ε must be chosen small relative to the norm of $\mathbf{X}$; moreover, it is wise to choose in such a way that the magnitude of ϕ does not affect the computation, as only its direction is of interest. Thus, a practical choice is: $\varepsilon = \frac{||\mathbf{X}||}{||\phi||} \times 10^{-6}$. Alternatively, computing this term by an AFT approach is possible, if analytical expressions of second derivatives in time are available. In that case:

$$(\mathbf{R}_{\mathbf{X}}\phi)_{\mathbf{X}} = (\Gamma_H^{-1}\otimes\mathbf{I}_n)\left\{\frac{\partial(\mathbf{r}_{\mathbf{x}}\varphi)}{\partial\mathbf{x}}(\Gamma_H\otimes\mathbf{I}_n)+\omega\frac{\partial(\mathbf{r}_{\mathbf{x}}\varphi)}{\partial\dot{\mathbf{x}}}(\Gamma_H\nabla\otimes\mathbf{I}_n)\right\} \tag{A.13}$$

where:

$$\begin{cases} \dfrac{\partial(\mathbf{r}_{\mathbf{x}}\varphi)}{\partial\mathbf{x}} = \dfrac{\partial}{\partial\mathbf{x}}\left(\dfrac{\partial\mathbf{f}_{\mathrm{NL}}}{\partial\mathbf{x}}\varphi\right)+\dfrac{\partial}{\partial\mathbf{x}}\left(\dfrac{\partial\mathbf{f}_{\mathrm{NL}}}{\partial\dot{\mathbf{x}}}\dot{\varphi}\right) \\ \dfrac{\partial(\mathbf{r}_{\mathbf{x}}\varphi)}{\partial\dot{\mathbf{x}}} = \dfrac{\partial}{\partial\dot{\mathbf{x}}}\left(\dfrac{\partial\mathbf{f}_{\mathrm{NL}}}{\partial\mathbf{x}}\varphi\right)+\dfrac{\partial}{\partial\dot{\mathbf{x}}}\left(\dfrac{\partial\mathbf{f}_{\mathrm{NL}}}{\partial\dot{\mathbf{x}}}\dot{\varphi}\right) \end{cases} \tag{A.14}$$

and $\varphi = (\Gamma_H\otimes\mathbf{I}_n)\phi$, $\dot{\varphi} = \omega(\Gamma_H\nabla\otimes\mathbf{I}_n)\phi$. The remaining terms, i.e. $\mathbf{R}_{\mathbf{X}\omega}\phi$ and $\mathbf{R}_{\mathbf{X}\alpha}\phi$, can be computed by finite differences in two ways: by perturbing $\mathbf{R}_{\mathbf{X}}$ with respect to either ω or α and then multiplying by ϕ, or by perturbing either $\mathbf{R}_\omega$ or $\mathbf{R}_\alpha$ in the direction

of ϕ (see Eq.(A.12)). In the case of frequency, the dynamic stiffness matrix also has a contribution:

$$\mathbf{R}_{\mathbf{X}\omega}\phi = \left[2\omega\nabla^2 \otimes \mathbf{M} + \nabla \otimes \mathbf{C} + \frac{\partial \mathbf{F}_{\mathrm{NL}}}{\partial \mathbf{V}}(\nabla \otimes \mathbf{I}_n) + \frac{\partial \mathbf{F}_{\mathrm{NL}}}{\partial \omega}\right]\phi \tag{A.15}$$

For comparison, the Jacobian matrix of the LP bifurcation is given next in the case of a non-autonomous system:

$$\mathbf{J}_{\mathrm{LPA}} = \begin{bmatrix} \mathbf{R}_{\mathbf{X}} & \mathbf{0} & \mathbf{R}_{\alpha} \\ (\mathbf{R}_{\mathbf{X}}\phi)_{\mathbf{X}} & \mathbf{R}_{\mathbf{X}} & \mathbf{R}_{\mathbf{X}\alpha}\phi \\ \mathbf{0}^T & 2\phi^T & 0 \end{bmatrix} \tag{A.16}$$

where α can be either the forcing frequency or any other parameter. The case of BP bifurcations is analogous in any case, the only differences being the inclusion of an artificial unfolding parameter γ and the degeneracy equation $\mathbf{R}_{\alpha}^T\phi = 0$, as seen in Sect. 2.1.4.1.

Case 2: $m_0 = 1$

The null-space of $\mathbb{H}$ has a rank defect of one, meaning that it is only spanned by φ. Thus, use of Eq. A.7 will inevitably fail, since there is no eigenvector orthogonal to φ in said null-space. To solve this issue, one must consider -similarly to the case of the R1 bifurcation of Sect. 2.2.3- the generalized eigenvector ϕ which forms a Jordan chain. Using any of the formulations for Hill's matrix, manipulation of Eq. 2.106 leads to the extended system :

$$\mathbf{Y}_{\mathrm{LPA}}(\mathbf{X}, \omega, \phi, \alpha) = \begin{bmatrix} \mathbf{R} \\ g(\mathbf{X}) \\ \mathbf{R}_{\mathbf{X}}\phi + \mathbf{D}_1\varphi \\ \varphi^T\phi \end{bmatrix} \tag{A.17}$$

with the corresponding Jacobian matrix:

$$\mathbf{J}_{\mathrm{LPA}} = \begin{bmatrix} \mathbf{R}_{\mathbf{X}} & \mathbf{R}_{\omega} & \mathbf{0} & \mathbf{R}_{\alpha} \\ \mathbf{g}_{\mathbf{X}} & 0 & \mathbf{0}^T & 0 \\ (\mathbf{R}_{\mathbf{X}}\phi)_{\mathbf{X}} & \mathbf{R}_{\mathbf{X}\omega}\phi + \mathbf{D}_{1\omega}\varphi & \mathbf{R}_{\mathbf{X}} & \mathbf{R}_{\mathbf{X}\alpha}\phi + \mathbf{D}_{1\alpha}\varphi \\ \mathbf{0}^T & 0 & \varphi^T & 0 \end{bmatrix} \tag{A.18}$$

A.2.2 Dynamic bifurcations

Stability is lost in this case by a pair of complex conjugate Floquet exponents crossing the imaginary axis. Thus, there is no ambiguity between the trivial and critical exponents, and dynamic bifurcations can be localized without using the shifted matrix $\mathbf{R}_{\mathbf{X}\mathbf{s}}$. The autonomous and non-autonomous cases differ only through the presence (or absence) of the phase condition. For an autonomous system, the Jacobian matrix corresponding to a NS bifurcation is given by:

$$\mathbf{J}_{\text{NSA}} = \begin{bmatrix} \mathbf{R}_{\mathbf{X}} & \mathbf{R}_{\omega} & \mathbf{0} & \mathbf{0} & \mathbf{0} & \mathbf{R}_{\alpha} \\ \mathbf{g}_{\mathbf{X}} & 0 & \mathbf{0}^T & \mathbf{0}^T & 0 & 0 \\ (\mathbf{R}_{\mathbf{X}}\phi_R)_{\mathbf{X}} & \mathbf{R}_{\mathbf{X}\omega R} & \mathbf{R}_{\mathbf{X}} - \kappa^2\mathbf{D}_2 & -\kappa\mathbf{D}_1 & \mathbf{R}_{\mathbf{X}\kappa R} & \mathbf{R}_{\mathbf{X}\alpha}\phi_R - \kappa\mathbf{D}_{1\alpha}\phi_I \\ (\mathbf{R}_{\mathbf{X}}\phi_I)_{\mathbf{X}} & \mathbf{R}_{\mathbf{X}\omega I} & \kappa\mathbf{D}_1 & \mathbf{R}_{\mathbf{X}} - \kappa^2\mathbf{D}_2 & \mathbf{R}_{\mathbf{X}\kappa I} & \mathbf{R}_{\mathbf{X}\alpha}\phi_I + \kappa\mathbf{D}_{1\alpha}\phi_R \\ \mathbf{0}^T & 0 & \mathbf{p}^T & \mathbf{0}^T & 0 & 0 \\ \mathbf{0}^T & 0 & \mathbf{0}^T & \mathbf{p}^T & 0 & 0 \end{bmatrix} \tag{A.19}$$

where the variables $\mathbf{R}_{\mathbf{X}\omega R} = \mathbf{R}_{\mathbf{X}\omega}\phi_R - \kappa\mathbf{D}_{1\omega}\phi_I$ and $\mathbf{R}_{\mathbf{X}\omega I} = \mathbf{R}_{\mathbf{X}\omega}\phi_I + \kappa\mathbf{D}_{1\omega}\phi_R$ have been introduced, as well as: $\mathbf{R}_{\mathbf{X}\kappa R} = -(2\kappa\mathbf{D}_2\phi_R + \mathbf{D}_1\phi_I)$ and $\mathbf{R}_{\mathbf{X}\kappa I} = -(2\kappa\mathbf{D}_2\phi_I - \mathbf{D}_1\phi_R)$. With respect to the previous case, the only novelty are derivatives of $\mathbf{D}_1$, as given by:

$$\begin{aligned} \mathbf{D}_{1\omega} &= 2\nabla \otimes \mathbf{M} + \frac{\partial^2 \mathbf{F}_{\text{NL}}}{\partial\omega\partial\mathbf{V}} \\ &= 2\nabla \otimes \mathbf{M} + (\mathbf{\Gamma}_H^{-1} \otimes \mathbf{I}_n) \left[\frac{\partial^2 \mathbf{f}_{\text{NL}}}{\partial\omega\partial\dot{\mathbf{x}}} + \frac{1}{\omega}\frac{\partial}{\partial\dot{\mathbf{x}}}\left(\frac{\partial \mathbf{f}_{\text{NL}}}{\partial\dot{\mathbf{x}}}\dot{\mathbf{x}}\right) \right] (\mathbf{\Gamma}_H \otimes \mathbf{I}_n) \end{aligned} \tag{A.20}$$

A.3 Bifurcations for memory systems

Hill's method yields the eigenvalue problem Eq. (2.72). As explained in Sect. 2.2.1.3, every convolution term with exponential kernel can be replaced by an additional linear equation with equivalent effect on the dynamics of the main system. In turn, this leads to additional rows and columns in the Hill matrix $\mathbb{H}$, as well as to supplementary Floquet exponents. The purpose of this section is to show that extended algebraic systems characterizing codim-1 bifurcations retain their forms in the presence of memory terms. Indeed, those for static bifurcations are identical to their memoryless counterparts. The same holds in the dynamic case, where a correction is nevertheless added to the usual matrices $\mathbf{D_1}$ and $\mathbf{D_2}$. For brevity, the following developments are shown in the case of a single convolution term; however, as the generalization to an arbitrary number of terms is trivial, the final results are given in their most general form.

Static bifurcations: $\lambda = 0$

The eigenvalue problem reads: $\mathbb{H}\phi = \mathbf{0}$, with the Hill matrix given explicitly by:

$$\mathbb{H} = \begin{bmatrix} -\omega\nabla \otimes \mathbf{I}_n & \mathbf{I}_{nL} & \mathbf{0}_{nL} \\ -\mathbf{E}_1 & -\omega\nabla \otimes \mathbf{I}_n - \mathbf{E}_2 & -\mathbf{I}_L \otimes (\mathbf{M}^{-1}\mathbf{L}_1) \\ \mathbf{I}_{nL} & \mathbf{0}_{nL} & -\omega\nabla \otimes \mathbf{I}_n - a_1\mathbf{I}_{nL} \end{bmatrix} \tag{A.21}$$

where:

$$\begin{cases} \mathbf{E}_1 = \left(\mathbf{I}_L \otimes \mathbf{M}^{-1}\right)\left[\mathbf{I}_L \otimes \mathbf{K} + \dfrac{\partial \mathbf{F}_{\text{NL}}}{\partial \mathbf{X}}\right] \\ \mathbf{E}_2 = \left(\mathbf{I}_L \otimes \mathbf{M}^{-1}\right)\left[\mathbf{I}_L \otimes \mathbf{C} + \dfrac{\partial \mathbf{F}_{\text{NL}}}{\partial \mathbf{V}}\right] \end{cases}$$

Partitioning the eigenvector as $\phi = \left[\phi_x^T, \phi_v^T, \phi_{L1}^T\right]^T$, the first and third (block-wise) rows lead to: $\phi_v = \omega(\nabla \otimes \mathbf{I}_n)\phi_x$ and $\phi_{L1} = (\mathbf{B}_1(\omega) \otimes \mathbf{I}_n)\left[a_1\mathbf{I} - \omega\nabla \otimes \mathbf{I}_n\right]\phi_x$. Thus, multiplying the second line through by $(\mathbf{I}_L \otimes \mathbf{M})$ and introducing these expressions yields the condition:

$$\mathbf{R}_\mathbf{X}\phi_x = 0 \tag{A.22}$$

where the Jacobian includes added stiffness and damping effects. Thus, for an arbitrary number n_e of terms:

$$\mathbf{R}_\mathbf{X} = \left[\mathbf{Z}(\omega) + \sum_{i=1}^{n_e}(\mathbf{B}_i(\omega) \otimes \mathbf{L}_i)\left[a_1\mathbf{I} - \omega\nabla \otimes \mathbf{I}_n\right]\right] + \frac{d\mathbf{F}_{\mathrm{NL}}}{d\mathbf{X}} \tag{A.23}$$

Extended systems are formed from Eq. (A.22) and the equilibrium equations plus a normalization, and -if needed- a phase condition. For BPs, the degenerate nature of the singularity is characterized -as usual- by the relation $\phi_x^T\mathbf{R}_\alpha = 0$, where α is a continuation parameter.

Remark: when treating autonomous systems, the distinction between cases 1 and 2 in App. A.2 applies. Hence, when dealing with rank deficiency ($m_0 = 1$), Eq. (A.17) is to be used. The particularity of memory systems is that the matrix $\mathbf{D}_1$ in that expression must be replaced by a corrected term:

$$\tilde{\mathbf{D}}_1 = \mathbf{D}_1 - \sum_{i=1}^{n_e}(\mathbf{B}_i(\omega) \otimes \mathbf{L}_i)\tilde{\mathbf{M}}_i^{\,2} \tag{A.24}$$

where $\tilde{\mathbf{M}}_i = [a_i\mathbf{I} - \omega(\nabla \otimes \mathbf{I}_n)]$. The frequency-dependence of this matrix must be taken into account to ensure a correct operation of the Newton-Raphson solver.

Dynamic bifurcations: $\lambda = \pm i\kappa$

The eigenvector is complex in this case, i.e.: $\phi = \phi_R + i\phi_I$. Thus, separating real and imaginary parts, the eigenvalue problem (for $+i\kappa$) reads:

$$\begin{cases} \mathbb{H}\phi_R + \kappa\phi_I = \mathbf{0} \\ \mathbb{H}\phi_I - \kappa\phi_R = \mathbf{0} \end{cases} \tag{A.25}$$

The idea, as before, is to decompose the real and imaginary parts of the eigenvector as: $\phi_R = \left[\phi_{Rx}^T, \phi_{Rv}^T, \phi_{RL1}^T\right]^T$ and $\phi_I = \left[\phi_{Ix}^T, \phi_{Iv}^T, \phi_{IL1}^T\right]^T$. Substitution in Eq. (A.25) then yields the following set of coupled matrix equations:

$$\begin{cases} \phi_{Rv} - \omega(\nabla \otimes \mathbf{I}_n)\phi_{Rx} + \kappa\phi_{Ix} & = \mathbf{0} \\ -\mathbf{E}_1\phi_{Rx} - \left[\mathbf{E}_2 + \omega(\nabla \otimes \mathbf{I}_n)\right]\phi_{Rv} - (\mathbf{I}_L \otimes (\mathbf{M}^{-1}\mathbf{L}_1))\phi_{RL1} + \kappa\phi_{Iv} & = \mathbf{0} \\ \phi_{Rx} - \left[a_1\mathbf{I} + \omega(\nabla \otimes \mathbf{I}_n)\right]\phi_{RL1} + \kappa\phi_{IL1} & = \mathbf{0} \end{cases}$$

$$\begin{cases} \phi_{Iv} - \omega(\nabla \otimes \mathbf{I}_n)\phi_{Ix} - \kappa\phi_{Rx} & = \mathbf{0} \\ -\mathbf{E}_1\phi_{Ix} - \left[\mathbf{E}_2 + \omega(\nabla \otimes \mathbf{I}_n)\right]\phi_{Iv} - (\mathbf{I}_L \otimes (\mathbf{M}^{-1}\mathbf{L}_1))\phi_{IL1} - \kappa\phi_{Rv} & = \mathbf{0} \\ \phi_{Ix} - \left[a_1\mathbf{I} + \omega(\nabla \otimes \mathbf{I}_n)\right]\phi_{IL1} - \kappa\phi_{RL1} & = \mathbf{0} \end{cases}$$

which are redundant, as it is possible to express everything as a function of (ϕ_{Rx}, ϕ_{Ix}) alone. To see this, one must use the first, third, fourth and sixth equations to simplify the second and fifth ones, which yields the simplified form:

$$\begin{array}{l} \left(\mathbf{R_X} - \kappa^2 \mathbf{D_2}\right) \phi_{Rx} - \kappa \mathbf{D}_1 \phi_{Ix} + \kappa \tilde{\mathbf{M}}_1 \phi_{IL1} = \mathbf{0} \\ \left(\mathbf{R_X} - \kappa^2 \mathbf{D_2}\right) \phi_{Ix} + \kappa \mathbf{D}_1 \phi_{Rx} - \kappa \tilde{\mathbf{M}}_1 \phi_{RL1} = \mathbf{0} \end{array} \tag{A.26}$$

where $\tilde{\mathbf{M}}_1 = [a_1 \mathbf{I} - \omega(\nabla \otimes \mathbf{I}_L)]$. By introducing the sixth equation above into the third, and vice-versa, ϕ_{RL1} and ϕ_{IL1} are written as linear combinations of ϕ_{Rx} and ϕ_{Ix}, as follows:

$$\left\{ \begin{array}{rcl} \phi_{RL1} = & \left[(\mathbf{I} + \kappa^2 \tilde{\mathbf{M}}_1{}^2)^{-1} \tilde{\mathbf{M}}_1\right] \phi_{Rx} & + \left[\kappa (\mathbf{I} + \kappa^2 \tilde{\mathbf{M}}_1{}^2)^{-1} \tilde{\mathbf{M}}_1{}^2\right] \phi_{Ix} \\ \phi_{IL1} = & \left[\kappa (\mathbf{I} + \kappa^2 \tilde{\mathbf{M}}_1{}^2)^{-1} \tilde{\mathbf{M}}_1{}^2\right] \phi_{Rx} & - \left[(\mathbf{I} + \kappa^2 \tilde{\mathbf{M}}_1{}^2)^{-1} \tilde{\mathbf{M}}_1\right] \phi_{Ix} \end{array} \right. \tag{A.27}$$

Finally, by replacing these expressions into Eq. (A.26), the usual form of the eigenvector equation characterizing dynamic bifurcations is obtained:

$$\begin{array}{rcl} \left(\mathbf{R_X} - \kappa^2 \widetilde{\mathbf{D}_2}\right) \phi_{Rx} & - & \kappa \widetilde{\mathbf{D}_1} \phi_{Ix} = \mathbf{0} \\ \kappa \widetilde{\mathbf{D}_1} \phi_{Rx} & + & \left(\mathbf{R_X} - \kappa^2 \widetilde{\mathbf{D}_2}\right) \phi_{Ix} = \mathbf{0} \end{array} \tag{A.28}$$

where, for n_e convolution terms, the memory effect is in:

$$\left\{ \begin{array}{l} \widetilde{\mathbf{D}_2} = \mathbf{D}_2 + \sum_{i=1}^{n_e} (\mathbf{B}_i(\omega) \otimes \mathbf{L}_i) \tilde{\mathbf{M}}_i \left[(\mathbf{I} + \kappa^2 \tilde{\mathbf{M}}_i{}^2)^{-1} \tilde{\mathbf{M}}_i{}^2\right] \\ \widetilde{\mathbf{D}_1} = \mathbf{D}_1 - \sum_{i=1}^{n_e} (\mathbf{B}_i(\omega) \otimes \mathbf{L}_i) \tilde{\mathbf{M}}_i \left[(\mathbf{I} + \kappa^2 \tilde{\mathbf{M}}_i{}^2)^{-1} \tilde{\mathbf{M}}_i\right] \end{array} \right. \tag{A.29}$$

Extended systems are constructed from Eq. (A.28) together with the equilibrium equations, plus a normalization for each vector in the NS case, or a single one for PD (while imposing $\kappa = \omega/2$). For autonomous systems, a phase condition must be included as well. When using Newton-Raphson iterations to localize these bifurcations, the dependence of these matrices on the frequencies ω and κ must be taken into account for the computation of derivatives. Closed-form expressions are available:

$$\frac{\partial \widetilde{\mathbf{D}_2}}{\partial \kappa} = -2\kappa \sum_{i=1}^{n_e} \tilde{\mathbf{M}}_i \left[(\mathbf{I} + \kappa^2 \tilde{\mathbf{M}}_i{}^2)^{-1} \tilde{\mathbf{M}}_i{}^2 (\mathbf{I} + \kappa^2 \tilde{\mathbf{M}}_i{}^2)^{-1}\right] \tilde{\mathbf{M}}_i{}^2 \tag{A.30}$$

$$\frac{\partial \widetilde{\mathbf{D}_1}}{\partial \kappa} = 2\kappa \sum_{i=1}^{n_e} \tilde{\mathbf{M}}_i \left[(\mathbf{I} + \kappa^2 \tilde{\mathbf{M}}_i{}^2)^{-1} \tilde{\mathbf{M}}_i{}^2 (\mathbf{I} + \kappa^2 \tilde{\mathbf{M}}_i{}^2)^{-1}\right] \tilde{\mathbf{M}}_i \tag{A.31}$$

$$\begin{aligned} \frac{\partial \widetilde{\mathbf{D}_2}}{\partial \omega} = \sum_{i=1}^{n_e} \Bigg\{ & \left[\frac{\partial \tilde{\mathbf{M}}_i}{\partial \omega} - 2\kappa^2 (\mathbf{I} + \kappa^2 \tilde{\mathbf{M}}_i{}^2)^{-1} \tilde{\mathbf{M}}_i \frac{\partial \tilde{\mathbf{M}}_i}{\partial \omega}\right] (\mathbf{I} + \kappa^2 \tilde{\mathbf{M}}_i{}^2)^{-1} \tilde{\mathbf{M}}_i{}^2 \\ & + 2\tilde{\mathbf{M}}_i (\mathbf{I} + \kappa^2 \tilde{\mathbf{M}}_i{}^2)^{-1} \tilde{\mathbf{M}}_i \frac{\partial \tilde{\mathbf{M}}_i}{\partial \omega} \Bigg\} \end{aligned} \tag{A.32}$$

$$\frac{\partial \widetilde{\mathbf{D}_1}}{\partial \omega} = \frac{\partial \mathbf{D}_1}{\partial \omega} - \sum_{i=1}^{n_e} \left\{ \left[\frac{\partial \tilde{\mathbf{M}}_i}{\partial \omega} - 2\kappa^2 (\mathbf{I} + \kappa^2 \tilde{\mathbf{M}}_i{}^2)^{-1} \tilde{\mathbf{M}}_i \frac{\partial \tilde{\mathbf{M}}_i}{\partial \omega} \right] (\mathbf{I} + \kappa^2 \tilde{\mathbf{M}}_i{}^2)^{-1} \tilde{\mathbf{M}}_i \right.$$
$$\left. + \tilde{\mathbf{M}}_i (\mathbf{I} + \kappa^2 \tilde{\mathbf{M}}_i{}^2)^{-1} \frac{\partial \tilde{\mathbf{M}}_i}{\partial \omega} \right\} \tag{A.33}$$

Remark: Eq. (A.24) given above for the localization of static bifurcations is nothing more than the matrix from Eq. (A.29) evaluated at $\kappa = 0$.

Bibliography

[ACA 09] ACARY V. ; BROGLIATO B.
Numerical Methods for Nonsmooth Dynamics. Applications in Mechanics and Electronics. Springer, 2009.

[AHS 19] AHSAN Z., DANKOWICZ H., SIEBER J.
Optimization along families of periodic and quasiperiodic orbits in dynamical systems with delay. *Nonlinear Dynamics*, vol. 99, n° 1, 2019, pp. 837–854, Springer Science and Business Media LLC.

[ALC 19] ALCORTA R., BAGUET S., PRABEL B., PITEAU P., JACQUET-RICHARDET G.
Period doubling bifurcation analysis and isolated sub-harmonic resonances in an oscillator with asymmetric clearances. *Nonlinear Dynamics*, vol. 98, n° 4, 2019, pp. 2939–2960, Springer Science and Business Media LLC.

[ÁLV 18] ÁLVAREZ-BRICEÑO R., KANIZAWA F. T., RIBATSKI G., DE OLIVEIRA L. P.
Validation of turbulence induced vibration design guidelines in a normal triangular tube bundle during two-phase crossflow. *Journal of Fluids and Structures*, vol. 76, 2018, pp. 301–318, Elsevier BV.

[ANT 86] ANTUNES J.
Contribution Ã l'Ã©tude des vibrations de faisceaux de tubes en Ã©coulement transversal. Thèse de doctorat, UniversitÃ© Paris VI, 1986.

[ANT 90] ANTUNES J., AXISA F., BEAUFILS B., GUILBAUD D.
Coulomb friction modelling in numerical simulations of vibration and wear work rate of multispan tube bundles. *Journal of Fluids and Structures*, vol. 4, n° 3, 1990, pp. 287–304, Elsevier BV.

[ANT 92] ANTUNES J., AXISA F., VENTO M. A.
Experiments on Tube/Support Interaction With Feedback-Controlled Instability. *Journal of Pressure Vessel Technology*, vol. 114, n° 1, 1992, pp. 23–32, ASME International.

[ARQ 06] ARQUIER R. ; BELLIZZI S. . B. R. . C. B.
Two methods for the computation of nonlinear modes of vibrating systems at large amplitudes. *Computers and Structures (Elsevier)*, , 2006.

[ASC 79] ASCHER U. ; CHRISTIANSEN J. . R. R.
A Collocation Solver for Mixed Order Systems of Boundary Value Problems. *Mathematics of Computation, Volume 33, Number 146*, , 1979.

[AXI 88] AXISA F., ANTUNES J., VILLARD B.
Overview of Numerical Methods for Predicting Flow-Induced Vibration. *Journal of Pressure Vessel Technology*, vol. 110, n° 1, 1988, pp. 6–14, ASME International.

[AXI 90] AXISA F., ANTUNES J., VILLARD B.
Random excitation of heat exchangertubes by cross-flows. *Journal of Fluids and Structures*, vol. 4, n° 3, 1990, pp. 321–341, Elsevier BV.

[AXI 06] AXISA F., ANTUNES J.
Modelling of Mechanical Systems: Fluid-Structure Interaction. Butterworth-Heinemann, 2006.

[BAK 00] BAKER C. T.
Retarded differential equations. *Journal of Computational and Applied Mathematics*, vol. 125, n° 1-2, 2000, pp. 309–335, Elsevier BV.

[BEN 17] BENTVELSEN B., LAZARUS A.
Modal and stability analysis of structures in periodic elastic states: application to the Ziegler column. *Nonlinear Dynamics*, vol. 91, n° 2, 2017, pp. 1349–1370, Springer Nature.

[BER 07] BERNARDO M., BUDD C., CHAMPNEYS A. R., KOWALCZYK P.
Piecewise-smooth Dynamical Systems: Theory and Applications (Applied Mathematical Sciences). Springer, 2007.

[BLA 05] BLACKLEDGE J. M.
2D Fourier Theory. *Digital Image Processing*, pp. 30–49 Elsevier, 2005.

[BLE 74] BLEVINS R. D.
Fluid Elastic Whirling of a Tube Row. *Journal of Pressure Vessel Technology*, vol. 96, n° 4, 1974, pp. 263–267, ASME International.

[BOR 17a] BORSOI L., PITEAU P., DELAUNE X., ANTUNES J.
Competition between Turbulence and Fluid-Elastic Forces in the Response of a Loosely Supported Tube under Cross-Flow. *Procedia Engineering*, vol. 199, n° Supplement C, 2017, pp. 1282 - 1289. X International Conference on Structural Dynamics, EURODYN 2017.

[BOR 17b] BORSOI L., PITEAU P., DELAUNE X., ANTUNES J.
Gap Effect on the Random and Fluid-Elastic Forces Acting in the Vibration of a Loosely Supported Tube Under Cross-Flow. *Volume 4: Fluid-Structure Interaction* American Society of Mechanical Engineers, jul 2017.

[BOR 18] BORSOI L., PITEAU P., PRABEL B., DELAUNE X., ANTUNES J.
Evolution of the dynamics of loosely supported tubes under cross-flow with the flow velocity and the gaps' size. *FIV2018 Conference*, 2018.

[BOU 15] BOUZIDI S. E., HASSAN M.
An investigation of time lag causing fluidelastic instability in tube arrays. *Journal of Fluids and Structures*, vol. 57, 2015, pp. 264–276, Elsevier BV.

[BRO 99] BROGLIATO B.
Nonsmooth Mechanics. Springer-Verlag, 1999.

[CAI 92] CAI Y. ; CHEN S. S.
Chaotic Vibrations of Nonlinearly Supported Tubes in Crossflow. rapport, 1992, Argonne National Laboratory, Materials and Components Technology Division.

[CAI 99] CAILLAUD S., DE LANGRE E., PITEAU P.
The Measurement of Fluidelastic Effects at Low Reduced Velocities Using Piezoelectric Actuators. *Journal of Pressure Vessel Technology*, vol. 121, n° 2, 1999, pp. 232–238, ASME International.

[CAI 03] CAILLAUD S., DE LANGRE E., BAJ F.
Active Vibration Control for the Measurement of Fluidelastic Effects. *Journal of Pressure Vessel Technology*, vol. 125, n° 2, 2003, pp. 165–170, ASME International.

[CAM 89] CAMERON T. M. ; GRIFFIN J. H.
An Alternating Frequenct/Time Domain Method for Calculating the Steady-State Response of Nonlinear Dynamic Systems. *Journal of Applied Mechanics, ASME*, vol. 56, n° 1, 1989, pp. 149-154.

[CHE 68] CHEN Y. N.
Flow-Induced Vibration and Noise in Tube-Bank Heat Exchangers Due to von Karman Streets. *Journal of Engineering for Industry*, vol. 90, n° 1, 1968, pp. 134–146, ASME International.

[CHE 72] SHENG CHEN S., WAMBSGANSS M. W.
Parallel-flow-induced vibration of fuel rods. *Nuclear Engineering and Design*, vol. 18, n° 2, 1972, pp. 253–278, Elsevier BV.

[CHE 75] SHENG CHEN S.
Vibration of nuclear fuel bundles. *Nuclear Engineering and Design*, vol. 35, n° 3, 1975, pp. 399–422, Elsevier BV.

[CHE 83a] CHEN S. S.
Instability Mechanisms and Stability Criteria of a Group of Circular Cylinders Subjected to Cross-Flow. Part I: Theory. *Journal of Vibration and Acoustics*, vol. 105, n° 1, 1983, pp. 51–58, ASME International.

[CHE 83b] CHEN S. S.
Instability Mechanisms and Stability Criteria of a Group of Circular Cylinders Subjected to Cross-Flow—Part 2: Numerical Results and Discussions. *Journal of Vibration and Acoustics*, vol. 105, n° 2, 1983, pp. 253–260, ASME International.

[CHE 84] CHEN S.
Guidelines for the instability flow velocity of tube arrays in crossflow. *Journal of Sound and Vibration*, vol. 93, n° 3, 1984, pp. 439–455, Elsevier BV.

[CHU 81] CHUA L., USHIDA A.
Algorithms for computing almost periodic steady-state response of nonlinear systems to multiple input frequencies. *IEEE Transactions on Circuits and Systems*, vol. 28, n° 10, 1981, pp. 953–971, Institute of Electrical and Electronics Engineers (IEEE).

[COC 94] COCHELIN B., DAMIL N., POTIER-FERRY M.
Asymptotic-numerical methods and Pade approximants for non-linear elastic structures. *International Journal for Numerical Methods in Engineering*, vol. 37, n° 7, 1994, pp. 1187–1213, Wiley.

[COC 09] COCHELIN B. ; VERGEZ C.
A high order purely frequency-based harmonic balance formulation for continuation of periodic solutions. *Journal of Sound and Vibration*, vol. Volume 324, 2009, pp. 243-262.

[CON 70] CONNORS H. J.
Flow-Induced Vibration in Heat Exchangers, Chapter Fluidelastic vibration of tube arrays excited by cross-flow, pp. 42–56. ASME, 1970.

[CON 81] CONNORS H. J.
Flow-Induced Vibration and Wear of Steam Generator Tubes. *Nuclear Technology*, vol. 55, n° 2, 1981, pp. 311–331, Informa UK Limited.

[COO 65] COOLEY J. W., TUKEY J. W.
An algorithm for the machine calculation of complex Fourier series. *Mathematics of Computation*, vol. 19, n° 90, 1965, pp. 297–297, American Mathematical Society (AMS).

[COU 09] COUDEYRAS N., NACIVET S., SINOU J.-J.
Periodic and quasi-periodic solutions for multi-instabilities involved in brake squeal. *Journal of Sound and Vibration*, vol. 328, n° 4-5, 2009, pp. 520–540, Elsevier BV.

[CRI 81] CRISFIELD M.
A fast incremental/iterative solution procedure that handles “snap-through”. *Computers & Structures*, vol. 13, n° 1-3, 1981, pp. 55–62, Elsevier BV.

[DAI 14] DAI H., YUE X., YUAN J., XIE D.
A fast harmonic balance technique for periodic oscillations of an aeroelastic airfoil. *Journal of Fluids and Structures*, vol. 50, 2014, pp. 231–252, Elsevier BV.

[DAI 18] DAI H., YUE X., YUAN J., XIE D.
Dealiasing harmonic balance method for obtaining periodic solutions of an aeroelastic system. *Aerospace Science and Technology*, vol. 77, 2018, pp. 244–255, Elsevier BV.

[DAM 90] DAMIL N., POTIER-FERRY M.
A New method to compute perturbed bifurcations: Application to the buckling of imperfect elastic structures. *International Journal of Engineering Science*, vol. 28, n° 9, 1990, pp. 943–957, Elsevier BV.

[DAN 10] DANKOWICZ H., SCHILDER F.
An Extended Continuation Problem for Bifurcation Analysis in the Presence of Constraints. *Journal of Computational and Nonlinear Dynamics*, vol. 6, n° 3, 2010, ASME International.

[DAP 15] DAPAS M. L., DEAN W. M., TRACY G. M.
Review of Lessons Learned from the San Onofre Steam Generator Tube Degradation Event. rapport, 2015, US Nuclear Regulatory Commission.

[DET 14] DETROUX T., RENSON L., KERSCHEN G.
The Harmonic Balance Method for Advanced Analysis and Design of Nonlinear Mechanical Systems. *Nonlinear Dynamics, Volume 2*, pp. 19–34 Springer International Publishing, 2014.

[DET 15a] DETROUX T., HABIB G., MASSET L., KERSCHEN G.
Performance, robustness and sensitivity analysis of the nonlinear tuned vibration absorber. *Mechanical Systems and Signal Processing*, vol. 60-61, 2015, pp. 799–809, Elsevier BV.

[DET 15b] DETROUX T., RENSON L., MASSET L., KERSCHEN G.
The harmonic balance method for bifurcation analysis of large-scale nonlinear mechanical systems. *Computer Methods in Applied Mechanics and Engineering*, vol. 296, 2015, pp. 18–38, Elsevier BV.

[DHO 03] DHOOGE A., GOVAERTS W., KUZNETSOV Y. A.
MATCONT: A MATLAB package for numerical bifurcation analysis of ODEs. *ACM Transactions on Mathematical Software*, vol. 29, n° 2, 2003, pp. 141–164, Association for Computing Machinery (ACM).

[DHO 04] DHOOGE A., GOVAERTS W., KUZNETSOV Y. A.
Numerical Continuation of Branch Points of Limit Cycles in MATCONT. *Computational Science - ICCS 2004*, pp. 42–49 Springer Berlin Heidelberg, 2004.

[DID 13] DIDIER J., SINOU J.-J., FAVERJON B.
Nonlinear vibrations of a mechanical system with non-regular nonlinearities and uncertainties. *Communications in Nonlinear Science and Numerical Simulation*, vol. 18, n° 11, 2013, pp. 3250–3270, Elsevier BV.

[DIM 11] DIMITRIADIS G.
Shooting-Based Complete Bifurcation Prediction for Aeroelastic Systems with Freeplay. *Journal of Aircraft*, vol. 48, n° 6, 2011, pp. 1864–1877, American Institute of Aeronautics and Astronautics (AIAA).

[DIM 17] DIMITRIADIS G.
Introduction to nonlinear aeroelasticity. John Wiley & Sons Inc., West Sussex, UK, 2017.

[DOE 91] DOEDEL E., KELLER H. B., KERNEVEZ J. P.
Numerical analysis and control of bifurcation problems(i): bifurcation in finite dimensions. *International Journal of Bifurcation and Chaos*, vol. 01, n° 03, 1991, pp. 493–520, World Scientific Pub Co Pte Lt.

[DOE 03] DOEDEL E. J. ; GOVAERTS W. . K. Y. A.
Computation of Periodic Solution Bifurcations in ODEs Using Bordered Systems. *SIAM Journal of Numerical Analysis*, , 2003.

[DOE 12] DOEDEL E. ; OLDEMAN B.
AUTO-07P: Continuation and Bfurcation Software For Ordinary Differential Equations. rapport, 2012, Concordia University.

[DOK 89] DOKAINISH M., SUBBARAJ K.
A survey of direct time-integration methods in computational structural dynamics—I. Explicit methods. *Computers & Structures*, vol. 32, n° 6, 1989, pp. 1371–1386, Elsevier BV.

[DUA 08] DUAN C., SINGH R.
Isolated sub-harmonic resonance branch in the frequency response of an oscillator with slight asymmetry in the clearance. *Journal of Sound and Vibration*, vol. 314, n° 1-2, 2008, pp. 12–18, Elsevier BV.

[ENG 02] ENGELBORGHS K., LUZYANINA T., ROOSE D.
Numerical bifurcation analysis of delay differential equations using DDE-BIFTOOL. *ACM Transactions on Mathematical Software*, vol. 28, n° 1, 2002, pp. 1–21, Association for Computing Machinery (ACM).

[EPR02] Steam Generator Tube Integrity Risk Assessment: Volume 1: General Methodology, Revision 1 to TR-107623-V1. rapport, 2002, EPRI.

[FAA 11] FAAL R., DERAKHSHAN D.
Flow-Induced Vibration of Pipeline on Elastic Support. *Procedia Engineering*, vol. 14, 2011, pp. 2986–2993, Elsevier BV.

[FEE 98] FEENY B. ; GURAN A. . H. N. . P. K.
A historical review on dry friction and stick-slip phenomena. *Applied Mechanics Review, ASME*, , 1998.

[FER 88] FERRI A., DOWELL E.
Frequency domain solutions to multi-degree-of-freedom, dry friction damped systems. *Journal of Sound and Vibration*, vol. 124, n° 2, 1988, pp. 207–224, Elsevier BV.

[FER 09] FERRI A., LEAMY M.
Error Estimates for Harmonic-Balance Solutions of Nonlinear Dynamical Systems. *50th AIAA/ASME/ASCE/AHS/ASC Structures, Structural Dynamics, and Materials Conference* American Institute of Aeronautics and Astronautics, may 2009.

[FRI 77] FRIEDMANN P., HAMMOND C. E., WOO T.-H.
Efficient numerical treatment of periodic systems with application to stability problems. *International Journal for Numerical Methods in Engineering*, vol. 11, n° 7, 1977, pp. 1117–1136, Wiley.

[GAL 66] GALLI R., LORD B.
Calculation of maximum equilibrium pressure and temperature inside the containment of a pressurized water reactor following rupture of the primary coolant circuit. *Nuclear Engineering and Design*, vol. 4, n° 3, 1966, pp. 331–338, Elsevier BV.

[GEL 95] GELBE H., JAHR M., SCHRÃ¶DER K.
Flow-induced vibrations in heat exchanger tube bundles. *Chemical Engineering and Processing: Process Intensification*, vol. 34, n° 3, 1995, pp. 289–298, Elsevier BV.

[GEN 00] GENDELMAN O., MANEVITCH L. I., VAKAKIS A. F., M'CLOSKEY R.
Energy Pumping in Nonlinear Mechanical Oscillators: Part I—Dynamics of the Underlying Hamiltonian Systems. *Journal of Applied Mechanics*, vol. 68, n° 1, 2000, pp. 34–41, ASME International.

[GEN 11] GENDELMAN O. V.
Targeted energy transfer in systems with external and self-excitation. *Proceedings of the Institution of Mechanical Engineers, Part C: Journal of Mechanical Engineering Science*, vol. 225, n° 9, 2011, pp. 2007–2043, SAGE Publications.

[GIB 88] GIBERT R.
Vibrations des structures. Interactions avec les fluides. Sources d'excitation aleatoires. Ed. Eyrolles, 1988.

[GOR 76] GORMAN D. J.
Experimental Development of Design Criteria to Limit Liquid Cross-Flow-Induced Vibration in Nuclear Reactor Heat Exchange Equipment. *Nuclear Science and Engineering*, vol. 61, n° 3, 1976, pp. 324–336, Informa UK Limited.

[GOV 99] GOVAERTS W., KUZNETSOV Y. A., SIJNAVE B.
Bifurcations of Maps in the Software Package CONTENT. *Computer Algebra in Scientific Computing CASC'99*, pp. 191–206 Springer Berlin Heidelberg, 1999.

[GOV 00] GOVAERTS W., KUZNETSOV Y. A., SIJNAVE B.
Continuation of Codimension-2 Equilibrium Bifurcations in Content. *The IMA Volumes in Mathematics and its Applications*, pp. 163–184 Springer New York, 2000.

[GOV 05] GOVAERTS W. ; KUZNETSOV Y. A.
Numerical Continuation of Bifurcations of Limit Cycles in MATLAB. *SIAM Journal of Scientific Computing*, , 2005.

[GRA 96] GRANGER S.; PAÃ¯DOUSSIS M. P.
An improvement to the quasi-steady model with application to cross-flow-induced vibration of tube arrays. *Journal of Fluid Mechanics*, vol. 320, 1996, pp. 163-184, Cambridge University Press.

[GRE 17] GRENAT C. ; BAGUET S. . D. R. . L. C.-H.
Bifurcation analysis of Nonlinear Normal Modes with the Harmonic Balance Method. *ENOC*, 2017.

[GRE 19] GRENAT C., BAGUET S., LAMARQUE C.-H., DUFOUR R.
A multi-parametric recursive continuation method for nonlinear dynamical systems. *Mechanical Systems and Signal Processing*, vol. 127, 2019, pp. 276–289, Elsevier BV.

[GRO 01] GROLL G. V., EWINS D.
The Harmonic Balance Method with Arc-length Continuation in Rotor/Stator Contact Problems. *Journal of Sound and Vibration*, vol. 241, n° 2, 2001, pp. 223–233, Elsevier BV.

[GUC 83] GUCKENHEIMER J. ; HOLMES P. J.
Nonlinear Oscillations, Dynamical Systems, and Bifurcations of Vector Fields. Springer, 1983.

[GUI 19] GUILLOT L., COCHELIN B., VERGEZ C.
A Taylor series-based continuation method for solutions of dynamical systems. *Nonlinear Dynamics*, vol. 98, n° 4, 2019, pp. 2827–2845, Springer Science and Business Media LLC.

[GUI 20] GUILLOT L., LAZARUS A., THOMAS O., VERGEZ C., COCHELIN B.
A purely frequency based Floquet-Hill formulation for the efficient stability computation of periodic solutions of ordinary differential systems. *Journal of Computational Physics*, vol. 416, 2020, pp. 109477, Elsevier BV.

[HAL 91] HALE J. K., KOÇAK H.
Dynamics and Bifurcations. Springer New York, 1991.

[HEN 05] E. HENDERSON M.
Multiparamerer Parallel Search Branch Switching. *International Journal of Bifurcation and Chaos*, vol. 15, n° 03, 2005, pp. 967–974, World Scientific Pub Co Pte Lt.

[HES 09] HESTHAVEN J. S. ; GOTTLIEB S. . G. D.
Spectral Methods for Time-Dependent Problems. Cambridge University Press, 2009.

[HIN 84] HINDMARSH M. B., JEFFERIES D. J.
On the motions of the offset impact oscillator. *Journal of Physics A: Mathematical and General*, vol. 17, n° 9, 1984, pp. 1791–1804, IOP Publishing.

[HOW 87] HOWELL K. C., PERNICKA H. J.
Numerical determination of Lissajous trajectories in the restricted three-body problem. *Celestial Mechanics*, vol. 41, n° 1-4, 1987, pp. 107–124, Springer Science and Business Media LLC.

[HUN 75] HUNT K. H., CROSSLEY F. R. E.
Coefficient of Restitution Interpreted as Damping in Vibroimpact. *Journal of Applied Mechanics*, vol. 42, n° 2, 1975, pp. 440–445, ASME International.

[JEZ 91] JEZEQUEL L. ; LAMARQUE C.-H.
Analysis of Non-Linear Dynamical Systems by the Normal Form Theory. *Journal of Sound and Vibration*, , 1991.

[JIA 17] BIN JIANG N., RUI XIONG F., GANG ZANG F., XIONG ZHANG Y., HUAN QI H.
Analysis on vibration response of U-tube bundles caused by two-phase cross-flow turbulence. *Annals of Nuclear Energy*, vol. 99, 2017, pp. 328–334, Elsevier BV.

[JUN 97] JUNGBAUER D. E., ECKHARDT L. L.
Flow-Induced Turbocomprosser And Piping Noise And Vibration Problems - Identification, Diagnosis, And Solution. , 1997, Texas A&M University. Turbomachinery Laboratories.

[KAR 13] KARKAR S., COCHELIN B., VERGEZ C.
A high-order, purely frequency based harmonic balance formulation for continuation of periodic solutions: The case of non-polynomial nonlinearities. *Journal of Sound and Vibration*, vol. 332, n° 4, 2013, pp. 968–977, Elsevier BV.

[KEL 83] KELLER H. B.
The Bordering Algorithm and Path Following near singular points of higher nullity. *SIAM Journal on Scientific and Statistical Computing*, , 1983.

[KEL 86] KELLER H. B.
Lectures on Numerical Methods In Bifurcation Problems. Springer-Verlag, 1986.

[KER 13] KERSCHEN G., PEETERS M., GOLINVAL J. C., STÉPHAN C.
Nonlinear Modal Analysis of a Full-Scale Aircraft. *Journal of Aircraft*, vol. 50, n° 5, 2013, pp. 1409–1419, American Institute of Aeronautics and Astronautics (AIAA).

[KIM 97] KIM Y., CHOI S.-K.
A Multiple Harmonic Balance Method For The Internal Resonant Vibration Of A Nonlinear Jeffcott Rotor. *Journal of Sound and Vibration*, vol. 208, n° 5, 1997, pp. 745–761, Elsevier BV.

[KIM 05] KIM T., ROOK T., SINGH R.
Super- and sub-harmonic response calculations for a torsional system with clearance nonlinearity using the harmonic balance method. *Journal of Sound and Vibration*, vol. 281, n° 3-5, 2005, pp. 965–993, Elsevier BV.

[KRA 19] KRACK M., GROSS J.
Harmonic Balance for Nonlinear Vibration Problems. Springer International Publishing, 2019.

[KRY 50] KRYLOV N. M., BOGOLIUBOV N. N.
Introduction to Non-Linear Mechanics. (AM-11), Volume 11. Princeton University Press, 1950.

[KUZ 04] KUZNETSOV Y. A.
Elements of Applied Bifurcation Theory. Springer New York, 2004.

[LAI 19] LAI J., SUN L., LI P.
Two-phase flow-induced instability and nonlinear dynamics of a single tube in tube bundles in the transverse direction. *European Journal of Mechanics - A/Solids*, vol. 78, 2019, pp. 103858, Elsevier BV.

[LAN 91] DE LANGRE E.
Expose 12: Analyse vibratoire d'un composant. *Methodes d'analyse en mecanique non-lineaire des structures*, 1991.

[LAN 96] DE LANGRE E.; LEBRETON G.
An experimental and numerical analysis of chaotic motion in vibration with impact. PETTIGREW M., Ed., *Flow-Induced Vibration*, vol. 328 American Society of Mechanical Engineers, 1996, pp. 317-325.

[LAN 98] LANGRE E. D., VILLARD B.
An Upper Bound On Random Buffeting Forces Caused By Two-Phase Flows Across Tubes. *Journal of Fluids and Structures*, vol. 12, n° 8, 1998, pp. 1005–1023, Elsevier BV.

[LAU 82] LAU S. L., CHEUNG Y. K., WU S. Y.
A Variable Parameter Incrementation Method for Dynamic Instability of Linear and Nonlinear Elastic Systems. *Journal of Applied Mechanics*, vol. 49, n° 4, 1982, pp. 849–853, ASME International.

[LAU 83] LAU S. L., CHEUNG Y. K., WU S. Y.
Incremental Harmonic Balance Method With Multiple Time Scales for Aperiodic Vibration of Nonlinear Systems. *Journal of Applied Mechanics*, vol. 50, n° 4a, 1983, pp. 871–876, ASME International.

[LAZ 10] LAZARUS A. ; THOMAS O.
A harmonic-based method for computing the stability of periodic solutions of dynamical systems. *Comptes Rendus Mecanique*, , 2010.

[LEE 08] LEE Y. S., VAKAKIS A. F., BERGMAN L. A., MCFARLAND D. M., KERSCHEN G., NUCERA F., TSAKIRTZIS S., PANAGOPOULOS P. N.
Passive non-linear targeted energy transfer and its applications to vibration absorption: A review. *Proceedings of the Institution of Mechanical Engineers, Part K: Journal of Multi-body Dynamics*, vol. 222, n° 2, 2008, pp. 77–134, SAGE Publications.

[LEE 17] LEE I.-B., PARK S.
Improving Tube Design of a Problematic Heat Exchanger for Enhanced Safety at Minimal Costs. *Energies*, vol. 10, n° 8, 2017, pp. 1236, MDPI AG.

[LEI 98] LEINE R., VAN CAMPEN D., DE KRAKER A., VAN DEN STEEN L.
Stick-Slip Vibrations Induced by Alternate Friction Models. *Nonlinear Dynamics*, vol. 16, n° 1, 1998, pp. 41–54, Springer Science and Business Media LLC.

[LES 68] LESTER W. A.
De Vogelaere's method for the numerical integration of second-order differential equations without explicit first derivatives: Application to coupled equations arising from the SchrÃ¶dinger equation. *Journal of Computational Physics*, vol. 3, n° 2, 1968, pp. 322–326, Elsevier BV.

[LEV 82] LEVER J. H., WEAVER D. S.
A Theoretical Model for Fluid-Elastic Instability in Heat Exchanger Tube Bundles. *Journal of Pressure Vessel Technology*, vol. 104, n° 3, 1982, pp. 147–158, ASME International.

[LIU 04] LIU L., DOWELL E. H.
The Secondary Bifurcation of an Aeroelastic Airfoil Motion: Effect of High Harmonics. *Nonlinear Dynamics*, vol. 37, n° 1, 2004, pp. 31–49, Springer Science and Business Media LLC.

[LIU 07] LIU L., DOWELL E., THOMAS J.
A high dimensional harmonic balance approach for an aeroelastic airfoil with cubic restoring forces. *Journal of Fluids and Structures*, vol. 23, n° 3, 2007, pp. 351–363, Elsevier BV.

[LIV 62] LIVESEY J. L., DYE R. C. F.
Vortex Excited Vibration of a Heat Exchanger Tube Row. *Journal of Mechanical Engineering Science*, vol. 4, n° 4, 1962, pp. 349–352, SAGE Publications.

[MAC 96] MACDONALD P., SHAH V., WARD L., ELLISON P.
Steam generator tube failures. rapport, apr 1996, Nuclear Regulatory Commission, Washington, DC (United States). Div. of Safety Programs; Idaho National Engineering Lab., Idaho Falls, ID (United States).

[MEI 13] MEINI B.
A shift-and-deflate technique for quadratic matrix polynomials. *Linear Algebra and its Applications*, , 2013.

[MEL 65] MELICE M., MATHYS R., HERSPERGER R.
Time-temperature history in an underground cavity following rupture of a pressurized water nuclear reactor coolant system. *Nuclear Structural Engineering*, vol. 1, n° 1, 1965, pp. 14–20, Elsevier BV.

[MOO 05] MOORE G.
Floquet theory as a computational tool. *SIAM Journal of Numerical Analysis*, , 2005.

[MOR 88] MOREAU J. J., PANAGIOTOPOULOS P. D., Eds. *Nonsmooth Mechanics and Applications*. Springer Vienna, 1988.

[MOU 04a] MOULINEC C., HUNT J., NIEUWSTADT F.
Disappearing Wakes and Dispersion in Numerically Simulated Flows Through Tube Bundles. *Flow, Turbulence and Combustion formerly Applied Scientific Research*, vol. 73, n° 2, 2004, pp. 95–116, Springer Science and Business Media LLC.

[MOU 04b] MOULINEC C., POURQUIÉ† M., BOERSMA‡ B., T. BUCHAL¶ §., NIEUWSTADT|| F.
Direct Numerical Simulation on a Cartesian Mesh of the Flow through a Tube Bundle. *International Journal of Computational Fluid Dynamics*, vol. 18, n° 1, 2004, pp. 1–14, Informa UK Limited.

[MUR 94a] MUREITHI N., PAÃ¯DOUSSIS M., PRICE S.
The Post-Hopf-Bifurcation Response Of A Loosely Supported Cylinder In An Array Subjected To Cross-flow. Part II: Theoretical Model And Comparison With Experiments. *Journal of Fluids and Structures*, vol. 8, n° 7, 1994, pp. 853–876, Elsevier BV.

[MUR 94b] MUREITHI N., PRICE S., PAÃ¯DOUSSIS M.
The Post-Hopf-Bifurcation Response of a Loosely Supported Cylinder in an Array Subjected to Cross-Flow. Part I: Experimental Results. *Journal of Fluids and Structures*, vol. 8, n° 8, 1994, pp. 833–852, Elsevier BV.

[NAK 76] NAKHLA M., VLACH J.
A piecewise harmonic balance technique for determination of periodic response of nonlinear systems. *IEEE Transactions on Circuits and Systems*, vol. 23, n° 2, 1976, pp. 85–91, Institute of Electrical and Electronics Engineers (IEEE).

[NAR 91] NARAYANAN S., JAYARAMAN K.
Chaotic vibration in a non-linear oscillator with Coulomb damping. *Journal of Sound and Vibration*, vol. 146, n° 1, 1991, pp. 17–31, Elsevier BV.

[NAT 92] NATSIAVAS S., GONZALEZ H.
Vibration of Harmonically Excited Oscillators With Asymmetric Constraints. *Journal of Applied Mechanics*, vol. 59, n° 2S, 1992, pp. S284, ASME International.

[NAY 79] NAYFEH A. H. ; MOOK D. T.
Nonlinear Oscillations. John Wiley & Sons, 1979.

[NAY 89] NAYFEH A. H., BALACHANDRAN B.
Modal Interactions in Dynamical and Structural Systems. *Applied Mechanics Reviews*, vol. 42, n° 11S, 1989, pp. S175, ASME International.

[ODE 85] ODEN J., MARTINS J.
Models and computational methods for dynamic friction phenomena. *Computer Methods in Applied Mechanics and Engineering*, vol. 52, n° 1-3, 1985, pp. 527–634, Elsevier BV.

[OTT 81] OTT E.
Strange attractors and chaotic motions of dynamical systems. *Reviews of Modern Physics*, , 1981.

[PAD 95] PADMANABHAN C., SINGH R.
Dynamics of a piecewise non-linear system subject to dual harmonic excitation using parametric continuation. *Journal of Sound and Vibration*, vol. 184, n° 5, 1995, pp. 767–799, Elsevier BV.

[PAI 81] PAIDOUSSIS M.
Fluidelastic vibration of cylinder arrays in axial and cross flow: State of the art. *Journal of Sound and Vibration*, vol. 76, n° 3, 1981, pp. 329–360, Elsevier BV.

[PAI 83] PAIDOUSSIS M.
A review of flow-induced vibrations in reactors and reactor components. *Nuclear Engineering and Design*, vol. 74, n° 1, 1983, pp. 31–60, Elsevier BV.

[PAI 87] PAIDOUSSIS M. P.
Flow-induced Instabilities of Cylindrical Structures. *Applied Mechanics Reviews*, vol. 40, n° 2, 1987, pp. 163–175, ASME International.

[PAI 93] PAIDOUSSIS M., PRICE S., MUREITHI W.
Nonlinear and Chaotic Dynamics of a Two-Degree-of-Freedom Analytical Model for a Rotated Triangular Array in Cross-Flow. *Journal of Fluids and Structures*, vol. 7, n° 5, 1993, pp. 497–520, Elsevier BV.

[PAI 06] PAIDOUSSIS M.
Real-life experiences with flow-induced vibration. *Journal of Fluids and Structures*, vol. 22, n° 6-7, 2006, pp. 741–755, Elsevier BV.

[PAI 13] PAIDOUSSIS M. P., PRICE S. J., LANGRE E. D.
Fluid-Structure Interactions. Cambridge University Press, 2013.

[PAN 12] PANDEY A.
Analysis Of Flow Induced Vibration In Superheater Tube Bundles In Utility Boilers Using Computational Method. 2012.

[PAN 15] PANUNZIO A. M., SALLES L., SCHWINGSHACKL C., GOLA M.
Asymptotic Numerical Method and Polynomial Chaos Expansion for the Study of Stochastic Non-Linear Normal Modes. *Volume 7B: Structures and Dynamics* American Society of Mechanical Engineers, jun 2015.

[PAO 01] PAOLI L.
Time discretization of vibro-impact. *Philosophical Transactions of the Royal Society of London. Series A: Mathematical, Physical and Engineering Sciences*, vol. 359, n° 1789, 2001, pp. 2405–2428, The Royal Society.

[PET 91] PETTIGREW M., CARLUCCI L., TAYLOR C., FISHER N.
Flow-induced vibration and related technologies in nuclear components. *Nuclear Engineering and Design*, vol. 131, n° 1, 1991, pp. 81–100, Elsevier BV.

[PET 16] PETROV E. P.
Analysis of Bifurcations in Multiharmonic Analysis of Nonlinear Forced Vibrations of Gas Turbine Engine Structures With Friction and Gaps. *Journal of Engineering for Gas Turbines and Power*, , 2016.

[PIE 85] PIERRE C., FERRI A. A., DOWELL E. H.
Multi-Harmonic Analysis of Dry Friction Damped Systems Using an Incremental Harmonic Balance Method. *Journal of Applied Mechanics*, vol. 52, n° 4, 1985, pp. 958, ASME International.

[PIT 12] PITEAU P., DELAUNE X., ANTUNES J., BORSOI L.
Experiments and computations of a loosely supported tube in a rigid bundle subjected to single-phase flow. *Journal of Fluids and Structures*, vol. 28, 2012, pp. 56–71, Elsevier BV.

[PIT 15] PITEAU ; BORSOI L. D. X. P. I. A. J.
Computation of a loosely supported tube under cross-flow by a hybrid time-frequency method. *Proceedings of the ASME 2015 PVP Conference*, 2015.

[PIT 18] PITEAU P., BORSOI L., DELAUNE X., ANTUNES J.
Time-domain numerical simulations of a loosely supported tube subjected to frequency-dependent fluid–elastic forces. *Journal of Fluids and Structures*, vol. 81, 2018, pp. 383–398, Elsevier BV.

[PIT 19] PITEAU P., DELAUNE X., BORSOI L., ANTUNES J.
Experimental identification of the fluid-elastic coupling forces on a flexible tube within a rigid square bundle subjected to single-phase cross-flow. *Journal of Fluids and Structures*, vol. 86, 2019, pp. 156–169, Elsevier BV.

[PRA 18] PRABEL B., PITEAU P., BORSOI L., ANTUNES J.
Non-linear Vibration Of Heat Exchanger Tubes Subjected To Fluidelastic Forces. *Proceedings of 9th International Symposium on Fluid-Structure Interactions, Flow-Sound Interactions, Flow-Induced Vibration & Noise.*, 2018.

[PRI 84] PRICE S., PAIDOUSSIS M.
An improved mathematical model for the stability of cylinder rows subject to cross-flow. *Journal of Sound and Vibration*, vol. 97, n° 4, 1984, pp. 615–640, Elsevier BV.

[PRI 95] PRICE S.
A Review of Theoretical Models for Fluidelastic Instability of Cylinder Arrays in Cross-Flow. *Journal of Fluids and Structures*, vol. 9, n° 5, 1995, pp. 463–518, Elsevier BV.

[PRI 01] PRICE S. J.
An Investigation on the Use of Connors' Equation to Predict Fluidelastic Instability in Cylinder Arrays. *Journal of Pressure Vessel Technology*, vol. 123, n° 4, 2001, pp. 448–453, ASME International.

[PUT 14] PUTHANPURAYIL A. M. ; CARR A. J. . D. R. P.
A generic time domain implementation scheme for non-classical convolution damping models. *Engineering Structures*, , 2014.

[REN 16] RENSON L. ; GONZALEZ-BUELGA A. . B. D. A. W. . N. S. A.
Robust identification of backbone curves using control-based continuation. *Journal of Sound and Vibration*, , 2016.

[REN 17] RENSON L., BARTON D. A. W., NEILD S. A.
Experimental Tracking of Limit-Point Bifurcations and Backbone Curves Using Control-Based Continuation. *International Journal of Bifurcation and Chaos*, vol. 27, n° 01, 2017, pp. 1730002, World Scientific Pub Co Pte Lt.

[REN 19] RENSON L., SHAW A., BARTON D., NEILD S.
Application of control-based continuation to a nonlinear structure with harmonically coupled modes. *Mechanical Systems and Signal Processing*, vol. 120, 2019, pp. 449–464, Elsevier BV.

[RIZ 17] RIZNIC J., Ed. *Steam Generators for Nuclear Power Plants*. Elsevier, 2017.

[ROB 66] ROBERTS B.
Low frequency aeroelastic vibrations in a cascade of circular cylinders. *Mechanical Engineering Science Monograph, No. 4* Institution of Mechanical Engineers (London), 1966.

[ROS 62] ROSENBERG R. M.
The Normal Modes of Nonlinear n-Degree-of-Freedom Systems. *Journal of Applied Mechanics*, vol. 29, n° 1, 1962, pp. 7–14, ASME International.

[SAL 16] SALLES L., STAPLES B., HOFFMANN N., SCHWINGSHACKL C.
Continuation techniques for analysis of whole aeroengine dynamics with imperfect bifurcations and isolated solutions. *Nonlinear Dynamics*, vol. 86, n° 3, 2016, pp. 1897–1911, Springer Science and Business Media LLC.

[SAR 03] SARPKAYA T.
A Critical Review of the Intrinsic Nature of VIV. *IUTAM Symposium on Integrated Modeling of Fully Coupled Fluid Structure Interactions Using Analysis, Computations and Experiments*, pp. 159–161 Springer Netherlands, 2003.

[SEY 10] SEYDEL R.
Practical Bifurcation and Stability Analysis. Springer, 2010.

[SHA 09] SHAMPINE L. F., THOMPSON S.
Numerical Solution of Delay Differential Equations. *Delay Differential Equations*, pp. 1–27 Springer US, 2009.

[SHI 14] SHINDE V., MARCEL T., HOARAU Y., DELOZE T., HARRAN G., BAJ F., CARDOLACCIA J., MAGNAUD J., LONGATTE E., BRAZA M.
Numerical simulation of the fluid-structure interaction in a tube array under cross flow at moderate and high Reynolds number. *Journal of Fluids and Structures*, vol. 47, 2014, pp. 99–113, Elsevier BV.

[SMI 11] SMITH H.
An Introduction to Delay Differential Equations with Applications to the Life Sciences. Springer New York, 2011.

[STR 94] STROGATZ S. H.
Nonlinear Dynamics and Chaos. Addison-Wesley Publishing Company, 1994.

[SUB 89] SUBBARAJ K., DOKAINISH M.
A survey of direct time-integration methods in computational structural dynamics—II. Implicit methods. *Computers & Structures*, vol. 32, n° 6, 1989, pp. 1387–1401, Elsevier BV.

[SUN 97] SUNDARARAJAN P., NOAH S. T.
Dynamics of Forced Nonlinear Systems Using Shooting/Arc-Length Continuation Method—Application to Rotor Systems. *Journal of Vibration and Acoustics*, vol. 119, n° 1, 1997, pp. 9–20, ASME International.

[SUN 19] SUN N., JIA CHENG R., NAN ZHANG Y., QING LIU B., SUNDEN B.
Design guidelines for fluid-elastic instability of tube bundles subjected to two-phase cross flow. *Journal of Zhejiang University-SCIENCE A*, vol. 20, n° 8, 2019, pp. 577–589, Zhejiang University Press.

[SWA 84] SWARZTRAUBER P. N.
FFT algorithms for vector computers. *Parallel Computing*, vol. 1, n° 1, 1984, pp. 45–63, Elsevier BV.

[TAK 79] TAKAHASHI K.
A method of stability analysis for non-linear vibration of beams. *Journal of Sound and Vibration*, vol. 67, n° 1, 1979, pp. 43–54, Elsevier BV.

[TAN 81] TANAKA H., TAKAHARA S.
Fluid elastic vibration of tube array in cross flow. *Journal of Sound and Vibration*, vol. 77, n° 1, 1981, pp. 19–37, Elsevier BV.

[TAY 20] TAYLOR C. E., PETTIGREW M. J.
A Design Guideline for Random Excitation Forces Due to Two-Phase Cross Flow in Tube Bundles. *Journal of Pressure Vessel Technology*, vol. 142, n° 6, 2020, ASME International.

[TIL 18] VAN TIL J., ALIJANI F., VOORMEEREN S., LACARBONARA W.
Frequency domain modeling of nonlinear end stop behavior in Tuned Mass Damper systems under single- and multi-harmonic excitations. *Journal of Sound and Vibration*, vol. 438, 2018, pp. 139–152, Elsevier BV.

[TIS 01] TISSEUR F., MEERBERGEN K.
The Quadratic Eigenvalue Problem. *SIAM Review*, vol. 43, n° 2, 2001, pp. 235–286, Society for Industrial & Applied Mathematics (SIAM).

[VIG 18] VIGUÉ P., VERGEZ C., KARKAR S., COCHELIN B.
Assessment of the harmonic balance method on a self-oscillating one-degree-of-freedom system with regularized friction. *Nonlinear Dynamics*, vol. 92, n° 3, 2018, pp. 961–971, Springer Science and Business Media LLC.

[VIO 05] VIOLETTE R., PETTIGREW M. J., MUREITHI N. W.
Fluidelastic Instability of an Array of Tubes Preferentially Flexible in the Flow Direction Subjected to Two-Phase Cross Flow. *Journal of Pressure Vessel Technology*, vol. 128, n° 1, 2005, pp. 148–159, ASME International.

[VOU 20] VOURGANTI V., DESAI A., SAMUKHAM S., VYASARAYANI C. P.
Effect of nonlinear cladding stiffness on the stability and Hopf bifurcation of a heat-exchanger tube subject to cross-flow. *Meccanica*, , 2020, Springer Science and Business Media LLC.

[WAN 93] WANG J. H., CHEN W. K.
Investigation of the Vibration of a Blade With Friction Damper by HBM. *Journal of Engineering for Gas Turbines and Power*, vol. 115, n° 2, 1993, pp. 294, ASME International.

[WAN 19] WANG X., ZHU W., ZHAO X.
An Incremental Harmonic Balance Method With a General Formula of Jacobian Matrix and a Direct Construction Method in Stability Analysis of Periodic Responses of General Nonlinear Delay Differential Equations. *Journal of Applied Mechanics*, vol. 86, n° 6, 2019, ASME International.

[WEA 83] WEAVER D. S., SCHNEIDER W.
The Effect of Flat Bar Supports on the Crossflow Induced Response of Heat Exchanger U-Tubes. *Journal of Engineering for Power*, vol. 105, n° 4, 1983, pp. 775–781, ASME International.

[WEA 08] WEAVER D. S.
Some thoughts on the elusive mechanism of fluidelastic instability in heat exchanger tube array. *Proceedings of the 9th International Conference On Flow-Induced Vibration.*, vol. 1, Prague, Czech Republic, 2008 pp. 290–297.

[WHI 82] WHISTON G., THOMAS G.
Whirling instabilities in heat exchanger tube arrays. *Journal of Sound and Vibration*, vol. 81, n° 1, 1982, pp. 1–31, Elsevier BV.

[WIT 13] WITTE V. D., ROSSA F. D., GOVAERTS W., KUZNETSOV Y. A.
Numerical Periodic Normalization for Codim 2 Bifurcations of Limit Cycles: Computational Formulas, Numerical Implementation, and Examples. *SIAM Journal on Applied Dynamical Systems*, vol. 12, n° 2, 2013, pp. 722–788, Society for Industrial & Applied Mathematics (SIAM).

[WOI 20] WOIWODE L., BALAJI N. N., KAPPAUF J., TUBITA F., GUILLOT L., VERGEZ C., COCHELIN B., GROLET A., KRACK M.
Comparison of two algorithms for Harmonic Balance and path continuation. *Mechanical Systems and Signal Processing*, vol. 136, 2020, pp. 106503, Elsevier BV.

[XIE 15] XIE L. ; BAGUET S. . P. B. . D. R.
Parametric analysis of the nonlinear behavior of rotating structures. *Computers and Information in Engineering Conference*, , 2015.

[XIE 16] XIE L. ; BAGUET S. . P. B. . D. R.
Numerical Tracking of Limit Points for Direct Parametric Analysis in Nonlinear Rotordynamics. *Journal of Vibration and Acoustics, ASME*, , 2016.

[XIE 17] XIE L., BAGUET S., PRABEL B., DUFOUR R.
Bifurcation tracking by Harmonic Balance Method for performance tuning of nonlinear dynamical systems. *Mechanical Systems and Signal Processing*, vol. 88, 2017, pp. 445–461, Elsevier BV.

[YET 93a] YETISIR M., WEAVER D.
An Unsteady Theory For Fluidelastic Instability in an Array of Flexible Tubes in Cross-Flow. Part I: Theory. *Journal of Fluids and Structures*, vol. 7, n° 7, 1993, pp. 751–766, Elsevier BV.

[YET 93b] YETISIR M., WEAVER D.
An Unsteady Theory for Fluidelastic Instability in an Array of Flexible Tubes in Cross-Flow. Part II: Results and Comparison With Experiments. *Journal of Fluids and Structures*, vol. 7, n° 7, 1993, pp. 767–782, Elsevier BV.

[YOS 00] YOSHITAKE Y., SUEOKA A.
Forced Self-Excited Vibration with Dry Friction. *World Scientific Series on Nonlinear Science Series A*, pp. 237–259 WORLD SCIENTIFIC, apr 2000.

[ZIA 06] ZIADA S.
Vorticity shedding and acoustic resonance in tube bundles. *Journal of the Brazilian Society of Mechanical Sciences and Engineering*, vol. 28, n° 2, 2006, pp. 186–189, Springer Science and Business Media LLC.

FOLIO ADMINISTRATIF

THESE DE L'UNIVERSITE DE LYON OPEREE AU SEIN DE L'INSA LYON

NOM : ALCORTA DATE de SOUTENANCE : 27/05/2021

Prénoms : Roberto

TITRE : Prediction of non-linear responses and bifurcations of impacting systems: Contribution to the understanding of steam generator vibrations

NATURE : Doctorat Numéro d'ordre : 2021LYSEI032

Ecole doctorale : MEGA

Spécialité :Mécanique – Génie Mécanique – Génie Civil

RESUME : Dans les Générateurs de Vapeur (GV) des réacteurs nucléaires à eau pressurisée, le composant clé est un assemblage de tubes cintrés dont l'objectif est d'assurer l'échange de chaleur entre les écoulements du circuit primaire -en contact avec le réacteur- et secondaire -destiné à être évaporé-. En conséquence, la prédiction précise du comportement dynamique de ces tubes est cruciale pour bien estimer la durée de vie des équipements et permettre un fonctionnement sécurisé. Or, cette tâche est loin d'être triviale, en raison de la nature multi-physique du problème (vibrations induites par une instabilité du type fluide-élastique) et de son caractère fortement non-linéaire (contacts frottants entre les tubes et leur supports). Ce dernier aspect, en particulier, implique que les réponses susceptibles d'être observées dans la pratique sont fortement sensibles aux valeurs des paramètres du système : vitesse moyenne de l'écoulement, excentricité des tubes, raideur de choc, parmi d'autres. Les deux objectifs principaux de cette thèse sont : 1. développer les méthodes numériques nécessaires pour permettre un traitement efficace et robuste de ce problème, et 2. d'appliquer ces méthodes à des systèmes simplifiés dont la phénoménologie est représentative des vibrations des tubes de GV. Dans un premier temps, on étend notamment les algorithmes existants de continuation basés sur la méthode de la balance harmonique (HBM). Ainsi, une analyse complète des bifurcations peut être réalisée sur les réponses périodiques et quasi-périodiques pour des systèmes mécaniques non-linéaires de natures très diverses, et en particulier pour ceux faisant intervenir des termes à retard. Ensuite, les résultats des analyses approfondies menées sur les cas d'étude choisis sont présentés. Ceux-ci mettent en évidence la dynamique extrêmement riche des systèmes à impacts, permettant à la fois de démontrer la robustesse des méthodes développées et d'avancer dans la compréhension des vibrations des tubes de GV.
La thèse a été réalisée au Laboratoire de Mécanique des Contacts et des Structures, UMR CNRS 5259, INSA Lyon, Institut Carnot Ingénierie@Lyon et au laboratoire d'Etudes de Dynamique (DEN/DANS/DM2S/SEMT/DYN) du CEA Saclay.

MOTS-CLÉS : générateurs de vapeur, instabilité fluide-élastique, dynamique non-linéaire, systèmes à retards, balance harmonique, suivi des bifurcations, méthodes de continuation, réponses quasi-périodiques

Laboratoire (s) de recherche : Laboratoire de Mécanique des Contacts et des Structures
UMR CNRS 5259 – INSA de Lyon
Avenue Jean Capelle O
69100 Villeurbanne Cedex FRANCE

Directeur de thèse: M. Georges JACQUET

Président de jury : Mme Anne TANGUY

Composition du jury :

A. Tanguy	C. Touzé	A. Lazarus
G. Jacquet	S. Baguet	B. Prabel
S. Terrien	B. Cochelin	L. Salles